University of California
Santa Barbara

Nonlinear propagation and topographic diffraction of volcano infrasound

A dissertation submitted in partial satisfaction
of the requirements for the degree

Doctor of Philosophy
in
Earth Science

by

Sean Maher

Committee in charge:

Professor Robin Matoza, Chair
Professor Toshiro Tanimoto
Professor Zachary Eilon
Professor Chen Ji

June 2022

The Dissertation of Sean Maher is approved.

Professor Toshiro Tanimoto

Professor Zachary Eilon

Professor Chen Ji

Professor Robin Matoza, Committee Chair

June 2022

Nonlinear propagation and topographic diffraction of volcano infrasound

by

Sean Maher

Acknowledgements

First and foremost thank you to my advisor Robin Matoza for everything–the opportunity to do my PhD here, the data for my research, funding, guidance, feedback, meetings, recommendation letters, and general encouragement. Robin taught me to develop my own hypotheses and to test them in a systematic way, and he pushed me to interpret results in light of all relevant literature on the topic. He encouraged me to learn how to solve problems independently, but was responsive and insightful with his feedback when I needed help. His advisorship has certainly helped to make me a better scientist.

I am also grateful for my committee members Zachary Eilon, Chen Ji and Toshiro Tanimoto for taking the time to review my work and provide helpful criticism, and assess the feasibility of my proposed work. Thank you for being realistic about the number and scope of the projects needed to complete this dissertation.

Thank you to Catherine de Groot-Hedlin and Kent Gee, who were especially involved in answering my many questions about numerical modeling and nonlinear propagation physics. I appreciate the time and effort they spent to further my understanding.

Thank you also to the many co-authors that provided insight and feedback on my work, including David Fee, Keehoon Kim, Arthur Jolly, Akihiko Yokoo and Alexandra Iezzi. I am also grateful to co-authors Kathleen McKee, Cassandra Smith and Leighton Watson for the opportunities to collaborate on projects outside my PhD.

Thank you to Jeffrey Tepper, Darren Gravley, Katharine Cashman and Michael Kendall for being scientific role models during my undergraduate and masters education. Their enthusiasm for science and volcanoes helped inspire me to pursue a career in this field.

Thank you to Phillip Dawson and Alicia Hotovec-Ellis for hosting my internship with the UGSS California Volcano Observatory, and for accepting my postdoc application. I look forward to working with them more closely and developing new algorithms to study seismicity at California's volcanoes.

Thank you to Tracianne Nielson for hosting my visits to BYU, including me in the outdoor

balloon explosion experiments and taking time to discuss research with me.

Many thanks to the unsung heroes of UCSB Earth Science–Yann Ricard, Peter Green, Shannon Dalton, Yvette Howze, Kris Duckett and others. Your help with the logistics of grad school makes it easier for all of us to get through it.

Thank you to the geophysics grad students at UCSB for the many conversations and bonfires that helped to view science from a different perspective and make it more human. Looking at you Rodrigo, Richard, Hugo, Jeremy, Brennan, Jon, Han, Cristhian, Aaron, Jiong, Kaelynn, Mareike, and Annie.

Thanks to the friends I made along the way–Devin, Stephen, Tiffany, Thomas, Jenna, and Justin–and to the friends I was able to keep in touch with–Nick, Nate, Mike and Sonya. All the climbing, surfing, hiking and camping helped me stay sane. Special thanks to Brad and Campbell for humoring my attempts at song writing and band leadership.

Finally, thank you to my parents for all their love, support and encouragement. They taught me to respect science, to be curious and to pursue my passions. Most of all they believed in me when it seemed like no one else did. I couldn't have done it without them.

Curriculum Vitæ

Sean Maher

Education

2022	PhD in Geophysics, University of California, Santa Barbara
2017	MSc in Volcanology, University of Bristol
2016	BS in Geology, University of Puget Sound

Publications

2022	**Maher, S. P.**, Matoza, R. S., Jolly, A. D., de Groot-Hedlin, C. D., Gee, K., Fee, D., Iezzi, A.M., Evidence for near-source nonlinear propagation of volcano infrasound from strombolian explosions at Yasur volcano, Vanuatu: *Bulletin of Volcanology*, v. 84, doi: 10.1007/s00445-022-01552-w.
2022	Watson, L. M., Iezzi, A. M., Toney, L., **Maher, S. P.**, Fee, D., McKee, K., Ortiz, H.D., Matoza, R. S., Anderson, J. F., Witsil, A. J. C., Gestrich, J. E., Bishop, J. W., Johnson, J. B., Volcano Infrasound: Progress and Future Directions: *Bulletin of Volcanology*, v. 84, doi: 10.1007/s00445-022-01544-w.
2021	McKee, K., Smith, S., Reath, K., Snee, E., **Maher, S.**, Matoza, R., Carn, S., Roman, D., Mastin, L., Anderson, K., Damby, D., Itikara, I., Mulina, K., Saunders, S., Assink, J., de Negri Leiva, R., Perttu, A., Evaluating the state-of-the-art in remote volcanic eruption characterization Part II: Ulawun volcano, Papua New Guinea: *Journal of Volcanology and Geothermal Research*, v. 420, doi: 10.1016/j.jvolgeores.2021.107381.
2021	McKee, K., Smith, C., Reath, K., Snee. E., **Maher, S.**, Matoza, R. S., Carn, S., Mastin, L., Anderson, K., Damby, D., Roman, D., Degterev, A., Rybin, A., Chibisova, M., Assink, J., De Negri Leiva, R., Perttu, A., Evaluating the state-of-the-art in remote volcanic eruption characterization Part I: Raikoke volcano, Kuril Islands: *Journal of Volcanology and Geothermal Research*, v. 419, doi: 10.1016/j.jvolgeores.2021.107354.
2021	**Maher, S. P.**, Matoza, R. S., de Groot-Hedlin, Kim, K., Gee, K. L., Evaluating the applicability of a screen diffraction approximation to local volcano infrasound: *Volcanica*, v. 4(1), p. 67 – 85, doi: 10.30909/vol.04-.01.6785.
2020	**Maher, S. P.**, Matoza, R. S., de Groot-Hedlin, C., Gee. K. L., Fee, D., Yokoo, A., Investigating Spectral Distortion of Local Volcano Infrasound by Nonlinear Propagation at Sakurajima Volcano, Japan: *Journal of Geophysical Research*, v. 125, e2019JB01828, doi: 10.1029/2019JB018284.
2018	**Maher, S.**, and Kendall, J., Crustal anisotropy and state of stress at Uturuncu Volcano Bolivia, from shear-wave splitting measurements and magnitude – frequency distributions in seismicity: *Earth and Planetary Science Letters*, v. 495, p. 38-49, doi: 10.1016/j.epsl.2018.04.060.

Professional activities

2018–2022	Graduate Student Researcher, Department of Earth Science, UCSB
2017–2022	Graduate Teaching Assistant, Department of Earth Science, UCSB
June–August 2021	Intern, USGS California Volcano Observatory
June–July 2021	Mentor, UCSB Research Mentorship Program
2020	Peer Reviewer, Journal of Volcanology and Geothermal Research
July 2019	Workshop participant, CIDER
July 2018	Workshop participant, University at Buffalo Volcano Hazards Field-Scale Experiment
June 2018	Workshop participant, IRIS Workshop 2018
January–May 2016	Undergraduate Course Assistant, University of Puget Sound

Awards

2022	Geophysics Award (UCSB)
2021	Richard V. Fisher Scholarship in Volcanology (UCSB)
2020	Alumni Graduate Award for Research Excellence (UCSB)
2019	Harry Glicken Memorial Graduate Fellowship (UCSB)
2017	MSc with Distinction (University of Bristol)
2016	Cum Laude, Honors in Geology (University of Puget Sound)

Abstract

Nonlinear propagation and topographic diffraction of volcano infrasound

by

Sean Maher

Volcanic eruptions emit sound waves that are typically dominant at infrasonic frequencies (∼0.01–20 Hz) and that have been used to estimate eruption source parameters valuable for hazard mitigation. However, the accuracy of these estimates depends on the ability to recover the pressure-time history of the acoustic source, which may be distorted during propagation even at local recording distances (<15 km). We aim to quantify potential distortions caused by diffraction over topography and wave steepening during nonlinear propagation.

To investigate the effects of topographic diffraction, we evaluate the ability of a thin screen approximation to predict amplitude losses over topography at Sakurajima Volcano, Japan. Using synthetic data from numerical modeling, we show that amplitude losses from diffraction over volcano topography are systematically less than predicted for a thin screen. We propose that attenuation by diffraction may be counteracted by acoustic focusing (constructive interference between reflections along concave slopes). We conclude that thin screens are inappropriate proxies for volcano topography, and maintain that numerical simulations are required to account for wavefield interactions with topography.

To investigate the role of near-source nonlinear propagation in volcano infrasound, we apply a previously developed, quadspectral density-based nonlinearity indicator to observed and synthetic signals corresponding to explosive eruptions at Sakurajima Volcano, Japan and Yasur Volcano, Vanuatu. We hypothesize that significant nonlinearity will be expressed as energy transfer from low to high frequencies as the acoustic waves steepen towards shock waves. At Sakurajima Volcano we find evidence for spectral energy transfer in the synthetic data but inconclusive results from the observed signals, suggesting that nonlinearity signatures may be

present but obscured by complicating factors (e.g., topography, wind, waveform undersampling). At Yasur Volcano we find evidence for nonlinearity in both synthetics and observations, suggesting that nonlinearity is better observed at short source-receiver distances and with higher sampling rates. At both volcanoes we estimate that cumulative spectral changes by nonlinear propagation are small (<1% of source levels). We conclude that, for signal amplitudes associated with low-level explosions common in field campaigns, nonlinear propagation does not introduce significant errors to acoustically-based source parameter estimates when compared to a linear assumption.

Contents

Chapter 1

Introduction

1.1 Infrasound

Human ears can hear acoustic waves with frequencies between approximately 20 Hz and 20,000 Hz; sound with frequencies above 20,000 Hz is termed ultrasound while sound below 20 Hz is called infrasound (Pierce, 1981). Acoustic waves are pressure disturbances that propagate as compressions and rarefactions by the elastic restoring force of the particles in the medium (Pierce, 1981). Atmospheric disturbances at frequencies lower than ∼0.003 Hz are instead restored by the gravitational force and are known as gravity waves (Gossard and Hooke, 1975; Nappo, 2013). Acoustic waves propagate at a speed dependent on the temperature and density of the medium, which may vary with altitude and with the strength and direction of winds (e.g., Le Pichon et al., 2005; Whitaker and Norris, 2008; Kim et al., 2018). Infrasound is detected with pressure transducers specifically calibrated for low frequencies, and is digitally recorded at a sampling rate dependent on instrument capabilities and memory capacity (e.g., Marcillo et al., 2012; Anderson et al., 2018a; Nief et al., 2019). Atmospheric waves including infrasound may be recorded at a single sensor to simply characterize a signal (e.g., Reed, 1987; Sakai et al., 1996; Morrissey and Chouet, 1997; Johnson, 2019), at a network of sensors to assess differences in propagation to different locations (e.g., Johnson, 2003; Yokoo et al., 2014; Jolly et al., 2017), or at an array of linked sensors to determine the propagation direction (and thus

a backazimuth) of the wave (e.g., Ripepe and Marchetti, 2002; Matoza et al., 2007; Le Pichon and Cansi, 2003; Olson and Szuberla, 2008).

An infrasound recording is a convolution of processes occuring at the acoustic source and during propagation (Oppenheim et al., 1999; Johnson, 2003; Kim et al., 2015). Infrasound sources include many man-made and natural processes, such as nuclear explosions, fireworks, volcanic eruptions, ocean waves, meteorites and earthquakes (e.g., Whitaker and Norris, 2008; Edwards, 2010; Landès et al., 2012). An infrasound recording made near the source will closely resemble the pressure history of the source process, but recordings made a distance will have additional complications from propagation effects (e.g., Morrissey and Chouet, 1997; Lacanna et al., 2014; McKee et al., 2014). The amplitude of an acoustic wave reduces with source-receiver distance primarily due to geometrical spreading (energy spread over a larger area) and to absorption (energy transfer to the translation and rotation of air molecules), although absorption rates at infrasonic wavelengths are so low that they are typically neglected at recording distances less than ∼15 km (Sutherland and Bass, 2004; Whitaker and Norris, 2008). Amplitudes may further be reduced by diffraction and scattering from topography, refraction in wind or temperature gradients, and coupling into the ground as seismic waves (e.g., Embleton, 1996; Sabatini et al., 2016b; Bishop et al., 2022). Conversely, amplitudes may be increased by constructive interference of waves that have been reflected from topography or refracted by gradients in wind or temperature, and signals may feature multiple arrivals from reflected or refracted paths (Embleton et al., 1976; Embleton, 1996; Whitaker and Norris, 2008).

1.1.1 Linear propagation

The pressure disturbance of most sound waves is very small compared to the ambient pressure of the medium. For example, the amplitude of a two-person conversation is approximately 0.02 Pa (60 dB relative to 20 μPa), whereas the air pressure at sea level is approximately 101 kPa (194 dB re 20 μPa) (Pierce, 1981). Consequently, the passage of most sound waves has little effect on the medium of propagation, and the evolution of the signal properties obey

linear relationships with distance and time (Pierce, 1981; Atchley, 2005). This means that each component of the sound wave travels at the speed of medium regardless of its amplitude or frequency, so the wave will retain its original shape in the absence of geometrical spreading or absorption. In the presence of geometrical spreading each frequency component will lose amplitude at the same rate (e.g., $1/r$ for spherically spreading waves); in the presence of absorption, each frequency component will lose amplitude at a constant rate according to its absorption coefficient in the medium (Pierce, 1981; Sutherland and Bass, 2004). In the case of interactions between multiple linearly-propagated waves, the principle of linear superposition holds (i.e., the total effect is the sum of the individual effects) (Atchley, 2005). In the case of diffraction over a barrier or refraction in a sound speed gradient, a linearly-propagated wave will exhibit additional losses by geometrical spreading and absorption along the increased path length (Maekawa, 1968). This means that the properties of a linearly-propagated acoustic wave can be accurately approximated at an arbitrary distance given a known source-time function and properties of the medium and lower boundary.

1.1.2 Nonlinear propagation

When the amplitude of a pressure disturbance is large relative to the ambient pressure of the medium, the assumption of linear propagation breaks down. At high differential pressures the passage of a sound wave has non-negligble effects on the medium, including changes in temperature and particle velocity (Atchley, 2005; Hamilton and Blackstock, 2008). Higher-amplitude portions of a nonlinearly-propagating wave travel at higher speeds than lower-amplitude portions, causing distortions in the wavefield (Prunty, 2019). The highest-amplitude portion of such a wave may overtake the original onset of the wave, creating a sharp discontinuity in pressure known as a shock wave (Kinney and Graham, 1985). Similarly, the end of the wave may overtake the lowest-amplitude (rarefaction) portion of the wave, leading to the formation of sawtooth or N-waves (Wright, 1983). These changes in wave shape correspond to changes in frequency content, with the primary process being the transfer of spectral energy from low to

high frequencies (e.g., de Groot-Hedlin, 2012; Reichman et al., 2016a; Miller and Gee, 2018). Energy may also be transfered to lower frequencies during period lengthening of a sawtooth wave, although this process is less significant (Hamilton and Blackstock, 2008). The net effect of these spectral changes is higher energy than expected above the dominant frequency of a signal's power spectrum; this is expressed as unexpectedly shallow slopes in the roll-off of power spectra (e.g., Morfey and Howell, 1981; Petitjean et al., 2006; Gee et al., 2010).

Furthermore, since shock waves are unstable phenomena, the peak amplitude of a nonlinearly-propagated wave will decay faster than expected by geometrical spreading and absorption (Hamilton and Blackstock, 2008). Nonlinearly propagating waves transition to linear propagation as amplitude is reduced through geometrical spreading and absorption; however, the threshold amplitude between nonlinear and linear regimes is not clear. The transition threshold may be associated with the frequency-dependent Gol'dberg number which relates the length scale of absorption to the shock formation distance, however, the scaling relationship of the Gol'dberg number from audible to infrasonic frequencies is not clear (Gol'dberg, 1956; Rogers and Gardner, 1980; Gainville et al., 2010; Hamilton, 2016). Importantly, distortions accumulated during nonlinear propagation (e.g., anomolous high-frequency content) are preserved even after the wave transitions to linear propagation (Blackstock, 2006). Finally, intense changes to the medium during interaction between multiple high-amplitude waves (e.g., direct and ground-reflected shocks) may also result in nonlinear phenomena such as Mach stem formation, violating the principle of linear superposition (Hamilton and Blackstock, 2008; Vaughn et al., 2021; Ben-Dor, 2007).

Nonlinear propagation may occur in a weak or strong regime, depending on the speed and amplitude of the wave. Transition thresholds between regimes are not clear (e.g., Blackstock, 1962; Pestorius and Williams, 1974; Rudenko and Hedberg, 2013), but in general nonlinear propagation effects such as wave steepening and spectral energy transfer will increase with pressure amplitude. In the weak regime, wavefield distortion may occur without specifically culminating in a shock wave. At extreme pressures the ratio of perturbed density asymptotically

approaches a value of 6 while pressure may contrinue to increase, leading to the strong shock regime (Shapiro, 1954). Strong shock amplitudes decay by r^{-3} (Raspet, 1998) while weakly nonlinear amplitude decay rates have been reported between $r^{-1.4}$ and $r^{-1.1}$ (Rogers, 1977; Wright, 1983; Young et al., 2015). Various thresholds between weak and strong nonlinearity are proposed in the literature, including $p_2 >> \frac{\gamma+1}{\gamma-1}p_1$, where p_2 is the shock pressure, p_1 is ambient pressure and $\gamma = 1.4$ is the ratio of isobaric (constant pressure) to isochoric (constant volume) specific heat capacities (Dragoni and Santoro, 2020). In this case, strong nonlinearity and consequent shock waves require pressures at least $6\times$ greater than the ambient pressure. In contrast, Medici et al. (2014) state that strong shocks must have pressures greater than $50\times$ the ambient and Mach numbers greater than 7.6, where the Mach number is the ratio of wave speed to ambient sound speed (c_0). Reichman et al. (2016a) state that weakly nonlinear waves have amplitudes of $|p_2| << \rho_0 c_0^2$, implying that strong shocks start at pressures of $> \rho_0 c_0^2$, which is roughly $1.4\times$ greater than ambient pressure assuming $c_0 = 340$ m/s, $\rho_0 = 1.225$ kg/m^3, and $p_1 = 101$ kPa. Regardless of whether propagation occurs in the regime of weak or strong nonlinearity, the previously-mentioned spectral distortion will occur, making it challenging to relate observations made at a distance to the acoustic properties of the source process.

1.2 Volcanoes

Volcanoes provide some of the more dramatic reminders that Earth is a dynamic and constantly changing planet. Volcanic eruptions create numerous natural hazards that can be destructive to life, livelihood, and property (Loughlin et al., 2015). Approximately 14% of the world's human population lives within 100 km of a potentially active volcano (Freire et al., 2019), making the threat of volcanic hazards a lived reality for many. Even eruptions far from population centers may create hazards to aviation as volcanic ash can be distributed for hundreds of kilometers in the atmosphere (Prata and Rose, 2015). Effective mitigation of these volcanic hazards requires eruption detection and volcano monitoring, which is constantly being improved through fundamental research (Scarpa and Tilling, 1996).

Volcanoes exist in many and varied forms on Earth and other planetary bodies, but they can generally be defined as any "geologic environment that, at any scale, is characterized by three linked elements: magma, eruptions, and edifice" (Borgia et al., 2010). Volcanoes owe their existence to the explosion or extrusion of subterranean molten rock (magma) at the surface, and they feature a physical form (edifice) built by the accumulated products of those eruptions. In the sections that follow, each of these three elements is explored in more detail.

1.2.1 Magmas

Magma is a subterranean multiphase fluid consisting of liquids (molten rock), solids (solidified crystals or foreign rocks) and gasses (bubbles of exsolved volatile elements) (Schminke, 2004). Magmas form by the partial melting of Earth materials (or those of other planetary bodies), which may occur by the decompression of superheated rock (e.g., Langmuir et al., 1992; Jagoutz et al., 2011; Hole, 2015), by the addition of heat from other magmas (e.g., Hildreth, 1979; Ruprecht and Bachmann, 2010; Spera et al., 2016), or by the addition of volatile elements that lower the melting temperature (e.g., Peacock, 1990; Portnyagin et al., 2007; Walowski et al., 2016). Once formed, a magma will evolve toward a composition enriched in silica and volatiles as magnesium- and iron-bearing silica-poor minerals are removed through fractional crystallizaton and magma migration (e.g., Grove et al., 2003; González et al., 2013; Rogers, 2015). Magmas may stall underground and solidify to form intrusive igneous rocks, or they may migrate to the surface and erupt as lavas or pyroclastic material (e.g., Schminke, 2004; Browne and Szramek, 2015; Burgisser and Degruyter, 2015).

Magma formation in subduction zone tectonic settings is particularly relevant, as the volcanoes studied in this thesis are found in subduction settings. Subduction zones are plate boundaries where a tectonic plate of oceanic lithosphere is forced down into Earth's mantle during collision with another tectonic plate (i.e., a continental plate or oceanic plate) (Peacock, 1990; Stern, 2002; Ducea et al., 2015). Volatile elements released from the downgoing plate lower the melting temperature of mantle, leading to partial melting of peridotite to cre-

ate mafic magma (Iwamori, 1998; John et al., 2012; Grove et al., 2012). The reduced density of the magma compared to the surrounding mantle causes it to rise buoyantly and intrude the overlying lithosphere (Hall and Kincaid, 2001; McGary et al., 2014; Ducea et al., 2015). New magmas may then be created in the lithosphere due to the addition of heat and assimilation into the migrating magma (Hildreth, 1979; Ruprecht and Bachmann, 2010; Spera et al., 2016). Migration of these magmas to the surface (Browne and Szramek, 2015; Burgisser and Degruyter, 2015; Gonnermann and Taisne, 2015) leads to the eruption of lava or pyroclasts, and the accumulation of erupted products creates volcanic edifices.

1.2.2 Eruptions

While tectonic processes create the conditions for magma generation, the bouyancy of magmatic gasses is the primary cause of eruptions (Sparks, 1978; Lavallée et al., 2015; Schminke, 2004). As magmas chemically evolve or physically move toward the surface, volatile compounds such as H_2O, CO_2, and SO_2 concentrate in the melt and then, below a certain pressure, exsolve (transition from a liquid to a gas) (Sparks, 1978; Burgisser and Degruyter, 2015; Rogers, 2015). Volatile exsolution reduces the density of the magma, accelerating its ascent and increasing its overall volume (Taisne and Jaupart, 2011; Cashman and Scheu, 2015; Carroll and Holloway, 2015). Volume expansion pressurizes the surrounding rock, allowing for the opening of pre-existing weaknesses in the crust (Gonnermann and Taisne, 2015). When the pressure of the magma exceeds the confining strength of the surrounding rock, an eruption may occur (e.g., Woods, 1995; Iguchi et al., 2008; Cashman and Scheu, 2015).

Eruptions occur in a range of styles depending primarily on the viscosity and volatile content of the magma, which in turn depend on the magma composition (e.g., Schminke, 2004; Sides et al., 2014; Cassidy et al., 2018). Magmas with low viscosity and low volatile content (e.g., basalt) commonly erupt effusively, with minor plumes of tephra (10's–100's of meters tall) and voluminous slow-moving lava flows (Taddeucci et al., 2015). Magmas with higher viscosity and volatile content (e.g., dacite and rhyolite) may erupt more explosively, with rapidly-moving

pyroclastic flows and vertical eruption columns reaching as high as the mesosphere (>50 km; Carr et al., 2022). On a scale from most effusive to most explosive, eruptions are classified as Hawaiian, Strombolian, Vulcanian, sub-Plinian or Plinian (Schminke, 2004). This thesis primarily focuses on data from the volcanoes Yasur and Sakurajima, which typically erupt in Strombolian and Vulcanian fashion, respectively.

Strombolian-type eruptions are named after the activity of Stromboli volcano in the Aeolian islands eruptions, and are typically seen at island arc volcanoes above oceanic-oceanic subduction zones (Schminke, 2004; Taddeucci et al., 2015). Eruptions occur as small short-lived (seconds to minutes) explosions of basaltic to basaltic-andesitic lava with relatively large pyroclast sizes (>64 mm, blocks and bombs) and small proportions of gas and finer particles (ash and lapilli <64 mm) (Taddeucci et al., 2015). The eruptions are thought to be caused by rapid expansion of exsolved volcanic gasses ascending through a relatively open conduit system filled with low-viscosity magma (Harris and Ripepe, 2007; Ripepe et al., 2021). These eruptions may occur at regular intervals of several minutes or less, as at Stromboli and Yasur volcanoes, making them frequent targets for geophysical field experiments (e.g., Ripepe et al., 1996; Marchetti et al., 2013).

In contrast to Strombolian eruptions, Vulcanian eruptions are relatively more explosive, with longer durations, higher plumes, and higher degrees of fragmentation (e.g., Woods, 1995; Iguchi et al., 2008; Marchetti et al., 2009; Clarke et al., 2015; Gabrielli et al., 2020). Vulcanian eruptions are more common at oceanic-continental subduction zone volcanoes (e.g., Sakurajima Volcano) which have more evolved magmas that have higher viscosity, higher volatile contents and lower temperatures than Strombolian magmas (Clarke et al., 2015). The more viscous magma creates a plug over the vent that prevents the steady release of gasses, allowing pressure to build in the conduit (Woods, 1995). When the gas pressure exceeds the confining strength of the plug, rapid decompression leads to violent fragmentation of the plug and conduit magma (Iguchi et al., 2008; Cashman and Scheu, 2015). These eruptions generate shock waves, projectiles, hazardous pyroclastic flows, and moderatly-high columns of ash and gas (up to several kilometers), making

them potentially more dangerous than Strombolian eruptions (Baxter and Horwell, 2015).

1.2.3 Edifices

Volcanic edifices range in size and shape based on the eruptive history and magma types of a volcano (de Silva and Lindsay, 2015). Singular short-duration eruptions of basaltic magma may create a small cinder cone of accumultated pyroclasts (e.g., Parícutin, Mexico; Luhr and Simkin, 1993). Repeated effusive eruptions of low-viscosity basaltic lavas may create very voluminous shield volcanos with low-angle slopes and large surface areas (e.g., Mauna Loa, Hawaii; Lockwood and Lipman, 1987). Alternating eruptions of intermediate-composition lavas and tephra may build tall and steep-sided mountains called stratovolcanoes (e.g., Mount Fuji, Japan; Oguchi and Oguchi, 2009). Extremely voluminous explosions of highly-evolved rhyolitc magma may reduce the pressure in a magma reservoir, leading to the gravitational collapse of an edifice into a depression several kilometers wide known as a caldera (e.g., Crater Lake, Oregon; Bacon, 1983). In all cases, volcanic edifices are dynamic environments that change in response to each eruption and are highly prone to alteration by gravitational collapse (e.g., landslides; Normark et al., 1993) and to erosion (e.g., by glaciers; Mills, 1976).

1.3 Volcano Infrasound

Volcanic eruptions accelerate mass into the atmosphere, inducing pressure disturbances that propagate as acoustic waves (Garcés et al., 2013; Fee and Matoza, 2013). Examples of volcano-acoustic source processes include discrete explosions, sustained jet noise, pyroclastic density currents, and lahars (Figure 1.1) (e.g., Matoza et al., 2009a; Ripepe et al., 2009; Fee et al., 2014; Johnson and Palma, 2015; Allstadt et al., 2018). These acoustic source processes occur over length scales of meters to tens or hundreds of meters, resulting in sound with long wavelengths, or low frequencies (Garcés et al., 2013; Fee and Matoza, 2013). Since the sound is predominantly at frequencies below the threshold of human hearing (20 Hz), it is referred to as volcano infrasound.

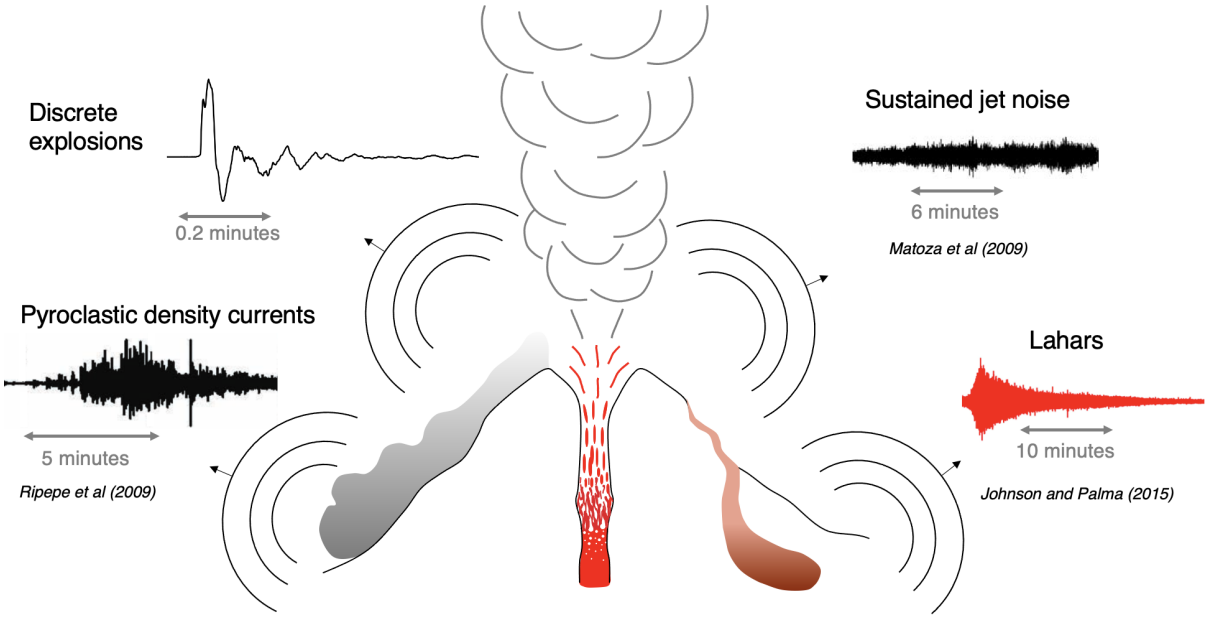

Figure 1.1: Examples of source processes of volcano infrasound, including explosions, jet noise, pyroclastic density currents, and lahars.

Over the past two decades infrasound studies have evolved from an academic curiosity to an important aspect of eruption monitoring (De Angelis et al., 2019; Matoza et al., 2019a; Watson et al., 2022). This section introduces some applications of volcano infrasound and discusses topics of active research in near-source propagation including shock waves and wavefield interactions with topography.

1.3.1 Applications of volcano infrasound

A major application of volcano infrasound is the detection and characterization of eruptive activity (e.g., Fee et al., 2010; Caudron et al., 2015; Matoza et al., 2017a; Marchetti et al., 2019; Sanderson et al., 2020). While seismic observation forms the foundation of many volcano monitoring networks (Thompson, 2015), it can be difficult to distinguish subaerial from shallow subterranean activity using seismic data alone. Additionally, seismicity from unmonitored volcanoes may be too attenuated to detect at remote (>250 km) or even regional distances (15–250 km). In contrast, infrasound signals have unambigously subaerial source processes and may propagate for thousands of kilometers without significant attenuation (Dabrowa et al.,

2011). Consequently, infrasound may be used to detect and locate remote eruptions that may be missed by other monitoring methods and may pose hazards to aviation (e.g., Matoza et al., 2011, 2017a; Sanderson et al., 2020). The high sampling rates of infrasound observations also allow for high time resolution characterization of eruption activity and discrimination of different phases of an eruption (e.g., Fee et al., 2010; McKee et al., 2021a,b). At local recording distances (<15 km), infrasound monitoring may be used to discriminate fine-scale eruptive activity such as multiple closely-spaced vents (e.g., Cannata et al., 2011; Spina et al., 2017; Fee et al., 2021), moving debris flows (e.g., Ripepe et al., 2009; Johnson and Palma, 2015; Allstadt et al., 2018), and changing crater geometry and vent conditions (e.g., Fee et al., 2017a; Ortiz et al., 2018; Matoza et al., 2022a).

Another application of volcano infrasound is the estimation of eruption source parameters (e.g., Vergniolle and Caplan-Auerbach, 2006; Caplan-Auerbach et al., 2010; Lamb et al., 2015; Fee et al., 2017b; Ripepe et al., 2013; Diaz-Moreno et al., 2019). Eruption source parameters include properties such as erupted mass, mass eruption rate, and plume height, and they are critical inputs to models of tephra disperal and thus hazard forecasting (Bonadonna et al., 2015). These source parameters have traditionally been estimated by a combination of direct visual observation and satellite remote sensing, but these methods are often inhibited by meteorological cloud cover (e.g., Sawada, 1996; Prata, 2009; Matoza et al., 2011). Acoustically-based estimates can be made regardless of weather conditions, although uncertainties between path and source effects may lead to inaccurate results. Volcano infrasound has been used to estimate a number of eruption source parameters including gas exit velocity (Woulff and McGetchin, 1976; Vergniolle and Caplan-Auerbach, 2006; Delle Donne and Ripepe, 2012; Matoza et al., 2013; McKee et al., 2017), erupted mass and volume (Firstov and Kravchenko, 1996; Dalton et al., 2010; Johnson and Miller, 2014; Kim et al., 2015; Delle Donne et al., 2016; Fee et al., 2017b; Yamada et al., 2017; Witsil and Johnson, 2018; Iezzi et al., 2019), plume height (Caplan-Auerbach et al., 2010; Ripepe et al., 2013; Lamb et al., 2015; Perttu et al., 2020), conduit and crater geometry (Buckingham and Garcés, 1996; Garces, 2000; Johnson et al., 2018a,b; Ortiz

et al., 2018; Muramatsu et al., 2018; Watson et al., 2019), and source directivity (Kim et al., 2012; Jolly et al., 2016, 2017; Iezzi et al., 2019, 2022). Improved understanding of path effects such as topographic diffraction and shock formation may help to increase the accuracy of infrasound-based eruption source parameters.

1.3.2 Shock waves

While Section 1.1.2 described nonlinear acoustic propagation processes in general, this section addresses shock waves from volcanic eruptions in particular. Shock waves, or blast waves, are discontinuities in pressure, density and temperature traveling at sonic or supersonic speeds in the atmosphere (Kinney and Graham, 1985; Needham, 2010). Shock waves often follow chemical explosions as rapid gas expansion creates large amplitude pressure pulses that steepen during nonlinear propagation (Garces, 2019). Shocks have been reported from volcanic explosions, both in the visible condensation of water vapor (flashing arcs; Nairn, 1976; Ishihara, 1985; Yokoo and Ishihara, 2007) and in acoustic pressure recordings (Morrissey and Chouet, 1997; Marchetti et al., 2013). In contrast to shocks from chemical explosions, explosion waves from volcanic eruptions may be sourced from a slower expansion of gasses in a multiphase magmatic fluid (Garcés et al., 2013). Volcanic explosion waves can be very loud and have broken windows 15 km from the 1958 eruption of Mount Asama, Japan, and have knocked people down as far as 13 km from Galeras Volcano, Colombia (Baxter and Horwell, 2015). Video analysis of volcanic explosion waves have determined near-source propagation speeds ranging from 344.6 m/s at Stromboli volcano (Genco et al., 2014) to greater than 500 m/s at Sakurajima Volcano (Ishihara, 1985; Yokoo and Ishihara, 2007).

Acoustic pressure recordings from explosive volcanic eruptions are often loosely described as “shock waves” or “blast waves” due to the asymmetric character of the waveforms which resemble the signatures of chemical explosions. The waveform asymmetry refers to the presence of a high amplitude short-duration compressional onset followed by a longer rarefaction with lower amplitude. Marchetti et al. (2013) compared amplitude-normalized waveforms from

Strombolian explosions at Yasur Volcano, Vanuatu to the Friedlander equation (Friedlander, 1946; Reed, 1977), which describes the expected waveform for chemical explosions. However, Matoza et al. (2019a) showed that appropriate scaling of the Friedlander equation for amplitude and receiver distance results in overestimation of source amplitudes and poor waveform fits to volcano infrasound. Additionally, waveform asymmetry has been alternatively explained by fluid dynamics near the source (Cerminara et al., 2016; Brogi et al., 2018; Watson et al., 2022) and wavefield interactions with topography (Kim and Lees, 2011). The role of shock formation and nonlinear propagation in the generation of asymmetric waveforms is therefore not staightforward.

Volcanic shock waves are difficult to study directly because they are expected to decay to regular lineary-propagating acoustic waves within a few hundred meters of the source (Medici et al., 2014). Eruption hazards and rugged topography typically prevent the safe deployment of scientific equipment in this near-source region. Medici et al. (2014) ran open-ended laboratory shock tube experiments intended to simulate volcanic shock waves. They proposed that strong shock theory could be used to accurately estimate the energy released by volcanic explosions and shock tube experiments, however, the strong shock theory significantly overestimated the wave speeds observed in their experiments. Strong shocks propagate at Mach numbers >7.6 and have peak amplitudes $> 50\times$ the ambient pressure (Shapiro, 1954) (see also Section 1.1.2), whereas their experimental shocks had Mach numbers $\leq$2.3 and pressure jumps of $\leq 6\times$ ambient pressure (Medici et al., 2014). The volcanic shock waves presented by Medici et al. (2014) all had Mach numbers $\leq$6.06 and estimated source pressures of $\leq 43\times$ ambient pressure.

Dragoni and Santoro (2020) developed analytical expressions for the thermodynamic properties of strong shocks with application to volcanic explosions. They solve for changes in air velocity, temperature, density and pressure due to shock propagation at amplitudes $> 6\times$ ambient pressure. At these high pressures the waveform is dominated by a single compressional shock with no rarefaction, unlike the weak shocks observed in Strombolian or Vulcanian eruptions. In fact, the authors note that the conditions required for strong shocks involve large explosions

such as in catastrophic caldera-forming eruptions (Dragoni and Santoro, 2020; Wohletz et al., 1984). Since smaller Strombolian and Vulcanian eruptions with weak shocks are much more common and well-documented, the study of weak volcanic shock phenomena is desirable.

Watson et al. (2021) performed aeroacoustic simulations that allowed for the study of fluid dynamics at the source of a starting pressure-balanced jet, and comparison between linear and nonlinear acoustic propagation. They showed that that wave steepening toward shock waves increased with jet exit velocity for nonlinear propagation, that advection contributed more strongly to changes in effective sound speed than temperature changes, and that errors in acoustically-based eruption area estimates increased with jet exit velocity (Watson et al., 2021). They also demonstrated that nonlinear effects may be more significant in the fluid dynamical source region than in the far-field acoustic propagation regime (Watson et al., 2021). This study was limited to pressure-balanced sources with flat lower boundaries, whereas real data may be influenced by overpressured sources and topography.

1.3.3 Topographic effects

Wavefield interactions with topography have gradually been recognized to have a first-order influence on infrasound waveforms. Matoza et al. (2009a) modeled anomalous distributions of infrasound amplitudes around Mount St. Helens via diffraction over an asymmetrical crater wall. Kim and Lees (2011) investigated synthetic infrasound propagated over different vent and crater geometries, finding significant modulation of waveform character by diffraction effects. Lacanna and Ripepe (2013) compared amplitudes of infrasound recorded around Stromboli volcano with different amounts of topography between the vent and receivers, finding up to 11 dB in power losses due to diffraction. Similarly, Kim and Lees (2014) observed up to 8 dB reductions in amplitude compared to geometric spreading due to topographic diffraction at Sakurajima Volcano, but they also observed amplitude increases of up to 2 dB at one station. These studies illustrate that amplitudes may reduced by diffraction over topographic obstructions, but also suggest that ground reflections may cause constructive interference. In addition

to amplitude modulation, topographic effects include time delays (Kim and Lees, 2014; Rowell et al., 2014), scattering (Kim et al., 2015), reflected arrivals (Yokoo et al., 2014), and coupling into ground of finite impedance (Embleton et al., 1976; Bishop et al., 2022).

The anomalous amplitude patterns and time delays introduced by topographic effects create challenges in using infrasound to estimate source properties. Topgraphy-related time delays were partially responsible for systematic offsets in semblance-based eruption source location estimates at Sakurajima Volcano (McKee et al., 2014). Consistent overestimation of eruption source height at Karymsky Volcano was also attributed to topographic influences by Rowell et al. (2014). Neglecting the 3D influence of topography was shown to result in up to 50% underestimation of erupted volume at Sakurajima (Kim et al., 2015). These studies point to the importance of accounting for the effects of topography when making acoustically-based estimates of eruption source properties.

Currently the effects of infrasound reflection, diffraction and scattering from volcano topography can be modeled to a high degree of accuracy with numerical simulations involving a rigid lower boundary (e.g., Kim et al., 2015; de Groot-Hedlin, 2017). The incorporation of coupling into ground of finite impedance is an area of active research (Fee et al., 2020; Bishop et al., 2022). While numerical modeling is useful in a research context to achieve good fits to observed data, it can be computationally expensive and time consuming to set up. It is therefore desirable to develop a simpler and more rapid approach to approximating the effects of topography that does not involve full wavefield simulations. Such an approximation could be used in time-restricted scenarios such as eruption response to improve estimates of eruption source parameters compared to the application of a geometrical spreading correction alone.

One potential method to rapidly account for topographic effects is to approximate the highest obstacle along an elevation profile between a source and receiver as a thin vertical barrier (screen). The acoustic shielding effect of thin screens was investigated empirically by Maekawa (1968), who recorded sound pressure behind a 2 m tall screen during a controlled indoor experiment and used the results to calculate the sound reduction compared to free field

propagation. The amplitude reduction by the screen can be related to the Fresnel number, which is the extra acoustic path length due to diffraction normalized by half a wavelength (Pierce, 1981). Maekawa (1968) presented an empirical chart of amplitude reduction as a function of Fresnel number which has become a standard reference for first-order noise reduction estimates in the field of audible acoustics (e.g., Hohenwarter, 1990; Ekici and Bougdah, 2003; Vu, 2007; Plotkin et al., 2009).

Ishii et al. (2020) aimed to use screen diffraction to rapidly account for topographic effects at Sakurajima Volcano by rotating 2D elevation profiles to match the elevations of the source and receivers, replacing topography with flat ground and a thin screen at the height and distance of the tallest obstruction, and computing the theoretical pressure fields for monopole radiation. Their results suggest that the relative amplitude distributions across stations on different sides of the volcano were better predicted by the screen diffraction approximation than by a $1/r$ spreading correction alone. However, Ishii et al. (2020) do not consider the absolute amplitudes, which may be more attenuated by screens than by volcano topography. Furthermore, the work by Ishii et al. (2020) neglects full wavefield effects such as interference between reflections along volcano slopes, and may therefore misrepresent the importance of diffraction as an isolated phenomenon.

1.4 Overview of Chapters

1.4.1 Chapter 2: Investigating Spectral Distortion of Local Volcano Infrasound by Nonlinear Propagation at Sakurajima Volcano, Japan

Nonlinear propagation is often cited as a source of uncertainty in studies of volcano infrasound, but the effects of nonlinearity on volcano acoustic signal properties have not been examined until recently. In this chapter we introduce to the volcano infrasound community a method developed by Reichman et al. (2016a) for the analysis of nonlinearity in jet noise acoustics. We apply the method to observed signals from Sakurajima Volcano because it is

well known for it's large amplitude explosion signals which may propagate nonlinearly. We further perform numerical simulations of nonlinear infrasound propagation at Sakurajima amplitudes using a finite-difference model developed by de Groot-Hedlin (2017). We find that the effects of nonlinearity were small yet quantifiable in the numerical simulations, but not in the observed data. We discuss the potential limiting factors in the observed data such as wind and topography.

1.4.2 Chapter 3: Evaluating the applicability of a screen diffraction approximation to local volcano infrasound

Acoustic wavefield interactions with topography are known to be a first-order process in modifying infrasound signals, but accounting for the effects of topography currently requires computationally-demanding numerical simulations. In this chapter we investigate a method to rapidly account for the effect of diffraction on reducing signal power, based on an empirical relationship proposed by Maekawa (1968) for diffraction due to thin barriers (screens). Ishii et al. (2020) proposed that a screen approximation provided improved predictions of relative amplitude distributions around Sakurajima Volcano compared to geometrical spreading alone. However, in this chapter, we show that amplitude losses to diffraction at Sakurjima are systematically and significantly lower than predicted by the screen diffraction approximation. We conclude that three-dimensional topographic effects at volcanoes, including constructive interference along concave slopes, may reduce the effects of diffraction when compared to thin screens.

1.4.3 Chapter 4: Evidence for near-source nonlinear propagation of volcano infrasound from strombolian explosions at Yasur volcano, Vanuatu

In this chapter we build upon the work of Chapter 2 by investigating nonlinear propagation effects in a different dataset at Yasur Volcano, Vanuatu. Compared to the study at Sakurajima, the Yasur study has instruments closer to the acoustic source with higher sample rates and less

intervening topography. This means that subtle wavefield changes near the source may be captured better at Yasur, improving the ability to study the effects of nonlinear propagation. In this chapter we observe quantitative evidence for nonlinear propagation in both observational data and numerical modeling results. We further show that the error introduced to erupted volume estimates by nonlinear propagation is small (<1%). These results suggest that nonlinear propagation occurs even in sound waves from relatively small Strombolian-style explosions, but the effect is small compared to influences from topography and geometrical spreading.

1.5 Permissions and Attributions

1. The contents of chapter 2 and appendix A are the results of a collaboration with Robin Matoza, Catherine de Groot-Hedlin, Kent Gee, David Fee, and Akihiko Yokoo, and has previously appeared in Journal of Geophysical Research Maher et al. (2020). They are reproduced here with the permission of American Geophysical Union: `https://agupubs.onlinelibrary.wiley.com/doi/full/10.1029/2019JB018284`.

2. The content of chapter 3 is the result of a collaboration with Robin Matoza, Catherine de Groot-Hedlin, Keehoon Kim and Kent Gee, and has previously appeared in Volcanica Maher et al. (2021). This article is reproduced here by copyright of the author according to the Creative Commons Attribution 4.0 International License: `https://creativecommons.org/licenses/by/4.0/legalcode`.

3. The content of chapter 4 is the result of a collaboration with Robin Matoza, Arthur Jolly, Catherine de Groot-Hedlin, Kent Gee, David Fee and Alexandra Iezzi, and has previously appeared in Bulletin of Volcanology Maher et al. (2022). The article is open access and reproduced under the terms of the Creative Commons CC BY license: `https://creativecommons.org/licenses/by/4.0/legalcode`.

Chapter 2

Investigating Spectral Distortion of Local Volcano Infrasound by Nonlinear Propagation at Sakurajima Volcano, Japan

This chapter appeared in this form in:

Maher, S.P., Matoza, R.S., de Groot-Hedlin, C., Gee, K.L., Fee, D., Yokoo, A., 2020. Investigating Spectral Distortion of Local Volcano Infrasound by Nonlinear Propagation at Sakurajima Volcano, Japan. Journal of Geophysical Research: Solid Earth 125, 1–25. doi:10.1029/2019JB018284.

2.1 Abstract

Sound waves generated by erupting volcanoes can be used to infer important source dynamics, yet acoustic source-time functions may be distorted during propagation, even at local recording distances (<15 km). The resulting uncertainty in source estimates can be reduced by

improving constraints on propagation effects. We aim to quantify potential distortions caused by wave steepening during nonlinear propagation, with the aim of improving the accuracy of volcano-acoustic source predictions. We hypothesize that wave steepening causes spectral energy transfer away from the dominant source frequency. To test this, we apply a previously-developed single-point, frequency domain, quadspectral density-based nonlinearity indicator to 30 acoustic signals from Vulcanian explosion events at Sakurajima Volcano, Japan, in an eight-day dataset collected by five infrasound stations in 2013 with 2.3-6.2 km range. We model these results with a 2D axisymmetric finite-difference method that includes rigid topography, wind, and nonlinear propagation. Simulation results with flat ground indicate that wave steepening causes up to ∼2 dB (1% of source level) of cumulative upward spectral energy transfer for Sakurajima amplitudes. Correction for nonlinear propagation may therefore provide a valuable second-order improvement in accuracy for source parameter estimates. However, simulations with wind and topography introduce variations in the indicator spectra on order of a few decibels. Non-random phase relationships generated during propagation or at the source may be misinterpreted as nonlinear spectral energy transfer. The nonlinearity indicator is therefore best suited to small source-receiver distances (e.g., <2 km) and volcanoes with simple sources (e.g., gas-rich strombolian explosions) and topography.

2.2 Introduction

Volcanic eruptions produce atmospheric sound waves below the 20 Hz frequency threshold of human hearing (infrasound) that can be used to monitor and characterize volcanic activity (e.g., Johnson and Ripepe, 2011; Fee and Matoza, 2013; Garcés et al., 2013; Matoza et al., 2019a). Recordings of volcano infrasound at regional (15-250 km) and global (>250 km) distances can be used to detect, locate and characterize remote eruptions (e.g., Dabrowa et al., 2011; Matoza et al., 2011, 2017a, 2019a). At these scales, acoustic wavefield distortion by propagation through the dynamic atmosphere is significant and constitutes an active area of research (Assink et al., 2012; Green et al., 2012; Fee et al., 2013b; Matoza et al., 2018; Waxler and Assink, 2019).

Early work in this field made the assumption that recordings at local distances (<15 km) were directly representative of the source process (e.g., Morrissey and Chouet, 1997); however, it has now been established that near-vent propagation dynamics influence the acoustic wavefield (Fee and Garces, 2007; Matoza et al., 2009b; Kim and Lees, 2011; Lacanna and Ripepe, 2013; Kim and Lees, 2014; Kim et al., 2015). Current work is attempting to develop the capability to use locally-recorded volcano infrasound to infer useful eruption source parameters such as gas exit velocity (Woulff and McGetchin, 1976; Matoza et al., 2013; McKee et al., 2017), erupted volume (Firstov and Kravchenko, 1996; Johnson and Miller, 2014; Kim et al., 2015; Yamada et al., 2017), erupted mass (Dalton et al., 2010; Delle Donne et al., 2016; Fee et al., 2017b), plume height (Caplan-Auerbach et al., 2010; Ripepe et al., 2013; Lamb et al., 2015), conduit geometry (Buckingham and Garcés, 1996; Garces, 2000), vent radius (Muramatsu et al., 2018), crater geometry (Johnson et al., 2018a,b; Watson et al., 2019), and source directivity (Kim et al., 2012; Jolly et al., 2017). Therefore, improved understanding of near-source distortions can lead to more accurate estimates of volcano-acoustic source characteristics.

One potential cause of near-source distortion is nonlinear acoustic propagation. While most sound can be accurately modeled by assuming a linear relationship between propagation distance and amplitude decay, this assumption breaks down when amplitudes are large or source processes are supersonic (Pierce, 1981; Atchley, 2005; Garcés et al., 2013). Sound with either of these properties compresses air sufficiently to drive transient adiabatic heating and self-advection that increases the local sound speed (Hamilton and Blackstock, 2008). Consequently, compressional phases travel faster than rarefactional phases such that initially-smooth temporal variations in pressure can steepen into shock waves (Fig 2.1a; Reichman et al., 2016a) .

Wave steepening causes spectral energy to transfer from the peak source frequency to higher frequencies that are coupled in phase (Kim and Powers, 1979). In the case of an initial sinusoid, these higher frequencies correspond to harmonics on the source frequency (Figure 2.1b; Reichman et al., 2016a). Energy can also be transferred from the peak source frequency to lower frequencies by period lengthening and/or shock coalescence (Hamilton and Blackstock,

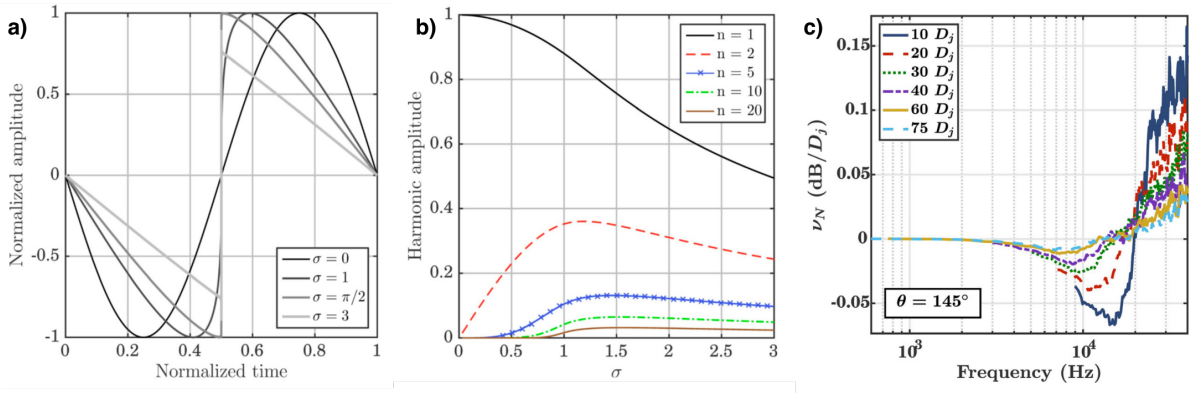

Figure 2.1: Previously-published work by Reichman et al. (2016a) and Miller and Gee (2018) illustrating the theory behind the quadspectral density nonlinearity indicator. **a)** Waveform evolution from an initial sinusoid to a shock wave during nonlinear propagation as predicted by the Burgers equation (Reichman et al., 2016a). σ represents wavefront propagation distance normalized by shock formation distance. **b)** Evolution in amplitude of harmonic frequency components (n) above the fundamental frequency of the initial sinusoid (n=1) as a function of σ (Reichman et al., 2016a). Wave steepening during nonlinear propagation causes spectral transfer from the fundamental to higher harmonics. **c)** Results of nonlinearity indicator analysis on high-frequency acoustic data from a controlled indoor experiment on model-scale jet noise (Miller and Gee, 2018). The indicator ν_N is here normalized by jet diameter (D_j=30 cm). Each line represents a result from a sensor at a different distance from the jet nozzle along a radial at an angle of $\theta = 145°$ from the jet axis. The reclined-S shape of ν_N shows that spectral power is transferred away from the peak source frequency at 10–20 kHz (ν_N<0) to higher frequencies at which ν_N>0. Figures are reproduced from Reichman et al. (2016a) and Miller and Gee (2018) with permission.

2008), although this process is less efficient. Spectral properties estimated from a nonlinearly-propagated signal may therefore not reflect properties of the source. For example, analyses of man-made jet noise (Gee et al., 2008; Petitjean et al., 2006) and rocket motor noise (Muhlestein et al., 2012) show that linear acoustic theory underestimates observed power at high frequencies due to upward energy transfer from the spectral peak. Since man-made jet noise exhibits similar characteristics to volcano-acoustic eruption tremor, analogous processes may influence both types of sound (Matoza et al., 2009a, 2013; Taddeucci et al., 2014; Cerminara et al., 2016). If nonlinear propagation of volcano infrasound causes energy transfer away from the dominant source frequency, then narrow band-passing filtering around the spectral peak (e.g., Fee et al., 2017b; Yamada et al., 2017) may cause underestimation of acoustic source power.

Volcano infrasound has long been thought to propagate nonlinearly near the source (e.g., Morrissey and Chouet, 1997; Garcés et al., 2013), but the distorting effects of this process have not been quantified. Visual observations of wavefronts above erupting vents imply near-source shock wave formation (Ishihara, 1985; Yokoo and Ishihara, 2007), but these waves do not necessarily indicate supersonic sources (Genco et al., 2014). Nonlinear propagation has been proposed as a possible explanation for asymmetric infrasound waveforms, which are commonly observed at volcanoes worldwide (e.g., Fee et al., 2013a; Marchetti et al., 2013; Medici et al., 2014; Anderson et al., 2018b; Matoza et al., 2018). However, this phenomenon can alternatively be explained with linear propagation and crater rim diffraction (Kim and Lees, 2011) or fluid flow at the source (Brogi et al., 2018). For lack of quantitative understanding of near-source acoustic nonlinearity, volcano-acoustic studies commonly assume linear propagation (e.g., Garcés et al., 2013).

In this study we aim to quantify distortions to volcano-acoustic waves by nonlinear propagation using a quadspectral density indicator developed in the high-frequency (audible range 20 Hz to 20 kHz) jet noise literature (Figure 2.1c; Reichman et al., 2016a). We apply the indicator to 30 eruption signals in a 2013 infrasound dataset from five sensors at Sakurajima Volcano, Japan (Figure 2.2). We further apply the method to synthetic pressure data from 2D

axisymmetric cylindrical finite-difference time-domain (FDTD) simulations (de Groot-Hedlin, 2016) to investigate the suitability of the indicator and its behavior in the presence of wind and topography. Our study represents the first application of the indicator to infrasound of which we are aware.

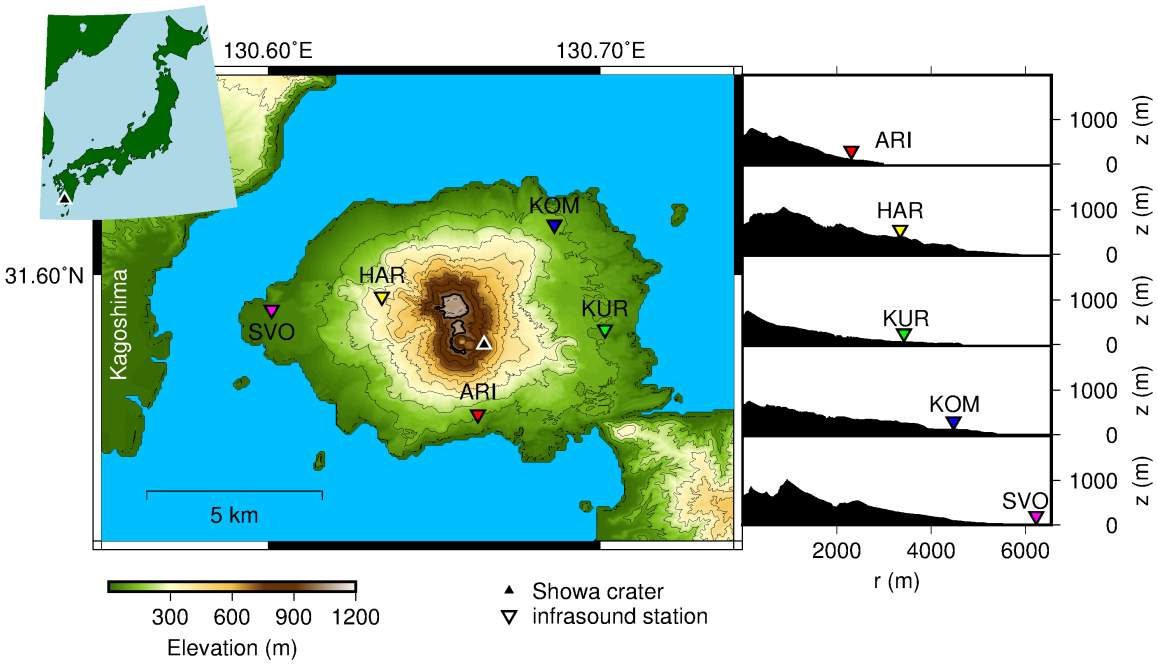

Figure 2.2: Map of Sakurajima Volcano with 1-m resolution digital elvation model from 2013 showing infrasound station locations (inverted triangles). The active vent in Showa crater (black triangle) is located ∼500 m below the dual summits of Kita-Dake (north) and Minami–Dake (south) on the southeast flank of the volcano. Inset map shows the location of Showa crater on Kyushu Island in southern Japan. Profiles at right compare the topography between Showa crater and each station.

2.2.1 Quantitative quadspectral density nonlinearity indicator

Various approaches have been used to investigate nonlinear propagation effects such as the statistics of the waveform (e.g., skewness) and its derivative (Gee et al., 2007b; Fee et al., 2013a; Gee et al., 2013; Anderson et al., 2018b), bicoherence (Kim and Powers, 1979; Gee et al., 2007a, 2010), and quadspectral density (Morfey and Howell, 1981; Gee et al., 2005; Petitjean et al., 2006; Reichman et al., 2016a; Miller et al., 2016; Miller and Gee, 2018). The quadspectral

density refers here to the imaginary part of the cross-spectrum of pressure and squared pressure (Q_{pp^2}). This spectrum represents phase coupling that arises during summing and differencing of frequency components when energy is transferred to harmonics of the spectral peak (Kim and Powers, 1979; Gagnon, 2011). Quadspectral density potentially provides an appropriate indicator for volcano acoustics since it can reveal quantitative changes in power spectra using single-point measurements.

Following work by Morfey and Howell (1981), Reichman et al. (2016a) adapted the frequency-domain Generalized Burgers Equation to quantify the spatial rate of change in an acoustic wave's sound pressure level from a single-point measurement. The sound pressure level (unit dB) is $L_p = 10\log_{10}(p_i/p_{ref}^2)$, where p_i is power spectral density (PSD) in an arbitrary frequency band i (unit $\mathrm{Pa}^2/\mathrm{Hz}$) and $p_{ref} = 20\ \mu\mathrm{Pa}/\sqrt{\mathrm{Hz}}$. Reichman et al. (2016a) define the rate of change of L_p with respect to source-receiver distance (r) as:

$$\begin{aligned}\frac{\partial L_p}{\partial r} &= -10\log_{10}(e) \times \left(\frac{2m}{r} + 2\alpha + \frac{\omega\beta}{\rho_0 c_0^3}\frac{Q_{pp^2}}{S_{pp}}\right) \\ &\equiv \nu_S + \nu_\alpha + \nu_N \\ &\equiv \nu,\end{aligned} \tag{2.1}$$

where $\frac{\partial L_p}{\partial r} = \nu$ is a sum of the effects of frequency-independent geometrical spreading (ν_S), frequency-dependent atmospheric absorption (ν_α) and frequency-dependent nonlinear propagation (ν_N), with unit dB/m. These components can be explicity defined:

$$\begin{aligned}\nu_S &= -10\log_{10}(e) \times \left(\frac{2m}{r}\right), \\ \nu_\alpha &= -10\log_{10}(e) \times (2\alpha), \\ \nu_N &= -10\log_{10}(e) \times \left(\frac{\omega\beta}{\rho_0 c_0^3}\frac{Q_{pp^2}}{S_{pp}}\right),\end{aligned} \tag{2.2}$$

where m is a nondimensional geometrical term equal to 0, 0.5 or 1 for planar, cylindrical, or spherical waves, respectively, $\alpha\,(\omega)$ is the frequency-dependent absorption coefficient of the

medium, ω is angular frequency, β is the coefficient of nonlinearity, ρ_0 is ambient density, c_0 is ambient sound speed, and $S_{pp}(\omega)$ is PSD of a pressure time-series. The nonlinearity coefficient β is a unitless constant, intrinsic to the medium, which characterizes the effect of finite-amplitude wave propagation on sound speed (Hamilton and Blackstock, 2008). In air, $\beta \approx 1.2$ and can be written as a function of the ratio of specific heats (γ) in an isobaric to an isochoric process, $\beta = \frac{1}{2}(\gamma + 1)$ (Hamilton and Blackstock, 2008). Derivation of Equation 2.1 and further discussion are presented in Appendix A.

Equations 2.1 and 2.2 assume that linear spectral changes can be fully described by ν_S and ν_α, neglecting potentially significant effects such as reflections from topography, refraction in temperature gradients, and refraction and advection in wind gradients. Spectral contributions from these processes are inaccurately treated by ν_N as a consequence of nonlinear propagation. The ability of ν_N to accurately describe nonlinear effects consequently depends on the complexity of the signal and recording environment. For example, previous application of a qualitative quadspectral density indicator to outdoor recordings of military jet noise observed evidence for nonlinearity that was modified by interference nulls related to reflections from topography (Gee et al., 2005).

Furthermore, while Equation 2.1 was developed for analysis of acoustic signals in the audible frequency range, its basis in the Burgers equation dictates that it should be valid for any wave that steepens during propagation due to finite-amplitude effects. Nonlinear steepening of infrasonic waves has previously been postulated at volcanoes (Morrissey and Chouet, 1997; Yokoo and Ishihara, 2007; Fee et al., 2013a; Marchetti et al., 2013; Lonzaga et al., 2015; Matoza et al., 2019a), so we consider the application of Equation 2.1 to Sakurajima infrasound appropriate.

In this study we focus on the ν_N component of Equation 2.1, since it isolates the effect of nonlinear propagation on the spectrum. Nonlinear acoustic theory predicts that ν_N will express spectral energy transfer as negative values at frequencies where energy is lost and positive values at frequencies where energy is gained. Applications of ν_N to data from indoor experiments on

model-scale supersonic jet noise (Miller and Gee, 2018) show that ν_N is negative just above the observed peak frequency and positive at higher frequencies, creating a reclined-S shape characteristic of upward spectral energy transfer (Figure 2.1c). The behavior of ν_N on more complex outdoor signals has not been investigated, and this study represents the first known application to volcano-acoustic data.

2.2.2 Study Overview

The aim of this study is to investigate the ability of a quadspectral density nonlinearity indicator to quantify distortions to volcano-acoustic signals as a result of nonlinear propagation dynamics. Specifically we define three hypotheses that are tested throughout this paper:

H1: Nonlinear acoustic propagation of Sakurajima eruption signals causes quantifiable upward spectral energy transfer associated with wave steepening. We test this hypothesis by applying ν_N to Sakurajima data (Sections 2.4.1, 2.5.4) and to synthetic pressure data from FDTD simulations (Sections 2.4.2, 2.5.1, 2.5.2).

H2: Acoustic wavefield interactions with topography cause complications in the waveform that obscure the nonlinear signature in ν_N. We test this hypothesis by comparing ν_N results from nonlinear FDTD modeling with and without topography (Sections 2.4.2, 2.5.1).

H3: Wavefield interactions with wind gradients obscure the nonlinear signature in ν_N. We test this hypothesis by comparing ν_N results between FDTD simulations with different wind speed gradients (Sections 2.4.2, 2.5.2).

2.3 Sakurajima Volcano and Infrasound Data

Sakurajima Volcano is an active andesitic-dacitic stratovolcano rising 1117 m above sea level on Kyushu Island in Southern Japan (Figure 2.2). The volcano's active vent, Showa crater, has produced approximately 1,000 vulcanian-style explosions per year since 2009 (Yokoo et al., 2013). This eruptive activity occurs only ∼8 km east of Kagoshima city and poses a constant

ash fall hazard to a population of >600,000. Sakurajima is consequently one of the world's best-monitored volcanoes (Iguchi et al., 2013), and scientific investigations there have played an important role in explaining Vulcanian eruption processes (¡e.g., Uhira and Takeo, 1994; Tameguri et al., 2002; Iguchi et al., 2008; Yokoo et al., 2009; Iguchi, 2013; Miwa and Toramaru, 2013; Yokoo et al., 2013; Clarke et al., 2015).

The dataset used in this study features eight days of publicly-available acoustic pressure records collected by five infrasound sensors with 200 Hz sample rate at distances of 2.4–6.2 km from Showa crater (Figure 2.2). The volcano was highly active during the study period (18–26 July, 2013) as evidenced by the detection of 34 high-amplitude explosions (Fee et al., 2014) and 74 total explosive events (Matoza et al., 2014). The 74 explosive events identified by Matoza et al. (2014) feature peak pressures of 0.01–449.48 Pa, station-averaged durations of 10–3000 seconds, and peak frequencies of 0.4–1 Hz. Typical eruption sequences (e.g., Figures 2.3a and 2.3e) feature an initial compression and rarefaction pair corresponding to an explosion (rapid release and expansion of overpressurized gas at the vent), and subsequent lower-amplitude oscillations related to venting of gas and tephra (Fee et al., 2014; Johnson and Miller, 2014) and reflections from topography (Yokoo et al., 2014).

To compare the power spectra of volcanic signals to the background noise range, we estimate the PSD for 50% overlapping 1-hour time windows for the entire dataset at each station in the 2013 infrasound deployment. We define network-wide low, median and high noise conditions as the network-averaged 5^{th}, 50^{th} and 95^{th} percentiles of the PSD curves, after Bowman et al. (2005) and Brown et al. (2014). Spectra for high-amplitude volcanic signals markedly exceed the 95^{th} percentile in the peak frequency range of approximately 0.4–1 Hz (e.g., Figures 2.3c and 2.3g).

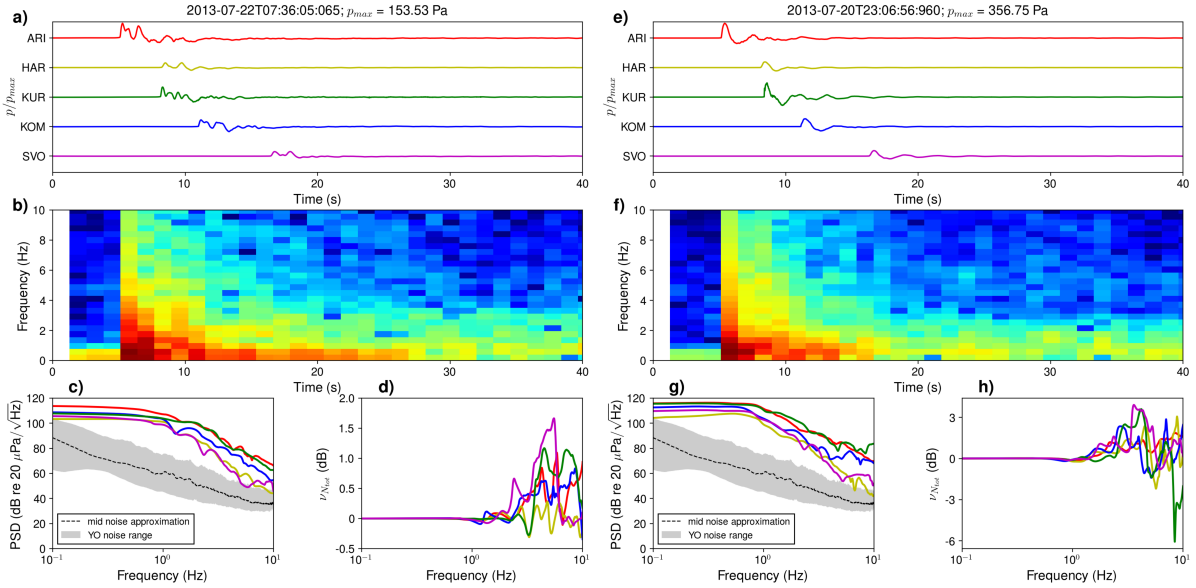

Figure 2.3: Example of waveforms, spectra and nonlinearity indicator results for two acoustic eruption events in the Sakurajima dataset. **a)** Unfiltered pressure (p) waveforms for a single event arranged in order of increasing vent-station distance from top to bottom. Spectral estimation is performed on unfiltered time windows starting 20 seconds before each station-specific trigger-on time and ending 20 seconds after the trigger-off time; cropped traces are detrended and multiplied with Tukey windows that taper the first and last 20 seconds. Signals are normalized by maximum pressure at ARI (p_{max}). **b)** Spectrogram showing power spectral density at station ARI for the waveform above. **c)** Power spectral density for the waveforms in Figure 2.3a, compared to the network-averaged noise range in grey. YO is the network code for the 2013 Sakurajima infrasound experiment. **d)** Cumulative nonlinearity indicator results ($\nu_{N_{tot}}$) for the spectra in Figure 2.3c and waveforms in Figure 2.3a. The ν_N analysis is band-limited to 0.1–10 Hz to avoid poor spectral resolution at low frequencies and cultural noise at high frequencies. **e-h)** As for parts a-d, but for a higher-amplitude event.

2.4 Methods

2.4.1 Estimation of Observed ν_N

We apply the ν_N nonlinearity indicator to 30 acoustic eruption signals with high signal-to-noise (SNR) ratios out of the 74 events detected by Matoza et al. (2014) using a network-coincident short-term average/long-term average method. We exclude 44 catalog events for which the power spectra of two or more stations fall below the network-averaged median noise condition spectrum in the 0.1–10 Hz frequency band (dashed grey line in Figures 2.3c and 2.3g). This approach mitigates the contamination of nonlinearity indicator results by wind

and/or cultural noise, and limits the analysis to higher-amplitude signals for which nonlinear propagation is more likely to be significant (peak pressures of 5.80–449.48 Pa at ARI). These events correspond to impulsive Vulcanian-type eruptions followed by lower-level gas and ash emissions, but significant variability in waveform character, peak pressures, event intensity, and frequency content (Fee et al., 2014; Matoza et al., 2014) suggests that the source process varies between events in terms of vent opening dynamics, volume flux rates (e.g., Johnson and Miller, 2014) and gas/ash ratio.

We estimate PSD and cross-spectral densities (CSD) of unfiltered waveforms and their squares using a sine multi-taper method (Riedel and Sidorenko, 1995). Time windows are defined by the station-specific start and end times of the catalog plus 20 seconds of Tukey-tapered noise on either side. The addition of 40 seconds of data increases the frequency resolution of the spectra, while Tukey-tapering preserves the amplitudes of the volcano-acoustic signals and eliminates pressure discontinuities at the window edges.

Nonlinearity indicator results are integrated with respect to station slant distance (i.e., line-of-sight distance) to estimate cumulative spectral changes ($\nu_{N_{tot}}$), as discussed in A.1. Integration assumes a constant rate of spectral change, when in fact the rate of change decreases with decaying signal amplitude (Miller and Gee, 2018). Since Sakurajima stations are several kilometers from the source, observed ν_N likely represents a smaller rate of change than what occurs near the source. Cumulative $\nu_{N_{tot}}$ therefore likely underestimates the total spectral changes, however, we present integrated results rather than raw ν_N because they are more applicable to a spectral correction scheme and because they are easier to compare to other distorting processes such as geometrical spreading.

To faciliate comparison of ν_N across all events we extract several metrics from $\nu_{N_{tot}}$ and associated signals (Figure 2.10) including:

- Centroid frequency, $f_c = \frac{\int_{f1}^{f2} f S_{pp} df}{\int_{f1}^{f2} S_{pp} df}$, where f_1 and f_2 are the high and low frequency bounds of interest, f is the bounded frequency range, and S_{pp} is power spectral density (Johnson, 2019). Use of f_c is preferable to peak frequency in this case because the spectral

peaks are broad at low frequencies (e.g., Figures 2.3c and 2.3g).

- PSD and $\nu_{N_{tot}}$ at f_c.

- Maximum and minimum $\nu_{N_{tot}}$ and associated frequencies.

- Maximum signal pressure.

Since wave steepening causes energy to transfer primarily to frequency components higher than the dominant source frequency, we expect to see $\nu_N < 0$ (energy loss) at f_c and $\nu_N > 0$ (energy gain) at $f > f_c$. We expect this to be expressed as a positive correlation between f of minimum $\nu_{N_{tot}}$ and f of maximum $\nu_{N_{tot}}$, and negative values of $\nu_{N_{tot}}$ at f_c. Furthermore, since higher pressures gives rise to greater phase speeds (Hamilton and Blackstock, 2008), we expect a positive correlation between maximum signal pressure and maximum $\nu_{N_{tot}}$ and a negative correlation between maximum signal pressure and minimum $\nu_{N_{tot}}$. These relationships have been qualitatively observed in applications to computationally-propagated waves (Reichman et al., 2016a; Miller et al., 2016) and model-scale jet noise (Miller and Gee, 2018), as shown in Figure 2.1c. This study is the first to extract quantitative metrics from ν_N.

2.4.2 Nonlinear FDTD Modeling of ν_N

We model the acoustic wavefield at Sakurajima with a FDTD method for nonlinear infrasound propagation developed by de Groot-Hedlin (2017). The method includes rigid stair-step topography at the lower boundary, vertical 1D gradients in sound and wind speeds, and spherical spreading in a 2D model plane by implementation of a cylindrical coordinate system that is axisymmetric about the left boundary. The model is bounded at the top and right by absorbing Perfectly Matched Layers (Berenger, 1994) set at a maximum range and height of 15 km. This choice ensures that any potential artificial reflections from the top and right boundaries do not reach the synthetic receivers (maximum range of 6.2 km) before the end of the simulation at 44 seconds. We use a linear sound speed gradient of 6°K/km from 348 m/s at sea level to 308 m/s at 11 km and constant above this.

At the start of each simulation the source function is initialized as a spatially-distributed Gaussian pulse of positive pressure with radius equal to three times the maximum source wavelength at the sound speed of the source altitude. The pulse is truncated at the source radius such that the pressures and densities in the rest of the model space are initialized to ambient values. Rapid wavefield changes during high-amplitude propagation can lead to numerical instability (de Groot-Hedlin, 2017), so we use flat topography within the source radius to avoid initializing complex interference patterns from reflections inside the crater (e.g., Figure 6). We approximate the source-time function (STF) by placing a synthetic receiver one grid cell from the left boundary and one grid cell above the top of the source radius and cropping the waveform before the arrival of the ground reflection. This yields a waveform with a nearly-symmetrical compression-rarefaction pair (Figure 2.4a). This source implementation produces peak frequencies of approximately one third the maximum input source frequency ($f_{\max}$) for linear propagation modeling; for the nonlinear modeling used here, spectral energy transfer may lead to lower peak frequencies.

We test the hypotheses presented in Section 2.2.2 by systematically varying the simulation inputs. Table 2.1 summarizes the input and discretization parameters for the ten simulation sets presented here (47 total simulations). Notably, the time step (Δt) and grid spacing (Δ) vary by simulation to meet the Courant stability criterion as a function of the maximum source frequency, maximum source pressure, and minimum number of grid nodes (NDX) per wavelength at $f_{\max}$. The Courant stability criterion Taflove and Hagness (2005) is $\Delta t \leq \Delta / c_{\max}\sqrt{3}$ where $c_{\max}$ is the maximum sound speed. At least ten grid nodes per wavelength are required at $c_{\max}$ to maintain numerical accuracy (Taflove and Hagness, 2005). In this study we require 20 NDX at a maximum source frequency of $f_{\max}$ =1.7 Hz in each simulation; this means that the 10 NDX criterion for stability is met for frequencies up to 3.4 Hz and 60-80 nodes per wavelength are present at the dominant frequency range below ∼0.8 Hz.

To test the accuracy of the frequency components we seperately ran a nonlinear simulation set with NDX=40 at 1.7 Hz (set S9). Increased discretization does not affect the shapes or

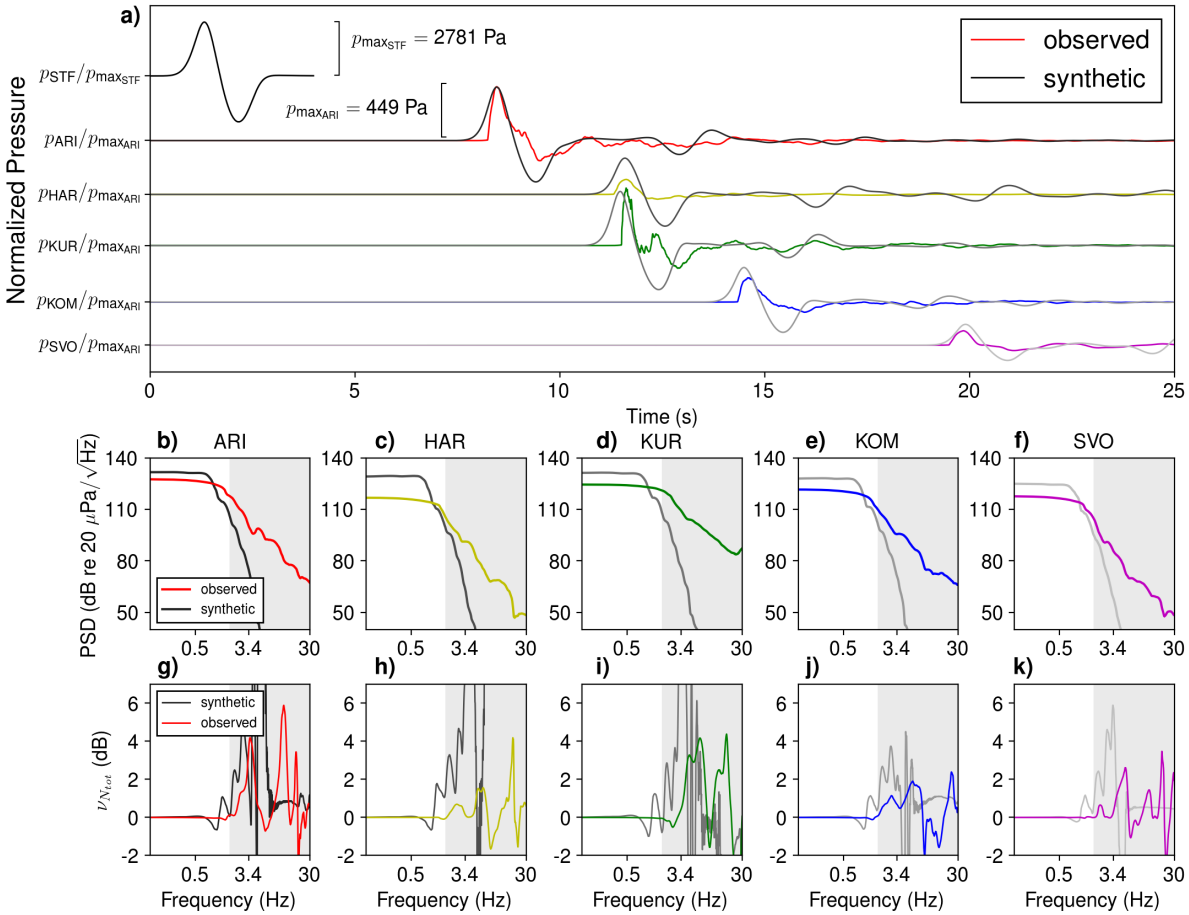

Figure 2.4: Comparison of synthetic data from windless nonlinear simulation set S1 (solid grey-scale lines) with observational data from a Sakurajima eruptive event at 23:21:49 UTC on 07/20/2013 (colored lines). **a)** Waveform comparison. The first trace shows the approximate source-time function (∼STF) as recorded by a synthetic receiver at 1 grid cell from the left boundary at the top of the source function (8.5 m range, 1274 m altitude). The five trace pairs below show observed and synthetic waveforms that are time-aligned by the time of peak pressure at real and synthetic ARI stations. Amplitudes of the STF are normalized by the peak pressure of the STF ($p_{\mathrm{max_{STF}}}$) while the other waveforms are normalized by the peak pressure at the real ARI station ($p_{\mathrm{max_{ARI}}}$). **b-f)** Power spectral densities for the waveforms in Figure 2.4a plotted by station. For each trace, the PSD is estimated on 31 second windows (7 seconds before and 24 seconds after peak pressure) that are detrended and tapered with a 20% Tukey window. **g-h)** Cumulative ν_N estimates for the spectra in Figures 2.4b-f. Note that synthetic frequency components are most accurate below 1.7 Hz whereas the observed spectra are have power over a broader frequency range. The grey shaded region indicates frequency components above 1.7 Hz for which synthetic spectra may be innaccurate due to numerical dispersion.

amplitudes of the power spectra or ν_N spectra at frequency components $f < 1.7$ Hz, but it does result in small increases in PSD and ν_N values with frequency above 1.7 Hz (Figures S1 and S2 in supporting information). From this we conclude that inaccuracies arising from numerical dispersion are negligible at frequencies less than 1.7 Hz but may impact results at higher frequencies. We therefore only interpret synthetic results at frequencies below 1.7 Hz. In this manuscript we show synthetic results up to 3.4 Hz but indicate frequencies greater than 1.7 Hz with grey shaded boxes.

Table 2.1: Summary of input and discretization parameters for FDTD modeling. S_{ID} is simulation set identification label, LB is lower boundary type (flat, topography, or both), SA is source amplitude, Δt is time step, Δ is grid spacing, NDX is number of grid cells required per wavelength at the maximum source frequency and minimum sound speed, and H_{ID} is hypothesis identification number in reference to Section 2.2.2. H_{ID} indicates which hypothesis the simulation set is intended to address. Simulations sets S1-S9 with topography include five simulations (one for each source-receiver profile) while those with flat ground feature one simulation with all receivers on the same profile. S10 includes eight simulations with different SA values.

S_{ID}	LB	SA (Pa)	Wind	Δt (ms)	Δ (m)	NDX	H_{ID}
S1	both	47500	no	7.4	9.0	20	H1
S2	topo	47500	toward ARI	7.0–7.6	8.5–9.5	20	H1
S3	topo	47500	toward HAR	7.0–7.6	8.5–9.5	20	H3
S4	topo	47500	toward KOM	7.0–7.6	8.5–9.5	20	H3
S5	topo	47500	toward KUR	7.0–7.6	8.5–9.5	20	H3
S6	topo	47500	toward SVO	7.0–7.6	8.5–9.5	20	H3
S7	flat	47500	toward all	7.6	9.5	20	H3
S8	flat	47500	away from all	6.9	8.4	20	H3
S9	both	47500	no	3.7	4.5	40	H1
S10	flat	1484–95000	no	7.4	9.0	20	H1

We run simulations over 2D topography profiles (Figure 2.2) using a 1-m resolution digital elevation model (DEM) to model ν_N results in the Sakurajima dataset. We use a 10-m resolution DEM covering a large area over Kagoshima Bay and a smaller 1-m resolution DEM covering Showa crater and the summit region of Sakurajima. The 10-m resolution DEM is interpolated to 1-m resolution using a bivariate spline approximation over a rectangular mesh and fused with the true 1-m resolution DEM. The 1-m resolution stair-steps are discretized to the 8.5–9.5 m grid spacing in the model space, but these larger steps are sufficiently small relative to the

shortest wavelength of interest in the simulations (∼100 m for 3.4 Hz at 340 m/s) to minimize the magnitude of artificial reflections. Small artificial reflections similar to diffraction grating (constructive interference between waves reflected from different stair-step faces) are possible even with very small steps (e.g., de Groot-Hedlin, 2004), however, the magnitude of these are small compared to the specular reflections.

We choose $f_{\max}$=1.7 Hz to match the approximate spectral peak of the Sakurajima signals (0.4–1 Hz), and a source overpressure of 47,500 Pa to match amplitudes at the closest station to that of the largest event in the dataset (449 Pa at 2.3 km). We use a nonlinear-linear transition threshold of 0.3% ambient pressure (transition at ∼304 Pa) after de Groot-Hedlin (2017). To test the influence of topography on ν_N, we compare these results to simulations run over flat ground (S1).

To test the influence of wind, we run five sets of simulations in which a wind speed profile of $w_0 = 2\log_{10}(z)$ is directed toward one station and rotated for the other stations by $w_n = w_0\cos(\theta)$, where θ is the azimuth difference between two stations (Figures 2.5a-e). We bracket the parameter space for the flat ground simulations by directing wind over flat ground toward and away from all the stations (Figure 2.5f). The wind profiles, following work by Jones et al. (1986), are not intended to simulate local meteorological conditions during the field deployment but rather to test the influence of wind on ν_N under maximum likely wind conditions.

Finally, we test the response of ν_N to variable strengths of nonlinearity by running eight simulations with different maximum input pressures ranging from 1.48 to 95.00 kPa (simulation set S10 in Table 2.1). We approximate free-field propagation by setting the source and receiver altitudes at 7.5 km above a flat lower boundary at sea level. Reflected waves from the upper and lower boundaries are avoided by stopping the simulations before the reflected arrivals. We measure changes very close to the source by placing ten synthetic receivers at 100 m intervals starting 10 m outside the edge of the source radius.

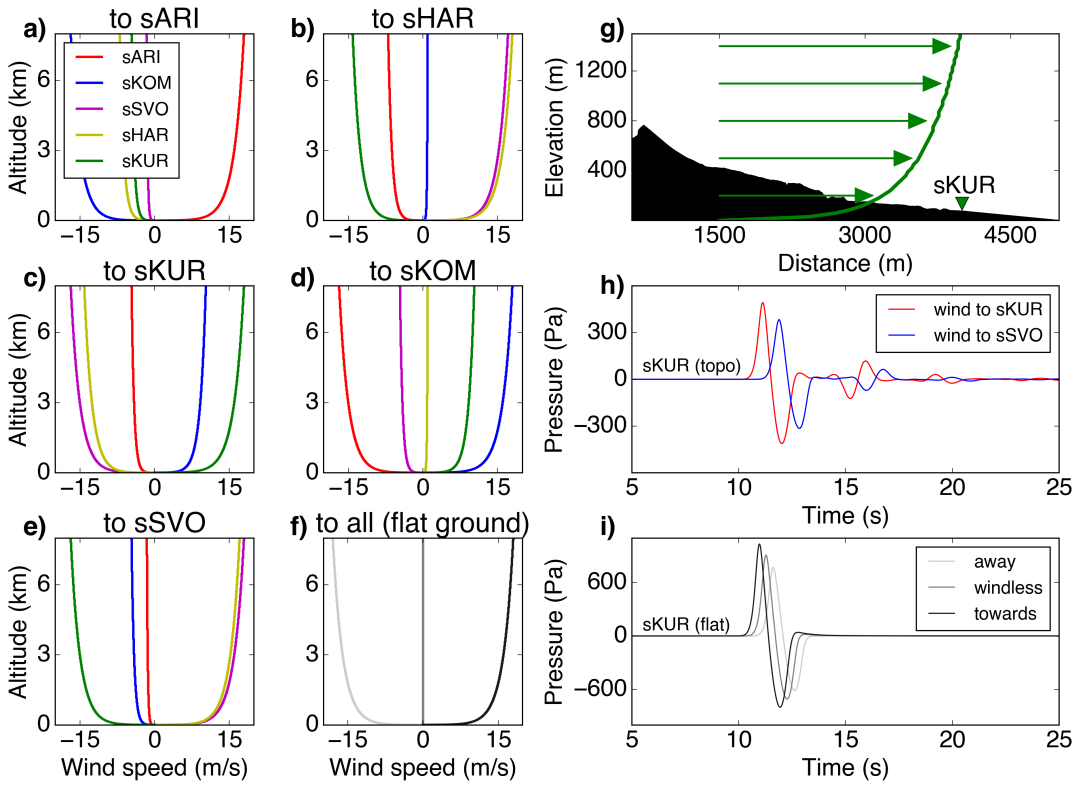

Figure 2.5: **a-e)** Logarithmic wind profiles for nonlinear FDTD simulations S2-S8 (Table 2.1). The maximum wind speed profile is directed towards the station in the subplot title, and wind profiles at other stations are rotated by the azimuth difference. **f)** Logarithmic wind profiles for the flat ground simulations including the windless condition (S1) and conditions for which wind is directed toward all stations (S7) or away (S8). **g)** Topographic profile for station sKUR (triangle) illustrating the wind condition for a wind speed vector directed towards the station (not to scale). Arrows show how wind speed increases with height. Vertical exaggeration is approximately 2:1. **h)** Waveforms at station sKUR for simulations with topography in which wind is blowing towards sKUR (red) and towards sSVO (blue). **i)** Waveforms at station sKUR for flat ground stations with windless condition and with wind blowing toward and away from the station. Compared to downwind propagation, upwind propagation results in a delayed travel times and reduced amplitudes.

2.5 Results

2.5.1 Influence of Topography on Modeled ν_N Results

Similar to previous work (Kim and Lees, 2011; Lacanna and Ripepe, 2013; Kim and Lees, 2014; Lacanna et al., 2014), our FDTD modeling shows that reflections from topography create arrivals that are visible in the wavefield (Figure 2.6) and as additional waveform arrivals following the source pulse (Figures 2.7a and 2.7i) that create irregularities in the associated PSD (Figures 2.7b and 2.7j). Propagation over rougher topography induces delayed travel times, amplitude reductions in the waveforms (Figures 2.7a and 2.7i), and power reductions in the spectra (Figures 2.7b, 2.7c, 2.7j and 2.7k) compared to propagation over flat ground. For example, at the distance of station SVO, nonlinear propagation simulations show that the peak pressure is reduced by 34% and the arrival time is delayed by 0.62 seconds when topography is included compared to flat ground.

Figure 2.7 shows that upward spectral energy transfer is modeled when nonlinear propagation equations are used. Power spectra for the results from the flat ground model space (Figure 2.7c) show a gain in power at frequencies above the spectral peak (1.2–3.4 Hz) compared to the approximate source time function. This energy gain is also visible in the PSDs from simulations with Sakurajima profiles (Figures 2.7b), but it is distorted by wavefield interactions with topography.

The $\nu_{N_{tot}}$ results from simulations with flat ground (Figures 2.7d-h) show the reclined S-shape indicative of upward spectral energy transfer as expected from previous studies (Miller and Gee, 2018) and shown in Figure 2.1c. These results show that $\leq$1 dB of spectral energy is transferred away from the 0.8–1.2 Hz frequency components primarily to higher frequencies (1.2–3.4 Hz), with up to 6.5 dB gain at 3.4 Hz at synthetic KUR. The spectral energy gains peak at approximately 1.35 Hz, 2.05 Hz, 2.75 Hz and 3.4 Hz, as estimated from the flat ground sKUR $\nu_{N_{tot}}$ spectra. These peaks correspond to harmonics on a 0.68 Hz fundamental frequency, but the peak frequency of the source-time function is 0.57 Hz. However, at this distance from

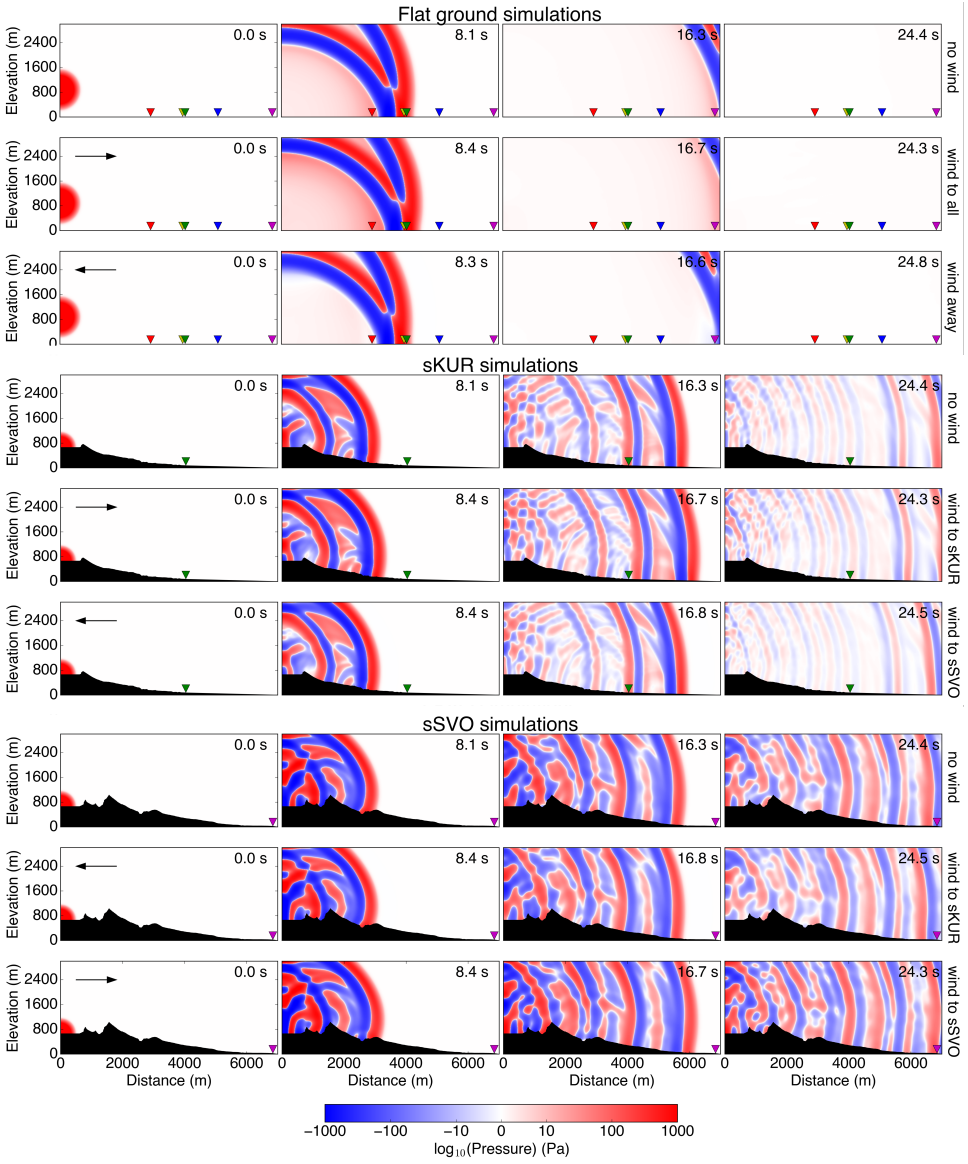

Figure 2.6: Wavefield snapshots for nonlinear acoustic propagation simulations over flat ground, Sakurajima station KUR topography, and station SVO topography using the method of de Groot-Hedlin (2017). Each row shows snapshots advancing in time from left to right for one lower boundary type and one wind condition. Triangles indicate synthetic receiver locations ("s" for synthetic). Text at right and arrows (where applicable) indicate the wind condition (see Figure 2.5 for wind profiles). The first three rows represent simulations over flat ground in simulation sets S1, S7 and S8 in Table 2.1. The middle three rows represent simulations over KUR topography in sets S1, S5 and S6. The lower three rows represent simulations over SVO topography in sets S1, S5 and S6.

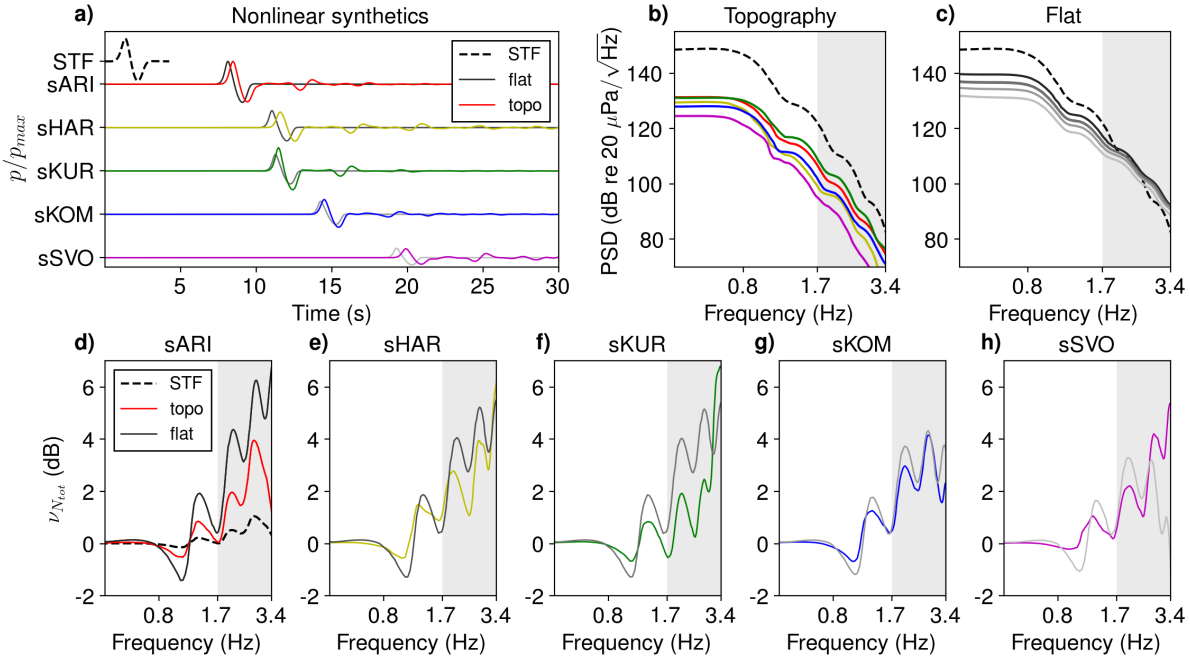

Figure 2.7: **a)** Synthetic ("s") waveforms from windless nonlinear FDTD simulation set S1 in Table 2.1. Colored waveforms correspond to simulations with Sakurajima topography and receivers at Sakurajima station distances. Solid grey-scale waveforms correspond to simulations over flat ground with receivers at slant station distances. The dashed black line shows the approximate source time function normalized by the maximum amplitude as described in the caption for Figure 2.4a and text. The other waveforms are normalized by the peak pressure at sARI (p_{max}). **b)** PSD estimates for the synthetic waveforms from Sakurajima topography simulations in Figure 2.7a. Tukey-tapered time windows of 31 seconds each are used, with 7 seconds before and 24 seconds after peak pressure. Colors correspond to stations as shown in Figure 7a while the dashed line corresponds to the STF. **c)** PSD estimates for the synthetic waveforms from flat ground simulations in Figure 2.7a. Grey-scale lines correspond to stations as shown in Figure 7a while the dashed line corresponds to the STF. **d-h)** Cumulative ν_N estimates ($\nu_{N_{tot}}$) for spectra from topography and flat ground simulations for each station (colored and grey-scale, respectively). The grey shaded regions indicate frequency components above 1.7 Hz for which synthetic spectra may be innaccurate due to numerical dispersion.

the center of the source a small amount of wave steepening by nonlinear propagation occurs, as evidenced by secondary peaks in the source PSD (Figures 2.7b and 2.7c) and non-zero $\nu_{N_{tot}}$ values (Figure 2.7d). The 0.57 Hz spectral peak may therefore be lower than the 0.68 Hz fundamental because a small amount of energy has transferred away from the peak source frequency. We also note the spectral peak is broad enough to include the 0.68 Hz fundamental (Figures 2.7b and 2.7c). Additionally, at the synthetic stations at Sakurajima distances, a small amount of power is also transferred downward by period lengthening ($\sim$0.1 dB between 0.4 and 0.8 Hz). Inclusion of Sakurajima topography reduces $|\nu_{N_{tot}}|$ levels and complicates the $\nu_{N_{tot}}$ spectral shapes (Figures 2.7d-h). However, the effect of topography is not sufficient to explain the complexity in the $\nu_{N_{tot}}$ results from the observed Sakurajima signals as shown in Figures 2.4g-k and discussed in Section 2.5.4.

2.5.2 Influence of Wind on Modeled ν_N Results

Since wavefield interactions with topography are insufficient to explain the complexity of the observed Sakurajima ν_N spectra (see Figures 2.4g-k), we investigate the effect of wind on the ability to observe nonlinear effects. Upwind propagation results in delayed arrival times and reduced amplitudes in the waveform (Figures 2.5h and 2.5i) and frequency-independent reductions in the PSD (Figures 2.8a-e). Conversely, upwind propagation over flat ground results in generally greater-magnitude $\nu_{N_{tot}}$ spectra relative to windless or downwind propagation (Figures 2.8f-j).

When topography is included the $|\nu_{N_{tot}}|$ levels are reduced compared to flat ground results as discussed in Section 2.5.1, and downwind propagation conditions (red lines in Figure 2.8) generally result in smaller-magnitude $\nu_{N_{tot}}$ levels than upwind conditions (blue lines in Figure 2.8). We tentatively interpret this result (Section 2.6.2) as a consequence of enhanced multipathing in the downwind direction that results in multiple arrivals that obscure the nonlinearly-generated phase coupling from wave steepening. However, each of these combinations of wind and topography yield a $\nu_{N_{tot}}$ spectrum with the reclined S-shape in general agreement with previous

studies (Miller and Gee, 2018) and theory (Reichman et al., 2016a). These results show that neither topography nor wind is sufficient to explain the complexity of $\nu_{N_{tot}}$ for the observed Sakurajima signals as shown in Figures 2.4g-k and discussed in Section 2.5.4.

2.5.3 Influence of Source Amplitude on Modeled ν_N Results

Since the strength of nonlinear wavefield changes (e.g., wave steepening and period lengthening) is thought to increase with amplitude, we hypothesize that the magnitude of ν_N will increase with source pressure. We test this by running eight simulations with source pressures ranging from 1.5 kPa to 95 kPa and receivers placed within 1 km from the edge of the source radius (Section 2.4.2). The results clearly show that larger source pressures lead to greater waveform asymmetry with increasing distance (Figure 2.9a) and enhanced power spectral density at higher frequencies (Figure 2.9b–f and 9l–p). The magnitude of $\nu_{N_{tot}}$ generally increases with source pressure (Figure 2.9g–k and 2.9q–u); for example the absolute values of $\nu_{N_{tot}}$ at 1.7 Hz as recorded at 313 m are 0.08, 0.12, 0.11, 0.07, 0.12, 0.16, and 0.34 dB for source pressures of 1.5, 2.7, 5.9, 11.9, 23.8, 35.6, 47.5 and 95.0 kPa, respectively. A degree of frequency-dependent variability and complexity is present in the relationships between $\nu_{N_{tot}}$ magnitude, source pressure, and distance, but the general trend shows that larger source pressures lead to greater nonlinear changes that can be detected with ν_N. Conversely, $\nu_{N_{tot}}$ tends towards zero for reduced source pressures that yield smaller nonlinear changes.

Inconsistencies in the relationships between source pressure, distance, ν_N magnitudes and the frequencies of $\nu_{N_{tot}}$ maxima and minima (Figure 2.9g–k and 2.9q–u) may reflect the highly nonlinear process by which spectral energy is transfered. For example, at 916 m the value of $\nu_{N_{tot}}$ is greater for a 47.5 kPa source than a 95.0 kPa source (0.64 and 0.37 dB), respectively. However, since spectral energy is transfered to progressively higher frequency components with distance (e.g., Hamilton and Blackstock, 2008), we speculate that the wave from a 95.0 kPa source may be primarily transferring more energy to a higher frequency component at 916 m while from a 47.5 kPa source may transfer more energy to 1.7 Hz. Since these simulations are

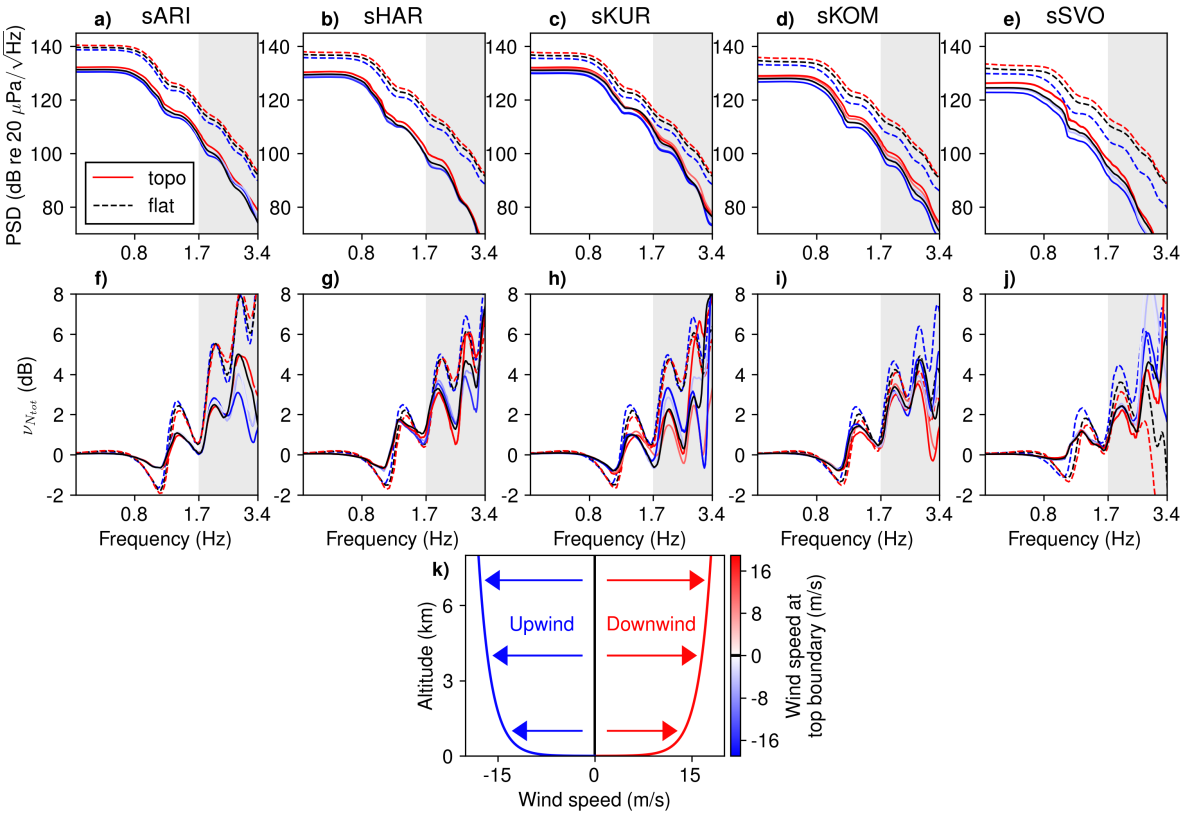

Figure 2.8: **a-e)** Synthetic PSD results from simulations with different wind conditions (simulation sets S1-S8) plotted by synthetic receiver ("s" for synthetic). Each line represents the spectrum for a different wind condition as recorded at the receiver in the subplot title. Colors represent wind speed at the upper boundary for the simulation as illustrated in Figure 2.8k. Results from the windless simulations (set S1) are shown in black for clarity. Solid lines show results from simulations with topography (sets S1-S6) while dashed lines are from simulations with flat ground (S1, S7 and S8). The grey shaded region indicates frequency components above 1.7 Hz for which synthetic spectra may be innaccurate due to numerical dispersion. **f-j)** Cumulative nonlinearity indicator results ($\nu_{N_{tot}}$) for the PSDs above. **k)** Example wind speed profiles to illustrate the color implementation. Red colors indicate wind blowing towards a station (downwind propagation) and blue colors indicate wind blowing away (upwind propagation). Arrows indicate the corresponding wind direction in a source-receiver plane.

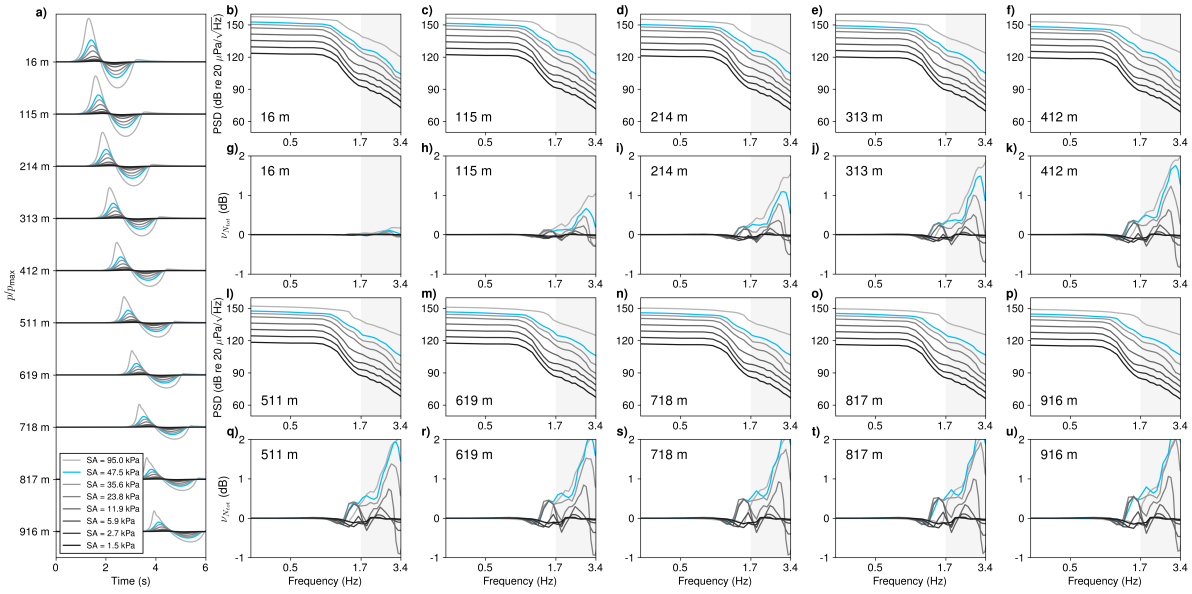

Figure 2.9: **a)** Synthetic waveforms for simulation set S10 (Table 2.1) recorded at 10 receivers for eight different maximum source pressures. Blue lines show results for the source pressure used in simulation sets S1–S9. **b–f)** Power spectral density for eight different source pressure conditions at five receivers with range of 16–412 m from the edge of the source radius. **g–k)** Cumulative nonlinearity indicator ($\nu_{N_{tot}}$) curves for the spectra in Figure 2.9b–2.9f. **l–p)** Power spectral density for eight different source pressure conditions at five receivers with range of 511–916 m from the edge of the source radius. **q–u)** Cumulative nonlinearity indicator ($\nu_{N_{tot}}$) curves for the spectra in Figure 2.9l–2.9p. The grey shaded regions indicate frequency components above 1.7 Hz for which synthetic spectra may be innaccurate due to numerical dispersion.

only reliable at frequencies ≤1.7 Hz (Section 2.4.2), we cannot confirm this with confidence. Further work outside the scope of this study could investigate the change in ν_N with distance over a broader frequency range.

2.5.4 Observed ν_N Results

Application of the ν_N indicator to 30 eruptive events in the Sakurajima dataset reveals cumulative distortions ranging from -10.4 dB to 10.1 dB in the 0.1–10 Hz frequency range (Figures 2.10a and 2.10c). However, most events feature cumulative ν_N changes on the order of $\leq 10^{-1}$ dB, and the shapes of the observed indicator spectra do not exhibit the reclined S-shape observed in previous studies (Figure 2.1c; Miller and Gee, 2018) or our numerical modeling results (Figures 2.4g-k). In many cases, observed $\nu_{N_{tot}}$ is generally positive above 1 Hz (e.g., Figures 2.3d and 2.3h) without proportional negative values at lower frequencies. We note here that a meaningful ν_N spectrum need not sum to zero due to the logarithmic scale of the indicator (e.g., Falco et al., 2006; Miller and Gee, 2018), however, the observed Sakurajima $\nu_{N_{tot}}$ results are clearly lacking in proportional losses at low frequencies seen in previous work (e.g., Figure 2.1c; Miller and Gee, 2018).

The lack of expected structure in the ν_N spectra is reflected in the metrics (Figure 2.10). Peak signal pressure has a weak positive correlation with maximum $\nu_{N_{tot}}$ (Figure 2.10a) and weak negative correlation with minimum $\nu_{N_{tot}}$ (Figure 2.10c). We expect these correlations based on the theory that nonlinear effects become stronger with increasing signal pressure. However, there is no correlation between the frequencies of maximum and minimum $\nu_{N_{tot}}$ (Figure 2.10b), or between $\nu_{N_{tot}}$ and f_c (Figure 2.10d). The grey shading in Figure 2.10b indicates a region where metric values are not expected according to theory, since energy is expected to primarily transfer upward in the spectrum, yielding a greater frequency of maximum $\nu_{N_{tot}}$ than the frequency of minimum $\nu_{N_{tot}}$. The occurence of results in this region indicates that the observed ν_N behavior does not agree with expectations from theory and previous work (e.g., Miller and Gee, 2018). The general occurence in Figure 2.10d of $\nu_{N_{tot}}>0$ values at the

centroid frequency may reflect period lengthening and/or shock coalescence below the peak source frequency of the source process, however, the scatter and low-magnitude values suggest that this feature is less significant than upward spectral energy transfer by wave steepening.

The general scatter and weak correlations in these metrics could indicate that acoustic propagation is linear, or that near-source nonlinearity is present but the associated spectral energy transfer is not accurately quantified by the ν_N indicator. We suggest in the following section that ν_N reveals potentially significant nonlinear spectral energy transfer but that the effects are poorly resolved in this dataset due to complicating factors arising from source and propagation processes.

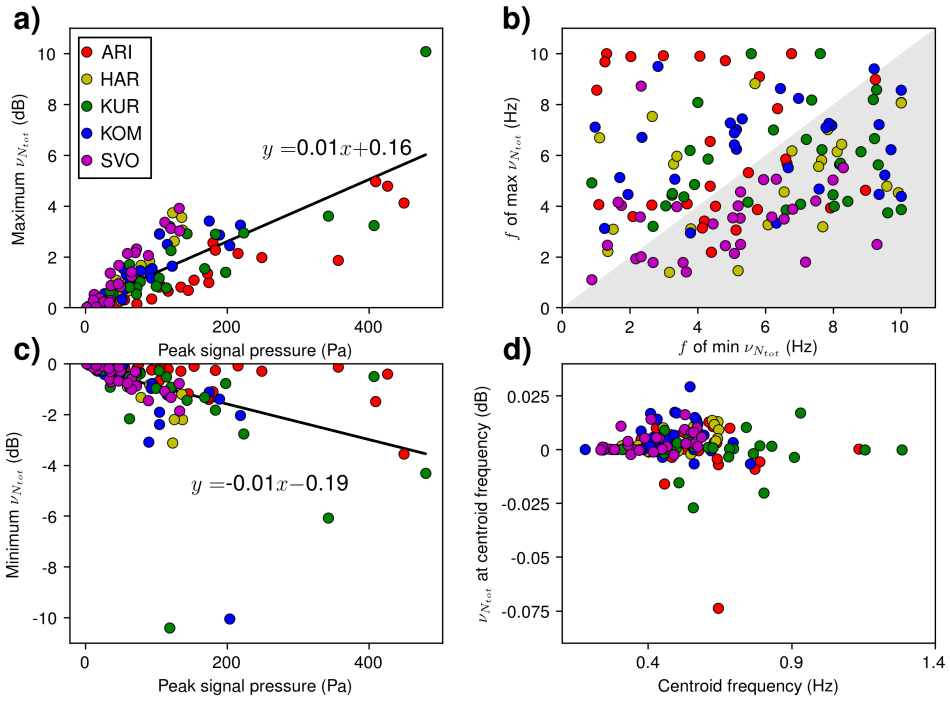

Figure 2.10: Nonlinearity indicator metrics for 30 high-SNR eruption events out of 74 in the (Matoza et al., 2014) catalog. All $\nu_{N_{tot}}$ spectra are integrated with respect to station slant distance (R_d). **a)** Maximum cumulative $\nu_{N_{tot}}$ as a function of maximum signal pressure. Black line and equation represent a linear least-squares fit. **b)** Frequency of maximum $\nu_{N_{tot}}$ plotted against the frequency of the minimum $\nu_{N_{tot}}$. Grey shaded region represents area of parameter space where results are not expected based on theory (see text and Figure 2.1c). **c)** Minimum cumulative ν_N as a function of maximum signal pressure. **d)** $\nu_{N_{tot}}$ at the centroid frequency versus the value of the centroid frequency. Not shown is an outlier of $\nu_{N_{tot}}$ = 0.23 dB at f_c = 0.99 Hz. All colors correspond to stations as per legend in Figure 2.10a.

2.6 Discussion

Application of a quadspectral density nonlinearity indicator to 30 Sakurajima acoustic eruption signals yields results suggestive of spectral energy transfer due to nonlinear wave steepening, while finite-difference propagation modeling unambiguously produces up to 2 dB of spectral energy transfer in the cases considered. Wavefield interactions with wind and topography modify the synthetic ν_N levels; however, neither wind nor topography are sufficient to explain the differences between observed Sakurajima ν_N spectra and expectations based on theory and previous studies. These results could indicate that acoustic propagation from Sakurjima volcano is linear at the distances considered; however, evidence from previous studies (Ishihara, 1985; Yokoo and Ishihara, 2007) and our nonlinear propagation modeling (Section 2.5.1) suggests that nonlinear changes to the wavefield may occur near the source. We suggest that nonlinear acoustic propagation effects may be significant at Sakurajima, but the ν_N indicator does not accurately quantify the spectral energy transfer in the observed signals because of complications from complex source dynamics and outdoor propagation effects.

2.6.1 Quantifying Spectral Energy Transfer in Sakurajima Acoustic Eruption Signals

Comparison of the cumulative effects of nonlinear propagation ($\nu_{N_{tot}}$) on synthetic Sakurajima signals to other distorting processes (Figure 2.11) shows that spectral energy transfer is less significant than the effects of geometrical spreading ($\nu_{S_{tot}}$) but more significant than atmospheric absorption ($\nu_{\alpha_{tot}}$). The frequency-dependent absorption losses are calculated using the approaches of Bass et al. (1984) and Sutherland and Bass (2004) as described in A.1. This indicates that corrections for nonlinear spectral energy transfer may provide a significant second-order improvement in accuracy for acoustically-based source parameter estimates. However, the disagreement between observed Sakurajima $\nu_{N_{tot}}$ and the ν_N behavior seen in previous studies (Reichman et al., 2016a; Miller and Gee, 2018) and our numerical modeling (Section 2.5.1, 2.5.2) suggest that the nonlinearity indicator does not accurately quantify spectral energy

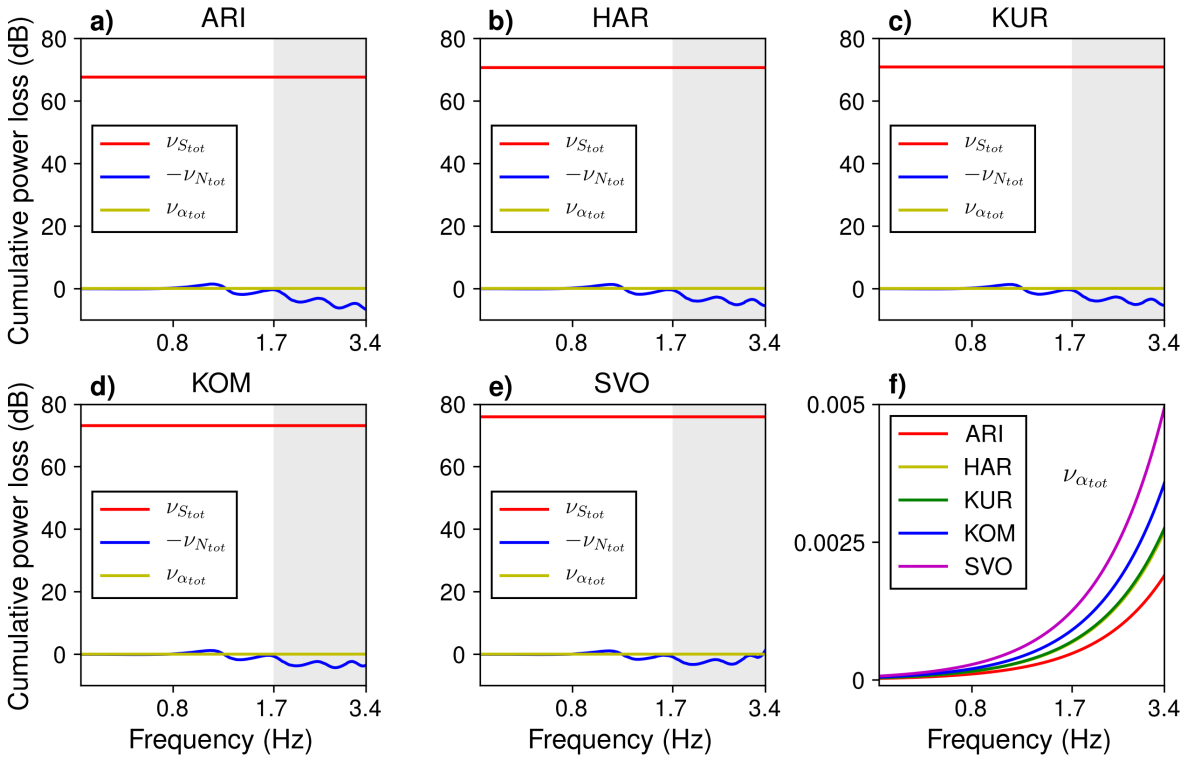

Figure 2.11: **a-e)** Comparisons of cumulative spectral power losses due to geometrical spreading ($\nu_{S_{tot}}$), absorption ($\nu_{\alpha_{tot}}$) and nonlinear effects ($\nu_{N_{tot}}$). The $\nu_{N_{tot}}$ results shown are from nonlinear, windless flat ground simulations (S1 in Table 2.1) and the sign of $\nu_{N_{tot}}$ is flipped ($-\nu_{N_{tot}}$) to be consistent with the other spectra (i.e., positive values indicate power loss). Note that losses to spherical spreading ($\nu_{S_{tot}}$) are frequency-independent while losses to absorption depend on frequency, but are too small to see at the scale of plots Figures 2.11a-e. The grey shaded region indicates frequency components above 1.7 Hz for which synthetic spectra may be innaccurate due to numerical dispersion. **f)** Frequency-dependence of $\nu_{\alpha_{tot}}$ at each station. Calculation of $\nu_{\alpha_{tot}}$ and $\nu_{S_{tot}}$ are described in A.1.

transfer in this dataset.

The large magnitudes of observed $\nu_{N_{tot}}$ results (up to ~10 dB) suggest that nonlinear propagation effects may be significant, but the inconsistencies in the shapes of the observed $\nu_{N_{tot}}$ spectra (Figures 2.3d and 2.3h) and poorly-correlated $\nu_{N_{tot}}$ metrics (Figure 2.10), indicate that ν_N does not accurately resolve nonlinear effects in the Sakurajima dataset. We suggest that ν_N does not accurately quantify these effects because of complications from source and propagation dynamics. While the assumptions underlying the ν_N equation (see Section 2.2.1 and A.1) can be reasonably met for computational propagation of the Burgers equation in the

free-field (Reichman et al., 2016a), and for model-scale jet noise propagation in an anechoic chamber (Miller and Gee, 2018), they are violated in the context of complex source processes and outdoor propagation effects. Volcano-acoustic spectra are affected by contributions from wavefield interactions with topography (reflections, diffraction, and scattering), refraction in local wind and temperature gradients, and nonlinear source dynamics with multiphase fluid flow, turbulent jetting and impulsive explosions (e.g., Matoza et al., 2019a). For example, it is possible that combinations of broadband power from explosions with lower-frequency jet noise may be treated by ν_N as spectral gains at high frequencies without corresponding losses at lower frequencies (e.g., Figure 2.3h).

2.6.2 Influence of Topography and Wind on ν_N

To investigate the effects of outdoor acoustic propagation on ν_N, we isolate the effects of topography by comparing synthetic results between numerical simulations with topography and with flat ground, and we isolate the effect of wind by comparing results between windless simulations and those with a variety of wind conditions (Table 2.1). We find that these effects create ν_N variations that modify the nonlinear signature, but neither process is sufficient to explain the departure of observed ν_N from modeling results.

Inclusion of topography in nonlinear simulations reduces $|\nu_N|$ levels compared to propagation over flat ground (Figures 2.7d-h). One potential explanation for this is preferential attenuation of high-frequency components due to acoustic scattering and reflection from topography. These losses counteract gains at high-frequencies due to nonlinear wave steepening, and lead to underestimation of spectral energy transfer by ν_N. Additionally, the nonlinearly-generated phase coupling quantified by Q_{pp^2} is obscured by offsets in phase between multipathed arrivals from various raypaths reflected from topography.

In contrast, wind differentially affects PSD and ν_N. Figure 2.8 shows that PSD is greater while $\nu_{N_{tot}}$ levels are lower at downwind stations compared to upwind. We interpret this behavior as a result of downwind-waveguiding that causes acoustic waves to multiply reflect

from the ground and the inverted sound speed gradient (Pierce, 1981; Bies et al., 2017). This process may cause offsets in arrival times of the reflected waves that cause phase shifts that artificially obscure the phase coupling induced by nonlinear propagation. Thus, downwind spectra may have relatively low-magnitude ν_N levels because the quadspectrum (Q_{pp^2}) cannot recover the coupled harmonics that are offset in arrival time.

In the true outdoor case, reflection from ground with finite-impedance or with near-surface air turbulence excited by solar heating can produce additional frequency-dependent phase shifts (Pierce, 1981; Bies et al., 2017) that may further obscure the phase coupling. The effects of impedance on low-frequency sound waves are small (Embleton et al., 1976; Piercy et al., 1977) and thus typically neglected in infrasound research (e.g., Bass, 1991; Whitaker and Norris, 2008; Sutherland and Bass, 2004). Rigid lower boundary conditions have been previously used to acheive strong agreement between observed and synthetic waveforms (e.g. Kim and Lees, 2011; Kim et al., 2015; Lacanna and Ripepe, 2013; Fee et al., 2017b), suggesting that the effects of finite impedance are negligible. However, low ground impedance due to loose tephra layers or shallow hydrothermal alteration (e.g., Matoza et al., 2009b) may be significant in the context of phase shifts upon reflection. This process is not accounted for in our FDTD simulations because the lower boundary is rigid such that phase is preserved on reflection. The effects of phase shifting on reflection of infrasound from finite-impedance ground could be a direction for future research outside the scope of this study.

To compare the relative magnitudes of topographic and wind effects on ν_N, we calculate differences in ν_N spectra between results from topography simulations and results from flat ground simulations (S1), and between windy simulations and windless simulations (S1-S8). Figure 2.12 shows the results of these analyses, where the dependent variables are $\Delta\nu_{N_{tot}}$ from flat (Figure 2.12a) and $\Delta\nu_{N_{tot}}$ from windless (Figure 2.12b). Larger amplitudes for $\Delta\nu_{N_{tot}}$ from flat indicate that the effect of topography is more significant than that of wind, and that effect is to reduce $|\nu_N|$. The smaller effect of wind depends on wind direction as discussed above.

We conclude that frequency-dependent distortions from wavefield interactions with topog-

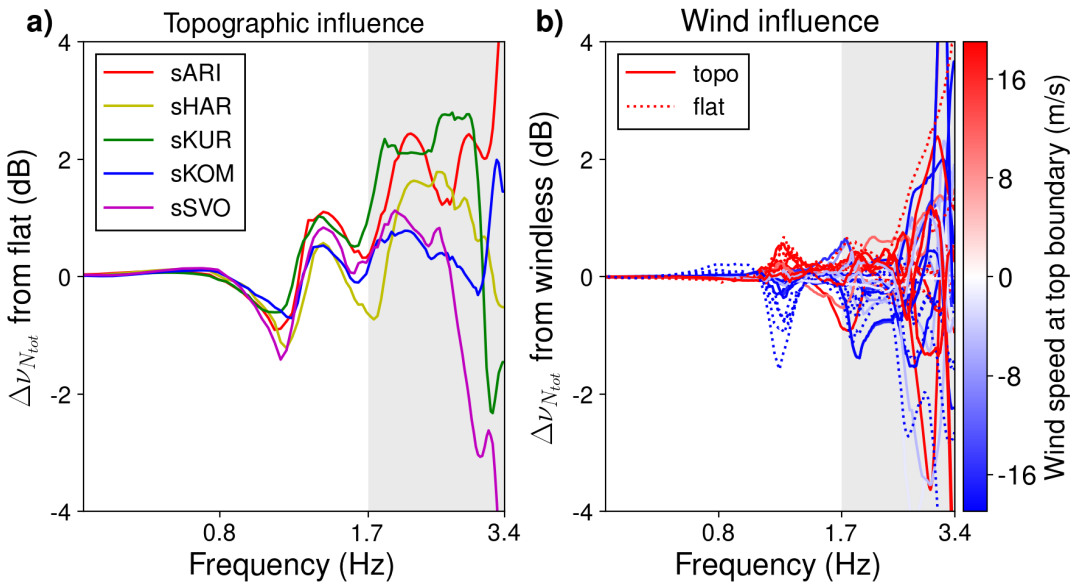

Figure 2.12: **a)** Topographic influence on $\nu_{N_{tot}}$ as expressed by the difference in $\nu_{N_{tot}}$ from FDTD simulation results with flat ground and with topography (i.e., $\Delta\nu_{N_{tot}}$ = flat result - topography result). The grey shaded region indicates frequency components above 1.7 Hz for which synthetic spectra may be innaccurate due to numerical dispersion. **b)** Influence of wind on $\nu_{N_{tot}}$ as expressed by the difference in $\nu_{N_{tot}}$ from FDTD simulation results with and without wind (i.e., $\Delta\nu_{N_{tot}}$ = windless result - windy result). Solid lines indicate results from simulations with topography while dashed lines indicate results from simulations with flat ground. Colors correspond to the wind speed at the top boundary of the model space as shown in Figure 2.8k.

raphy and wind may inhibit the effectiveness of the ν_N indicator by modifying the signature of spectral energy transfer due to wave steepening. Differences between observed Sakurajima ν_N and modeling results may be due to to additional complications from finer-scale meteorological structures (e.g., convective winds in canyons) and/or spectral contributions from complex source dynamics. Our modeling work has been limited to a simplistic Gaussian acoustic source function yielding nearly-symmetrical waveforms that poorly match observations (Figure 2.4), but recent work with fluid-dynamical sources have modeled asymmetrical waveforms even with linear acoustic propagation (Cerminara et al., 2016; Brogi et al., 2018). Three-dimensional wavefield effects are also likely significant, as our approach is limited to a 2D axisymmetric cylindrical geometry. For example, Kim et al. (2015) used linear 3D FDTD modeling to produce synthetic pressure waveforms in strong agreement with observed Sakurajima infrasound; however, their model did not test the effects of nonlinear wave steepening. We suggest that future ν_N applications may therefore be more successful in the presence of simpler topography for which 3D effects are less signficant, and with more realistic source-time functions for numerical modeling. Despite these limitations, our approach is sufficient to show that wavefield interaction with topography reduces the amplitude of the ν_N indicator. The true reduction in the presence of 3D topography may be greater.

We note here that these results may also be interpreted as an indication that nonlinear effects are insignificant for Sakurajima acoustic signals, and that consequently the linear propagation assumption is reasonable for estimating source parameters such as volume and mass flux (e.g., Johnson and Miller, 2014; Kim et al., 2015; Fee et al., 2017b) or gas exit velocity (e.g., Woulff and McGetchin, 1976; Matoza et al., 2013; McKee et al., 2017). However, the potential significance of nonlinear effects at Sakurajima is evidenced by observations of supersonic wave propagation (Ishihara, 1985; Yokoo and Ishihara, 2007) asymmetric pressure waveforms (e.g., Matoza et al., 2014), and acoustically-based source parameters that underestimate (Johnson and Miller, 2014) or overestimate (Fee et al., 2017b) values obtained by other methods. We tentatively conclude that the indicator is strongly influenced by additional outdoor propagation effects such as

phase shifts on reflection from finite-impedance ground, and complex source dynamics including turbulent jet noise and fluid flow following an initial explosion. These source and propagation effects are not accounted for in the nonlinearity indicator analysis or in our numerical modeling approach, and they therefore complicate the ability to resolve nonlinear spectral energy transfer. Future investigations of nonlinear propagation effects may therefore be more conclusive in applications to data collected at close range to the vent (e.g., < 2 km) on volcanoes with low-relief topography, large source amplitudes, and simple source-time functions (e.g., gas-rich strombolian explosions).

2.7 Conclusion

We investigated the suitability of a quadspectral density-based nonlinearity indicator (ν_N) developed by Reichman et al. (2016a) for quantifying distortions to local volcano infrasound by spectral energy transfer during nonlinear acoustic propagation. We hypothesized that wave steepening during near-source nonlinear acoustic propagation causes significant energy transfer from the spectral peak of the source process to higher frequencies, and that wavefield interactions with topography and wind complicate the quantifiable signature of this process. Application of ν_N to 30 acoustic eruption signals in an 8-day dataset at Sakurajima Volcano, Japan, suggests cumulative nonlinear spectral distortions on the order of $<10^1$ dB re 20 μPa, but the nonlinear signature, if present, is modified by complications from source processes and outdoor propagation dynamics. To investigate the effects of topography and wind on ν_N we model nonlinear acoustic propagation over Sakurajima topography using a FDTD method (de Groot-Hedlin, 2017).

The results of acoustic propagation simulations indicate that ν_N is indeed capable of detecting cumulative nonlinear spectral energy transfer on the order of 2 dB below 1.7 Hz at Sakurajima station distances, and that wind and topography influence the indicator's behavior. However, neither wind nor topography are sufficient to explain the observed complexity in ν_N behavior for the Sakurajima signals; we suggest that fine-scale propagation effects (e.g.,

wave interaction with local winds and temperature gradients) and/or source dynamics (e.g., fluid flow and gas-particle interactions) distort the nonlinear signature. This approach to quantifying nonlinear spectral energy transfer may therefore be more conclusive for datasets collected with simpler volcano-acoustic source-receiver geometries. Accounting for the effect of spectral energy transfer may provide a second-order improvement in accuracy of source spectral estimates compared to the commonly-used geometrical spreading correction.

2.8 Acknowledgements

We thank Editor Dr. Martha Savage and two anonymous reviewers whose comments led to improvements in the manuscript. We thank Professor Tracianne Neilsen for helpful discussions about this project. The infrasound data from the 2013 Sakurajima deployment is publicly available through the IRIS DMC as described by Fee et al. (2014). The DEMs used in this study were provided by the Japanese Ministry of Land, Infrastructure, Transport and Tourism. This project was supported by NSF grants EAR-1620576 and EAR-1847736.

Chapter 3

Evaluating the applicability of a screen diffraction approximation to local volcano infrasound

This chapter appeared in this form in:

Maher, S.P., Matoza, R.S., de Groot-Hedlin, C., Kim, K., Gee, K.L., 2021. Evaluating the applicability of a screen diraction approximation to local volcano infrasound. Volcanica 4, 67–85. doi:10.30909/vol.04.01.6785.

3.1 Abstract

Atmospheric acoustic waves from volcanoes at infrasonic frequencies (∼0.01-20 Hz) can be used to estimate important source parameters for hazard modeling, but signals are often distorted by wavefield interactions with topography, even at local recording distances (<15 km). We present new developments toward a simple empirical approach to estimate attenuation by topographic diffraction at reduced computational cost. We investigate the applicability of a thin screen diffraction relationship developed by Maekawa (1968). We use a 2D axisymmet-

ric finite-difference method to show that this relationship accurately predicts power losses for infrasound diffraction over an idealized kilometer-scale screen; thus providing a validation for the scaling to infrasonic wavelengths. However, the Maekawa relationship overestimates attenuation for realistic volcano topography (using Sakurajima Volcano as an example). The attenuating effect of diffraction may be counteracted by constructive interference of multiple reflections along concave volcano slopes. We conclude that the Maekawa relationship is insufficient as formulated for volcano infrasound, and suggest future modifications that may improve the prediction capability.

3.2 Introduction

Erupting volcanoes produce atmospheric acoustic waves dominant in the infrasonic frequency range (∼0.01–20 Hz) that can be used to detect, locate, and characterize ongoing eruptions, and to estimate important eruption source parameters (e.g., Johnson and Ripepe, 2011; Fee and Matoza, 2013; Matoza et al., 2019a; De Angelis et al., 2019). However, outdoor propagation effects complicate direct interpretation of source processes. For example, recordings of volcano infrasound have been used to estimate volume flux (e.g., Kim et al., 2015; Johnson and Miller, 2014; Iezzi et al., 2019), vent radius (Muramatsu et al., 2018) and crater geometry (Johnson et al., 2018a,b), but wavefield interactions with topography lead to variable source estimates from signals recorded at different azimuths (e.g., Lacanna and Ripepe, 2013; Kim and Lees, 2014; McKee et al., 2014; Iezzi et al., 2019; Maher et al., 2020).

In particular, diffraction over the crater rim and other topographic barriers (e.g., Kim and Lees, 2011; Lacanna et al., 2014) distorts waveform character and reduces acoustic power compared to predictions based on spherical spreading over flat ground. The effect of diffraction over topography on acoustic power can be accounted for in full wavefield numerical simulations (Matoza et al., 2009b; Lacanna and Ripepe, 2013; Kim et al., 2015; Fee et al., 2017b; Iezzi et al., 2019), but a rapid analytical approach would be useful in some scenarios. For example, rapid correction of observed signals is desirable when time constraints prohibit the use of numerical

modeling, such as when planning station locations for the deployment of a temporary infrasound network during a rapid eruption response. It could also be advantageous when infrasound is generated by valley-confined surficial mass movements (e.g., Allstadt et al., 2018) or eruptions from a crater with rapidly evolving morphology (e.g., Ortiz et al., 2018).

The simplest expression for acoustic power loss to diffraction assumes a single point of diffraction over a thin screen, as proposed by Maekawa (1968). This relationship was empirically derived from experiments in which attenuation was estimated as the difference in sound pressure levels behind a rigid screen and the predicted values for free field propagation. Later studies incorporated the thin screen approximation into expressions for thick barriers (Fujiwara et al., 1977) and wedges (Maekawa and Osaki, 1985). These and various other numerical approaches (e.g., Pierce, 1974; Hadden and Pierce, 1981) deal exclusively with audible-frequencies (20 Hz–20 kHz) and require complicated calculations and knowledge of the barrier geometry relative to the source and receiver.

The thin screen approximation has been discussed in the context of volcano infrasound by Lacanna and Ripepe (2013) and Ishii et al. (2020), but the accuracy of predictions made according to the Maekawa (1968) relationship have not been evaluated. Lacanna and Ripepe (2013) used a 2D finite-difference simulation to show that synthetic amplitudes recorded on a topographically-obstructed side of the crater rim of Stromboli Volcano are attenuated by 8 dB compared to those recorded at the same distance on a less topographically-obstructed side of the crater. Ishii et al. (2020) computed theoretical pressure fields in the vicinity of thin screen approximations to topography at Sakurajima Volcano, where the 2D topography profiles are rotated to match the elevations of source and receiver, then replaced by flat ground with a thin screen at the height and distance of the tallest obstruction. Ishii et al. (2020) calculate idealized pressure fields as a sum of two contour integrals representing geometrical and diffraction aspects for monopole radiation in cylindrical polar coordinates (Macdonald, 1915; Li and Wong, 2005).

The results of Ishii et al. (2020) suggest that accounting for the attenuation by the thin screen provided a better prediction of the relative amplitudes at several stations than a $1/r$

spreading correction alone. However, Ishii et al. (2020) did not compare their attenuation results to the empirical relationship proposed by Maekawa (1968), which could provide simpler and more rapid estimates than their analytical approach. Furthermore, the results of Ishii et al. (2020) neglect full-wavefield effects associated with realistic topography (e.g., focusing of reflections down concave slopes) and may therefore overestimate the true losses.

We seek to directly evaluate the applicability of the empirical relationship for thin screen diffraction (Maekawa, 1968) to infrasonic wavelengths in general and to volcano acoustics in particular. We use numerical modeling to generate synthetic waveforms for full wavefield propagation over flat ground and multiple barrier types, including Sakurajima topography, to obtain attenuation estimates directly comparable to the Maekawa (1968) experiments. Our approach is conceptually similar to that of Le Pichon et al. (2012), who used large numerical simulations to derive a semi-empirical predictive relationship for infrasound attenuation due to the influence of stratospheric winds on the acoustic wavefield during propagation over a global scale. Analogously, we use numerical simulations to provide progress towards a semi-empirical relationship for infrasound attenuation due to the effect of topographic diffraction on wavefield propagation at a local scale. Our study differs from Le Pichon et al. (2012) in that we use synthetic results to investigate the applicability of an existing empirical relationship rather than to propose a new empirical relationship. These results represent a first step towards the development of an accurate predictive relationship and directions for future research are discussed in Section 3.10.4.

This manuscript is organized as follows. Section 3.3 describes the thin screen diffraction theory that is investigated here in the context of volcano infrasound. Section 3.4 describes Sakurajima Volcano and the observational dataset that is used in this study. Section 3.5 describes our primary methodology for numerically simulating infrasound propagation. Section 3.6 presents the main results of our simulations. Section 3.7 compares the results of our simulations to those from a different methodology that has been previously used with Sakurajima (Kim and Lees, 2014). Section 3.8 examines attenuation by diffraction in the frequency do-

main. Section 3.9 compares our synthetic results and thin screen predictions to observational data from Sakurajima. Section 3.10 discusses the implications of the study, limitations of our methodology, and directions for future work. Section 3.11 concludes the manuscript with the main findings and interpretations of the study.

3.3 Thin screen diffraction theory

To first order, a barrier to acoustic propagation can be approximated by a screen with height and length much greater than its thickness. The acoustic shielding effect of a thin screen was quantified in a seminal study by Maekawa (1968), who investigated the efficiency of a thin screen to reduce sound pressure for general noise reduction applications (e.g., road noise). Maekawa (1968) recorded sound pressure behind a 2 m tall screen during a controlled indoor experiment and used the results to calculate the sound reduction compared to free field propagation. The shielding effect of the screen causes acoustic power losses during diffraction which can be related to the Fresnel number (N; Pierce, 1981). The Fresnel number is the extra diffracted path length normalized by half a wavelength:

$$N = \frac{(R_\mathrm{t} - R_\mathrm{d})}{\lambda/2}, \tag{3.1}$$

where R_t is the length of the diffracted path, R_d is the length of the direct path to a receiver (line-of-sight slant distance) and λ is wavelength. The orange and green lines over the volcano topography profiles in Figure 3.1 show example line-of-sight and diffracted paths, respectively, where the diffracted path is computed as the shortest possible source-receiver path over obstructions.

Maekawa (1968) present an empirical chart of insertion loss as a function of Fresnel number which has become a standard reference for first-order noise reduction estimates in the field of audible acoustics (e.g., Hohenwarter, 1990; Ekici and Bougdah, 2003; Vu, 2007; Plotkin et al., 2009). Lacanna and Ripepe (2013) present a logarithmic fit to this chart which was originally

introduced by Tatge (1973) and is commonly used in engineering applications:

$$IL_{\mathrm{pT}} = 10\log(3 + 20N), \tag{3.2}$$

where IL_{pT} is the "predicted" insertion loss, in decibels, with subscript "T" indicating the study (i.e., Tatge, 1973). This expression carries the advantage of fitting the entire range of Fresnel numbers considered in the chart; however, the accuracy of the fit is reduced at $N < 1$, because the abscissa is adjusted to make the fit a straight line in the range -0.3< N < 1 (Maekawa, 1968). Note that negative Fresnel numbers indicate regions with direct line of sight to the source, but close enough to the shadow zone to feature influence of diffraction effects.

Since the source-receiver geometries at Sakurajima mainly feature $N < 1$, greater accuracy in this range is desirable. We therefore follow the approach of Yamamoto and Takagi (1992), who provide independent fits in the ranges $-0.3 < N < 1$ and $N \geq 1$, with a maximum deviation of 0.5 dB in the range $-0.3 < N < 1$:

$$IL_{\mathrm{pY}} = \begin{cases} 5 + 8|N|^{0.438} & \text{for } -0.3 < N < 1 \\ 10\log_{10}(N) + 13 & \text{for } N \geq 1 \end{cases} \tag{3.3}$$

It is important to note that while the Maekawa (1968) chart is commonly used as a first-order noise reduction estimate regardless of source-receiver geometry (e.g., Scholes et al., 1971; Ettouney and Fricke, 1973; Ekici and Bougdah, 2003; Vu, 2007; Plotkin et al., 2009; Young et al., 2015), Maekawa (1968) state that it is intended for cases where the source and receivers are in the air. This condition allows direct comparison between diffracted measurements and free-field estimates since the influence of ground reflection can be avoided. However, in volcano infrasound studies, the sources and receivers are commonly on the ground. A chart relating N to attenuation for the case when sources and receivers are on the ground is provided by Fehr (1951) and can be fit by the equation:

$$IL_{\mathrm{pF}} = 10 + 10\log_{10}(N). \tag{3.4}$$

We find that Equation 3.4 generally predicts the attenuation for our synthetic volcano infrasound results better than Equations 3.2 and 3.3; however, the original paper by Fehr (1951) unfortunately does not provide explanation or justification for the relation. The chart is nonetheless reproduced in Figure 3 of Maekawa (1968) and was commonly cited before Maekawa's empirical relation became popular (e.g., Purcell, 1957; Scholes et al., 1971; Jonasson, 1972; Ettouney and Fricke, 1973).

The predicted insertion loss given by Equations 3.2, 3.3 and 3.4 can be tested against experimental results described by modeled insertion loss (IL_{m}) (Lacanna and Ripepe, 2013):

$$IL_{\mathrm{m}} = -20 \log \left(\frac{p_{\mathrm{s}}}{p_{\mathrm{r}}} \right), \tag{3.5}$$

where p_{s} is peak pressure behind an obstacle and p_{r} is peak pressure at the same distance without the obstacle. Here, p_{s} is peak pressure of the first wave cycle of a synthetic signal recorded behind a rigid obstacle using a finite-difference time-domain (FDTD) method for linear infrasound propagation (Section 3.5; de Groot-Hedlin, 2017). The synthetic peak pressure p_{r} is recorded at the same receiver location but with a flat lower boundary. We mainly use peak waveform pressures instead of Fourier amplitudes at a specific frequency because signal frequency content may vary inconsistently with different source processes such that a single frequency component may not be dominant in every event. However, in Section 3.9 we compare Fourier amplitudes at 0.5 Hz between observations, predictions, and synthetics to allow direct comparison to results from (Ishii et al., 2020).

We hereafter refer to Equations 3.2, 3.3 and 3.4 as "predicted" insertion loss and to Equation 3.5 as "modeled" insertion loss in order to express the difference between predictions and our results from numerical modeling. We hypothesize that modeled insertion loss will be well approximated by predicted insertion loss if the attenuating effect of the barrier in question (e.g., wedge, Sakurajima topography) is similar to that of a thin screen.

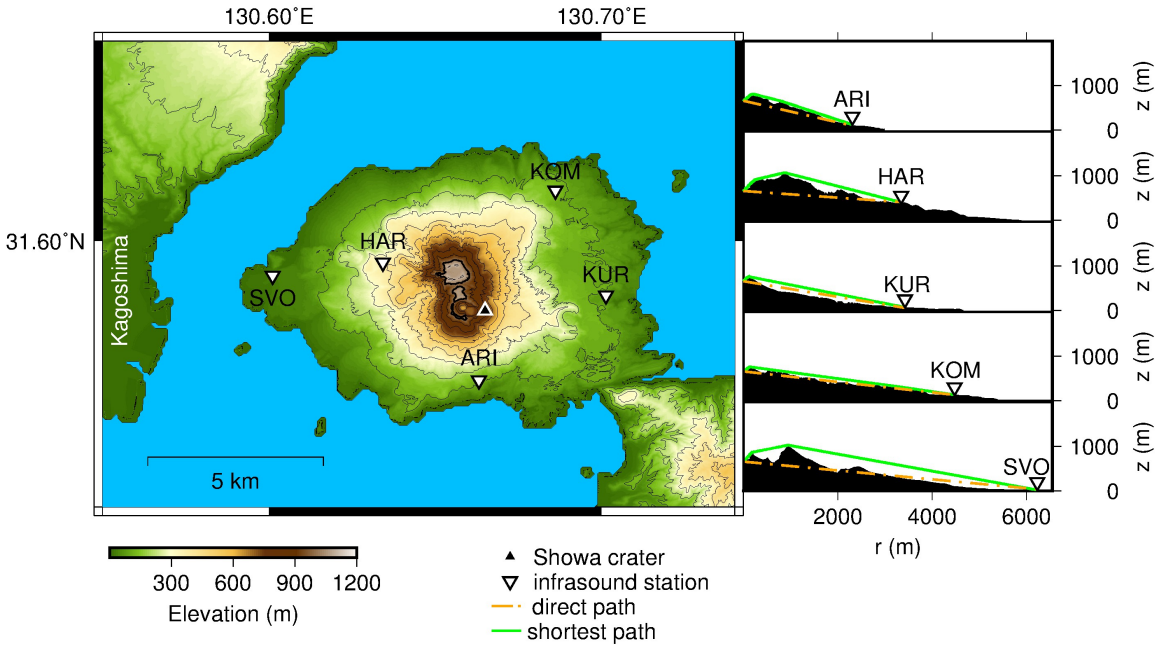

Figure 3.1: Map of Sakurajima Volcano in southern Japan with 1 m resolution around the crater and 10 m resolution around the perimeter (interpolated to 1 m resolution). Contours are marked at 200 meters and the 1000 meter contour is marked in bold. The active vent is in Showa crater (upward triangle). Downward triangles represent infrasound sensors deployed for eight days in 2013 (Fee et al., 2014). Profiles at right show topography between the vent and each sensor. Dash-dotted and solid lines show the direct and shortest diffracted raypaths, respectively, with lengths corresponding to R_{d} and R_{t} in Equation 3.1, respectively.

3.4 Sakurajima Volcano

Sakurajima is a highly active andesite-dacite stratovolcano in southern Kyushu, Japan, near the southern rim of the Aira Caldera (Figure 3.1). The 20 km^3 edifice consists of lava flows and pumice fall deposits from at least 12 Plinian eruptions (Aramaki, 1984). From 1955 to present the eruptive activity is characterized by ash-rich Vulcanian explosions (Ishihara, 1985). During the periods 1955–2006 and 2017–present, eruptions occurred from the summit vent of Minamidake, whereas from 2006 to 2017 eruptions occurred from a vent in Showa Crater on the southeast flank of Minamidake (Iguchi et al., 2013).

Due to the volcano's frequent activity (∼1000 events per year since 2009) and proximity to the city of Kagoshima, Sakurajima is one of the world's best-instrumented volcanoes (e.g.,

Iguchi et al., 2013) and a common target for infrasound studies. Acoustic waves generated by the explosive Vulcanian eruptions feature large amplitudes (449 Pa at 2.3 km; Fee et al., 2014; Matoza et al., 2014) and are sometimes visually observed as shock-like changes in luminance (Ishihara, 1985; Yokoo and Ishihara, 2007). These studies and others (e.g., Kawakatsu et al., 1992; Uhira and Takeo, 1994; Garcés et al., 1999; Tameguri et al., 2002; Morrissey et al., 2008; Maryanto et al., 2008; Yokoo et al., 2009; Iguchi et al., 2013; Miwa and Toramaru, 2013; Aizawa et al., 2016; Cimarelli et al., 2016; Smith et al., 2018) illustrate the value of Sakurajima as an archetypal research target.

3.5 Finite-difference modeling

Our primary methodology involves numerical simulations of linear infrasound propagation with the FDTD code developed by de Groot-Hedlin (2017). The model features a 2D cylindrical coordinate system in a source-receiver plane that is axisymmetric about the left boundary. This quasi-2D geometry models amplitude decreases with range identically to spherical spreading from a point source in 3D Cartesian space ($1/r$ decay without topography). In a 2D Cartesian model, the amplitude decrease with range would instead reflect a line source ($1/\sqrt{r}$ decay). References in this manuscript to "2D" modeling refer to the axisymmetric method of de Groot-Hedlin (2017) rather than a 2D Cartesian model. The simulations are advanced in time with finite differences over two time-steps using the modified midpoint method of Press et al. (1996), yielding second order accuracy in time of the solution. The program uses a staggered grid in which pressure is updated in cell centers while particle velocities are updated at cell boundaries. This staggered grid approach provides second order accuracy in the spatial derivates of the finite differences (Ostashev et al., 2005). The lower boundary features rigid stair-step topography while the top and right boundaries feature absorbing perfectly matched layers (Berenger, 1994) layers.

The main results described in Section 3.6 are obtained from simulations performed in a 12 km by 12 km model space with a constant sound speed of 340 m/s and an ambient density

of 1.229 kg/m^3. We require a minimum of 20 grid cells per wavelength at 5 Hz, yielding grid spacings of 3.4 m, time steps of 2.4 ms. The accuracy of synthetic frequency components is generally considered acceptable for discretization up to 10 grid nodes per wavelength (Taflove and Hagness, 2005). In these simulations the discretization criterion of 10 nodes per wavelength is met up to a frequency of 10 Hz, so synthetic results can be considered accurate up to 10 Hz. However, we chose to only interpret frequencies up to 5 Hz to maintain confidence in the numerical accuracy of the results. Note that in Section 3.7 we present simulations with a maximum source frequency of 1 Hz and a constant sound speed of 349 m/s to facilitate direct comparison to 3D modeling by Kim and Lees (2014).

We run simulations with a variety of lower boundary conditions including flat ground, an idealized thin screen 800 m in height, (Figure 3.2, third row), a 1 km wide by 800 m tall wedge (Figure 3.2, fourth row), and 1 km by 800 m square barrier (Figure 3.2, fifth row). The height and distance of the thin screen is designed to scale the Maekawa (1968) experiment to infrasonic wavelengths and to create overlap in Fresnel numbers with the Sakurajima topography profiles. The geometries of the wedge and wide barrier are designed to create overlap in Fresnel numbers, facilitating direct comparison of the resulting attenuation to that of the screen and Sakurajima. We calculate Fresnel numbers for the synthetic stations assuming a wavelength of 340 m, corresponding to $\sim$1 Hz peak frequency in the synthetic signals, and the homogeneous sound speed of 340 m/s.

For volcano topography we use Sakurajima Volcano as a case study because it is a common target for volcano infrasound research (see Section 3.4) and features rugged topography that complicates the acoustic wavefield (Kim and Lees, 2014; McKee et al., 2014; Johnson and Miller, 2014; Lacanna et al., 2014). We use 2D topography profiles for each of five infrasound sensors deployed at Sakurajima, Japan in July 2013 (Fee et al., 2014) (Figure 3.1). We place the acoustic source inside Showa crater at the left boundary and propagate the wavefield over topographic profiles corresponding to the azimuths to the sensors in the 2013 deployment. For the lower boundary we use Sakurajima topography profiles from a 10-m resolution digital elevation model

(DEM) covering a broad area over Kagoshima Bay and a smaller 1-m resolution DEM covering the summit region and Showa crater. We fuse the two DEMS together after interpolating the 10-m resolution DEM to 1-m resolution over a rectangular mesh using a bivariate spline approximation. While our approach may be generalized to any topographic profile, the results presented here follow from previous work on the 2013 dataset (Fee et al., 2014; Johnson and Miller, 2014; McKee et al., 2014; Yokoo et al., 2014) and may inform future studies that use the same data.

Synthetic peak pressures are recorded at 100 m spacing behind each obstruction (Figure 3.2) and compared to those recorded over flat ground to estimate IL_{m} (Eqn. 3.5). We use peak pressure to calculate IL_{m} such that the direct wavefront is measured rather than later-arriving reflections. Our approach allows us to thoroughly compare modeled insertion loss to predicted insertion loss by providing synthetic pressures at low computational cost for numerous source-receiver geometries representing a range of Fresnel numbers.

3.6 Results

The primary results of our study are the comparisons between predicted insertion loss from Maekawa's empirical relationship (Equation 3.3) and modeled insertion loss (Equation 3.5) based on the peak pressures of synthetics from 2D axisymmetric FDTD simulations. Figure 3.2 shows wavefield snapshots for five simulations. The compressional source is centered at an altitude of 660 m, the height of Showa crater. In the flat ground case, most acoustic energy is concentrated at the wavefront and the singular ground reflection behind it. In the Sakurajima KUR case, multiple reflections down the concave slope (see also Figure 3.1) lead to wavefield complexity and focusing, as also noted previously by Lacanna et al. (2014). In the cases of the thin screen, wedge, and square barrier, diffraction reduces amplitudes behind the obstruction compared to the portions of the wavefield propagating higher than the obstruction. Reflections from the mirrored obstruction across the axisymmetric left boundary appear in the last one or two snapshots, but these phases do not influence the peak pressure insertion loss results because

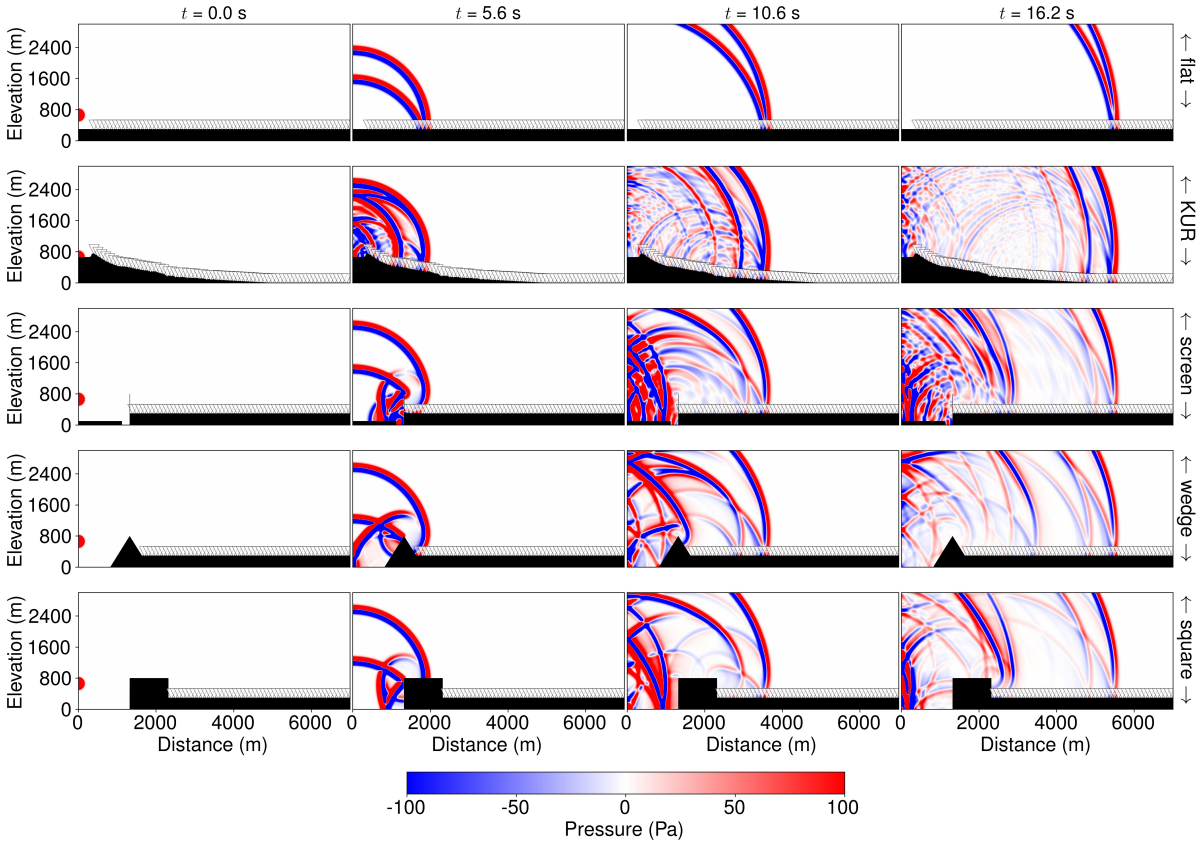

Figure 3.2: Wavefield snapshots for infrasound propagation simulations over five lower boundary types. Each row represents a time sequence from left to right for one lower boundary. From top to bottom these lower boundaries are flat ground, Sakurajima topography (KUR profile), thin screen, wedge, and wide barrier, respectively. Downward triangles represent synthetic receivers. The full model space dimensions are 12 km by 12 km and simulation run times are 34 seconds.

only the first arriving wave cycles are used in the analysis.

Figure 3.3a shows IL_{m} results all synthetic receivers over each lower boundary type. For $1 < N < 6$ the thin screen results (red circles) show good agreement (<1 dB difference) with Equation 3.3 (black line). For the square barrier (cyan squares) and wedge (yellow triangles), the attenuation is underpredicted and overpredicted, respectively, by Maekawa's empirical relationship by a few dB, as expected from previous studies (e.g., Fujiwara et al., 1977; Maekawa and Osaki, 1985; Pierce, 1974). Attenuation at synthetic Sakurajima receivers (diamonds in Figure 3.3a) is significantly overpredicted by Eqnuation 3.3 and even negative at low Fresnel numbers ($N < 0.1$), indicating gains in power relative to the flat ground case, rather than losses,

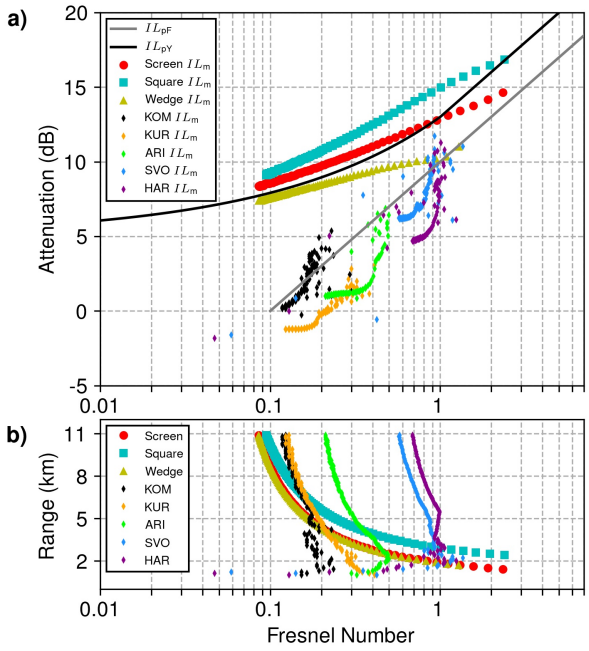

Figure 3.3: **a)** Attenuation as a function of Fresnel number for synthetic peak pressures from 2D cylindrical simulations with multiple lower boundary types (screen, wedge, square, and five azimuths at Sakurajima Volcano) compared to flat ground. The black line shows predicted insertion loss from the Yamamoto and Takagi (1992) fit to the Maekawa (1968) empirical chart (Equation 3.3) while markers show modeled insertion loss (IL_{m}; Equation 3.5) from numerical simulations with receivers spaced at 100 m intervals. The grey line shows the predicted insertion loss according to Fehr (1951) (Equation 3.4). **b)** Variation in Fresnel number with range for each lower boundary type. Colors and markers are the same as in Figure 3.3a.

due to topographic focusing effects. The volcano results are better predicted by Equation 3.4 (grey line), which is formulated for sources and receivers on the ground, but which only covers $N > 0.1$.

As a guide, Figure 3.3b shows how the Fresnel number of each receiver varies with range (distance from the left boundary). Fresnel numbers generally decrease with distance as the difference between R_{t} and R_{d} decreases; however, at close ranges over the Sakurajima profiles, Fresnel numbers can increase with range as the propagation path becomes more obstructed by the crater rim.

3.7 Comparison of 2D cylindrical to 3D Cartesian modeling

To corroborate the results of our 2D numerical modeling in an axisymmetric geometry, we run additional simulations for direct comparison to previous 3D Cartesian finite-difference modeling with Sakurajima topography (Kim and Lees, 2014). As in the simulations presented by Kim and Lees (2014), we implement a homogeneous atmosphere with 349 m/s sound speed, a maximum source frequency of 1 Hz with a discretization of 30 nodes per wavelength. Synthetics are recorded at the five stations of the July 2013 deployment with topography profiles as shown in Figure 3.1. We additionally run new 2D cylindrical and 3D Cartesian simulations that approximate flat-ground propagation for the same source-receiver distances so that attenuation by topography may be estimated using Equation 3.5. In the 2D cylindrical case, the flat ground simulation features a flat surface at sea level, with the source on the ground at the left boundary. Receivers are placed on the ground at distances corresponding to the slant distances (R_d) of the Sakurajima stations, measured from the edge of the source radius. We calculate Fresnel numbers for the synthetic stations assuming a wavelength of 873 m, corresponding to ∼0.4 Hz peak frequency in the synthetic signals, and the sound speed 349 m/s. We approximate the source function of this simulation by placing a receiver 10 m outside the source radius. The source radius is 1386 m and the model dimensions are 12 km by 12 km.

Both methods use a staggered grid scheme (Ostashev et al., 2005) such that synthetic pressures are recorded at grid cell centers. This means that receivers cannot be placed directly on the ground and are instead located 5 meters above the surface in these simulations. When the height of a receiver is large compared to its range and the acoustic wavelength this may introduce undesired interference between the direct and ground-reflected waves which would be in-phase on the surface. This effect is largely insignificant for the wavelengths considered here and at receivers more than a few hundred meters from the source. However, in the 3D Cartesian case, the source function receiver is placed 10 meters from the point source and thus is subject to phase-shifting in the ground-reflected wave. For this reason we approximate flat ground propagation in the 3D Cartesian case by recording pressure in the free field and multiplying

the amplitudes by two. This approach accurately models the constructive interference of the in-phase direct and ground-reflected waves in the flat ground case by accounting for the image sources inherent to flat ground propagation (Morse and Ingard, 1986; Kim et al., 2012). For the 2D cylindrical case, the source function receiver is placed at a significant distance from the center of the source (1386 meters) compared to the 5.5 m distance between the ground and the receiver, making negligible the interference of ground-reflected waves.

Figure 3.4 compares waveforms and power spectral density (PSD) estimates for the 2D cylindrical and 3D Cartesian simulations described above. In the 2D cylindrical cases the waveforms exhibit bipolar main pulses with relatively symmetrical compression and rarefaction phases (Figure 3.4a), while the PSDs feature broad peaks around 0.4 Hz (Figures 3.4c, 3.4d). Waveforms from 2D cylindrical simulations with topography are generally time-delayed and reduced in amplitude compared to the simulations with flat ground (Figure 3.4a). In contrast, the 3D Cartesian simulations feature strongly asymmetrical waveforms with single main compression phases (Figure 3.4b) and nearly white power spectra (Figures 3.4e, 3.4f). The differences in waveform shape can be largely attributed to the different source functions. The 2D axisymmetric models uses a spatially-distributed Gaussian pulse at time zero, while the 3D model uses a time-varying function (Blackman-Harris window) at a point-source.

Figure 3.5 compares the distribution of peak amplitudes and modeled attenuation (IL_{m}; Equation 3.5) for the 2D cylindrical and 3D Cartesian synthetic cases described above. In both the 2D and 3D cases, peak amplitudes for the flat-ground approximations decay linearly with distance from the source function receiver, as expected for spherical spreading (Figures 3.5a and 3.5b, respectively). When topography is included, the amplitudes are reduced at each station in the 2D case (Figure 3.5a), whereas in the 3D case, the amplitudes are increased at ARI, KOM and KUR (Figure 3.5b). These differences are reflected in the IL_{m} results (Figure 3.5c), which feature positive attenuation at every station in the 2D cases but only at HAR and SVO in the 3D cases. However, both modeling approaches produce the same relative amplitude and distribution across the network (e.g., ARI is always more attenuated than KUR and less

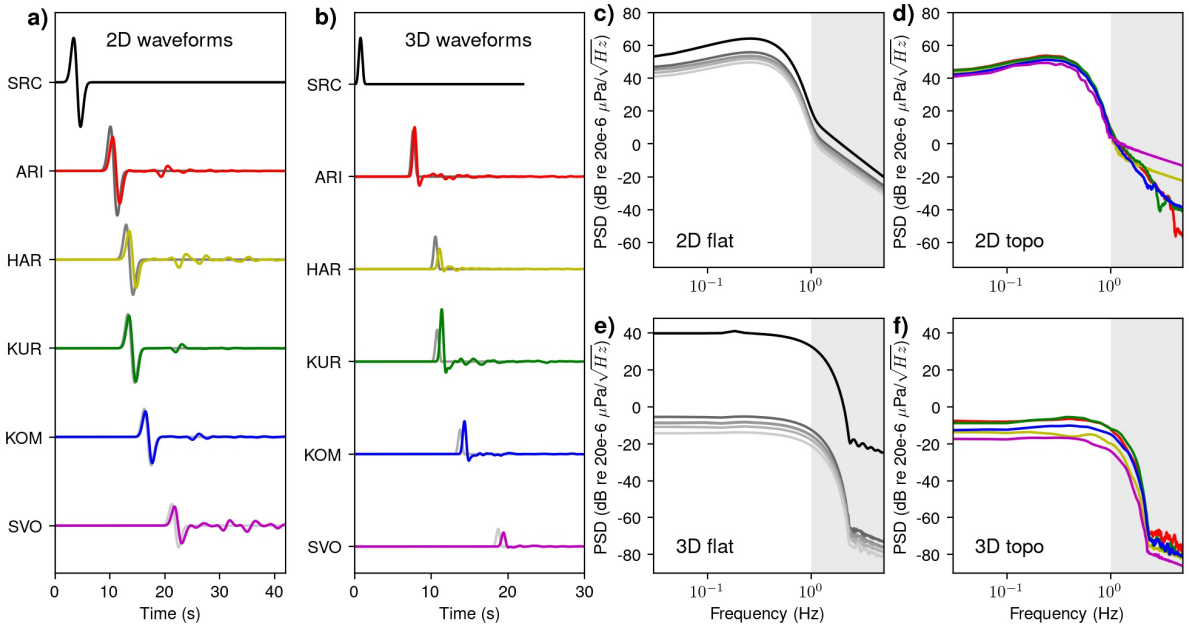

Figure 3.4: Synthetic waveforms and spectra for comparable 2D cylindrical and 3D Cartesian modeling methods. **a)** Synthetic waveforms from 2D modeling with topography (color) and flat ground (grey scale). Amplitudes are normalized for ease of visualization; the source function (SRC) is normalized by the maximum at SRC while all other waveforms are normalized by the maximum at ARI with flat ground. **b)** Synthetic waveforms from 3D modeling with topography (color; Kim and Lees, 2014) and with a free field (grey scale). Free field values are multiplied by two to approximate flat ground. Amplitudes are normalized in the same manner as Figure 3.4a. Multitaper PSD estimates are shown for synthetic wavefroms from **c)** 2D flat ground simulations; **d)** 2D topography simulations; **e)** 3D free field simulations; **f)** 3D topography simulations. Grey shaded regions indicate frequencies above 1 Hz (maximum source frequency) for which results may be inaccurate.

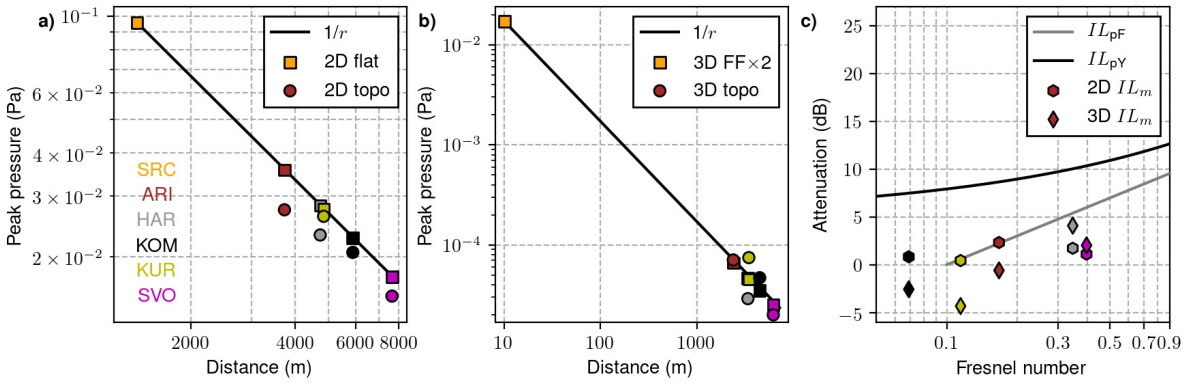

Figure 3.5: **a)** Peak pressure of 2D synthetic waveforms at Sakurajima station distances for lower boundaries with topography (circles) and flat ground (squares). The orange square represents the approximate source pressure as recorded 10 m outside the boundary of the source region. **b)** Peak pressure of 3D synthetic waveforms over Sakurajima topography (circles) (Kim and Lees, 2014) and through the free field (FF, squares). Free field values are multiplied by two to approximate flat ground propagation (constructive interference of the direct and ground reflected waves). **c)** Modeled insertion loss (IL_m, Equation 3.5) compared to predicted insertion loss according to Yamamoto and Takagi (1992) (IL_{pY}, Equation 3.3) and Fehr (1951) (IL_{pF}, Equation 3.4) for the 2D peak pressures (hexagons) and 3D peak pressures (diamonds) shown in Figure 3.5a and Figure 3.5b, respectively.

attenuated than HAR). The attenuation predicted by IL_{pY} is clearly greater than the IL_{m} results from both 2D and 3D modeling.

While both the 2D cylindrical and 3D Cartesian models present validated solutions to the wave equation (Kim and Lees, 2014; Kim et al., 2015; de Groot-Hedlin, 2017; Fee et al., 2017b; Iezzi et al., 2019; Maher et al., 2020), several differences between the methods may account for the larger amplitude reductions in the 2D topography simulations compared to the 3D simulations. In the 2D model the source function is a spatially-distributed Gaussian pulse, whereas in the 3D case the source is a time-varying Blackman-harris window at a single grid node. These different source clearly produce wavefields with different frequency content as exemplified by the 0.4 Hz peak in the 2D flat synthetics (Figure 3.4c) in comparison to the white spectrum in the 3D free field synthetics (Figure 3.4e). Since attenuation increases with frequency (see Section 3.8), we speculate that the less attenuated low-frequency components (¡0.5 Hz) in the 3D model may contribute to the heightened amplitudes when compared to the 2D model. Our comparison between 2D and 3D simulations is inherently limited by these different source func-

tions; however, adapting the methods to achieve equivalent source implementations is outside the scope of this study.

Additionally, the 2D model operates in an axisymmetric geometry, assuming azimuthal symmetry in topography around the source-receiver plane, whereas the 3D model uses a Cartesian geometry that allows for more realistic topography. Wavefield interactions with topography outside the 2D azimuthal plane may account for some discrepancies between the methods. For example, the line-of-sight propagation path for KUR follows a drainage channel (Figure 3.1) that may allow for constructive interference of reflections from the valley walls. This presumably increases recorded amplitudes at KUR compared to both spherical spreading over flat ground and to the 2D model, which does not account for the channel. Ray tracing (e.g., Blom and Waxler, 2012; Green et al., 2012; Fee et al., 2013a; Blom, 2020) could potentially be used to investigate the influence of off-path reflections on the waveform; however, this is outside the scope of this study. Regardless, the preliminary comparison presented here corroborates the main finding of our 2D simulations, which is that attenuation of infrasound at Sakurajima is overpredicted by screen diffraction theory.

3.8 Frequency Dependence of Attenuation

While Equations 3.2 and 3.5 estimate attenuation for time domain amplitudes at fixed wavelengths (e.g., 340 m in Section 3.6 and 349 m in Section 3.7) the thin screen approximation also enables analysis of the frequency-dependence of attenuation. We hypothesize that, if the thin screen approximation holds true for volcano infrasound, attenuation of 2D and 3D synthetics for Sakurajima topography will consistently increase with frequency to match the logarithmic relationship proposed by Maekawa (1968). We investigate this aspect by first defining a new frequency-dependent variable for the Fresnel number $\left(\hat{N}\right)$, where the wavelength in Equation 3.1 is written as a function of ambient sound speed (c_0) and a frequency vector (f):

$$\hat{N} = \frac{2(R_\mathrm{t} - R_\mathrm{d})}{c_0/f}. \tag{3.6}$$

This reformulated Fresnel number can be substitued into Equation 3.3 to express the empirical relation of Maekawa (1968) in the frequency domain $\left(\widehat{IL}_p\right)$:

$$\widehat{IL}_{\mathrm{pY}} = \begin{cases} 5 + 8|\hat{N}|^{0.438} & \text{for } -0.3 < \hat{N} < 1 \\ 10\log_{10}\left(\hat{N}\right) + 13 & \text{for } \hat{N} \geq 1 \end{cases} \tag{3.7}$$

Finally, the predictions can be compared to estimates from numerical modeling $\left(\widehat{IL}_m\right)$ by substituting the waveform amplitudes in Equation 3.5 for power spectra:

$$\widehat{IL}_m = -10\log\left(\frac{\hat{p}_s}{\hat{p}_r}\right), \tag{3.8}$$

where $\hat{p}_s$ is a PSD estimate (unit $\mathrm{Pa}^2/\mathrm{Hz}$) for a synthetic waveform from a simulation with topography at the lower boundary, and $\hat{p}_r$ is PSD for a synthetic waveform from a simulation with a flat lower boundary.

We examine the frequency dependence of predicted attenuation for five Sakurajima stations and modeled attenuation for the 2D and 3D simulations with Sakurajima topography described in Section 3.7. Figure 3.6 shows results for each station. As expected, $\widehat{IL}_p$ increases as a logarithmic function of frequency, with y-intercepts controlled by $\hat{N}$. Predicted attenuation increases by approximately 5 dB from 0.1 to 1 Hz, about half an order of magnitude in units of $\mathrm{Pa}^2/\mathrm{Hz}$. Similarly, $\widehat{IL}_m$ for the 2D simulations generally increases with frequency; however, the values are lower than predicted by $\widehat{IL}_p$, and the increases are smaller (e.g., 2 dB increase from 0.1 to 1 Hz at SVO). Values of $\widehat{IL}_m$ for 3D simulations are also lower than $\widehat{IL}_p$; however, different patterns are observed for stations with relatively low $\hat{N}$ (ARI, KUR and KOM) than for stations with higher $\hat{N}$ (HAR and SVO). For example, at KUR, 3D $\widehat{IL}_m$ decreases with frequency and becomes negative above 0.1 Hz (Figure 3.6c), whereas at SVO the 3D $\widehat{IL}_m$ is relatively constant at approximately 3 dB below 1 Hz (Figure 3.6e). Artificial increases of high-frequency energy in finite-difference models may be produced by spurious reflections from corners in from stair-step topography (e.g., de Groot-Hedlin, 2004); however, this effect may be

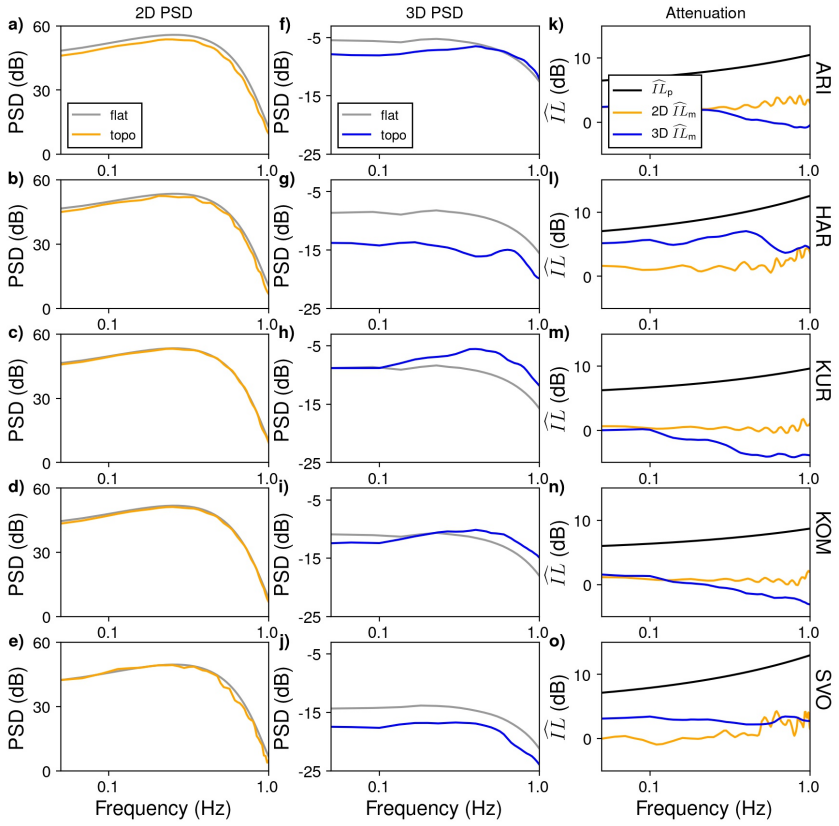

Figure 3.6: **a-e)** PSD curves for synthetics from 2D simulations with flat ground (grey) and Sakurajima topography (orange) at the lower boundaries. Each row represents a Sakurajima station as indicated by text at far right (from top to bottom, these are ARI, HAR, KUR, KOM and SVO). **f-j)** PSD curves for synthetics from 3D simulations representing flat ground (grey lines) and Sakurajima topography (blue lines) at the lower boundaries. In this case the flat ground is approximated by doubling the pressure amplitudes from a free-field simulation. **k-o)** Frequency dependence of attenuation for Sakurajima stations according to predictions from thin screen theory (Equation 3.7; black lines), 2D numerical modeling (Equation 3.8; orange lines) and 3D numerical modeling (Equation 3.8; blue lines).

considered negligible at frequencies for which topography is finely discretized. We ran additional 2D and 3D simulations with finer discretization (5 m grid spacing) and observed no changes in the frequency range of interest (∼0.1–1 Hz). We therefore interpret the decreased attenuation with frequency in the 3D model as a result of wavefield interactions with topography outside the source-receiver plane, such that they are not captured in the 2D model. This finding provides further evidence for the influence of full wavefield effects in counterbalancing power losses by diffraction.

The results of this frequency-dependent analysis provide further evidence to suggest that the thin screen approximation overestimates the diffraction losses for volcano infrasound. However, several limitations are inherent to this approach. The synthetic spectra are highly dependent on the source function, which differs significantly between the 2D and 3D methods (see Figures 3.4a, 3.4b, 3.4c and 3.4e), and may be changed to model different source types (e.g., Kim et al., 2012; Iezzi et al., 2019). Furthermore, the approach cannot distinguish between the effect of diffraction and other wavefield-topography interactions such as reflections and scattering, which may also vary with frequency (e.g., Pierce, 1981; Embleton, 1996) and with topography outside the 2D azimuthal plane. Numerical artifacts may also influence the spectra. For example, spurious reflections may occur from stair-step boundaries in the discretized topography (e.g., de Groot-Hedlin, 2004). However, we consider this effect negligible in our case since we use a relatively fine grid spacing of 30 nodes per wavelength at 1 Hz, in comparison to the minimum of 10 nodes per wavelength (Taflove and Hagness, 2005). Further work to investigate these numerical limitations is outside the scope of this study; however, our results for the cases and frequencies considered suggest that attenuation by topography is less than predicted by Maekawa's empirical relationship.

3.9 Comparison of Synthetic Results to Observed Data

In this study we primarily investigate numerical simulations because they allow direct estimation of wavefield changes for different lower boundary conditions; however, the ultimate goal of evaluating the thin screen approximation is to rapidly estimate attenuation in observed signals. Here we assess the applicability of our results to 30 eruption events recorded by five stations at Sakurajima during 18-26 July, 2013 (Fee et al., 2014). These events represent a subset of 74 STA/LTA detections made by Matoza et al. (2014). Events in this subset feature high signal-to-noise ratios (SNR) as evidenced by three or more stations with power spectra above the median of network-averaged noise spectra in the 0.1- to 10-Hz frequency band (e.g., Figure 3.7b; details in Maher et al., 2020). The signals vary in waveform character from sustained

low-amplitude jet noise to high-amplitude explosions (up to 449 Pa at 2.4 km) with asymmetrical shock-like waveforms (Fee et al., 2014; Matoza et al., 2014). To accurately reproduce the variety of observed signal types would require multiple modifications to the synthetic source functions, which is outside the scope of this study; however we observe a general agreement between synthetic and observed data as described here.

Figure 3.7 shows an example of one event out of 30 and features an explosion followed by lower amplitude oscillations for tens of seconds. The waveform shapes lie in between the symmetry of the 2D synthetics (Figure 3.4a) and the strong asymmetry of the 3D synthetics (Figure 3.4b). The shape of the power spectra agree with synthetics in that a broad peak is present below 1 Hz (Figure 3.7b). The observed peak pressures (squares) are overpredicted by $1/r$ relationship at each station, reflecting anomalously high amplitude at KUR. The amplitude decay for this event is also compared to the 2D and 3D simulation results, where the synthetics are scaled up to match the observation at KUR (circles and diamonds in Figure 3.7c). The 2D synthetic peak pressures follow $1/r$ at KOM and SVO while the 3D synthetics are reduced, more closely matching the observations.

While Figure 3.7 exemplifies one event in the dataset, the amplitudes of all the events are summarized in Figure 3.8a. The boxplots show the distribution of observed peak amplitudes normalized to the amplitudes at KUR (p_{KUR}), while markers show the corresponding values for 2D synthetics (blue circles), 3D synthetics (green diamonds), thin screen predictions (red squares) and spherical spreading predictions (black line). The broad ranges in observed amplitudes reflect variability in source and propagation conditions across the 30 events recorded over an eight day period. These process potentially include variable source directionality (e.g., Matoza et al., 2013; Jolly et al., 2017; Iezzi et al., 2019), eruption style (e.g., Fee et al., 2014; Matoza et al., 2014), winds (e.g., Lacanna et al., 2014; Sabatini et al., 2016b; de Groot-Hedlin, 2017; Kim et al., 2018), temperature inversions (e.g., Fee and Garces, 2007) and changes in vent/crater geometry (e.g., Fee et al., 2017a; Ortiz et al., 2018). Our synthetics and predictions therefore do not provide a direct representation of each individual event; however, the

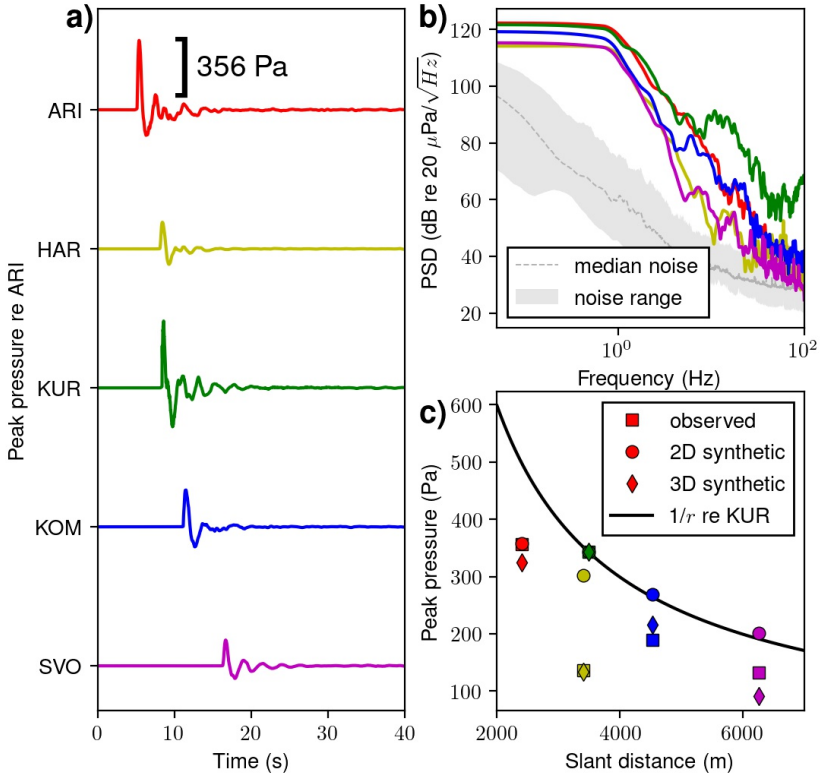

Figure 3.7: **a)** Example of observed waveforms for one event at Sakurajima at 23:06:56.960 on 07/20/2013 (UTC). Amplitudes are normalized by the maximum at ARI (356 Pa) for ease of plotting. **b)** Multitaper PSD estimates for the waveforms in Figure 3.7a (original waveform amplitudes). The grey shaded region indicates the noise range across the network as defined by the 5^{th} and 95^{th} percentiles of network-averaged PSD curves for 50% overlapping hourly time-windows during the deployment (Maher et al., 2020). The dashed grey line is the median noise condition (50^{th} percentile). **c)** Peak pressure vs distance for the waveforms in Figure 3.7a (squares). The peak pressures for 2D simulations with topography (circles), 3D simulations with topography (diamonds). The synthetic and predicted amplitudes are scaled to match the observed KUR amplitude. Black line represents expected amplitude decay from spherical spreading based on KUR amplitude. This example is one out of 30 events used to construct the boxplots in Figure 3.8.

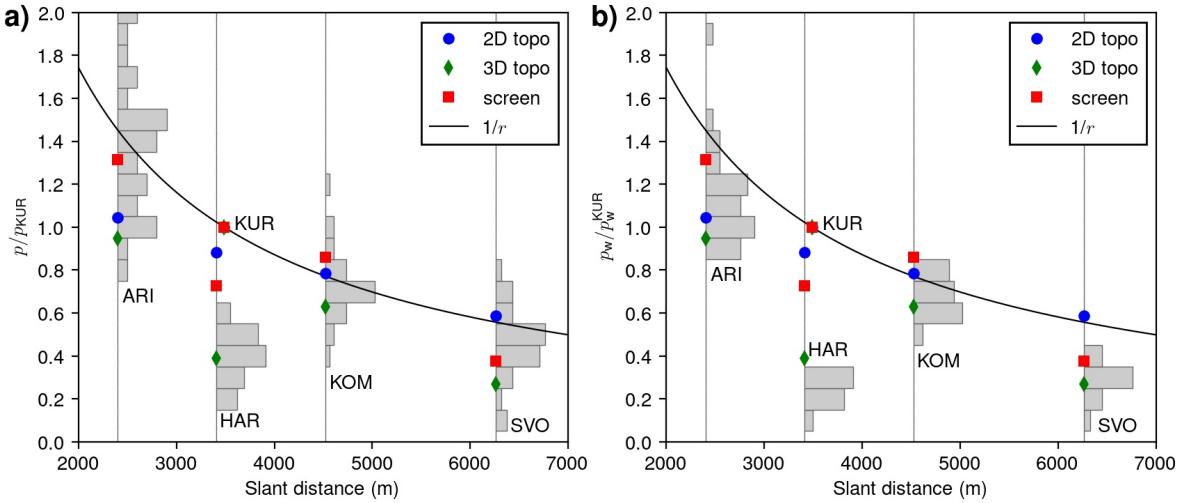

Figure 3.8: **a)** Comparison of relative peak pressure values between observations and results from all methods (2D modeling, 3D modeling, screen predictions, and spherical spreading). Values are normalized by peak pressure at KUR to show relative amplitude distributions across the network. Histograms show the distribution of observed values at each station in bins of 0.1 p/p_{KUR}. **b)** As for Figure 3.8a but using the Fourier amplitude at 0.5 Hz (p_{w}) instead of peak pressure. Note that vertical gray lines indicate zero counts in the histogram bins.

general agreement in relative amplitude distribution validates our methodologies against the observations.

Figure 3.8b shows the distributions considering the Fourier amplitude at 0.5 Hz (p_{w}) rather than peak pressure. Figure 3.8b may be compared to Figure 3c of Ishii et al. (2020), although the events considered are different, and screen predictions are based on Equations 3.2 and 3.5 rather than pressure field calculations. Use of the Fourier amplitude decreases the spread of observed values at each station and more clearly shows the overestimation of ARI, HAR, SVO values by the $1/r$ prediction.

The values from 3D synthetics fall within the peak pressure range of observations at all stations, while the values from other methods fall within the observation ranges at ARI, KOM, and SVO, but are overpredicted at HAR (largest N). The predicted values according to the screen theory generally agree with the values obtained by Ishii et al. (2020), although the value at KOM is slightly larger than the $1/r$ value. This finding shows that our method based on the empirical relationship of Maekawa (1968) gives similar relative amplitudes arrived at

by Ishii et al. (2020); however, we argue that it is misleading to normalize the amplitudes by KUR in this way. By making the values relative to KUR rather than to the source, the normalization obscures the overestimation of attenuation by the screen theory in the case of volcano topography (Figure 3.3a). Furthermore, the values obtained according to the screen theory do not appear to provide an appreciable improvement in matching the observations when compared to $1/r$ or results from numerical modeling (Figure 3.8).

3.10 Discussion

We aim to develop a correction scheme for improved accuracy in volcano-acoustic source parameter estimates by evaluating a rapid method for predicting diffraction losses. A thin screen approximation to diffraction has been proposed in the context of volcano infrasound as an improvement over the $1/r$ spreading correction alone (Ishii et al., 2020); however, the predictive ability of the original empirical relationship for diffraction losses (Maekawa, 1968) has not been evaluated for volcano infrasound. In this study we use FDTD modeling (de Groot-Hedlin, 2017) to show that Maekawa's original empirical relationship (Section 3.3) successfully predicts power losses due to infrasound diffraction over an idealized kilometer-scale thin screen. This finding validates the scaling of Maekawa's relation to large length scales and infrasonic wavelengths. Furthermore, the empirical relationship yields comparable relative amplitude distributions across the Sakurajima network to the approach taken by Ishii et al. (2020). However, the absolute amplitudes predicted by the screen theory overestimate the attenuation in the case of realistic volcano topography. We interpret this finding as a consequence of reflections from topography counteracting losses from diffraction.

3.10.1 Application of the thin screen approximation to infrasonic wavelengths

The IL_{m} results from our scaled thin screen simulation Figure 3.3a) agree well with the empirical relationship of Maekawa (1968), indicating that Eqn. 3.3 is a reasonable approximation

for infrasonic wavelengths recorded on the ground in the case of a kilometer-scale thin screen. Furthermore, this agreement suggests that the 2D axisymmetric geometry of our numerical model space is adequate to describe losses for a thin screen. Moreover, the insertion loss results for a wedge and wide barrier generally agree with the empirical prediction (<5 dB difference), suggesting that the theory gives a reasonable first-order estimate of infrasound diffraction losses for a variety of simple long barrier types when receivers are on the ground. Equation 3.3 therefore provides a rapid method to estimate acoustic power losses for infrasound diffraction over simple barriers without resort to time- or computationally-intensive numerical simulations.

3.10.2 Implications for modeling diffraction of volcano infrasound

The IL_{m} results from our 2D simulations with Sakurajima Volcano topography are systematically smaller than predicted by IL_{pY} with differences on order of 10^1 dB (Figure 3.3). These findings are corroborated by 3D simulations with Sakurajima topography, which feature even smaller IL_{m} than the 2D results (Figure 3.5c). In the 3D simulations IL_{m} is negative at stations ARI, KUR, and KOM, indicating gains in amplitudes relative to flat ground propagation (Figure 3.5c). This suggests that this predictive empirical relationship is not adequate to describe losses to diffraction over complex volcano topography. The losses are better predicted by a different relation proposed by Fehr (1951) and represented by Eqn. 3.4, as shown by grey lines in Figures 3.3a and 3.5c. This relation is relevant in that it is meant for scenarios with sources and receivers on the ground; however, it is not very useful in that it is given no justification by Fehr (1951), and is only applicable at $N \geq 0.1$, whereas volcano infrasound recording geometries may have lower Fresnel numbers.

Our conclusions contrast with the those of Ishii et al. (2020), who suggest that the observed relative amplitude distribution at Sakurajima is better modeled when accounting for the effect of a thin screen than when only geometrical spreading is considered. We found comparable relative amplitude distributions to Ishii et al. (2020) using our method (Figure 3.8); however we consider it misleading to normalize the screen-predicted amplitudes relative to station KUR in

Table 3.1: Standard deviation distances (S) for predictions from screen theory and $1/r$ spreading.

Stations	Screen	$1/r$
ARI	0.33	0.11
HAR	2.43	5.10
KOM	0.57	0.01
SVO	1.71	1.19

this way. Our synthetics show that attenuation at KUR is nearly zero or even negative (Figure 3.5c), whereas the screen theory would predict 8 dB attenuation for the corresponding Fresnel number. Direct use of the Maekawa (1968) empirical relationship results in overprediction of losses to diffraction in the case of volcano infrasound. Consequently we consider the screen approximation inappropriate, even if normalization by KUR causes the relative amplitude distribution to be comparable to observations.

Furthermore, while Ishii et al. (2020) claim that the predictions from the screen approximation offer an improvement over predictions based on $1/r$ spreading for 31 events in 2017, we do not see an improvement for 30 events in 2014 (Figure 3.5). They used the standard deviation distance ($S = |X - \mu|/\sigma$, where X is the predicted amplitude, μ is the mean of the observations and σ is the standard deviation of the observations) to show that S values are generally are lower for the screen prediction than $1/r$. We calculated S for the observations in Figure 3.8 and found larger values for the screen method than the $1/r$ method at stations ARI, KOM and SVO (Table 3.1). While this analysis is clearly limited by small sample size (30 events) and only four stations, it illustrates the lack of appreciable improvement of the screen method compared to $1/r$.

We conclude that the primary cause of relatively small IL_{m} values for volcano topography is the focusing of the acoustic wavefield by multiple reflections down concave-upward slopes (e.g., Figure 3.2). Focusing has been previously postulated at Sakurajima to explain amplitude variations with azimuth (e.g., Kim and Lees, 2014; Lacanna et al., 2014). Ishii et al. (2020) also observed that amplitudes from 31 Vulcanian explosions during August to September 2017 were consistently higher than expected from spherical spreading at one station (JIG). Notably, Ishii

et al. (2020) used KUR as a reference station to estimate relative amplitude distrubtions based on $1/r$, yet the topographic profile for KUR has one of the most concave slopes in the network. Out of the stations considered in this study, KUR also has the lowest IL_{m} values, indicating the least attenuation losses to diffraction. Acoustic focusing at this station may explain why the KUR-relative amplitudes are larger than observed amplitudes at several stations including ARI, HAR and SVO. We interpret that the concavity of the slope facilitates constructive interference of reflected waves which counteract amplitude losses from diffraction.

3.10.3 Limitations of our methodology

Our results suggest that the diffraction of infrasound over volcano topography produces significantly less attenuation than predicted for a thin screen with equivalent Fresnel number; however, several limitations in our methodology must be acknowledged.

Firstly, our numerical simulations are limited in their treatment of atmospheric propagation effects which may increase or decrease power losses depending on the conditions. We use a homogeneous atmosphere to isolate the effect of diffraction and allow direct comparison to the empirical relationship of Eqn. 3.3, but in real outdoor propagation the sound speed generally decreases with altitude (Pierce, 1981; Embleton, 1996). This vertical gradient enhances upward refraction of the wavefield and leads to reduced acoustic power at the receivers (greater IL_{m}) compared to the homogeneous atmosphere case. Lacanna et al. (2014) showed that wind and atmopsheric temperature gradients contributed to spatial and temporal deviations from $1/r$ amplitude decay at Sakurajima over a 21 month period. Additionally, atmospheric variability can change the propagation conditions over short time periods (e.g., Fee and Garces, 2007; Matoza et al., 2009b; Chunchuzov et al., 2011; Green et al., 2012; Johnson et al., 2012; de Groot-Hedlin, 2017; Iezzi et al., 2018; Ortiz et al., 2018; Sanderson et al., 2020). For example, changes in atmospheric conditions in the boundary layer (lowermost ∼3 km of troposphere) caused up to ∼10 dB pressure differences in recordings of controlled chemical explosions at local distances (¡10 km; Kim et al., 2018). Consequently, our comparison between synthetic and predicted

amplitudes to observations (Figure 3.8) is limited by the unmodeled atmospheric variability.

Secondly, the rigid topography used in our simulations may introduce minor variations in the synthetic waveforms compared to the observations. Real volcano topography can feature ground of finite-impedance (e.g., loose volcanic tephra layers) that may absorb some acoustic energy or convert it to seismo-acoustic coupled waves (e.g., Matoza et al., 2009b) and consequently increase IL_{m} values. A heterogenous distribution of impedance around the volcano could contribute to variations in the relative amplitudes across the network. This effect is commonly assumed negligible for infrasonic wavelengths and <20 km path lengths (Matoza et al., 2019a), but warrants further consideration since volcanic landscapes often feature loosely-consolidated near-surface materials (e.g., tephra layers or soil). Additionally, our simulations feature stair-step topography which may lead to spurious reflections artificial diffraction side-lobes (de Groot-Hedlin, 2017); however, these are much smaller in amplitude than the compressional first arrivals that we use to calculate IL_{m}. We also ran additional simulations with finer discretization (5 m grid spacing in both the 2D and 3D models) and observed no changes in the frequency range of interest ($\sim$0.1–1 Hz), indicating negligible influence of artifacts arising from topography discretization.

Finally, we acknowledge that the 2013 infrasound network at Sakurajima is not an optimal configuration for thorough diffraction analysis, since there are only five receivers and they are distributed azimuthally rather than radially. We attempted to improve this in our simulations by placing synthetic receivers at 100 m intervals on the topographic profiles (Figure 3.2) such that we are able to represent a range of Fresnel numbers (Figure 3.3). However, for comparison to observations we are limited to the five stations and 30 events (Figure 3.8). Further investigation of the thin screen diffraction approximation should target a volcano with more events and stations, preferably with a radial line configuration, such as at Yasur Volcano (Jolly et al., 2017; Matoza et al., 2017b). Our focus on Sakurajima has allowed direct comparison to the results of Ishii et al. (2020) in addition to previous studies that have addressed topographic effects at this volcano (e.g., Kim and Lees, 2014; McKee et al., 2014; Yokoo et al., 2014; Lacanna et al.,

2014).

3.10.4 Directions for future work

Our results suggest that thin screen diffraction theory is inadequeate to describe power losses for volcano infrasound, providing a first step towards the development of an analytical method for this purpose. Computationally-intensive numerical simulations remain the most accurate tool for estimating these losses, but future research could work towards a more rapid predictive relationship. For example, we only considered power losses over five topographic profiles at Sakurajima Volcano, but a larger simulation set involving multiple volanoes and azimuths could be used to derive a new semi-empirical relationship between N and IL_{m}. Such an analysis could incorporate regional (15–250 km) to remote (>250 km) recording distances to generalize the relationship for applications beyond local deployments. We note that in addition to N, it may also be useful to consider some measure of topographic roughness (e.g., 2D Fourier power spectral analysis of topography; Perron et al., 2008; Richardson and Karlstrom, 2019), since multiple small barriers could reduce recorded acoustic power without increasing the Fresnel number.

Finally, our conclusions draw attention to the significance of acoustic focusing during propagation down concave slopes. This phenomenon has been previously postulated at Sakurajima (e.g., Lacanna et al., 2014) and seems to counteract the losses due to diffraction. The focusing effect could be further investigated with a geometrical acoustics approach such as ray tracing (e.g., Blom and Waxler, 2012; Green et al., 2012; Fee et al., 2013a). A comprehensive correction scheme for topographic effects should account for the most significant processes; however, the relative contributions from diffraction, focusing, scattering and reflections are currently unclear. Further analysis of these effects is required to achieve a rapid correction scheme to account for topography without costly numerical simulations.

3.11 Conclusions

We used synthetic pressure results from a 2D FDTD method for linear infrasound propagation in an axisymmetric geometry to numerically model the acoustic power losses to diffraction over kilometer-scale barriers including a thin screen, a wedge, a wide barrier, and Sakurajima Volcano topography. We found that the modeled acoustic power losses for the kilometer-scale screen are well-predicted by an empirically-derived relationship (Maekawa, 1968) for diffraction of audible sound (20–20,000 Hz) over thin meter-scale screens, thus affirming the applicability of the relationship to infrasonic wavelengths. The power losses are also well predicted to first order for diffraction over the wedge and wide barrier, but the empirical relationship overpredicts losses for Sakurajima topography by $\sim 10^1$ dB. We corroborate these results by comparison to 3D simulations with Sakurajima topography (Kim and Lees, 2014), which also feature smaller attenuation values than predicted by Maekawa's empirical relationship. The relative amplitude distributions for 2D synthetics, 3D synthetics and thin screen predictions generally agree with data from 30 eruption events at Sakurajima, but the screen predictions do not provide an appreciable improvement over the commonly-used correction for geometrical spreading.

We conclude that the thin screen approximation proposed by Maekawa (1968) is an inappropriate model for diffraction by volcano topography because attenuation is overestimated in the topography case. This conclusion contrasts with that of Ishii et al. (2020), who conclude that their implementation of a thin screen approximation improves predictions of relative amplitude distributions at Sakurajima compared to geometrical spreading alone. We hypothesize that the true attenuation is smaller than predicted by Maekawa's empirical relationship because constructive interference of reflections down the concave volcano slopes (focusing) causes amplitude increases that counteract losses by diffraction.

Full wavefield numerical simulations such as finite-difference methods remain the most appropriate approach to account for topography (Kim et al., 2015; Iezzi et al., 2019; Lacanna and Ripepe, 2013; Kim and Lees, 2014; Lacanna et al., 2014; Maher et al., 2020). However, an analytical or empirically-derived method that depends only on readily-available topographic

information is desirable for rapid interpretations of infrasound data in a rapid deployment or network planning scenario. Future work towards this goal could benefit from the development of a new semi-empirical relationship based on a large suite of numerical simulations with numerous volcanoes and a variety of recording distances.

Acknowledgements

We thank Professor Tracianne Neilsen for helpful discussions in the preparation of this manuscript. The digital elevation models for Sakurajima Volcano were provided by the Japanese Ministry of Land, Infrastructure, Transport and Tourism. This research was supported by National Science Foundation (NSF) grants EAR-1620576 and EAR-1847736.

Author contributions

Maher is a graduate student under the supervision of Matoza. Maher and Matoza formulated the work and experimental design in consultation with de Groot-Hedlin and Gee. Maher ran the 2D simulations and wrote the initial draft of the manuscript. Kim performed the 3D Cartesian propagation simulations. All authors provided input and feedback throughout the research and manuscript preparation.

Data availability

Infrasound data from the 2013 Sakurajima deployment (network code YO; Fee et al., 2014) are publicly available through the Data Management Center of the Incorporated Research Institutions for Seismology (`https://www.fdsn.org/networks/detail/YO_2013/`).

Chapter 4

Evidence for near-source nonlinear propagation of volcano infrasound from strombolian explosions at Yasur volcano, Vanuatu

This chapter appeared in this form in:

Maher, S.P., Matoza, R.S., Jolly, A.D., de Groot-Hedlin, C., Gee, K.L., Fee, D., Iezzi, A.M., 2022. Evidence for near-source nonlinear propagation of volcano infrasound from strombolian explosions at Yasur volcano, Vanuatu. Bulletin of Volcanology 84. doi:10.1007/s00445-022-01552-w.

4.1 Abstract

Volcanic eruption source parameters may be estimated from acoustic pressure recordings dominant at infrasonic frequencies (<20 Hz), yet uncertainties may be high due in part to poorly understood propagation dynamics. Linear acoustic propagation of volcano infrasound

is commonly assumed, but nonlinear processes such as wave steepening may distort waveforms and obscure the source process in recorded waveforms. Here we use a frequency-domain nonlinearity indicator developed by Reichman et al. (2016a) to quantify spectral changes due to nonlinear propagation primarily in 80 signals from explosions at Yasur Volcano, Vanuatu. We find evidence for $\leq 10^{-3}$ dB/m spectral energy transfer in the band 3–9 Hz for signals with amplitude on order of several hundred Pa at 200–400 m range. The clarity of the nonlinear spectral signature increases with waveform amplitude, suggesting stronger nonlinear changes for greater source pressures. We observe similar results in application to synthetics generated through finite-difference wavefield simulations of nonlinear propagation, although limitations of the model complicate direct comparison to the observations. Our results provide quantitative evidence for nonlinear propagation that confirm previous interpretations made on the basis of qualitative observations of asymmetric waveforms.

4.2 Introduction

Volcanic eruptions produce acoustic waves dominant at infrasonic frequencies (<20 Hz) that are increasingly studied in both research and monitoring contexts due to their usefulness in detecting, locating and characterizing eruptive activity (e.g., De Angelis et al., 2019; Johnson, 2019; Matoza et al., 2019a). At local recording distances (<15 km), infrasound has been used in attempts to make quantitative estimates of eruption source parameters such as vent and crater geometry (e.g., Johnson et al., 2018b; Muramatsu et al., 2018; Watson et al., 2019), mass and volume flux (e.g., Moran et al., 2008; Johnson and Miller, 2014; Kim et al., 2015) and plume height (e.g., Caplan-Auerbach et al., 2010; Ripepe et al., 2013; Lamb et al., 2015). These estimates have largely been made assuming linearity in the acoustic source process and during wave propagation (De Angelis et al., 2019), yet significant nonlinear dynamics are expected near the source (e.g., Morrissey and Chouet, 1997; Yokoo and Ishihara, 2007; Marchetti et al., 2013). Acoustic wavefields may be modulated at the source by processes such as fluid flow and jet turbulence (e.g., Matoza et al., 2009a, 2013; Taddeucci et al., 2014; Watson et al.,

2021) and during propagation by wave steepening and period lengthening (e.g., Hamilton and Blackstock, 2008; Marchetti et al., 2013; Maher et al., 2020). These processes may distort the waveforms and frequency content of observed signals, causing inaccurate interpretation of the source mechanism when linear generation and propagation are assumed (Maher et al., 2020; Watson et al., 2021). Improved understanding of nonlinear dynamics is therefore needed to reduce uncertainty in infrasound-based estimation of source parameters; here, we focus on nonlinear propagation.

Nonlinear propagation occurs when the applied pressure is significant compared to the ambient pressure, causing local changes in particle velocities and temperatures (Atchley, 2005; Hamilton and Blackstock, 2008). In this case the sound speed becomes pressure-dependent such that higher amplitude and compressional portions of the wave travel faster than lower-amplitude and rarefaction portions (Hamilton and Blackstock, 2008). This causes the wavefield to steepen towards a shock wave, which is a pressure discontinuity where the point of peak pressure overtakes the wave onset (Hamilton and Blackstock, 2008). Wave steepening in the time domain may be correlated with positive skewness of pressure and the first time derivative of pressure, although these statistical analyses require large sampling rates and high signal-to-noise ratios (McInerny et al., 2006; Gee et al., 2013; Reichman et al., 2016b). In the frequency domain, wave steepening corresponds to spectral energy transfer: energy is lost from the dominant frequency components and gained at successively higher harmonics (Hamilton and Blackstock, 2008). Energy may also be transferred to lower frequencies (period lengthening) once wave steepening has generated an N-wave, but this process is less efficient than upward energy transfer because the front and leading edges of the wave must be shock-like (Hamilton and Blackstock, 2008). A consequence of these phenomena is that nonlinearly propagated volcano acoustic signals may be richer in high-frequency content and lower in peak pressure than expected for an equivalent source pressure based on linear acoustic theory (Morfey and Howell, 1981; Hamilton and Blackstock, 2008).

Although nonlinear propagation of volcano infrasound has long been suspected and cited as

a source of uncertainty (e.g., Morrissey and Chouet, 1997; Garcés et al., 2013), quantification of the nonlinear processes remains challenging. Asymmetric waveforms (large short-duration compression phases followed by longer lower-amplitude rarefaction phases) have been interpreted as possible evidence of nonlinear sources and/or propagation (Brogi et al., 2018; Marchetti et al., 2013; Goto et al., 2014; Anderson et al., 2018b; Matoza et al., 2018; Matoza and Fee, 2018), but they have also been explained in terms of crater rim diffraction (Kim and Lees, 2011) and fluid flow at the source (Brogi et al., 2018; Watson et al., 2021). Similarly, visual observations of luminance changes corresponding to the passage of volcano-acoustic waves through water vapor have been interpreted as evidence of supersonic (nonlinear) propagation (Ishihara, 1985; Yokoo and Ishihara, 2007; Marchetti et al., 2013). However, the estimates of wavefront velocity are not always supersonic (Genco et al., 2014), and uncertainty ranges on the estimates do not rule out ambient (sonic) propagation speeds. Nonlinear propagation may still occur at sonic propagation speeds if shocks are balanced across zero dynamic pressure, such as for sawtooth waveforms (Hamilton and Blackstock, 2008).

Several quantitative models for nonlinear infrasound propagation have recently been proposed. Dragoni and Santoro (2020) provide analytical relationships for shock wave properties including pressure with distance from the source; however, these are valid for strong shocks (pressures greater than six times atmospheric pressure, or >607,800 Pa at sea level) which are larger in amplitude than observed signals (up to 1,200 Pa at 2 km; Anderson et al., 2018b). Watson et al. (2021) perform aeroacoustic simulations that illustrate nonlinear waveform steepening and how erupted volumes are underestimated when linear propagation is assumed. Maher et al. (2020) applied a quantitative indicator of nonlinearity (developed by (developed by Reichman et al., 2016a) to data and synthetics corresponding to explosion signals at Sakurajima Volcano, Japan. Their results from numerical modeling suggested that the indicator could quantify several decibels of spectral energy transfer at Sakurajima explosion amplitudes, but applications to the observed data were complicated by additional outdoor propagation dynamics (e.g., refraction in wind gradients and topographic scattering). Topographic scattering was

shown to dominate the distortion of the waveform, but nonlinear spectral energy transfer was found to be an important secondary process (Maher et al., 2020).

In this study we extend the work of Maher et al. (2020) by applying a quantitative nonlinearity indicator to infrasound signals from explosions at Yasur Volcano, Vanuatu. While the analysis at Sakurajima (Maher et al., 2020) was complicated by complex topography and few stations with wide azimuthal coverage, a 2016 field campaign at Yasur (Jolly et al., 2017; Matoza et al., 2017b, 2022a; Iezzi et al., 2019) affords detailed study of the near-source wavefield (0.2–1 km). The topography in the Yasur deployment is relatively minimal compared to volcanoes such as Sakurajima where the wavefield interacts with multiple topographic barriers such as ridges and valleys, although complexity may still be introduced by topography in the crater and around the crater rim. The infrasound deployment included 15 receivers including two to three sensors aboard a tethered aerostat and a six-element radial line array, enabling observation of wavefield changes with distance and height (Jolly et al., 2017; Matoza et al., 2017b). We primarily apply the indicator to signals from 80 explosions and to synthetics generated from 2-D axisymmetric finite-difference modeling of nonlinear infrasound propagation (de Groot-Hedlin, 2012, 2017). We also consider 2,068 events as recorded at a single station over a two-day period to investigate changes through time, and we estimate potential errors in source volume estimates due to the nonlinear propagation effects.

4.3 Quadspectral Density Nonlinearity Indicator

Although nonlinear acoustic propagation is a well-understood phenomenon from a theoretical perspective (Hamilton and Blackstock, 2008), it is not straightforward to identify in recorded waveforms. Various methods have been proposed as indicators of nonlinearity, especially in studies of man-made jet noise signals at audible frequencies (20–20,000 Hz), such as the skewness of the waveform and its derivative (McInerny and Ölçmen, 2005; Gee et al., 2013), bicoherence (Kim and Powers, 1979; Gee et al., 2010) and quadspectral density (Morfey and Howell, 1981; Petitjean et al., 2006; Pineau and Bogey, 2021). Similarities in power spectra have

been observed between volcano infrasound and man-made jet noise, leading to the hypothesis that both types of signals are created by similar processes (turbulence and shearing between ambient air and a momentum driven fluid flow) (Matoza et al., 2009a). As a result, methods designed for indicating nonlinearity in jet noise at audible frequencies, such as skewness, have found novel applications to volcanic signals at infrasonic frequencies (<20 Hz) (e.g., Fee et al., 2013a; Anderson et al., 2018b). These approaches effectively yield proxies for nonlinearity without direct physical interpretation; for example, positive values of waveform derivative skewness indicate steep compressional onsets that may then be interpreted as shock fronts (e.g., Muhlestein and Gee, 2011; Shepherd et al., 2011). Recently a quantitative quadspectrum-based indicator (ν_N) was developed which gives the rate of change in spectral level (unit dB/m) at a single point due to nonlinear propagation processes (Reichman et al., 2016a). The method has been shown to yield results consistent with nonlinear acoustic theory for supersonic model-scale jet noise (Miller and Gee, 2018) and full-scale military aircraft noise (Gee et al., 2018). Maher et al. (2020) were the first to apply ν_N to infrasonic frequencies and volcano acoustic data, using explosion signals from Sakurajima Volcano as a case study.

The ν_N indicator constitutes the nonlinear term of a frequency domain form of the Generalized Burgers Equation adapted by Reichman et al. (2016a) following work by Morfey and Howell (1981). This equation describes the spatial rate of change in a wave's sound pressure level (L_p) due to geometrical spreading (ν_S), absorption (ν_α) and finite amplitude effects (ν_N):

$$\begin{aligned} \frac{\partial L_p}{\partial r} &= -10\log_{10}(e) \times \left(\frac{2m}{r} + 2\alpha + \frac{\omega\beta}{\rho_0 c_0^3} \frac{Q_{pp^2}}{S_{pp}} \right) \\ &\equiv \nu_S + \nu_\alpha + \nu_N, \end{aligned} \tag{4.1}$$

where $\frac{\partial L_p}{\partial r} = \nu$ is the dB/m rate of change in distance (r), of the sound pressure level:

$$L_p = 10\log_{10}\left(p_i / p_{ref}^2\right), \tag{4.2}$$

where p_i is power spectral density in an arbitrary frequency band and pref is a reference pressure (here 20 μPa). The term m is a nondimensional geometrical spreading term equal to 0, 0.5 or 1 for planar, cylindrical, or spherical waves, respectively, and α is the frequency dependent absorption coefficient of the medium. We are interested in the nonlinear term:

$$\nu_N = -10 \log_{10}(e) \times \left(\frac{\omega \beta}{\rho_0 c_0^3} \frac{Q_{pp^2}}{S_{pp}} \right), \tag{4.3}$$

where $e \approx 2.718$, ω is angular frequency, β is the medium's coefficient of nonlinearity, ρ_0 is ambient density, c_0 is ambient sound speed, and Q_{pp^2} is the quadspectral density (imaginary part of the cross-spectral density) of the waveform p and its square p^2, and S_{pp} is power spectral density (PSD) of the waveform. The nonlinearity coefficient β is a unitless constant that characterizes the effect of finite-amplitude wave propagation on sound speed; in air $\beta \approx 1.2$ (Hamilton and Blackstock, 2008). The quadspectrum Q_{pp^2} reflects phase coupling between frequency components that arises during nonlinear spectral energy transfer (Kim and Powers, 1979; Gagnon, 2011). The ν_N indicator quantifies the rate of spectral energy transfer (dB/m) at the measurement point, giving negative values at frequencies where energy is lost and positive values at frequencies where energy is gained.

The applicable frequency range of ν_N depends on sample rate (Fs) and recording distance (r). The theoretical upper frequency limit is $Fs/4$ because Q_{pp^2} compares the waveform and its square, and squaring the waveform doubles its frequency components. The square of the $Fs/4$ component is therefore compared to Nyquist, and higher frequencies are not constrained. The lower frequency must satisfy the quasi-plane wave assumption of the generalized Burgers equation that $kr >> 1$ (Hamilton and Blackstock, 2008), where k is the angular wavenumber ($k = 2\pi f/c$). We limit our analysis to frequencies where $kr > 10$, which for $c = 346$ m/s and $200 \leq r \leq 1000$ m corresponds to lower limits of 0.6–2.8 Hz depending on the source vent and receiver. Miller and Gee (2018) used $kr > 29$ in their analysis, but they observed significant spectral changes with distance due to source directivity of their model-scale jet (independent of nonlinear propagation) and therefore needed greater distances to avoid the near-field for low

frequencies. At Yasur the explosions are well-modeled by a monopole source (Iezzi et al., 2019) for which all frequency components are generated at the same location. Use of $kr > 29$ at Yasur would produce minimum frequency limits of 1.5–6.9 Hz and cut in to relevant band for ν_N analysis surrounding and immediately above the dominant frequencies ($\sim$1–10 Hz). We therefore consider a lower $kr > 10$ threshold appropriate.

The expected behavior of ν_N for various signal types is illustrated in Figure 4.1. Figure 4.1a shows an example waveform for sustained jet noise generated by a model scale jet with supersonic exit velocities, Figure 4.1b shows the power spectra for several of these waveforms recorded at different distances, and Figure 4.1c shows the corresponding ν_N results (data from Miller and Gee, 2018). The analysis reveals negative ν_N values at frequencies just above the dominant observed frequency range of 3–10 kHz, and positive values at higher frequencies (>20 kHz). Maher et al. (2020) referred to this signature as a reclined S-shape that indicates upward spectral energy transfer, i.e., power is lost in the dominant frequency range of the source process and transferred to higher harmonics. These data from Miller and Gee (2018) represent nonlinear propagation; results for linear propagation can approximated by generating white noise waveforms sampled from normal distributions with the same means and standard deviations as the observed jet noise. Figure 4.1d shows an example of this corresponding to the jet noise in Figure 4.1a, Figure 4.1e shows the corresponding power spectra for each white noise waveform, and Figure 4.1f shows the ν_N results. Clearly, for linear propagation, the ν_N magnitudes are reduced and the reclined S-shape does not appear. Finally, in Figures 4.1g-i, results are shown for a short-duration impulsive waveform representing the shock wave from an exploding oxyacetelyne balloon (data from Young et al., 2015). These results show that the expected reclined S-shape of ν_N is observed for impulsive nonlinear signal types in addition to sustained noise.

While the examples shown in Figure 4.1 demonstrate expected ν_N behavior for audible frequency acoustics (20 Hz – 20 kHz), the method was previously validated for infrasonic frequencies in numerical simulations of volcano infrasound (Maher et al., 2020). The expected

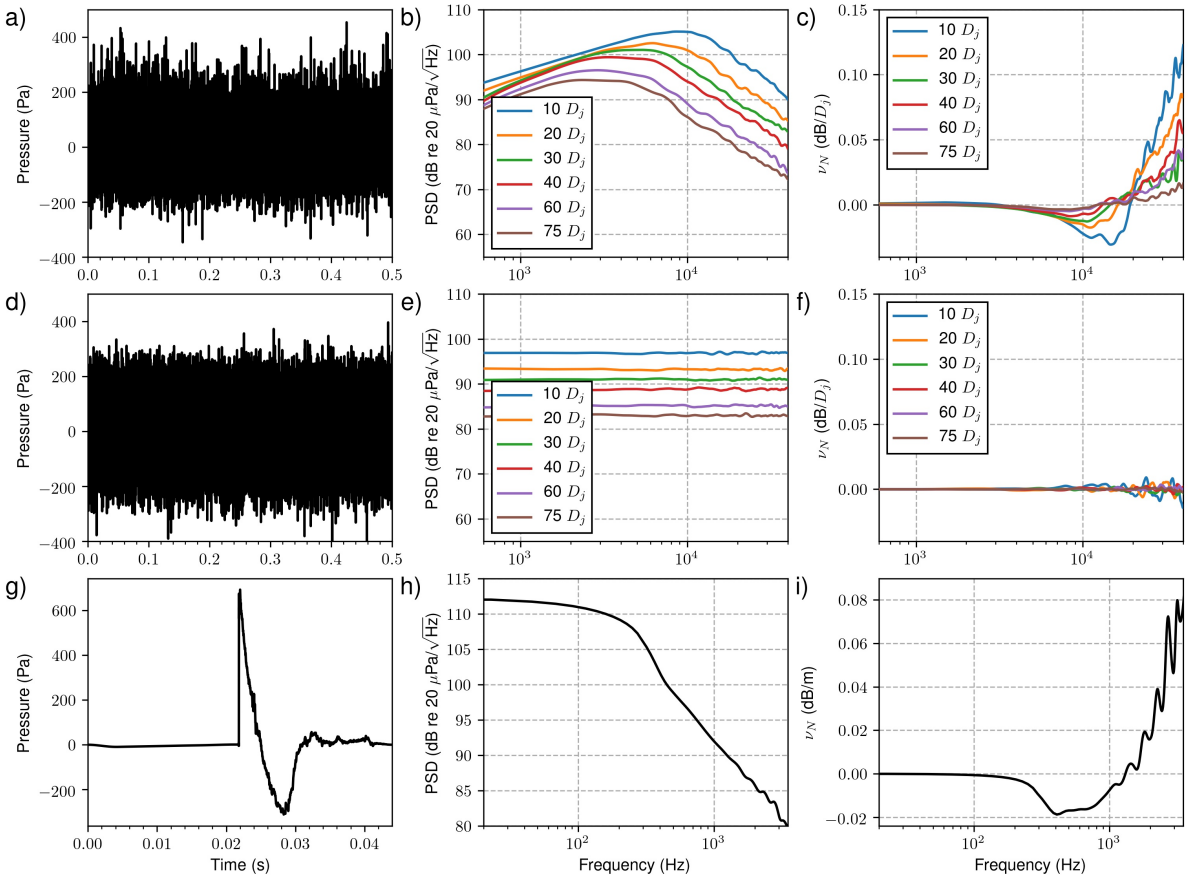

Figure 4.1: Waveforms (a, d, g), power spectra (b, e, h) and ν_N results (c, f, i) for supersonic model scale jet noise (a, b, c), numerically gener- ated white noise (d, e, f) and an exploding oxyacetelyne balloon (g, h, i). Model scale jet noise data are from Miller and Gee (2018) and the distances are scaled by jet diameter (D_j = 0.035 m). Waveforms in 4.1a and 4.1d correspond to 75 D_j. Exploding balloon data are from Young et al. (2015) and were recorded at 76.2 m distance and 0.9 m above the ground.

reclined S-shape was observed in results from synthetic waveforms generated by numerical modeling of nonlinear infrasound propagation, but not for observed signals from Sakurajima Volcano (Maher et al., 2020). These findings suggest that propagation nonlinearity is potentially observable with ν_N at the amplitudes observed at Sakurajima, but complicating factors in outdoor propagation (e.g., refraction, diffraction and reflections) obscured its signature in ν_N. We hypothesize that ν_N is better able to quantify nonlinearity in Yasur explosion signals due to close source-receiver distances and less obstructive topography.

4.4 Yasur Volcano and Dataset

4.4.1 Background

Yasur volcano is a basaltic-andesitic cone of lava and pyroclastic deposits on the island of Tanna in the Vanuatu Archipelago of the South Pacific (Figure 4.2). The volcano has produced consistent eruption activity for the past 800 years (Firth et al., 2014), with near-continuous gas emissions and up to several explosions occurring every minute (Métrich et al., 2011; Vergniolle and Métrich, 2016). The eruptions are primarily Strombolian, and mildly-Vulcanian activity is only rarely observed (Firth et al., 2014). Infrasound from the explosions is regularly detected 400 km away and has been used to probe seasonal changes in atmospheric structure (Le Pichon et al., 2005). The persistent eruptions and the approachability of the crater rim have made Yasur a research target for open-vent systems, with studies in recent years examining activity with visual, UV and thermal imaging, seismicity, infrasound, and Doppler radar (e.g., Kremers et al., 2013; Marchetti et al., 2013; Battaglia et al., 2016; Spina et al., 2016; Meier et al., 2016; Jolly et al., 2017; Iezzi et al., 2019; Fitzgerald et al., 2020; Simons et al., 2020; Fee et al., 2021; Matoza et al., 2022a).

The edifice consists of a roughly 400 m wide crater with maximum rim elevation ∼360 m above sea level, steep slopes to the north and west, and a level ash plain to the south and east (Figure 4.2). In 2016 the crater hosted three active vents in two sub-craters separated

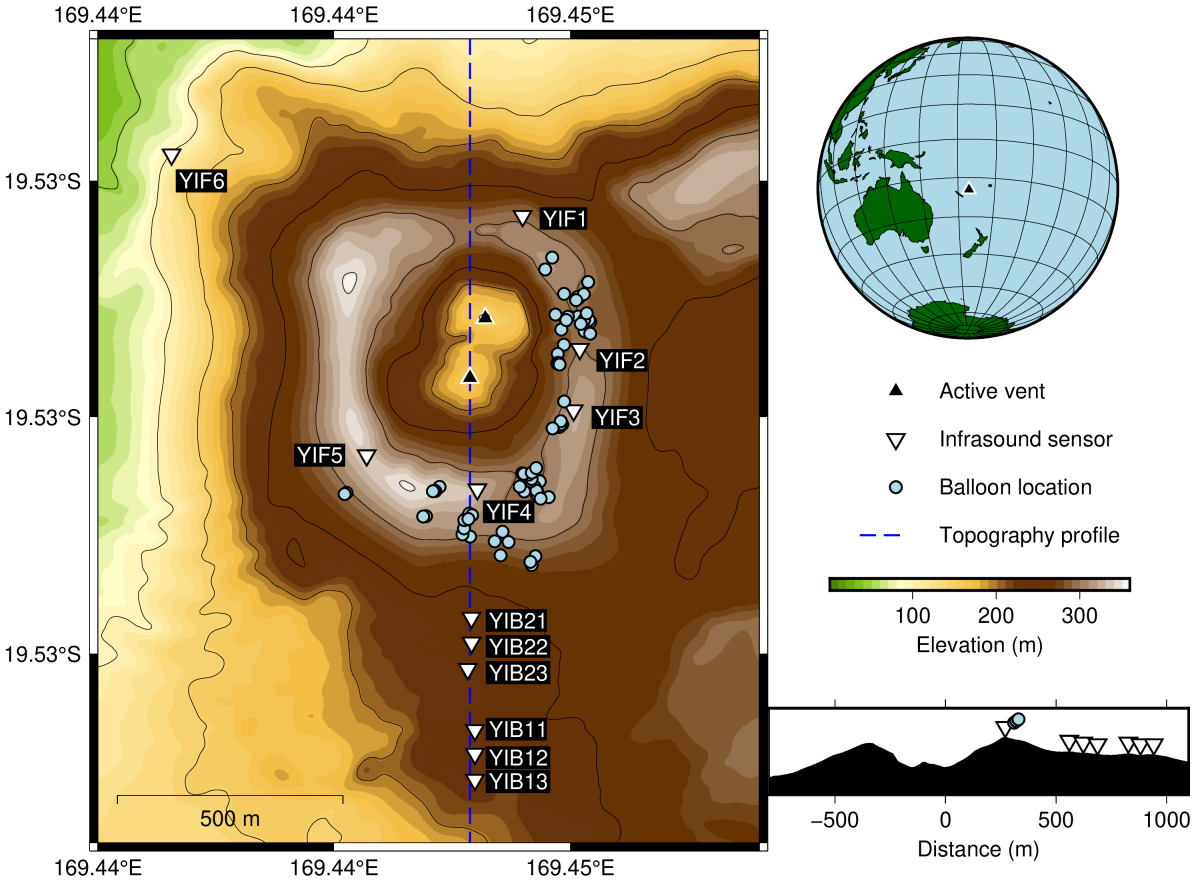

Figure 4.2: Map of the Yasur Volcano during the July–August 2016 deployment using a 2 m resolution digital elevation model (for details, see Iezzi et al., 2019) and 50 m contours. Downward triangles indicate ground-based infrasound stations, and circles represent aerostat locations during the 80 events studied here. The active north and south vents are indicated by black triangles. The dashed line corresponds to the topographic profile at the lower right. Inset globe shows the volcano location (black triangle) on Tanna Island in the Vanuatu archipelago.

by a low barrier; these vents have been termed, from south to north, vents A and B in the south crater and vent C in north crater (Oppenheimer et al., 2006). Vent A typically produces more frequent and violent explosions than vent B (e.g., Marchetti et al., 2013; Iezzi et al., 2019; Simons et al., 2020) and the separation between the two vents is small(∼20–40 m; Simons et al., 2020). Additionally, explosion sources from Reverse Time Migration cluster in only one location in the south crater rather than two (Fee et al., 2021). We therefore simplify our terminology to consider the source locations as north crater and south crater, with the understanding that high-amplitude signals from the South Crater are likely to arise from explosions at vent A (Jolly et al., 2017; Matoza et al., 2022a). We use a 2 m resolution digital elevation model (DEM) previously developed by Iezzi et al. (2019) which combines ASTER Global and Worldview02 DEMS far from the crater with a higher-resolution DEM of the crater area created with data from an unmanned aerial vehicle and structure-from-motion methods (Fitzgerald, 2019).

4.4.2 Infrasound deployment and dataset

In July and August 2016, a field campaign at Yasur was conducted by researchers at University of California Santa Barbara, University of Alaska Fairbanks, GNS Science New Zealand, University of Canterbury and the Vanuatu Meteorology and Geohazards Department (Jolly et al., 2017; Matoza et al., 2017b, 2022a; Iezzi et al., 2019; Fitzgerald et al., 2020; Fee et al., 2021). The infrasound deployment included six ground-based sensors around the crater rim (YIF1–YIF6), six ground-based sensors arranged in a line radiating 180° azimuth from the south crater (YIB11–YIB23), and three sensors suspended from an aerostat around the crater rim (YBAL1–3) (Figure 4.2). Sensors YIF1 and YIB11–YIB23 did not have direct lines-of-sight to the vents due to the intervening crater rim. The ground-based sensors are Chaparral Physics Model 60 UHP with a ±1,000 Pa pressure range and flat response between 33 s and Nyquist. The aerostat sensors are InfraBSU type and have a flat response from 30 s to Nyquist. All data were digitized with Omnirecs DATA-CUBE digitizers. Ground-based sensors were sampled at 400 Hz while aerostat sensors were sampled at 200 Hz. All ground-based sensors except YIF6.1

collected data from 27 July to 1 August, while some elements of the line array (YIB*) were operational on July 26 and August 2. Station YIF6 only collected data on July 28–29 and is excluded from this study.

The aerostat was floated between 30 and 100 m above the local topography with three sensors hung from a string at 10 m vertical spacing below the balloon. The bottom of the string was weighted with a digitizer and on-board GPS unit, giving location estimates with errors approximated at 10 m laterally and 15 m vertically (Jolly et al., 2017). The aerostat was moved every 15–60 min to 38 loiter positions around the north to southeast crater rim during daylight hours from July 29 to August 1 (for details, see Jolly et al., 2017).

Volcanic activity during the study period was nearly con- tinuous with persistent degassing and explosions every ∼1 to 4 min. Jolly et al. (2017) used continuous phase lag processing between stations YIF1 and YIF4 to distinguish the dominant crater activity in 20 s time windows, finding 2132 windows that favored the south crater and 859 windows that favored the north crater. Fee et al. (2021) applied a new technique they term reverse time migration-finite-difference time-domain (RTM-FDTD) to 12 h of data on July 28–29, 2016 and identified 1589 events during this interval alone, with the majority relocating in clusters close to vent A (south crater) and vent C (north crater). Beginning on July 31, the activity increased in intensity and shifted from predominantly the north crater to the south crater (Jolly et al., 2017; Iezzi et al., 2019; Fitzgerald et al., 2020; Matoza et al., 2022a). Iezzi et al. (2019) used STA/LTA detection on an aerostat sensor during time periods when the aerostat was tethered and with good constraints on its geographic location. They identified 201 impulsive events and used the relative arrival times at crater rim stations to distinguish between north and south vents. They then chose 40 events from each crater with a wide range in aerostat positions to invert for a multipole source mechanism and minimum residual source location. We primarily focus on the 80 events analyzed by Iezzi et al. (2019) because they feature good constraints on source location and aerostat position.

4.5 Observational results

To test for evidence of nonlinear propagation, we apply the ν_N indicator to data from all available sensors during each of the 80 explosive events analyzed by Iezzi et al. (2019). We use a multitaper method (Riedel and Sidorenko, 1995) to estimate power spectra and cross spectra for p and p^2 in 20 s time windows centered on peak pressure at each sensor. Prior to spectral estimation, the waveforms are detrended and tapered with a 40% Tukey window. The Tukey window tapers a percentage of the edges of the series while leaving the center unaffected; a 0% shape factor represents a box car function while 100% is equivalent to a Hann function. We then smooth the power spectra and quadspectra using a locally weighted least squares method. This smoothing method allows users to control the percentage of input points fit in each window for least-squares smoothing; we choose 0.9% to reduce variance at high frequencies while preserving resolution at low frequencies. Finally, we estimate the PSD at all stations during a 2 min period without explosions due to relatively lower activity (July 31, 01:47:30–01:49:30) and average across the different sensor groups (crater rim, line array, and aerostat) to compare signals to noise as a function of frequency. We avoid interpreting ν_N at frequencies for which the signal-to-noise ratio (SNR) of power spectra (in unit $\mathrm{Pa}^2/\mathrm{Hz}$) is less than six.

When calculating ν_N, we assume $c_0 = 346$ m/s, $\rho_0 = 1.18$ kg/m^3, corresponding to a representative air tem- perature value of 25° C observed during the campaign (Iezzi et al., 2019), and $\beta = 1.201$ (Hamilton and Blackstock, 2008). We present ν_N results directly in unit dB/m rather than integrating with respect to distance, as done by Maher et al. (2020). They assumed a constant rate of change with distance to obtain a cumulative estimate of the nonlinear changes ($\nu_{N_{tot}}$); however, the rate is unlikely to be constant. Nonlinear changes increase with amplitude and thus proximity to the source and the behavior of each frequency component changes with distance as spectral energy is transferred.

Figure 4.3 shows an example set of waveforms, power spectra, and ν_N results for a single event in the south crater as recorded at all stations. For ease of viewing the results are grouped in

three columns by sensor sets (aerostat, crater rim, and line array). The waveforms are generally asymmetric at the aerostat (Fig. 4.3a) and line array sensors (Fig. 4.3c) with a high-amplitude compressional onset followed by a lower amplitude rarefaction phase. The waveforms at the crater rim are more symmetric (Fig. 4.3b), suggesting a possible focalization effect whereby the wavefield is distorted by topography (Kim and Lees, 2011; Lacanna and Ripepe, 2020). The power spectra (Fig. 4.3d–f) show peak power around 2–3 Hz at the aerostat and crater rim stations that appears to move to lower frequencies ($\sim$1 Hz) at the line array. The ν_N spectra (Fig. 4.3g–i) show the characteristic reclined S-shape between $\sim$3 and 8 Hz indicating 10^{-4} to 10^{-3} dB/m upward spectral energy from $\sim$5 to 7 Hz. At frequencies higher than 10 Hz, the variance in ν_N becomes too high to discern true nonlinear features, and at the line array, ν_N is screened by the SNR above 40 Hz. Note that at the aerostat and some crater rim stations, the lower frequencies (<3 Hz) are not shown where $kr < 10$ (see Section 4.3 for details).

While Fig. 4.3 shows one event at all stations, Fig. 4.4 shows ν_N results for all events at three stations with increasing distance from the craters: YIF4 on the crater rim (Fig. 4.4a), YIB21 on the near side of the line array (Fig. 4.4b) and YIB13 on the far side of the line array (Fig. 4.4c). In this figure, the smoothing parameter is increased to 2.5% to emphasize the dominant trend. Spectra are colored by the peak pressure in the corresponding waveform at YIB21 such that each event has the same color at each station shown. In general, the magnitude of ν_N increases with peak pressure and decreases with receiver distance as expected, since nonlinearity increases with amplitude (note that the scale is 10^{-3} dB/m for YIF4 vs 10^{-4} for YIB21 and YIB13). Conversely, the stability of the ν_N shape generally increases with receiver distance, e.g., at YIB13, ν_N features consistent troughs at 4–6.5 Hz and peaks at 7–9 Hz, whereas at YIF4, these structures occur over broader and less consistent frequency ranges. Thus, the ν_N signature becomes clearer as a function of waveform amplitude and receiver distance for the cases considered here.

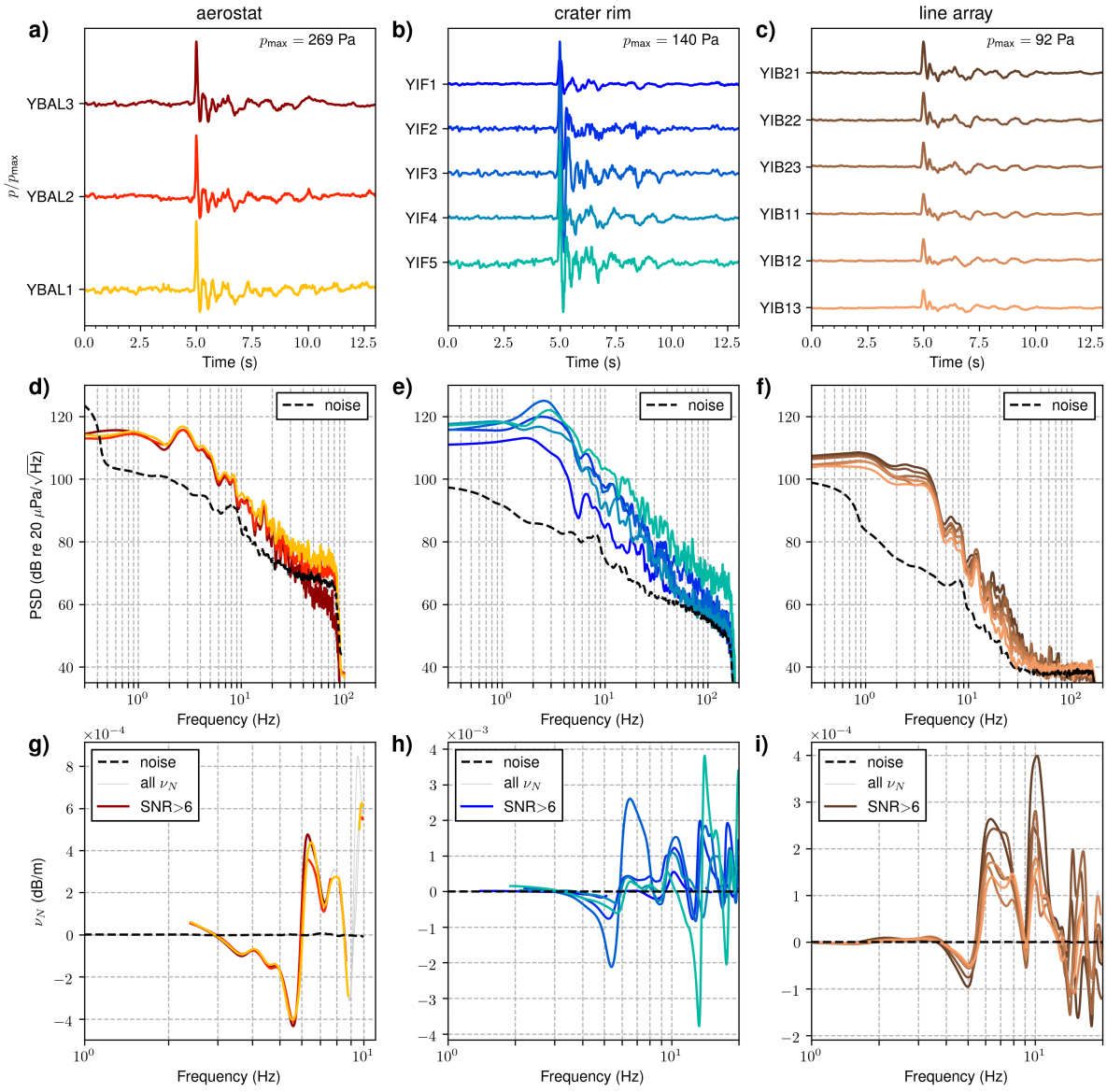

Figure 4.3: a–c) Waveforms, d–f) PSD curves, and g–i) ν_N results for a single event at 03:21:59.42 on August 1, 2016 (UTC). Waveforms and spectra are grouped by aerostat sensors (first column), crater rim sensors (second column), and line array (third column). Waveform amplitudes are normalized by the maximum (p_{max}) at the top-most sensor in each group (e.g., by YBAL3 in 4.3a). Dashed black "noise" curves in 4.3d–i show spectra at one sensor in each group during a quiet period of ambient noise. Light gray ν_N curves in 4.3g–i indicate frequencies for which SNR $\leq$ 6.

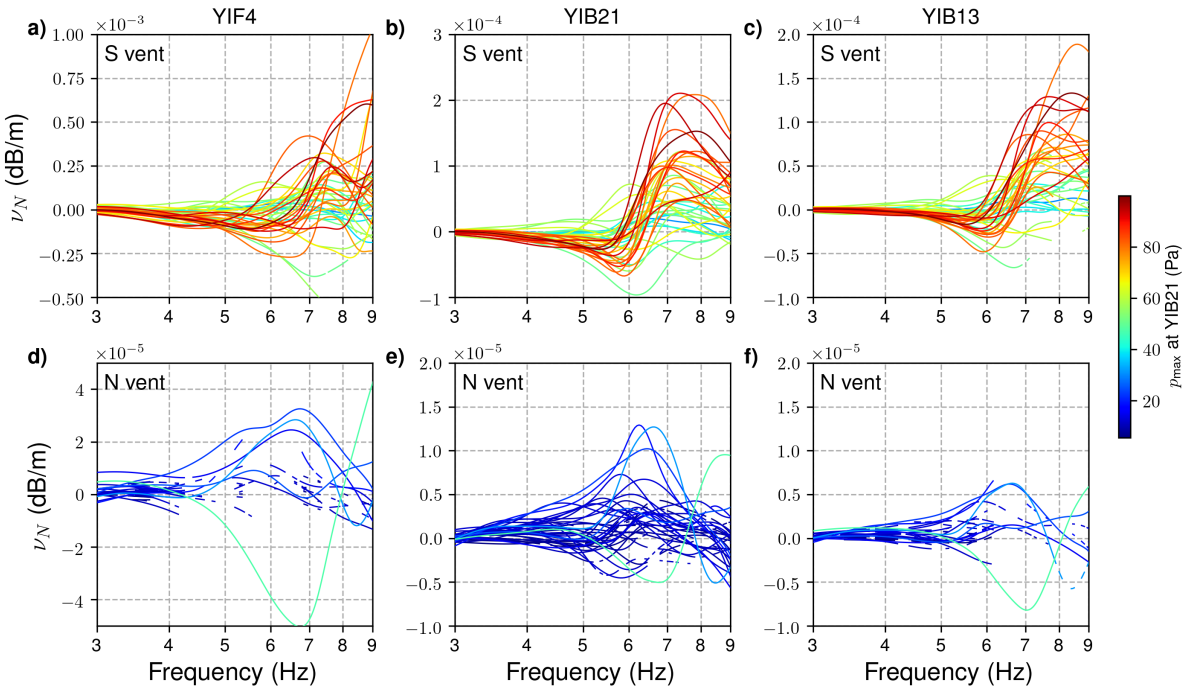

Figure 4.4: Spectra of ν_N in the frequency range 3–9 Hz for south vent events recorded at a) YIF4, b) YIB21, and c) YIB13, and for north vent events recorded at d) YIF4, e) YIB21, and f) YIB13. Spectra are smoothed in 2% bands and colored by peak waveform pressure (p_{max}) at YIB21. Results are only plotted at frequencies where SNR > 6 and $kr > 10$.

4.6 Numerical modeling

To further investigate possible topographic effects on the ability to recover nonlinearity in the Yasur Volcano explosion waves, we applied ν_N to synthetic pressure waveforms generated by numerical wavefield modeling that allows for nonlinear propagation and topography. We hypothesize that if the observed ν_N features (e.g., Figs. 4.3g–i) are caused by nonlinear propagation, then they should be closely reproduced by synthetics when comparable pressure amplitudes (∼250 Pa at ∼400 m) and frequencies (∼3–8 Hz) are simulated.

4.6.1 Finite-difference method

We ran numerical wavefield simulations using a finite-difference time-domain (FDTD) method for nonlinear infrasound propagation developed by de Groot-Hedlin (2012, 2017). The method solves the Navier–Stokes equations with second-order accuracy in the space and time derivatives (de Groot-Hedlin, 2012, 2017). This method was previously used to investigate the effects of nonlinearity (Maher et al., 2020) and topographic diffraction (Maher et al., 2021) on explosion signals at Sakurajima Volcano, Japan. The simulations are run in a cylindrical coordinate system with an axisymmetric geometry about the left boundary, allowing for modeling of spherical spreading in a 2D source-receiver plane. The model includes rigid stair-step topography at the lower boundary and absorbing perfectly matched layers at the top and right boundaries (Berenger, 1994). The source is initialized as a spatially distributed Gaussian pulse centered at the lower-left corner of the model space at time zero, requiring a flat topographic area within the source region. To accommodate this, we add an artificial 175 m wide flat area to the left side of each topographic profile at the elevation of the crater floor (e.g., see Fig. 4.5a). This configuration is required for numerical stability and precludes alteration of the source without significant modification to the method. This limitation means that we cannot manipulate the source-time function to minimize waveform residuals and are limited to reproducing comparable peak amplitudes.

We ran five separate simulations with lower boundaries corresponding to the topographic

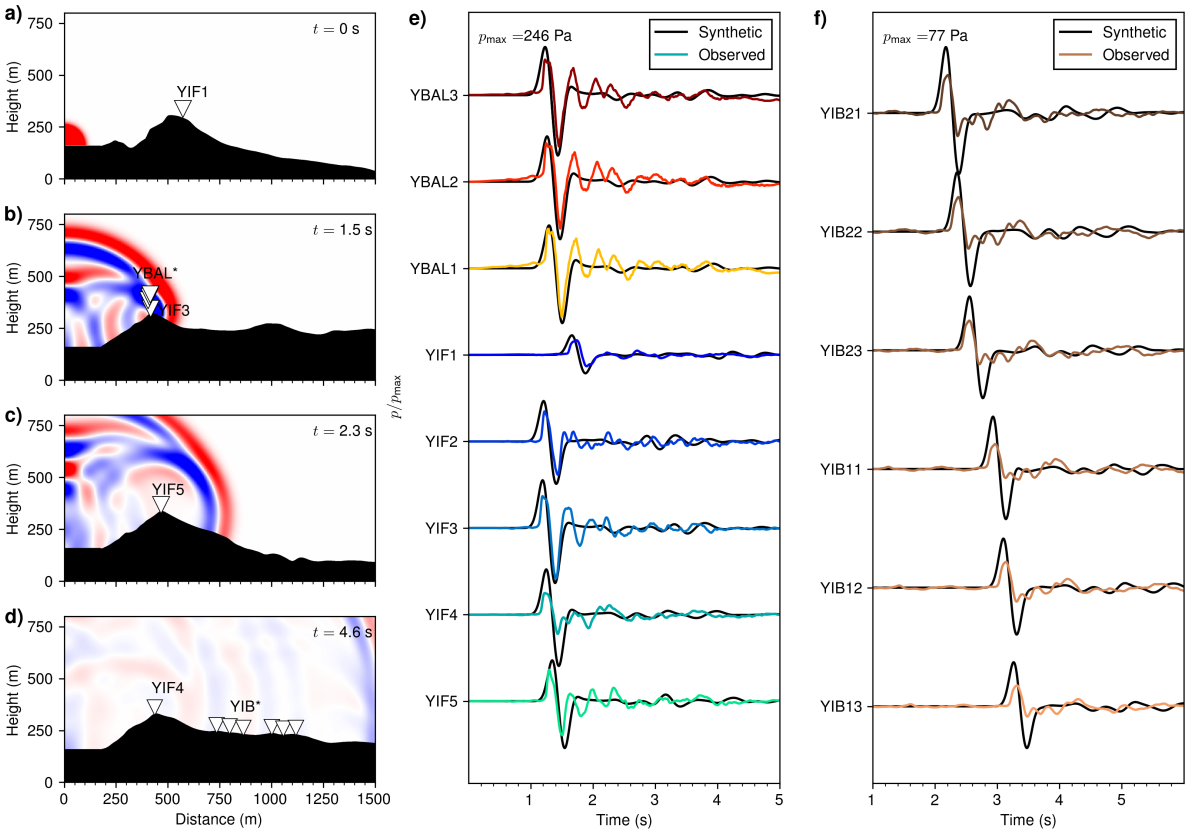

Figure 4.5: Synthetic wavefields at a) $t = 0$ s over YIF1 topography, b) $t = 1.5$ s over YIF3 topography, c) $t = 2.3$ s over YIF5 topography, d) $t = 4.6$ s over YIF4 topography, and e) comparison of synthetic waveforms (black) to observed (color) at aerostat and rim stations for an event at 04:53:12.87 on August 1, 2016. Amplitudes are normalized by maximum pressure at synthetic YBAL3 (p_{max}). Observed wave- form times are matched by peak pressure at YBAL3. f) Waveform comparison for line array stations. Amplitudes normalized by maximum pressure at synthetic YIB21

profiles along azimuths between the south vent and each receiver in the rim net- work (YIF1–YIF5; Fig. 4.2). We modeled a single event when the aerostat was located near YIF3 (August 1, 2016, at 04:53:12.87 UTC). Since the method is a forward model, the source pressure must be adjusted to approximate the amplitudes observed at the receivers. We chose a maximum source pressure of 7000 Pa to approximate the peak pressure at YBAL3 (Fig. 4.5e). We used a homogeneous atmospheric sound speed of 346 m/s, which corresponds to observed temperatures during the deployment (Iezzi et al., 2019) and gives reasonable arrival times across the network (Fig. 4.5e). We used a 4×4 km model space and 10 s simulation run time such that the wavefront does not reach (or spuriously reflect from) the top or right boundaries.

Finite-difference models require adequate discretization in time and space to ensure numerical accuracy at the frequencies of interest. Taflove and Hagness (2005) stated that at least 10 grid nodes per wavelength are required. For a grid spacing Δ and maximum sound speed c_{max}, the corresponding time step Δt must also meet the Courant–Friedrichs–Lewy condition $\Delta t \leq \Delta c_{max}\sqrt{3}$ (Taflove and Hagness, 2005). In our method, the discretization and frequency content is determined as a function of the number of nodes per wavelength desired at a maximum source frequency and minimum sound speed in the model. For example, an input of 10 nodes per wavelength at 5 Hz and 340 m/s yields $\Delta = 5.9$ m, $\Delta t = 4.7$ ms, and 30–50 nodes per wavelength at dominant frequencies around 1 Hz (de Groot-Hedlin, 2017). In this study, we chose 25 nodes per wavelength at 6 Hz and 346 m/s, yielding $\Delta = 2.3$ m and $\Delta t = 1.9$ ms. This gives 75–125 nodes per wavelength at dominant frequencies around 1.5 Hz and 19–50 nodes per wavelength in our primary analysis band of 3–8 Hz. The Courant–Friedrichs–Lewy condition for numerical accuracy at 10 nodes per wavelength is met up to 15 Hz; above this frequency, artifacts from numerical dispersion may become significant. Note that Maher et al. (2020) performed a finely discretized simulation with 40 nodes per wavelength to check for inaccuracies due to numerical dispersion, but they did not observe changes to the frequency components of interest in their study. We are therefore confident in the numerical accuracy of our simulations at the frequencies of interest for ν_N analysis at Yasur Volcano (∼3–8 Hz).

4.6.2 Modeling results

We ran five simulations, one for each topographic profile from the south vent to each receiver in the crater rim network and recorded synthetic waveforms at 14 locations corresponding to the active sensors during an event on August 1, 2016, at 04:53:12.87 UTC. The three aerostat sensors were located near YIF3 and so were included in the YIF3 simulation with positions shown in Fig. 4.5b. The line array sensor positions coincide with the YIF4 profile and so were included in the YIF4 simulation as shown in Fig. 4.5d. Figures 4.5a–d shows example snapshots of the wavefield at different times in four of the simulations (YIF2 not shown). The maximum pressures are concentrated at the wavefront, though reflection from the crater walls and rim creates complexity in the trailing wavefield. Figure 4.5e shows that the synthetic waveforms (black lines) show good agreement in relative amplitudes and arrival times with the observations (colored lines). In some cases, the observed waveforms feature more rapid compressional onsets than the synthetics (e.g., YBAL3 and YIF3). This feature is likely a result of the spatially distributed Gaussian source function (see Section 4.6.1).

The PSD and ν_N spectra corresponding to the waveforms in Fig. 4.5e are shown in Fig. 4.6. Results are grouped in columns by sensor locations; i.e., results for aerostat sensors, crater rim stations, and line array elements are shown in the first, second, and third columns, respectively. The first row (Fig. 4.6a–c) shows PSD for synthetics (grayscale) and observations (color), the second row (Fig. 4.6d–f) shows ν_N spectra for the synthetics, and the third row (Fig. 4.6g–i) shows nu_N for the observations. Synthetic and observed power spectra generally agree in peak power and dominant frequencies (∼1–3 Hz), although the synthetic spectra roll off rapidly toward the upper limit of numerical accuracy at 15 Hz (Section 4.6.1). The ν_N spectra feature the expected reclined S-shape for both synthetics and observations, indicating energy transfer from ∼4–5 to 6–7 Hz. The ν_N magnitudes are larger for the synthetics than the observations (e.g., 10^{-3} dB/m at the synthetic line array vs 10^{-4} dB/m in the observations), and the minima in synthetic ν_N occur at frequencies approximately 0.5 Hz higher than in the observed ν_N.

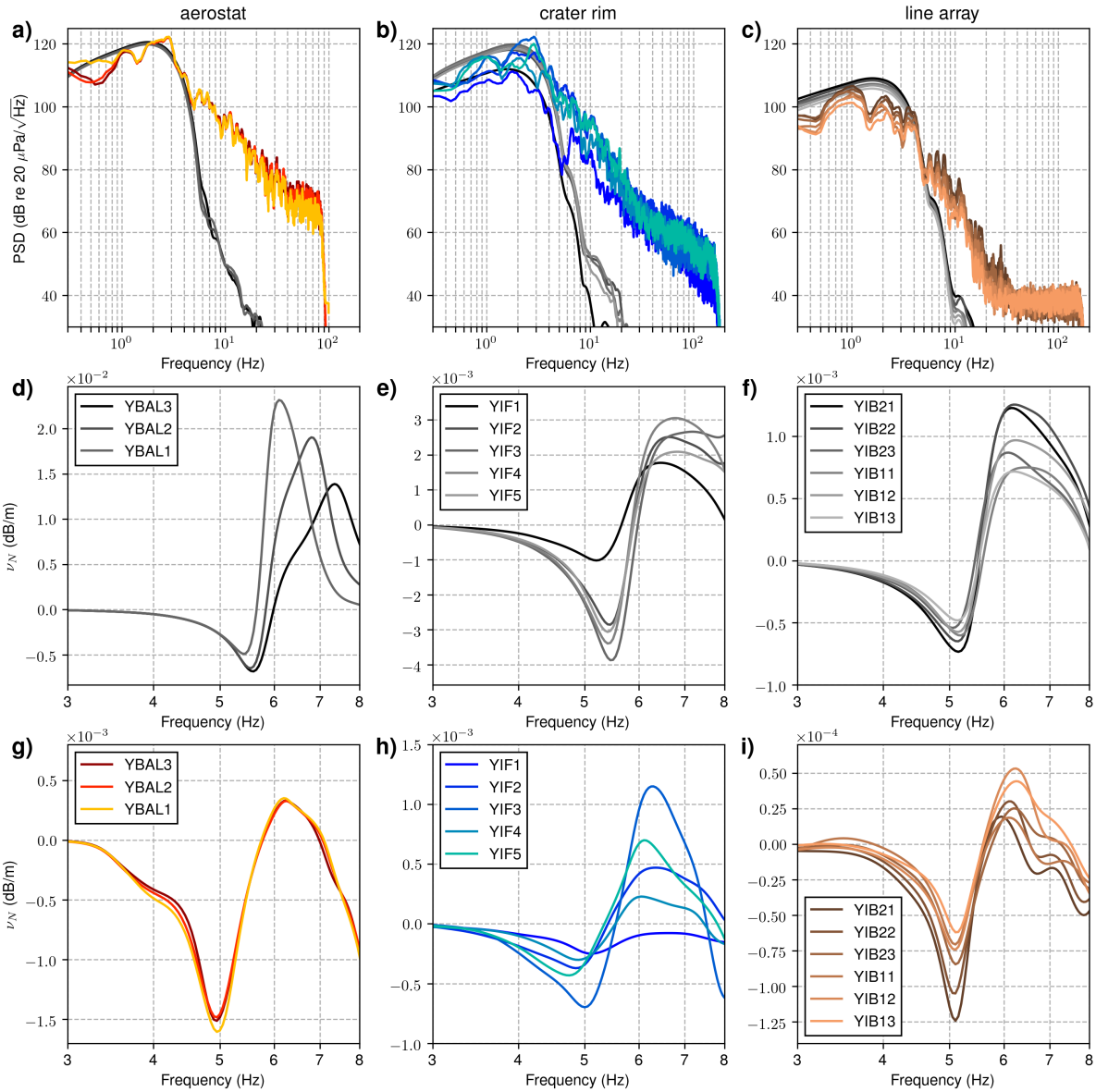

Figure 4.6: Spectra corresponding to the waveforms shown in Fig. 4.5e. a–c) PSD curves for synthetic waveforms (grayscale) and corresponding observed waveforms (color) for an event at 04:53:12.87 on August 1, 2016. Spectra are grouped by sensors at the aerostat (first column), crater rim (second column), and line array (third column). d–f) ν_N curves for synthetic signals at the aerostat, crater rim, and line array sensors, respectively. g–i) ν_N curves for observed signals at the aerostat, crater rim, and line array sensors, respectively. Note the smaller scale on the y-axis in g–i than d–f

4.7 Cumulative distortion and source volume estimation

Here we present a technique for using observed ν_N to estimate the error in source volume calculations due to nonlinear propagation effects. The principle is to estimate cumulative nonlinear distortion ($\nu_{N_{tot}}$) and use it as a correction factor for a source spectrum obtained assuming linear propagation. The source volume estimates can then be compared using the linear and nonlinear-corrected source spectra as inputs.

4.7.1 Cumulative nonlinear distortion

The first step is to use observed ν_N measurements to estimate cumulative nonlinear changes ($\nu_{N_{tot}}$) between the source and each station. Since the goal is to directly subtract $\nu_{N_{tot}}$ power spectra, ν_N must first be converted to a suitable unit. The decibel unit of ν_N is not the same as the unit used for sound-pressure levels representing power spectral density. Sound-pressure levels (L_p) are represented by Eq. 4.2, whereas ν_N represents a change in L_p with distance (Miller, 2016) in unit dB/m:

$$\nu_N = \lim_{dx\to 0} \frac{10\log_{10}(p_2^2/p_{ref}^2) - 10\log_{10}(p_1^2/p_{ref}^2)}{dx} = \lim_{dx\to 0} \frac{10\log_{10}(p_2^2/p_1^2)}{dx}, \tag{4.4}$$

where p_1 is pressure measured at distance x and p_2 is hypothetical pressure at a small distance away ($x + dx$). Solving for the derivative of squared pressure gives ν_N in the desired unit of Pa^2/m (Miller, 2016):

$$\frac{dp^2}{dx} = \lim_{dx\to 0} \frac{p_2^2 - p_1^2}{dx} = \lim_{dx\to 0} \frac{p_1^2}{dx}\left(10^{\nu_N dx/10-1}\right) = \frac{p_1^2\nu_N}{10}\ln(10)\,. \tag{4.5}$$

The converted ν_N values have units of Pa^2/m, so integration of each frequency component over the source-receiver distance will give a cumulative distortion estimate ($\nu_{N_{tot}}$) in unit Pa^2. Since the evolution of ν_N between the source and most proximal receiver is not known, an assumption must be made as to the spatial rate of change. Maher et al. (2020) assumed a constant rate such that $\nu_{N_{tot}} = \nu_N \times r$, but this is unlikely to be true because nonlinear

propagation effects should increase with amplitude toward the source. Here we assume that the rate increases toward the source by $1/r$, in proportion with pressure amplitudes for spherical spreading.

The $\nu_{N_{tot}}$ calculation process is illustrated in Fig. 4.8. Observed ν_N spectra (unit dB/m) are shown in Fig. 4.8a for a single event at stations along a single azimuth from the crater (YIF4 and YIB11–YIB23). In Fig. 4.8b, the ν_N spectra are converted to unit Pa^2/m with Eq. 4.5. In Fig. 4.8c, ν_N values are extracted at six frequency components and plotted as a function of source-receiver distance. Curves for $1/r$ decay are fit to the values at the closest station (YIF4). The observed ν_N values at the line array are less than predicted by $1/r$ decay for lower frequencies (3, 4, and 5 Hz), however, the observed values are likely lower than true due to topographic effects, as illustrated by numerical modeling in Fig. 4.7f. Integration of the $1/r$ curves for every frequency component from $r = 1$ m to each station yields the cumulative distortion spectra ($\nu_{N_{tot}}$) in Fig. 4.8d. These curves largely overlap since most of the distortion occurs in the near-source region.

4.7.2 Volume estimation

The second step is to estimate source volumes (V) from power spectra using $\nu_{N_{tot}}$(Fig. 4.8d) as a correction term for nonlinearity. Our motivation is to approximate the errors associated with the nonlinear propagation effect rather than to robustly determine source volume, which requires accounting for source directionality, atmospheric conditions, and other factors (Iezzi et al., 2019). Consequently, we use a relatively simple single-station approach to volume estimation, which assumes a monopole source and the equivalence of excess pressure to the rate of change of displaced atmosphere at the source (Lighthill, 1978). The method is based on this classic monopole assumption (e.g., Vergniolle et al., 2004; Moran et al., 2008; Johnson and Miller, 2014; Yamada et al., 2017):

$$V = \frac{2\pi r}{\rho_0} \iint_{t_1}^{t_2} [p(r,t)]\, dt^2, \tag{4.6}$$

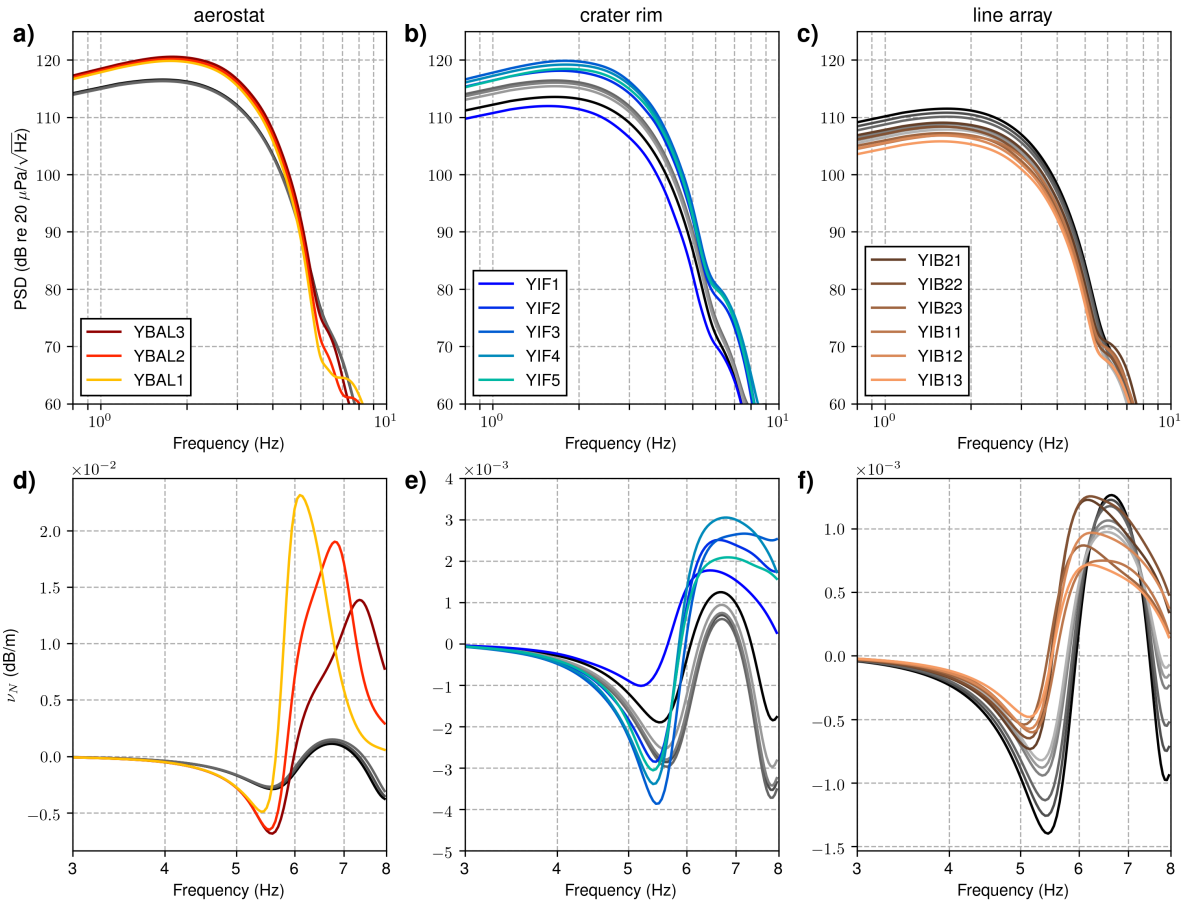

Figure 4.7: Comparison of synthetic spectra for simulations with topography (color) versus flat ground (grayscale). a–c) PSD for aerostat, crater rim, and line array sensors, from left to right respectively. d–e) ν_N for aerostat, crater rim, and line array sensors, from left to right, respectively.

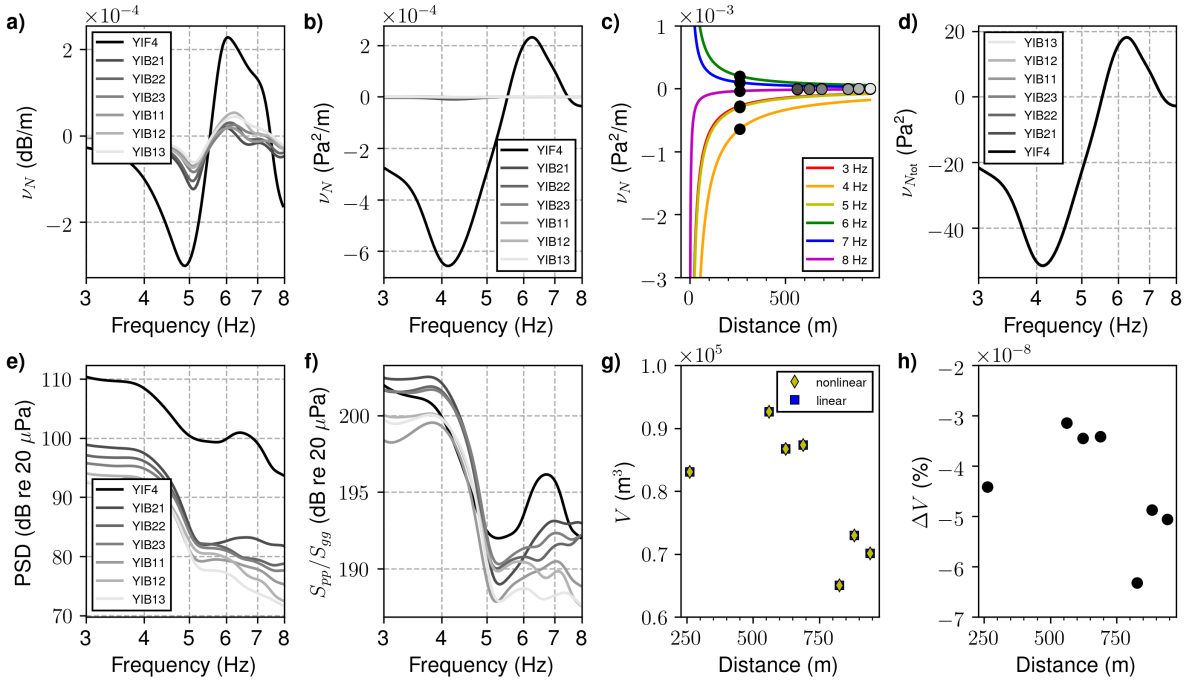

Figure 4.8: a) ν_N for the observed event at 04:53:12 on August 1, 2016. b) The same ν_N converted to units of Pa^2/m. c) ν_N values as a function of distance for six frequency components. Colored lines show $1/r$ fit to ν_N values at YIF4. d) Cumulative $\nu_N(\nu_{N_{tot}}$; unit $Pa^2)$ at each station. e) Observed power spectral densities for the event. f) Source power spectra (S_{pp} divided by the PSD of synthetic Green's function, S_{gg}). g) Source volume estimates based on linear source spectra (blue squares) and $\nu_{N_{tot}}$–corrected source spectra (yellow diamonds). h) Percentage difference in source volume estimate between linear and nonlinear source spectra.

where t_1 and t_2 are the starting and ending times of the signal. We modify Eq. 4.6 to operate in the frequency domain assuming Parseval's theorem, and we further correct the power spectra to account for topographic effects by dividing by the PSD of a synthetic Green's function:

$$V = \frac{1}{\rho_0} \iint_{\sqrt{f_1}}^{\sqrt{f_2}} \left[\frac{\sqrt{S_{pp}}}{\sqrt{S_{gg}}} \right] d\sqrt{f}, \tag{4.7}$$

where S_{pp} and S_{gg} are power spectral densities of the signal and the Green's function, respectively. Note that square roots are taken to ensure units of Pa, and the spherical spreading term in Eq. 4.6 ($2\pi r$) is implicit in the Green's function. We use Green's functions generated by linear three-dimensional (3D) finite-difference simulations as described and parametrized by Iezzi et al. (2019), which account for topography (2-m grid spacing) and a homogenous sound speed of 346.4 m/s. We normalize the Green's functions by the peak amplitude of the source function (1 Pa).

Equation 4.7 represents the volume based on linear propagation; accounting for nonlinearity takes the form:

$$V = \frac{1}{\rho_0} \iint_{\sqrt{f_1}}^{\sqrt{f_2}} \left[\frac{\sqrt{S_{pp}}}{\sqrt{S_{gg}}} - \nu_{N_{tot}} \right] d\sqrt{f}. \tag{4.8}$$

Subtraction of $\nu_{N_{tot}}$means that power lost to nonlinearity during propagation (negative ν_N) is reintroduced to the source spectra and vice versa.

The volume estimation process is illustrated in Fig. 4.8. Observed power spectra are shown in Fig. 4.8e for a single event at stations along a single azimuth from the crater (YIF4 and YIB11–YIB23). In Fig. 4.8f, the power spectra are divided by the Green's functions to give the estimated source spectra for linear propagation. Source volume estimates for linear (Eq. 4.7) and nonlinear propagation (Eq. 4.8) are shown in Fig. 4.8g. The volume estimates are reasonable (10^4 m^3) in comparison to previous results from full-waveform inversion (Iezzi et al., 2019). The percentage difference between linearly and nonlinearly estimated source volumes (ΔV) are very small (10^{-8}%) (Fig. 4.8h). Although the percentage difference is negligible, the

negative values indicate that volumes are underestimated rather than overestimated using the linear assumption, in agreement with previous work (Watson et al., 2021). We expect larger differences for signals that are higher amplitude (more nonlinear) than considered here, such as for Vulcanian or Plinian eruptions.

In Fig. 4.9, we investigate variations in ν_N, V, and ΔV with peak waveform amplitude (p_{max}) at one station (YIF4) for 2068 events on July 31st and August 1st, when explosivity increased and shifted predominantly to the south vent (Jolly et al., 2017; Iezzi et al., 2019; Fitzgerald et al., 2020; Matoza et al., 2022a). We detect these events with a simple peak-finder algorithm (Duarte and Watanabe, 2018; Matoza et al., 2022a) using a minimum event separation time of 60 s and amplitude threshold of 1 Pa. As expected, the $\nu_N$magnitudes (Fig. 4.9d) and linear volume estimates (Fig. 4.9e) increase with p_{max}. The relationships appear to be linear over the entire amplitude range (3–665 Pa), suggesting that there is not a threshold amplitude value below which nonlinear propagation effects are insignificant. The magnitudes (absolute values) of ΔV values also increase with p_{max} as expected (Fig. 4.9f), but the values are very small ($<10^{-7}$%). There are both positive and negative trends in Fig. 4.9f, but only the negative trend is expected since linearly estimated volumes are expected to be smaller than true (Maher et al., 2019; Watson et al., 2021). We interpret these results to suggest that nonlinear propagation effects are present, but they are either not accurately quantified by $\nu_N$or they do not cause a significant error (i.e., >1%) in source volume estimates.

4.8 Discussion

We applied a single-point quadspectral density nonlinearity indicator (ν_N) to waveforms primarily from 80 explosion events at Yasur Volcano recorded by 14 sensors located between ∼200 and 1080 m from the source and to synthetic waveforms generated by nonlinear wavefield modeling for one event. In both the synthetic $\nu_N$and many observational results, we observe a qualitative resemblance to the reclined S-shape previously observed for supersonic model-scale jet noise (Fig. 4.1; Miller and Gee, 2018). The feature generally occurs below 10 Hz and suggests

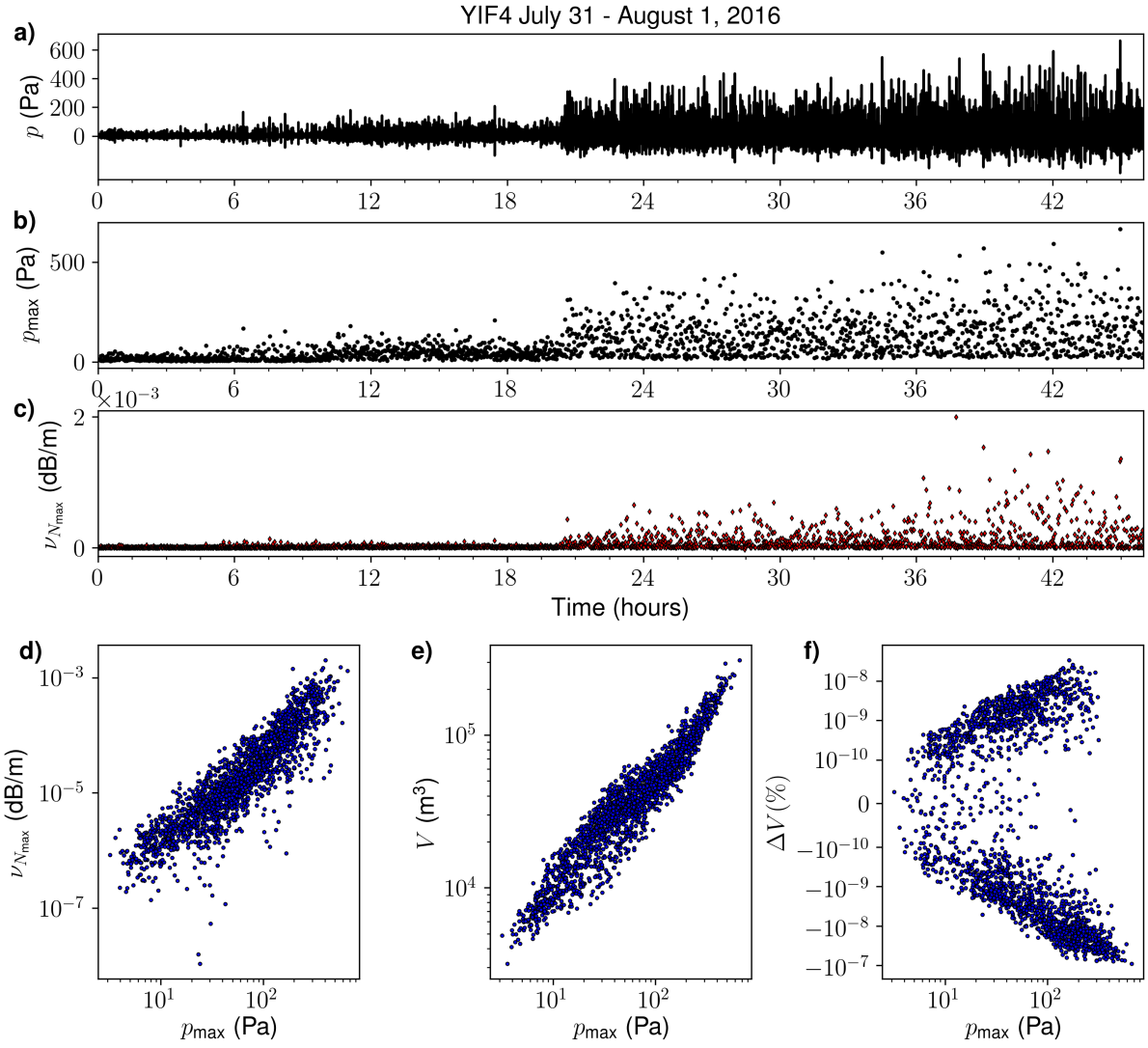

Figure 4.9: a) Waveform at YIF4 on July 31 and August 1, 2016. b) Peak amplitudes (p_{max}) of each picked event. c) Maximum ν_N values between 3 and 8 Hz for each picked event. d) Comparison of maximum ν_N with peak amplitudes. e) Comparison of linear source volume estimates with peak amplitudes. f) Percentage difference between linear and nonlinear source volume estimates as a function of peak amplitude

spectral energy transfer from lower frequencies (5–6 Hz) to higher frequencies (6–10 Hz), while results at frequencies greater than ∼10 Hz are made uncertain by high variance and low signal-to-noise ratio. The $\nu_N$magnitudes decrease with distance as expected from theory (Reichman et al., 2016a) and previous observations for frequencies of 600–40,000 Hz (Miller and Gee, 2018).

4.8.1 Comparison of observations to previous studies

The $\nu_N$indicator is a relatively new method that has been applied to only a few datasets, making our results a novel contribution but also complicating their interpretation. Reichman et al. (2016a) derived the expression from the spectral generalized Burgers equation presented by Morfey and Howell (1981). They demonstrated the predicted behavior of $\nu_N$through application to two numerical solutions to the generalized Burgers equation for an initially sinusoidal plane wave. They observed expected changes with distance in the spectral level of harmonics on the sinusoid frequency, showing that $\nu_N$quantifies spectral energy transfer in an idealized case. Miller and Gee (2018) applied $\nu_N$to jet noise signals (600–40,000 Hz) recorded over a range in distances and angles from a supersonic model-scale jet in an anechoic chamber. They found good agreement between observed $\nu_N$and theory, with a reclined S-shape and magnitudes decreasing with range (Fig. 4.1c). Finally, Maher et al. (2020) were the first to apply $\nu_N$to infrasonic frequencies, using data and synthetics corresponding to signals from eruptions at Sakurajima Volcano in Japan (0.1–10 Hz). Their results from the synthetic signals exhibited reclined S-shaped indicative of upward spectral energy transfer. However, they found inconclusive $\nu_N$results from the observed waveforms and speculated on complications related to outdoor propagation (e.g., wind, topography, ground impedance) and source dynamics (e.g., fluid flow and jet turbulence).

We find good agreement in $\nu_N$magnitudes between the Yasur Volcano observations and results from supersonic model scale jet noise at audible frequencies (Miller and Gee, 2018) and Sakurajima Volcano eruptions at infrasonic frequencies (Maher et al., 2020). For large-amplitude signals from the Yasur Volcano's south vent at YIF4, we observe $\nu_N$on the order of

10^{-3} dB/m at a distance of 261 m (Fig. 4.9d). Assuming an approximately 10 m vent diameter (D_j), our result corresponds to 10^{-2} dB/D_j at 26 D_j, which is comparable to $\nu_N$magnitudes observed by Miller and Gee (2018) at 20–30 Dj for frequencies ∼1–40 kHz (Fig. 4.1c). Maher et al. (2020) integrated Sakurajima Volcano $\nu_N$results with respect to distance, assuming a constant rate of change to obtain a cumulative estimate of total nonlinear changes ($\nu_{N_{tot}}$). They found consistent $\nu_{N_{tot}}$magnitudes of $\leq$ 2 dB in observational results and synthetics with a wide range of topography and wind conditions. For ν_N= 10^{-3} dB/m at YIF4 and 261 m to the south vent, $\nu_{N_{tot}}$= 0.261 dB. Although this value is smaller than obtained at Sakurajima Volcano, the waveform amplitudes at Yasur Volcano are also lower than at Sakurajima Volcano, so the nonlinear processes are expected to be weaker.

Marchetti et al. (2013) observed wavefront speeds of 341–403 m/s in thermal imagery and estimated Mach numbers ($Ma = u/c_0$, where u is wave velocity) of up to 1.28 using the Rankine–Hugoniot relation for fluid properties across a one-dimensional shock wave (Dewey, 2018):

$$p_0 = p_{atm}\left[1 + \frac{2\gamma}{\gamma+1}(Ma^2 - 1)\right], \tag{4.9}$$

where p_{atm} is the atmospheric pressure (10^5 Pa), $\gamma = 1.4$ is heat capacity of dry air, $p_0 = p_{atm} + p_{acu} \times r$, and p_{acu} is the observed acoustic pressure. The waveforms recorded in our experiment are higher in amplitude than those analyzed by Marchetti et al. (2013); they observed peak amplitudes of up to 106 Pa at 700 m, whereas we observe up to 665 Pa at 261 m (∼248 Pa when scaled to 700 m) (e.g., Fig. 4.9). According to Eq. 4.9, this amplitude corresponds to Mach 1.58, or a propagation speed at the source of 546 m/s assuming an ambient velocity of 346 m/s.

Marchetti et al. (2013) also showed a comparison of amplitude-normalized waveform properties to the Friedlander equation (Reed, 1977) for blast waves from chemical explosions. While the general shape of the Friedlander equation is reminiscent of Yasur explosion waveforms, appropriate scaling of the Friedlander equation for distance and amplitude is known to provide

poor fits to observed waveforms (Garces, 2019). Matoza et al. (2019a) showed that accurate scaling of the Friedlander equation results in over-prediction of source strength for a waveform at Sakurajima Volcano. The Friedlander equation was empirically derived for blast waves from the detonation of chemical high explosives, whereas volcano acoustic source processes are slower and more closely resemble boiling liquid expanding vapor explosions (Garcés et al., 2013). In contrast, the $\nu_N$indicator is based on the generalized Burgers equation, which is an analytical description of finite-amplitude wave steepening that makes no assumption of the sourcing process. The generalized Burgers equation is valid for weak nonlinearity ($|p| << \rho_0 c_0^2$) (Reichman et al., 2016a), or overpressures less than 141,265 Pa for $\rho_0 = 1.18$ kg/m^3 and $c_0 = 346$ m/s.

4.8.2 Difference between observations and synthetics

We modeled waveforms, PSDs, and ν_N spectra for a single event Yasur Volcano using a finite-difference method for nonlinear infrasound propagation (de Groot-Hedlin, 2017) and found good agreement in waveform arrival times and amplitudes (Fig. 4.5e), spectral power at dominant frequencies of 1 to 3 Hz (Fig. 4.6a–c), and $\nu_N$spectral shape in the band 3–8 Hz (Fig. 4.6d–i). However, the magnitudes of $\nu_N$are larger for the synthetics than the observations. This difference suggests stronger nonlinearity in the simulations than in the observed event, which may be related to the limitations of the modeling method. Although near-source topography may significantly modulate the acoustic wavefield (e.g., Kim and Lees, 2011; Matoza et al., 2009b), our modeling method requires that topography must be flat in the source region to maintain numerical stability (Section 4.6.1). This required us to add artificial 175 m-wide flat surfaces into the crater area of the topographic profiles for each simulation (see Figs. 4.6a–d), causing the receivers to fall further from the center of the source. We consequently used a higher maximum source pressure than expected in order to overcome the extra amplitude losses from geometrical spreading. Since the method uses a forward approach, we adjusted the source pressure to approximate the peak amplitude at the closest receiver (YBAL3). This same interpretation explains why the minima in synthetic $\nu_N$occur at frequencies ∼0.5 Hz higher

than in the observations (e.g., 5.5 Hz in Fig. 4.6e vs 5 Hz in Fig. 4.6h); stronger nonlinearity results in distortions at higher frequencies. Increased spectral energy transfer to higher frequencies at larger source pressures has been previously observed in nonlinear infrasound modeling (de Groot-Hedlin, 2012, 2016, 2017; Maher et al., 2020).

We additionally tested for the effect of topography on synthetic $\nu_N$by generating a simulation with the source and receivers on the ground at sea level. In this case, horizontal source distances were the same as in the topography simulations, and the aerostat receivers were the same height above the surface. The source pressure was kept the same to isolate the effect of topography. Figure 4.7 compares the synthetic PSD (Fig. 4.7a–c) and $\nu_N$results (Fig. 4.7d–f) for the topography simulations (color) and flat ground (grayscale). The spectral shapes and magnitudes are comparable between the simulations for the crater rim (Fig. 4.7b,e) and line array sensors (Fig. 4.7c,f), suggesting minimal complications from topography. In contrast, at the aerostat sensors, the magnitudes of PSD (Fig. 4.7a) and ν_N(Fig. 4.7d) are lower for the flat ground simulation than the topography simulation. This result may reflect the influence of acoustic focusing: in the topography case, multiple reflections up the crater wall constructively interfere to increase pressure at the aerostat. In the case of a flat lower boundary, the ground reflection does not constructively interfere with the wavefront at the aerostat location, resulting in lower amplitudes.

Finally, we note 3D wavefield interactions with topography outside the source-receiver plane may introduce differences between synthetics and observations. The FDTD method used here operates in a 2D source-receiver plane with axisymmetry about the left boundary (de Groot-Hedlin, 2017), so topographic complexity outside the plane is not accounted for. Infrasound simulations at Yasur Volcano using 3D finite differences suggest that full wavefield effects may be significant (Iezzi et al., 2019; Fee et al., 2021); however, those methods assume linear propagation and do not currently allow for investigation of nonlinear propagation effects. Maher et al. (2021) compared the effects of topography on simulated waveforms for Sakurajima Volcano using a linear version of the FDTD method used here (de Groot-Hedlin, 2016) and the 3D Cartesian

FDTD method developed by Kim and Lees (2014) and later used by Iezzi et al. (2019) and Fee et al. (2021). Maher et al. (2021) found that synthetic amplitudes were more strongly reduced by topographic effects (diffraction, scattering) in the 2D axisymmetric method than in the 3D Cartesian method, but both methods yielded similar relative amplitude distributions across an azimuthally distributed network with varying topography. From this, we conclude that the simulations with Yasur Volcano topography may feature stronger topographic attenuation than true; however, we also ran simulations with flat ground that produced similar $\nu_N$results at the crater rim and line array stations (Fig. 4.7e,f). A FDTD method that incorporates both 3D topography and nonlinear propagation is desirable but outside the scope of the present work.

4.8.3 Limitations of the $\nu_N$method

Although our $\nu_N$results show strong evidence for nonlinear propagation in higher-amplitude Yasur Volcano signals, several challenges remain in using the method as a quantitative indicator.

Firstly, our assessment of a clear result is made on the basis of qualitative comparison to previous results from supersonic jet noise that is known to propagate nonlinearly (Fig. 4.1 Miller and Gee, 2018). A more quantitative assessment of result quality is desired, but the construction of such a method is outside the scope of this study.

Secondly, we observe clear $\nu_N$signatures in the band 3–9 Hz (e.g., Fig. 4.4) but find high variance results at higher frequencies that do not accurately quantify nonlinear energy transfer ($\sim$10 Hz to $Fs/4$; Fig. 4.3g–i). In this study, we introduced a spectral signal-to-noise threshold that screens $\nu_N$at some higher frequencies (e.g., >40 Hz in Fig. 4.3i) but does not completely eliminate the $\nu_N$results that are presumed spurious. Further work is needed to adapt $\nu_N$to infrasound and determine appropriate frequency bounds in the presence of outdoor noise sources, which were not an issue for previous studies by Reichman et al. (2016a) and Miller and Gee (2018).

Finally, we note that the use of power spectral density is not ideal for discrete explosions since the assumption of signal stationarity in the Fourier transform is not met. For Yasur

Volcano, the explosion signals are only a few seconds in duration, but PSD estimation requires longer time windows (10^1 s) to ensure accuracy at low frequencies. Several seconds of ambient noise must therefore be included in the windows, leading to underestimation of spectral power when values are averaged across signal and noise. Additionally, the asymmetric nature of the waveforms results in non-zero signal means, which translates to spectral leakage and spurious non-zero power at low frequencies. Despite these limitations, PSD estimates are commonly used in volcano infrasound studies, and it is required for the $\nu_N$method as currently formulated (Eq. 4.3). Future work should consider the use of energy spectral density (e.g., Haskell, 1964; Kanamori and Anderson, 1975; Garces, 2013) or wavelet transforms (e.g., Lees and Ruiz, 2008; Cannata et al., 2013; Lapins et al., 2020), which are better suited to impulsive and non-stationary signals.

4.9 Conclusions

We investigated infrasound signals from Strombolian explosion events at Yasur Volcano using a single-point frequency-domain indicator of nonlinear propagation (ν_N; Reichman et al., 2016a). We hypothesized that the $\nu_N$method would quantify spectral energy transfer associated with nonlinear wavefield changes at infrasonic frequencies (0.1–20 Hz) similar to what was previously observed in experiments with supersonic model-scale jet noise at audible frequencies (600–40,000 Hz) (Miller and Gee, 2018). Our $\nu_N$results for the larger amplitude events ($\sim 10^2$ Pa at 200–300 m) resemble those of the jet noise study both in relative spectral character (the reclined S-shape around 3–9 Hz) and in magnitude (10^{-2} dB/D_j at 20–30 D_j). The clarity of the $\nu_N$signature increases with peak waveform amplitude, consistent with expectations of stronger nonlinearity at higher pressures. We interpret these results as evidence for nonlinear acoustic propagation whereby wave steepening causes spectral energy transfer from frequency components at 3–6 Hz to higher frequencies (6–8 Hz).

We further performed finite-difference simulations of nonlinear infrasound propagation (de Groot-Hedlin, 2017) to model waveforms, power spectra, and $\nu_N$results for a representative Yasur Vol-

cano event. Despite limitations in the model, we observe similar $\nu_N$spectral shapes in synthetics in the band 3–8 Hz, corroborating the nonlinearity quantified in the observations. Challenges remain in accurately accounting for both topography and nonlinearity in finite-difference simulations.

Our results confirm previous interpretations of nonlinear propagation at Yasur Volcano on the basis of asymmetric waveforms (Marchetti et al., 2013). We also extend the work of Maher et al. (2020), who observed clear $\nu_N$signatures for synthetics but not observations at Sakurajima Volcano by showing these $\nu_N$spectral shapes for both observations and synthetics at Yasur Volcano. This suggests that infrasound- based source parameter estimates based on linear propagation at Yasur Volcano and other volcanoes may give inaccurate results, e.g., underestimation of erupted volume (Maher et al., 2019; Watson et al., 2021). We made preliminary calculations of $<1\%$ error in source volume estimates using a simple single-station monopole approach, which suggests that source parameter estimates for these data are not greatly affected by nonlinear propagation effects. However, larger errors are expected for more explosive eruption styles at other volcanoes (e.g., Vulcanian and Plinian eruptions), and future work is needed to fully account for nonlinear processes in source parameter estimation.

4.10 Acknowledgements

We thank Anna Perttu, Matthew Haney, an anonymous reviewer, and editors Sylvie Vergniolle and Andrew Harris for their help in improving this manuscript. The Vanuatu Meteorological and Geohazards department provided field and hazard monitoring support during the field campaign. We thank Janvion Cevuard, Atahana Worwor, Julius Mala (VMGD), and Richard Johnson (GNS Science) for field support and Esline Garaebiti and Sandrine Cevuard for volcano monitoring. Any use of trade, firm, or product names is for descriptive purposes only and does not imply endorsement by the U.S. Government.

4.11 Funding

Matoza acknowledges support by National Science Foundation (NSF) grants EAR-1620576 and EAR-1847736. Fee acknowledges support from NSF grant EAR-1901614. Iezzi acknowledges support from NSF grant EAR-1952392.

4.12 Data availability

The Yasur Volcano infrasound data are available through the IRIS Data Management Center under temporary network code 3E (10.7914/SN/3E_2016).

4.13 Code availability

We used the Python libraries NiTime (nipy.org/nitime) for multitaper power spectral estimation, ObsPy (Beyreuther et al., 2010) for data handling, and statsmodels (statsmodels.org) for LOWESS smoothing. Any use of trade, firm, or product names is for descriptive purposes only and does not imply endorsement by the U.S. Government.

Chapter 5

General conclusions

Prior to the present work, methods to identify and model nonlinear propagation effects in volcanic infrasound were limited (Garcés et al., 2013; Matoza et al., 2019a). Nonlinear effects had been hypothesized to explain asymmetric waveforms (e.g., Morrissey et al., 2008; Marchetti et al., 2013; Fee et al., 2013a; Goto et al., 2014) and supersonic wavefront speeds (Ishihara, 1985; Yokoo and Ishihara, 2007; Marchetti et al., 2013). Nonlinear acoustic propagation had also been investigated in shock tube experiments (Medici et al., 2014; Médici and Waite, 2016) and numerical simulations (e.g., de Groot-Hedlin, 2012, 2016; Sabatini et al., 2016a,b) (for more on previous work, please see Sections 1.1.2 and 1.3.2). However, nonlinear effects had not been quantified in observed data. Similarly, the applicability of screen diffraction to volcano infrasound had been introduced (Lacanna and Ripepe, 2013), but had not been validated either for infrasonic frequencies or volcano topography. The research presented in these chapters makes progress towards developing methods to quantify the effects of nonlinear propagation and losses by diffraction directly from observational data gathered during field deployments. These efforts complement ongoing work by other research groups to more accurately account for infrasound wavefield changes during propagation (e.g., Dragoni and Santoro, 2020; Watson et al., 2021; Fee et al., 2020; Ishii et al., 2020; Bishop et al., 2022).

In Chapter 3 we investigated the applicability of a thin screen approximation to predicting

amplitude losses by diffraction of infrasound over volcano topography. In contrast to Ishii et al. (2020), who promote the screen approximation as an improvement over a geometrical spreading correction alone, we find that loss predictions based on thin screens are significantly greater than observed in numerical simulations with Sakurajima topography. We conclude that constructive interference of reflections along concave slopes may counteract the losses from diffraction, pointing to the importance of full wavefield effects in modulating volcano acoustic signals. Numerical modeling of wavefield propagation therefore remains the most effective method of accounting for topographic effects, although future work could consider acoustic focusing effects instead of diffraction alone.

In Chapters 2 and 4 we investigated nonlinear propagation of infrasound from low-level explosive activity at two volcanoes. We were the first to apply a recently-developed spectral indicator of nonlinear propagation (ν_N; Reichman et al., 2016a) to infrasonic wavelengths and to volcano infrasound data in particular. We initially expected to see stronger evidence for nonlinearity at Sakurajima Volcano where acoustic amplitudes are higher ($\sim$1,033 kPa at 1 m reference distance) than at Yasur Volcano ($\sim$174 kPa at 1 m reference distance). However, we instead saw stronger evidence for nonlinearity at Yasur, suggesting that nonlinear propagation occurs at both volcanoes but is better captured at short source-receiver distances with minimal topography and higher sampling rate values. At Yasur we estimated that the error in source volume estimates due to neglecting nonlinear effects is very small ($<< 1\%$), suggesting that spectral changes due to nonlinear propagation are not a significant source of distortion at the amplitudes of Strombolian-style explosions.

It is important to note that the explosions analyzed in Chapters 2 and 4 represent the type of repetitive activity commonly observed in geophysical field campaigns, but they are relatively small in comparison to less frequent but more violent eruptions that produce higher-amplitude infrasound (e.g., the January 2022 eruption of Hunga volcano; Matoza et al., 2022b). Nonlinear propagation effects may be more significant for these larger-amplitude waves, but are currently more difficult to quantify due to a lack of local instrumentation with high sampling rates. As

the availability of high-quality data continues to increase, future work may find evidence for stronger nonlinear distortions from more explosive eruption styles than studied here.

Finally, it is important to note that Chapters 2 and 4 focus on nonlinear processes occuring during acoustic propagation, but nonlinear effects may also occur in the source region. The properties of sound are commonly assumed to be linearly related to the rate and volume of displaced air at the source (e.g., Lighthill, 1978; Woulff and McGetchin, 1976; Vergniolle and Caplan-Auerbach, 2006; Caplan-Auerbach et al., 2010), but complications from phenomena in the source region such as heat, multi-phase particle interactions, advection and fluid flow (e.g., vortex rings; Taddeucci et al., 2021; Watson et al., 2021) may violate this assumption. Waveform characteristics such as compression-rarefaction asymmetry and positive skewness could be due to nonlinearity either during propagation or at the source (Fee et al., 2013a; Anderson et al., 2018b; Matoza et al., 2018). Further work is needed to determine the relative significance of nonlinear processes in the source region and during propagation.

Chapter 6

Future work

The most significant limitation throughout this work has been fitting observed waveforms with synthetic data from numerical modeling of nonlinear propagation. We ran simulations using a method developed by de Groot-Hedlin (2017), however, this method is limited by its fixed spatially-distributed source function and by its 2D axisymmetric geometry. This method was useful for examining nonlinear propagation effects but often did not accurately model the asymmetric nature of observed volcano acoustic waveforms. Future work should aim to develop a propagation model incorporating nonlinear propagation, 3D topography and a point source with modular source-time function (Fee et al., 2020). Such a model could be used to interogate outstanding questions such as the difference in waveform fits between linear and nonlinear propagation, errors in source parameter estimates due to nonlinearity, and thresholds in amplitude and receiver proximity above which nonlinearity is signifcant.

Another avenue for future work involves the assessment and interpretation of ν_N results. In our work we made qualitative comparisons between results for volcano acoustic signals and previous results for model-scale jet noise, specifically looking for the reclined S-shape seen in work by Miller and Gee (2018). It would be desirable to have a quantitative measure of ν_N quality that could be used to assess the performance of the indicator on signals within the same dataset or between datasets. Initial work toward this goal could include nonlinear curve

fitting of the reclined S-shape that is scalable in magnitude and frequency, analagous to work by Gestrich et al. (2021) for fitting jet noise similarity spectra.

Another direction for future work is the development of a rapid method for approximating the influence of topography on acoustic waveform properties. In Chapter 3 we established that 3D wavefield effects such as acoustic focusing may counteract diffraction, suggesting that the empirical relationship between Fresnel number and insertion loss for thin screens (Maekawa, 1968) is not appropriate for volcano infrasound. Future work should consider additional variables beyond the Fresnel number in acccounting for the effects of topography, such a measure of slope concavity or topographic roughness (e.g., Stambaugh and Guyette, 2008).

Appendix A

Appendix of Chapter 2

A.1 Derivation and Integration of Nonlinear Propagation Equation

The following discussion summarizes derivations by Morfey and Howell (1981) and Reichman et al. (2016a) of a quadspectral density-based nonlinearity indicator. Derivation of the Generalized Burgers Equation (GBE) from the 1-D plane wave equation is primarily summarized from Hamilton and Morfey (2008).

Acoustic waves are pressure disturbances to the ambient state of a material with properties governed by the fundamental conservations of mass, momentum, entropy and thermodynamic state. The propagation of a pressure disturbance p in one dimension can be written:

$$\frac{\partial^2 p}{\partial x^2} - \frac{1}{c^2}\frac{\partial^2 p}{\partial t^2} = 0, \tag{A.1}$$

where p is travelling in the x direction with sound speed c over time t (Pierce, 1981). This second-order partial differential equation describes linear plane wave propagation in the absence of dispersion and losses to the medium.

A second-order approximation can be made by substituting the first two terms of the Taylor series expansion of the pressure-density relationship ($\frac{p}{p_0} = (\frac{\rho}{\rho_0})^\gamma$, where γ is the ratio of specific

heats) into the equations of continuity, momentum, and state, and by neglecting Lagrangian density ($\mathcal{L} = \frac{1}{2}\rho_0 u^2 - \frac{p^2}{2\rho_0 c_0^2}$), which is equal to zero for plane progressive waves (Hamilton and Morfey, 2008). For one dimensional propagation in the x direction this gives the Westervelt equation:

$$\frac{\partial^2 p}{\partial x^2} - \frac{1}{c_0^2}\frac{\partial^2 p}{\partial t^2} + \frac{\delta}{c_0^4}\frac{\partial^3 p}{\partial t^3} = -\frac{\beta}{\rho_0 c_0^4}\frac{\partial^2 p^2}{\partial t^2}, \tag{A.2}$$

where δ is a thermoviscous coefficient describing sound diffusion in air, $\delta = \frac{1}{\rho_0}\left(\frac{4}{3}\mu + \mu_B\right) + \frac{\kappa}{\rho_0}\left(c_v^{-1} - c_p^{-1}\right)$ where ρ_0 is ambient density, μ is shear viscosity, μ_B is bulk viscosity, κ is thermal conductivity, c_v is isochoric specific heat and c_p is isobaric specific heat, and β is a nondimensional dispersion (nonlinearity) coefficient in air (Hamilton and Morfey, 2008). The nonlinearity coefficient β is an intrinsic quantity to the medium that characterizes the effect of finite-amplitude wave propagation on sound speed (Hamilton and Morfey, 2008). The relationship to sound speed can be written as $c = c_0\left(1 + \frac{\beta p}{\rho_0 c_0^2}\right)$, such that larger values of β and p result in larger increases in speed (Hamilton and Morfey, 2008). In air, $\beta \approx 1.2$ and can be written as a function of the ratio of specific heats, $\beta = \frac{1}{2}(\gamma + 1)$, where $\gamma = c_p/c_v$ (Hamilton and Morfey, 2008).

Simplification of the Westervelt equation into one dimension (a forward-propagating plane wave) and a retarded time scale ($\tau = t - x/c_0$) yields the Burgers equation:

$$\frac{\partial p}{\partial x} - \frac{\delta}{2c_0^3}\frac{\partial^2 p}{\partial \tau^2} = \frac{\beta p}{\rho_0 c_0^3}\frac{\partial p}{\partial \tau}, \tag{A.3}$$

which predicts waveforms as a function of distance and time for plane wave propagation with nonlinear effects and diffusion in a thermoviscous medium. Generalization of the Burgers equation to spherical and cylindrical waves is acheived by addition of a geometrical spreading term:

$$\frac{\partial p}{\partial r} + \frac{m}{r}p - \frac{\delta}{2c_0^3}\frac{\partial^2 p}{\partial \tau^2} = \frac{\beta p}{\rho_0 c_0^3}\frac{\partial p}{\partial \tau}, \tag{A.4}$$

where r is now source-receiver distance and $m = 0$, 0.5 or 1 for planar, cylindrical, or spherical

waves, respectively. Equation A.4 is the Generalized Burgers Equation. Transformation of the GBE into the frequency domain gives:

$$\frac{\partial \tilde{p}}{\partial r} + \frac{m}{r}\tilde{p} + \frac{\omega^2 \delta}{2c_0^3}\tilde{p} = \frac{i}{2}\frac{\beta}{\rho_0 c_0^3}\omega \tilde{q}, \tag{A.5}$$

where $\tilde{p}$ and $\tilde{q}$ are the complex Fourier transforms of $p(\tau)$ and $p^2(\tau)$, respectively (Morfey and Howell, 1981). Multiplication of Equation A.5 by r^m, simplification, and substitution of $\omega^2\delta/2c_o^3$ for α' (a combination of dispersion and linear attenuation coefficients, where the linear absorption coefficient of sound is $\alpha = Re\{\alpha'\}$) yields:

$$\left(\frac{\partial}{\partial r} + \alpha'\right)(r^m \tilde{p}) = \frac{i}{2}\frac{\beta\omega}{\rho_0 c_0^3} r^m \tilde{q}, \tag{A.6}$$

which is equivalent to Equation 3 of Morfey and Howell (1981) and Equation 5 of Reichman et al. (2016a). Equation A.6 is valid for sound of moderate intensity ($\leq$165 dB=3557 Pa) recorded in the far field ($r > \lambda$) with weak attenuation and dispersion ($|\alpha'| \ll \omega/c$) and weak nonlinearity (Morfey and Howell, 1981). Furthermore, Equation A.6 is deterministic in that it can ostensibly be used to predict spectra rather than to statistically describe spectral changes from a single measurement. The statistical form is derived by multiplying Equation A.6 through by r and by the complex conjugate of $\tilde{p}$, then ensemble averaging the real part to give:

$$\frac{\partial}{\partial r}\left(r^{2m} e^{2\alpha r} S_{pp}\right) = -\frac{\beta\omega}{\rho_0 c_0^3} r^{2m} e^{2\alpha r} Q_{pp^2}, \tag{A.7}$$

where S_{pp} is the autospectral density of p and Q_{pp^2} is the quadspectrum of p and p^2, which is the imaginary part of the cross-spectral density between p and p^2:

$$Q_{pp^2} = \mathrm{Im}\left\{E\left[\mathcal{F}^*\left\{p(t)\right\}\mathcal{F}\left\{p^2(t)\right\}\right]\right\} \tag{A.8}$$

where E indicates the expectation value, $\mathcal{F}$ denotes a Fourier transform, and * denotes a complex conjugate (Miller and Gee, 2018).

The term on the left-hand side of Equation A.7 represents the spatial rate of change in the power spectral density of a spreading wave, and should be equal to zero if the propagation is linear because the spectrum is corrected for geometrical spreading and absorption. Nonlinear propagation effects are represented by non-zero values of the right-hand side of this equation. The nonlinearity coefficient β describes the intrinsic nonlinear property of the medium (change in sound speed due to finite-amplitude effects). Q_{pp^2} describes phase coupling between p and p^2 during spectral energy transfer to higher harmonics. Phase coupling arises from the summing and differencing of frequency components as a wave steepens and spectral energy is transferred between frequencies (Kim and Powers, 1979). The quadspectrum highlights phase-coupled frequencies because individual harmonic components of p^2 can be mathematically represented as a sum of the products between all individual pair-wise harmonics of p; the phase information of the Fourier-transformed cross-covariance function of p and p^2 consequently peaks in absolute value when harmonics are phase-coupled (Gagnon, 2011).

Equation A.7 gives a qualitative indication of which frequencies gain and lose energy during nonlinear propagation, but it does not give quantitative estimates of the amount of power transfer. To make the Morfey and Howell (1981) formulation more quantitative, Reichman et al. (2016a) manipulate Equation A.7 to give the spatial rate of change in spectral level, $\frac{\partial L_p}{\partial r}$, where L_p is the spectral level in an arbitrary frequency band ($L_p = 10\log_{10}(p_i^2/p_{ref}^2)$, where p_i is pressure in an arbitrary frequency band and p_{ref} is a reference pressure, typically 20 μPa). They start by expanding the derivative on the left-hand side of Equation A.7 using the product rule, dividing by $r^{2m}e^{2\alpha r}S_{pp}$, and moving terms to give

$$\frac{1}{S_{pp}}\frac{\partial S_{pp}}{\partial r} = -\frac{2m}{r} - 2\alpha - \frac{\omega\beta p_{rms}}{\rho_0 c_0^3}\frac{Q}{S}, \tag{A.9}$$

where p_{rms} is root-mean-squared pressure and Q/S is the normalized quadspectrum ($Q/S = Q_{pp^2}/S_{pp}p_{rms}$). A property of logarithms is then employed to consolidate the S_{pp} terms into the spatial derivative:

$$\frac{1}{S_{pp}}\frac{\partial S_{pp}}{\partial r} = \frac{\partial}{\partial r}\{\ln(S_{pp})\} = \frac{\partial}{\partial r}\left\{\frac{\log_{10}(S_{pp})}{\log_{10}(e)}\right\}, \tag{A.10}$$

where e is Euler's number ($e \approx 2.71828$). The autospectral density of p is replaced using the identity $L_p = 10\log_{10}(p^2/p_{ref}^2) = 10\log_{10}(S_{pp}/p_{ref}^2)$:

$$\frac{\partial}{\partial r}\left\{\frac{\log_{10}(S_{pp})}{\log_{10}(e)}\right\} = \frac{\partial}{\partial r}\left\{\frac{1}{\log_{10}(e)}\left(\frac{L_p}{10} + 2\log_{10}(p_{ref})\right)\right\}, \tag{A.11}$$

Substituting Equation A.11 into Equation A.9, neglecting the p_{ref} term since it cancels upon differentiation, moving the e term, and cancelling the p_{rms} terms gives the desired result:

$$\frac{\partial L_p}{\partial r} = -10\log_{10}(e)\left(\frac{2m}{r} + 2\alpha + \frac{\omega\beta}{\rho_0 c_0^3}\frac{Q_{pp^2}}{S_{pp}}\right), \tag{A.12}$$

which is the equation used in this study. This equations assumes that linear spectral changes can be fully described by ν_S and ν_α, neglecting potentially significant effects such as reflections from topography and refraction in temperature gradients. Spectral contributions from these processes are inaccurately treated by ν_N as a consequence of nonlinear acoustic propagation. The ability of ν_N to accurately describe nonlinear effects consequently depends on the complexity of the signal. Furthermore, while the equation was developed for analysis of acoustic signals of audible frequency (20-20,000 Hz), its basis in the Burgers equation dictates that it should be valid for any wave that steepens during propagation due to finite-amplitude effects. Nonlinear steepening of infrasonic waves is a well-established phenomenon at volcanoes (Lonzaga et al., 2015; Matoza et al., 2019a), so we consider the application of Equation 2.1 to Sakurajima data appropriate.

In this study we integrate Equation A.12 with respect to distance to estimate the cumulative distortion effects over the source-receiver paths. This integration is performed as:

$$
\begin{aligned}
L_p &= -10\log_{10}(e)\int_1^r \left(\frac{2m}{r} + 2\alpha + \frac{\omega\beta}{\rho_0 c_0^3}\frac{Q_{pp^2}}{S_{pp}}\right) dr \\
&= -10\log_{10}(e)\left(2m\ln(r) + 2\alpha r + r\frac{\omega\beta}{\rho_0 c_0^3}\frac{Q_{pp^2}}{S_{pp}}\right) + C \\
&= -10\log_{10}(e)\left(2m\ln(r) + 2\alpha r + r\frac{\omega\beta}{\rho_0 c_0^3}\frac{Q_{pp^2}}{S_{pp}}\right) + L_{p_1} \\
&\equiv \nu_{S_{tot}} + \nu_{\alpha_{tot}} + \nu_{N_{tot}} + L_{p_1}, \\
&\equiv \nu_{tot},
\end{aligned}
\tag{A.13}
$$

where the constant of integration C is equal to the level at 1 m from the source (L_{p_1}). For infrasonic wavelengths on the order of tens to hundreds of meters we assume that wavefield propagation changes including absorption, geometrical spreading and spectral energy transfer are negligibly small between the source ($r = 0$) and $r = 1$ m. The subscript *tot* indicates total (cumulative) effects. The individual components of ν_{tot} correspond to the elements of the equation as per Equation 2.1. Integration assumes a constant rate of spectral change, when in fact the rate of change varies within the nonlinear propagation regime (Miller and Gee, 2018). Since Sakurajima stations are several kilometers from the source, observed $\nu_{N_{tot}}$ likely underestimates the total spectral changes.

In this study, $\nu_{N_{tot}}$ is estimated assuming an ambient sound speed of 349 m/s, ambient density of 1.225 kg/m^3, and a nonlinearity coefficient of 1.201. ν_S is estimated assuming spherical spreading since the wavelength of the dominant frequency (∼873 m for 0.4 Hz) is significant relative to the receiver distances (∼37% of the closest receiver distance). ν_α is estimated using the equations of Sutherland and Bass (2004) assuming average relative humidity (80%) and average temperature (28.5°C) for Kagoshima City in July. This approach accounts for absorption due to molecular translation, rotation, vibrational relaxation of O_2 and N_2, and diffusion. We calculate the vibrational component using the equations of Bass et al. (1984), which is justified under the assumption that normalized relaxing specific heat $<< 1$ for temperatures near sea level (Sutherland and Bass, 2004).

Appendix B

Comparing performance of quadspectral density and bicoherence indicators for nonlinear acoustic propagation across ten volcano infrasound datasets

B.1 Introduction

In this study we aim to assess the performance of the quadspectral density indicator through application to multiple (10) volcano acoustic datasets representing different eruption styles, instrumentation, and source-receiver geometries. To corroborate the results of ν_N we further introduce the bicoherence indicator $b^2(f_1, f_2)$ which qualitatively reflects the cumulative impact of nonlinear phase coupling on the signal (Kim and Powers, 1979; Gee et al., 2010). We hypothesize that significant nonlinearity will be expressed as values of ν_N and $b^2(f_1, f_2$ that are larger for signals than for noise at a given station, and accurate quantification by ν_N

will be expressed as a reclined S-shape. Conversely, linear propagation would be expressed as comparable values between results from signals and noise at each station, and a lack of a reclined S-shape in the ν_N spectra. In cases where ν_N results are ambiguous, but bicoherence is high, the propagation is hypothesized to be nonlinear but inaccurately quantified by ν_N.

B.2 Nonlinearity Indicators

B.2.1 ν_N

For detailed descriptions of the ν_N indicator please see Chapter 2, Chapter 4 and Appendix A.

Figures B.1a and B.1b show examples of ν_N results for tests cases of continuous signal types representing nonlinear and linear propagation, respectively. Figure B.1a reproduces results from Miller and Gee (2018), in which supersonic jet noise was recorded in an anechoic chamber at multiple recording distances from the source (distances shown in terms of jet diameter, D_j = 0.035 m). The nonlinearitity is evidenced by relatively large ν_N values (10^0 dB) and reclined S-shapes in the ν_N spectra that reflect upward spectral energy transfer (Figure B.1a-iii). To compare these results with linear propagation of a continuous signal, we generated white noise time series by random sampling from normal distributions with the same means and standard deviations as the supersonic jet noise (Figure B.1b). In these cases, the ν_N spectra do not exhibit reclined S-shapes, and the magnitudes of the ν_N values are smaller (10^{-1} dB). The bicoherence results shown in this figure are discussed in Section B.2.2.

We validate the use of ν_N for impulsive signal types by application to nonlinearly- and linearly-propagated example signals in Figures B.1c and B.1d, respectively. Figure B.1c shows results for a shock wave generated by an exploding oxyacetlyne balloon recorded at 76.2 m distance and 0.9 m height above the ground (data from Young et al. (2015)). As expected, ν_N exhibits a reclined S-shape indicative of nonlinear spectral energy transfer from frequency components near the roll-off in the PSD (200–1,000 Hz) to higher frequencies (>1,500 Hz). In

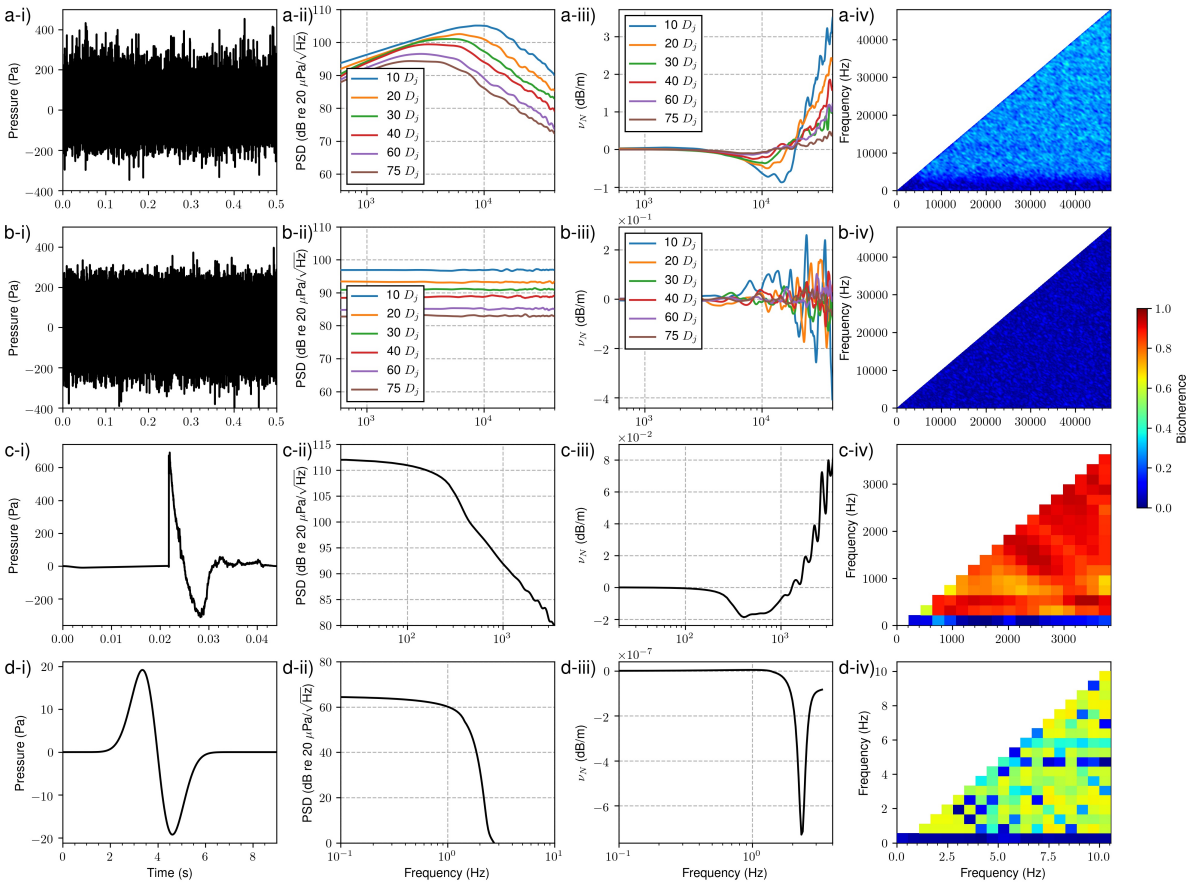

Figure B.1: Comparison of time- and frequency-domain features of signals from a) indoor experiments with supersonic model scale jet noise from Miller and Gee (2018), b) numerically-generated Gaussian white noise, c) outdoor recording of exploding oxyacetelyne ballon from Young et al. (2015), d) numerical modeling of linearly-propagated Gaussian pulse using code by de Groot-Hedlin (2016). i) Waveforms, ii) Power spectral densities, iii) ν_N results, iv) bicoherence matrices.

contrast, Figure B.1d shows a synthetic waveform generated by numerical modeling with linear propagation (from Maher et al. (2021)). The ν_N values are much smaller (10^{-7} dB/m) than for the shock wave from the exploding balloon (10^{-2} dB/m), and the reclined S-shape is absent. These cases illustrate that the ν_N indicator can behave as expected for both continuous and impulsive signal types with linear and nonlinear propagation. However, it should be noted that ν_N values may generally be smaller for impulsive signal types than for continuous signal types with comparable nonlinearity (e.g., Figure B.1a-iii and Figure B.1c-iii).

B.2.2 Bicoherence

While ν_N quantifies the rate of change of spectral energy at a single point due to nonlinearity, it does not indicate the relationships between coupled frequency components or the cumulative spectral changes due to nonlinearity. Furthermore, ν_N is subject to the limitations of the generalized Burger's equation, which assume far-field recording distances and weak nonlinearity. In contrast, the bicoherence spectrum makes no assumptions about propagation physics and instead indicates the degree of coupling between frequency components due to cumulative nonlinear processes.

Bicoherence is a normalized form of bispectral density, which is a complex-valued third order spectra that has been used to analyze quadratic nonlinearity in a variety of physical processes including acoustic waves (Gee et al., 2010), plasma fluctuations (Kim and Powers, 1979), and ocean waves (Hasselmann et al., 1963). Bispectral density (S_{ppp}) is the convolution of three Fourier transforms, $P(f)$, of the input signal: one for the seperate but identical frequency vectors f_1 and f_2, and one for the sum of these frequency vectors ($f_1 + f_2$). The bispectrum can be written:

$$S_{ppp}(f_1, f_2) = \lim_{T\to\inf}(1/T)\,\langle P(f_1)P(f_2)P^*(f_1+f_2)\rangle\,, \tag{B.1}$$

where T is period and * denotes a complex conjugate. Since frequencies are added together in $P^*(f_1+f_2)$, frequencies above Nyquist are introduced, and bispectral analysis is therefore valid

only at frequencies below $Fs/4$. It may be noted here that the terminology can be confusing because the bispectrum involves the multiplication of three spectra rather than two. In contrast, the "quadspectrum" used in ν_N (Appendix A) involves only two spectra. The quadspectrum is also known as the quadrature spectrum and is used to identify quadratic phase coupling arising by nonlinear interactions between frequency components.

To isolate the nonlinear phase coupling reflected in the resulting spectrum, the bispectrum is often normalized to yield the bicoherence (Gee et al., 2010):

$$b^2(f_1, f_2) = \frac{|S_{ppp}(f_1, f_2)|^2}{Z(f_1, f_2) S_{pp}(f_1 + f_2)}, \tag{B.2}$$

where

$$S_{pp}(f_1 + f_2) = \lim_{T \to \inf}(1/T) \left\langle P(f_1 + f_2) P^*(f_1 + f_2) \right\rangle, \tag{B.3}$$

and

$$Z(f_1, f_2) = \lim_{T \to \inf}(1/T) \left\langle |P(f_1) P^*(f_2)|^2 \right\rangle. \tag{B.4}$$

The bicoherence spectrum (Equation B.2) is a 2-D matrix of values bounded between 0 and 1 that represents the proportion of energy shared between frequency components in f_1 and f_2 due to quadratic phase coupling during nonlinear propagation. Theoretically, a bicoherence value of 1 means that 100% of the energy present at the frequency pair is due to nonlinear propagation effects. In practice, however, nonlinear propagation of the broadband signals created by jets and explosions will have cascading sum- and difference-frequency generation that make it impossible to isolate the relationships between individual frequency components. The bicoherence spectrum can therefore be considered a qualitative indication of the cumulative nonlinearity in the signal, with higher values indicating stronger nonlinearity.

Figures B.1a-iv and B.1b-iv show examples of bicoherence results for tests cases of continuous signal types representing nonlinear and linear propagation, respectively. Figure B.1a-iv

shows the result for supersonic model-scale jet noise recorded a distance of 75 D_j, with relatively homogenous bicoherence values of 0.2–0.4 at frequencies above ∼5,000 Hz. These values are above the 99% confidence threshold for significant bicoherence (0.02), for a waveform with this sample rate and duration (Elgar and Guza, 1988). In contrast, Figure B.1b-iv shows bicoherence values of <0.1 for a numerically-generated white noise signal with the same sample rate, mean amplitude and standard deviation.

In Figure B.1c-iv and B.1d-iv we investigate the behavior of bicoherence for tests cases of impulsive signal types representing nonlinear and linear propagation, respectively. The bicoherence values for the nonlinearly propagated waveform (Figure B.1c-iv) are larger than for the linearly propagated waveform (Figure B.1d-iv), but the values overall are much larger than for the continuous signal types shown in Figures B.1a-iv and B.1b-iv. The 99% confidence thresholds for significant bicoherence are 0.26 and 0.13 for Figures B.1c-iv and B.1d-iv, respectively. These results suggest that bicoherence values may be inherently larger for impulsive signal types than for continuous signals, so care must be taken when comparing results between different events.

B.3 Datasets

In this study we aim to assess the performance of ν_N and $b(f_1, f_2)$ through application to multiple (ten) volcano acoustic datasets representing different eruption styles and source-receiver geometries. Table B.1 summarizes the receivers and signals for each volcano. We do not analyze every event at every station for each dataset; we choose representative events and stations for comparative purposes. In general we use the five highest-amplitude signals from each dataset but manually screen for time windows with only one main event. In some cases (Villarrica and Yasur) the events are so closely spaced that extra smaller signals may be included in some windows and these may potentially compromise the spectral indicators. When distributed multi-element arrays are available we analyze beamforms rather than each individual waveform. Further details on each dataset are provided in Sections B.3.1–B.3.10.

Table B.1: Fs = sampling rate, B = beamform, PJ = Plinian jetting, SPJ = Subplinian jetting, VE = Vulcanian explosion, LLR = lava lake roiling, SE = Strombolian explosion

Volcano	Receivers	Ranges (km)	Fs (Hz)	Signals	Style
Augustine	AUE	3.2	100	1	VE
Calbuco	GO07	216	40	5	SPJ
Cotopaxi	CIS (B)	8.3	100	5	SE
Nabro	IS19 (B)	264	20	5	PJ
Popocatepetl	ATLI (B)	15.8	200	5	VE
Reventador	MC2	1.4	100	5	VE
Sakurajima	KUR	3.5	200	5	VE
Tungurahua	LOW 02	3.2	100	1	VE
Villarrica	VID (B)	6.4	100	5	LLR
Yasur	YIB21	0.6	400	5	SE

B.3.1 Augustine

We use one high-amplitude waveform (100 Pa at 3.2 km) from a large Vulcanian eruption on January 11, 2006 as recorded at AUE (100 Hz sample rate). Details are provided by Petersen et al. (2006).

B.3.2 Calbuco

We use one trace from single-channel station GO07 (216 km range, 40 Hz sample rate). We picked the five highest-amplitude signals from bandpass filtered data (0.5–9 Hz) during the period 2015/04/22T19:00:00 - 2015/04/23T13:03:19. Nonlinearity in this signal was previously postulated by Matoza et al. (2018).

B.3.3 Cotopaxi

We use a beamform of six-element array data at 8.3 km range with 100 Hz sample rate. For each of the 89 tornillo signals identified by Johnson et al. (2018a) we perform a gridsearch over a range of backazimuths and apparent velocities to determine the p_{rms} of the resulting beamform. We then select the five best signals for which the p_{rms} grid maximum is close to the backazimuth of 142° and the apparent velocity of 0.328 km/s that were used by Johnson et al. (2018a)

B.3.4 Nabro

We use a beamform of array data from IS19, 264 km range from Nabro, with 20 Hz sample rate. We used a backazimuth of 321° and an apparent velocity of 0.38 km/s as determined by grid search for maximum p_{rms} of the beam. We pick the five highest-amplitude signals from highpass filtered beam at 0.1 Hz during June 13, 2011, from 00:00:00 to 06:00:00 UTC, when coherent signals with Nabro backazimuth were consistently detected by Fee et al. (2013a).

B.3.5 Popocatepetl

We use a beamform of data from a four-element array (ATLI) at 15.8 km range with 200 Hz sample rate. The beams are provided in the supplementary material of Matoza et al. (2019b) and correspond to a backazimuth of 283.7° and an apparent velocity of 0.35 km/s. We analyze signals from five events in November 2017 (Matoza et al., 2019b).

B.3.6 Reventador

We focus on the five highest-amplitude signals from January 2015 to June 2019 as recorded by a single sensor at 1.4 km with 100 Hz sample rate. Data are by Ortiz et al. (2021).

B.3.7 Sakurajima

We use data from one station (KUR) with 200 Hz sample rate and 3.487 km range during a 2013 temporary deployment (Fee et al., 2014). We focus on five highest-amplitude signals out of the 30 events with highest signal-noise ratios as determined in Maher et al. (2020). For detailed analysis of ν_N behavior at all five stations in the deployment see Maher et al. (2020).

B.3.8 Tungurahua

We focus on a single Vulcanian explosion signal on July 14, 2013, with exceptionally high amplitude (1,192 Pa at 1.86 km). The deployment included two-three element arrays, HIGH 1–3 and LOW 1–3, but all signals at HIGH are contaminated by electrical glitches, and signals

at LOW 1 and LOW 2 clipped (Anderson et al., 2018b). We therefore analyze the signal at LOW 2, with 3.16 km range and 100 Hz sample rate.

B.3.9 Villarrica

We use continuous data for the six days leading up to a paroxysm on March 3, 2015 (Johnson et al., 2018b). We focus on the five-highest amplitude signals picked from highpass-filtered beamform at 0.5 Hz using data from the closest array. We analyze beamforms from one three-element array (VID) with 100 Hz sample rate at 6.4 km range. For beamforming we use a backazimuth of 146° and an apparent velocity of 0.340 km/s as determined by grid search for maximum p_{rms}. We don't use VIC array (4 km range) because we couldn't get a good beamform (stations are oriented in a line perpendicular to the backazimuth, so high uncertainty in apparent velocity)

B.3.10 Yasur

We manually inspected the 100 highest-amplitude events that occured during the 2016 deployment described by Jolly et al. (2017) and Matoza et al. (2017b), and chose the five best windows that were dominated by a single event. Due to the high rate of volcanic activity, some of these windows contain additional smaller events. For this analysis we use a single sensor (YIF4) at a distance of roughly 260 m from the vent in the south crater. The sample rate is 400 Hz. For detailed analysis of ν_N behavior at all sensors in the deployment see Maher et al. (2022).

B.4 Signal Processing

In order to compare results across multiple datasets with differing instrumentation and sample rates, we aim to regularize the signal processing. We resample every waveform to 400 samples per second with a bivariate spline method and choose 40 second windows centered on the peak pressure. We detrend the series, subtract the mean and apply a 20% Tukey taper.

We also zero pad to 80 seconds to improve spectral resolution. We calculate power spectra (S_{pp}) and quadspectra (Q_{pp^2}) using a multitaper method (Riedel and Sidorenko, 1995), and we smooth these spectra with a locally weighted least squares method (0.9% smoothing factor). We repeat these methods for 40 second noise windows at each station in order to estimate a signal to noise (SNR) ratio in the frequency domain. We divide signal power spectra by noise power spectra (unit Pa^2/Hz) and do not consider ν_N at frequencies where SNR is less than a threshold.

Bicoherence is estimated using a periodogram method with ensemble averaging of windows with 512 samples and 50% overlap, as per best practices recommended by Gee et al. (2010).

When distributed multi-element arrays are available we analyze beamforms rather than each individual waveform. When beamforming, care must be taken to ensure proper choices of backazimuth and apparent velocity, otherwise distortions may be introduced by improper alignment of individual traces. For each array we perform a grid search over apparent velocity and backazimuth and select the pair that maximizes the p_{rms} of the resulting beam (improperly aligned traces destructively interfere to reduce p_{rms}).

B.5 Results

Figures B.2 and B.3 show results for one example signal at each volcano. In the PSD plots (second column) the PSD of the signal is shown in black and the PSD of a noise window is shown in blue. In the ν_N plots (third column) the spectra are grey where the SNR<8, and the maximum ν_N frequency shown is $Fs/4$. Observations and interpretation for each volcano are listed below:

- Augustine: Moderate nonlinearity accurately quantified by ν_N and corroborated by b. The waveform is asymmetric, ν_N has the reclined S-shape with magnitude 10^{-4} dB/m at frequencies 0.2–4 Hz, and bicoherence has large values at frequencies 1–10 Hz. David Fee has noted that there was a problem frequencies greater than about 10 Hz (difficulties with a wind reduction system I think).

- Calbuco: The shape of ν_N is ambiguous and the ν_N magnitude is small (10^{-7} dB/m), but bicoherence suggests nonlinearity at frequencies >1 Hz. The signal is a peak in jet noise recorded at 216 km, so phases may be contaminated by multipathed arrivals. The analysis may also suffer from undersampling (Fs=40 Hz).

- Cotopaxi: The propagation is expected to be linear as the amplitudes are small (<1 Pa at 8 km). Values of ν_N and bicoherence are small, reflecting the linearity.

- Nabro: Evidence for nonlinearity is seen in the reclined S-shape of ν_N and moderate bicoherence values at frequencies of 1–5 Hz. However, ν_N values are very small (10^{-7} dB/m), reflecting weak nonlinearity or a "preserved" nonlinear signature in linear propagation conditions.

- Popocatepetl: Nonlinearity is expected due to high amplitude (60 Pa at 16 km) but ν_N shape is ambiguous. Bicoherence suggests nonlinearity at 1–10 Hz.

- Reventador: Nonlinearity is expected due to high amplitude (300 Pa at 1.4 km) but ν_N shape is ambiguous. ν_N magnitudes are high though (10^{-3} dB/m) and bicoherence suggests nonlinearity at 1–25 Hz.

- Sakurajima: Nonlinearity is expected due to high amplitude (200 Pa at 3.5 km) but ν_N shape is ambiguous. ν_N magnitudes are high though (10^{-3} dB/m) and bicoherence suggests nonlinearity at 1–25 Hz. Topography may be an issue (Maher et al., 2020).

- Tungurahua: Strong nonlinearity is expected due to exceptionally high amplitude (600 Pa at 3.2 km) but ν_N shape is ambiguous. ν_N magnitudes are high though (10^{-3} dB/m) and bicoherence suggests nonlinearity at 2–25 Hz. Source complexity may be an issue as the initial compression has multiple steps instead of a single shock (Anderson et al., 2018b).

- Villarrica: Nonlinearity suggested by ν_N shape and bicoherence even though waveform amplitudes not that large (6 Pa at 6.4 km). Potential issues with additional smaller events and long-period noise in the window.

- Yasur: Weak to moderate nonlinearity suggested by ν_N shape and bicoherence at frequencies <10 Hz. Potential issues with additional smaller events and continuous noise/degassing in the window.

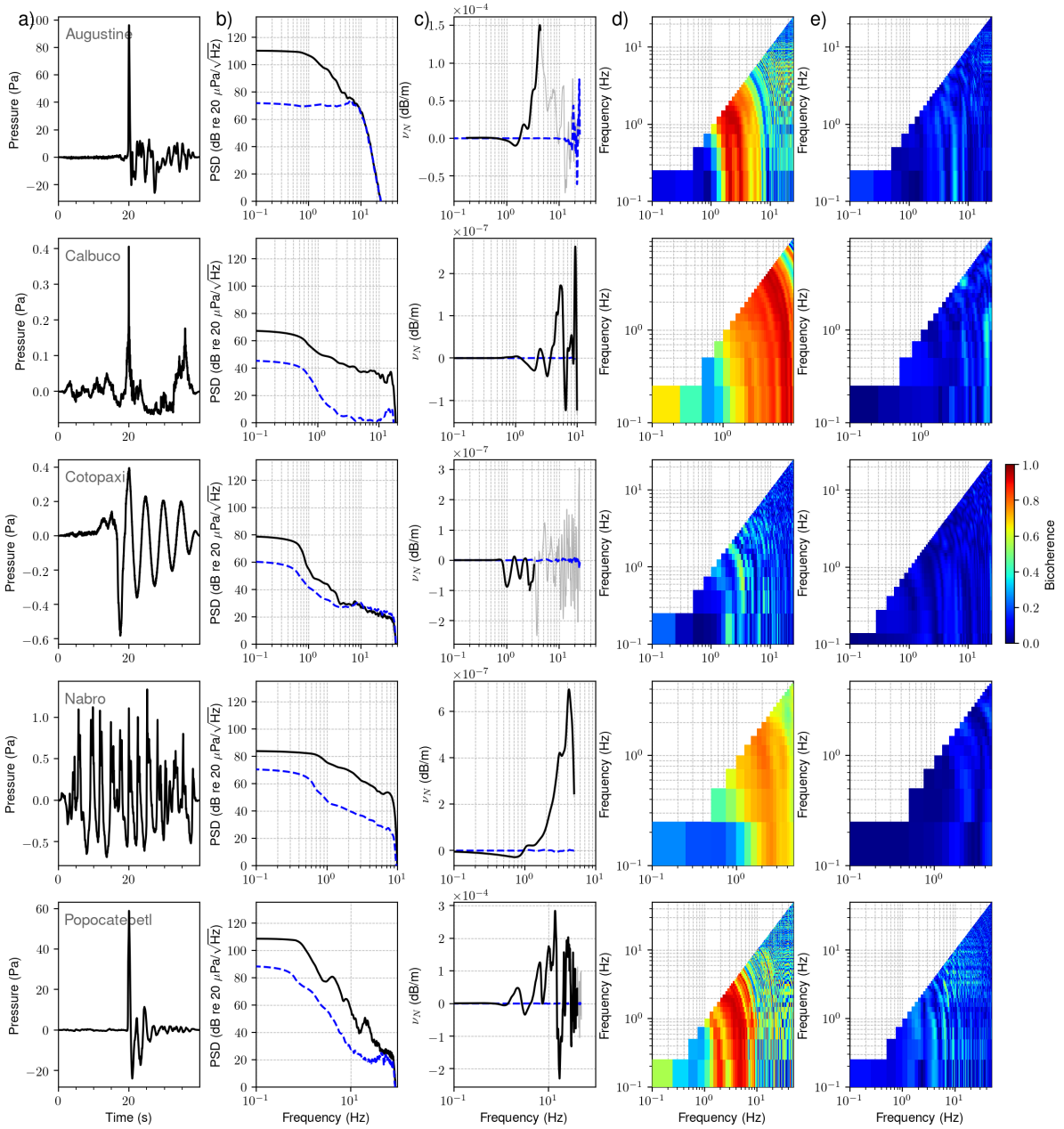

Figure B.2: a) Waveforms, b) power spectra, c) ν_N spectra and d) bicoherence matrices for one signal from each volcano. e) Bicoherence matrix for a noise window at that volcano. Each row represents a different volcano as indicated by grey text in a). Blue dashed lines show results for ambient noise windows and light grey lines show ν_N where SNR<8.

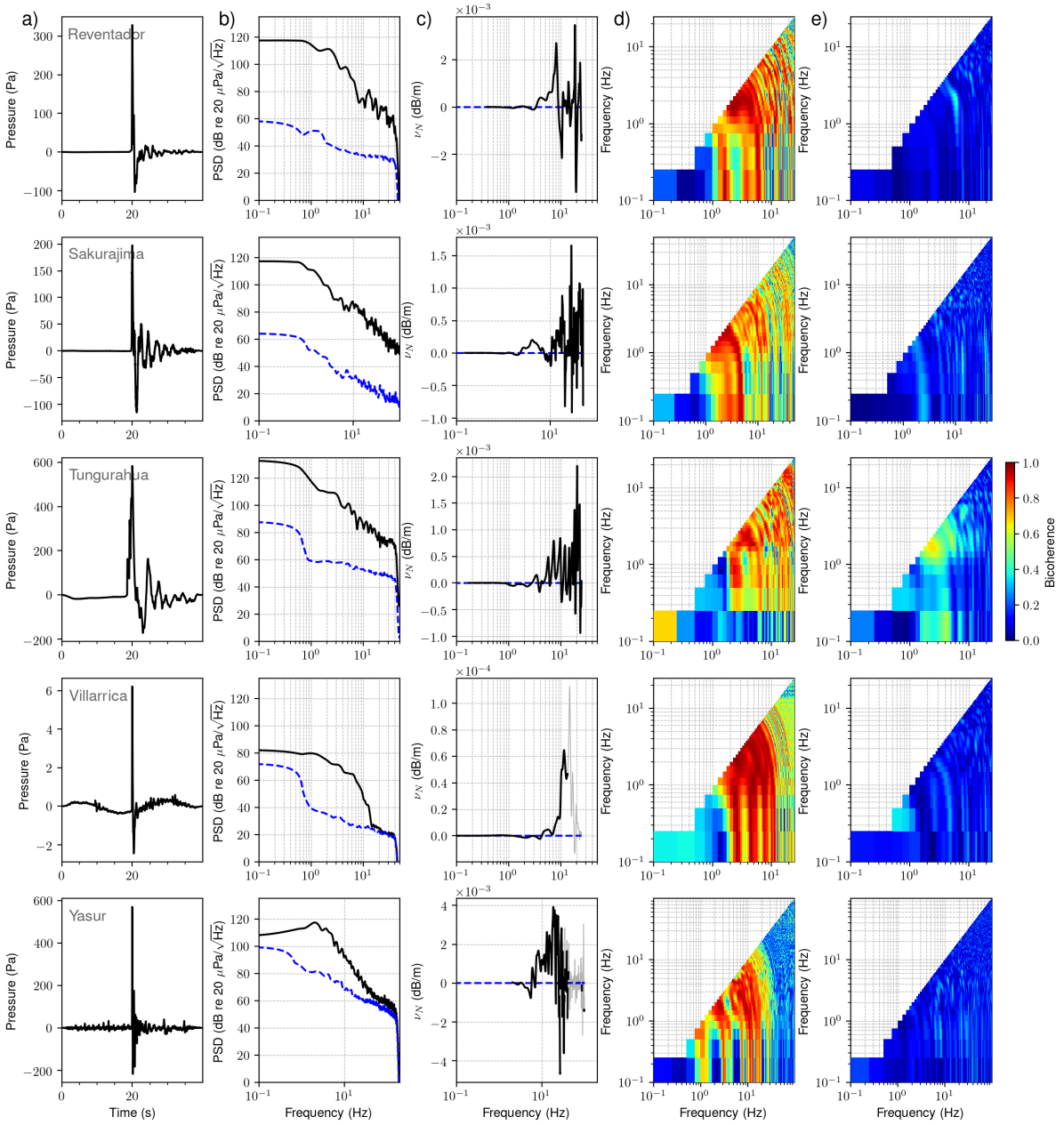

Figure B.3: Continuation of Figure B.2.

B.6 Metrics comparison

While qualitative insights can be gained by assessing the results in Figures B.2 and B.3, a quantitative comparison is desirable. Previous work at Sakurajima attempted to extract metrics such as the values and frequencies of maximum and minimum ν_N, and to compare those with properties such as the centroid PSD frequency and peak signal pressure (Maher et al., 2020). However, it did not work very well due to difficulties with topography. At Yasur, shorter source-receiver distances and minimal topography enable metrics extraction with more reliable results. Figure B.4 shows how the metrics behave for ∼2000 events at Yasur as recorded at seven stations with different distances along a single azimuth. Observations and discussion for each metric are listed below:

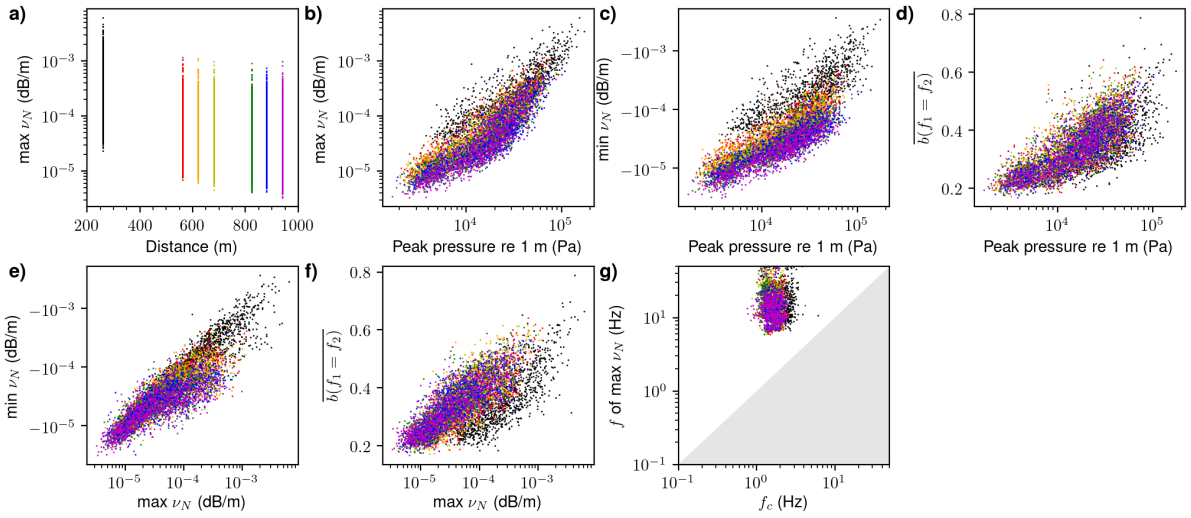

Figure B.4: Signal properties and nonlinearity indicator metrics for 2000+ signals from Yasur at seven receivers. a) Maximum ν_N as a function of distance. b) Maximum ν_N, c) minimum ν_N, and d) mean of the diagonal of the bicoherence matrix $\left(\overline{b(f_1 = f_2)}\right)$ as a function of peak pressure scaled to 1 m by spherical spreading. e) Minimum ν_N and f) $\overline{b(f_1 = f_2)}$ as a function of maximum ν_N. g) Comparison of PSD centroid frequency (f_c) with the frequency of maximum ν_N. Grey shaded region denotes frequencies where results are not expected (f_c greater than frequency of maximum ν_N).

B.4a) Maximum ν_N magnitudes generally decrease with receiver distance, as expected, since nonlinear propagation effects reduce with reducing amplitude by spherical spreading.

There is wide variability at each station because the 2000+ signals vary in amplitude from 10^0 Pa to 10^2 Pa.

B.4b) Maximum ν_N magnitudes generally increase with scaled peak pressure as expected, since nonlinear propagation effects increase with amplitude. Peak pressures at each receiver are scaled to a distance of 1 m assuming spherical spreading.

B.4c) Minimum ν_N magnitudes increase with scaled peak pressure as expected. Note that the y-axis is reversed to show increase in magnitude of negative values.

B.4d) Bicoherence values increase with scaled peak pressure as expected. The bicoherence value is represented by the mean of the diagonal of the bicoherence matrix $\left(\overline{b(f_1 = f_2)}\right)$. There seems to be an increase in slope around 10^4 Pa, possibly suggesting a threshold for significance of nonlinearity and/or bicoherence.

B.4e) The magnitudes of minimum and magnitude ν_N are linearly correlated as expected.

B.4f) Bicoherence values increase with maximum ν_N magnitude, suggesting that both indicators reflect nonlinearity.

B.4g) The frequency of maximum ν_N is almost always higher than the centroid frequency of the PSD (f_c), as expected, since wave steepening results in upward spectral energy transfer.

The Yasur results (Figure B.4) demonstrate the expected behavior of ν_N metrics. When the metrics are extracted for each of the datasets in the comparison study, the results are less straight forward (Figure B.5). Discussion of each of the subplots is listed below:

B.5a) Maximum ν_N magnitudes generally decrease with receiver distance, as expected, but Cotopaxi is an outlier since the propagation is linear.

B.5b) Maximum ν_N magnitudes generally increase with scaled peak pressure as expected, but Calbuco and Nabro are outliers with lower ν_N than expected. The receivers for Calbuco and Nabro are more remote than the other volcanoes (200+ km), so raypaths likely

included stratospheric/thermospheric propagation over a longer distance than predicted by simple geometrical spreading.

B.5c) Minimum ν_N magnitudes generally increase with scaled peak pressure as expected, but Calbuco and Nabro are outliers with lower ν_N magnitude than expected.

B.5d) Poor correlation between bicoherence and peak pressure. Calbuco and Villarrica have larger bicoherence values than expected while Popocatepetl has lower bicoherence than expected.

B.5e) The magnitudes of minimum and magnitude ν_N are linearly correlated as expected.

B.5f) Poor correlation between bicoherence and ν_N magnitude. Calbuco, Villarrica and Nabro have larger bicoherence values than expected.

B.5g) The frequency of maximum ν_N is generally higher than the centroid frequency of the PSD (f_c), as expected, since wave steepening results in upward spectral energy transfer. Some results from Villarrica, Nabro and Calbuco do not follow the trend.

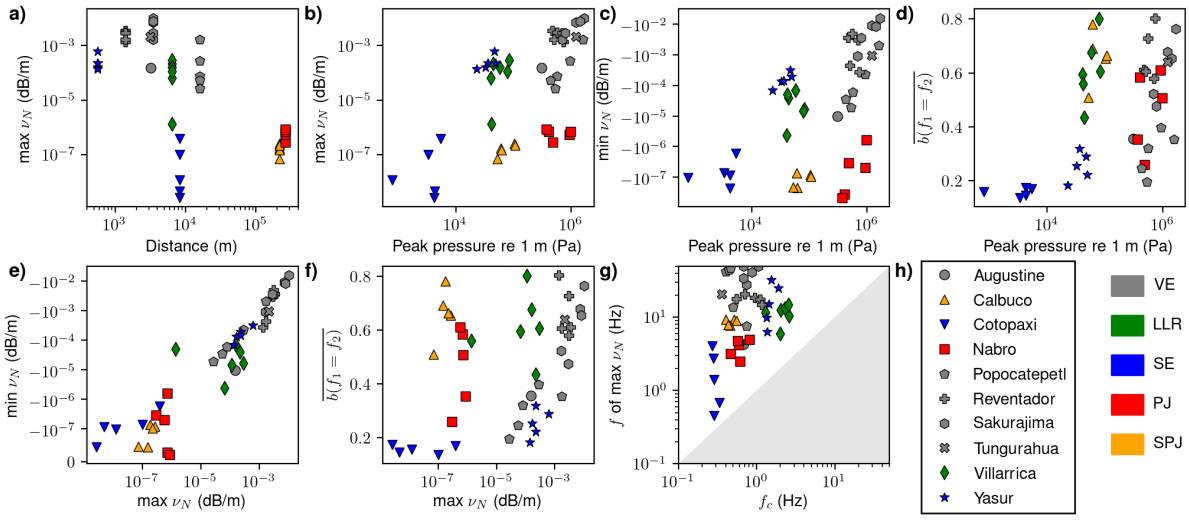

Figure B.5: a-g) metrics as per Figure B.5, but extracted from signals from each dataset. Markers represent different volcanoes and colors represent eruption style. VE = Vulcanian Explosion, LLR = Lava Lake Roiling, SE = Strombolian Explosion, PJ = Plinian Jetting, SPJ = Subplinian Jetting.

B.7 Influence of sample rate

In Figure B.6 we compare results of ν_N and bicoherence for different sampling rates on a single signal at Yasur Volcano recorded at sensor YIB21 on 4:54:02, 8/1/2015. The original sampling rate is 400 Hz, and the signal has been decimated 200, 100, 40 and 20 Hz for demonstration. The ν_N results for the original sampling rate feature a reclined S-shape indicative of nonlinear spectral energy transfer at frequencies between $\sim$3 and 8 Hz. As the sampling rate is reduced, the signature becomes more and more difficult to identify. These results suggest that high sampling rates are needed where possible to resolve nonlinear features with ν_N.

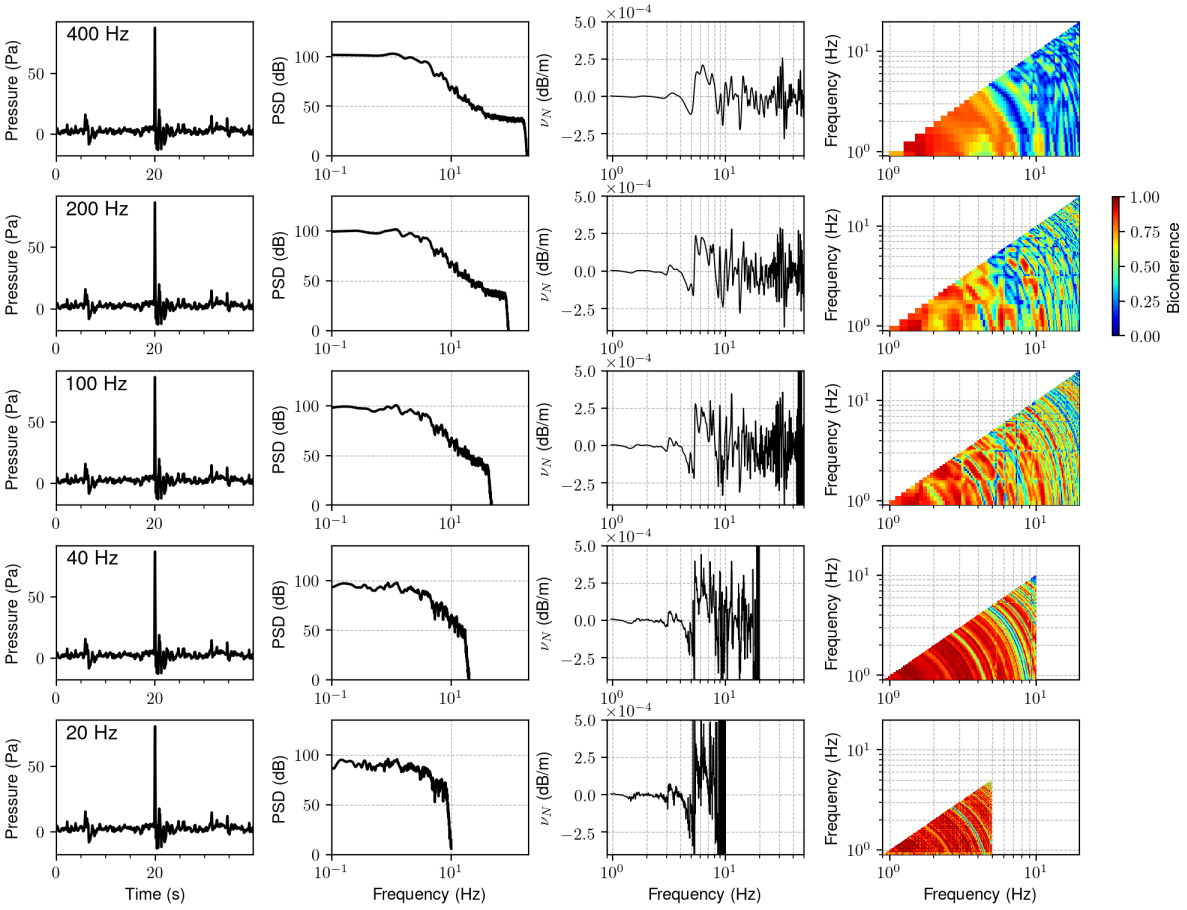

Figure B.6: Test of sample rate on ability to recover nonlinearity features in ν_N and bicoherence for an explosion signal at Yasur. Each row shows results for the same signal but at different sampling rates acheived by decimation. The sampling rate is indicated in the first column of each row. The first column shows the waveforms, second column shows power spectra, third column shows ν_N results and fourth column shows bicoherence.

Bibliography

Aizawa, K., Cimarelli, C., Alatorre-Ibargüengoitia, M.A., Yokoo, A., Dingwell, D.B., Iguchi, M., 2016. Physical properties of volcanic lightning: Constraints from magnetotelluric and video observations at Sakurajima volcano, Japan. Earth and Planetary Science Letters 444, 45–55. doi:10.1016/j.epsl.2016.03.024.

Allstadt, K.E., Matoza, R.S., Lockhart, A.B., Moran, S.C., Caplan-Auerbach, J., Haney, M.M., Thelen, W.A., Malone, S.D., 2018. Seismic and acoustic signatures of surficial mass movements at volcanoes. Journal of Volcanology and Geothermal Research 364, 76–106. doi:10.1016/j.jvolgeores.2018.09.007.

Anderson, J.F., Johnson, J.B., Bowman, D.C., Ronan, T.J., 2018a. The Gem Infrasound Logger and Custom-Built Instrumentation. Seismological Research Letters 89, 153–164. doi:10.1785/0220170067.

Anderson, J.F., Johnson, J.B., Steele, A.L., Ruiz, M.C., Brand, B.D., 2018b. Diverse Eruptive Activity Revealed by Acoustic and Electromagnetic Observations of the 14 July 2013 Intense Vulcanian Eruption of Tungurahua Volcano, Ecuador. Geophysical Research Letters 45, 2976–2985. doi:10.1002/2017GL076419.

Aramaki, S., 1984. Formation of the Aira caldera, Southern Kyushu, ˜22,000 Years Ago. Journal of Geophysical Research 89, 8485–8501. doi:10.1029/JB089iB10p08485.

Assink, J.D., Waxler, R., Drob, D., 2012. On the sensitivity of infrasonic traveltimes in the

equatorial region to the atmospheric tides. Journal of Geophysical Research Atmospheres 117, 1–14. doi:10.1029/2011JD016107.

Atchley, A.A., 2005. Not your ordinary sound experience: a nonlinear-acoustics primer. Acoustics Today 1, 19–24. doi:10.1121/1.2961122.

Bacon, C.R., 1983. Eruptive history of Mount Mazama and Crater Lake Caldera, Cascade Range, U.S.A. Journal of Volcanology and Geothermal Research 18, 57–115. doi:10.1016/0377-0273(83)90004-5.

Bass, H.E., 1991. Atmospheric Acoustics, in: Encyclopedia of Applied Physics. VCH, New York, pp. 145–179.

Bass, H.E., Sutherland, L.C., Piercy, J., Evans, L., 1984. Absorption of Sound by the Atmosphere, in: Physical Acoustics Volume XVII. Academic Press, Orlando, Florida. chapter 3, pp. 145–232.

Battaglia, J., Métaxian, J.P., Garaebiti, E., 2016. Short term precursors of Strombolian explosions at Yasur volcano (Vanuatu). Geophysical Research Letters 43, 1960–1965. doi:10.1002/2016GL067823.

Baxter, P.J., Horwell, C.J., 2015. Impacts of Eruptions on Human Health. Second edi ed., Elsevier Inc. doi:10.1016/b978-0-12-385938-9.00060-2.

Ben-Dor, G., 2007. Shock Wave Reflection Phenomena. Second ed., Springer.

Berenger, J.P., 1994. A Perfectly Matched Layer for the Absorption of Electromagnetic Waves. Journal of Computational Physics 114, 185–200. doi:10.1006/jcph.1994.1159.

Beyreuther, M., Barsch, R., Krischer, L., Megies, T., Behr, Y., Wassermann, J., 2010. ObsPy: A Python Toolbox for Seismology. Seismological Research Letters 81, 530–533. URL: http://srl.geoscienceworld.org/cgi/doi/10.1785/gssrl.81.3.530, doi:10.1785/gssrl.81.3.530.

Bies, D.A., Hansen, C., Howard, C., 2017. Sound propagation, in: Engineering Noise Control. 5 ed.. CRC Press, Taylor & Francis Group, Boca Raton. chapter 5, pp. 59–86. doi:10.1201/9781351228152.

Bishop, J.W., Fee, D., Modrak, R., Tape, C., Kim, K., 2022. Spectral Element Modeling of Acoustic to Seismic Coupling Over Topography. Journal of Geophysical Research: Solid Earth 127. doi:10.1029/2021JB023142.

Blackstock, D.T., 1962. Propagation of Plane Sound Waves of Finite Amplitude in Nondissipative Fluids. The Journal of the Acoustical Society of America 34, 9–30. doi:10.1121/1.1909033.

Blackstock, D.T., 2006. "Once Nonlinear, Always Nonlinear", in: Atchley, A., Sparrow, V.W., Keolian, R.M. (Eds.), CP838, Innovations in Nonlinear Acoustics: 17th International Symposium on Nonlinear Acoustics, American Institute of Physics. pp. 601–606. doi:10.1063/1.2210425.

Blom, P., 2020. The influence of irregular terrain on infrasonic propagation in the troposphere. The Journal of the Acoustical Society of America 148, 1984–1997. doi:10.1121/10.0002128.

Blom, P., Waxler, R., 2012. Impulse propagation in the nocturnal boundary layer: Analysis of the geometric component. The Journal of the Acoustical Society of America 131, 3680–3690. doi:10.1121/1.3699174.

Bonadonna, C., Costa, A., Folch, A., Koyaguchi, T., 2015. Tephra Dispersal and Sedimentation. Second edi ed., Elsevier Inc. doi:10.1016/b978-0-12-385938-9.00033-x.

Borgia, A., Aubert, M., Merle, O., Van Wyk De Vries, B., 2010. What is a volcano? Special Paper of the Geological Society of America 470, 1–9. doi:10.1130/2010.2470(01).

Bowman, J.R., Baker, G.E., Bahavar, M., 2005. Ambient infrasound noise. Geophysical Research Letters 32, 1–5. doi:10.1029/2005GL022486.

Brogi, F., Ripepe, M., Bonadonna, C., 2018. Lattice Boltzmann modeling to explain volcano acoustic source. Scientific Reports , 1–8doi:10.1038/s41598-018-27387-0.

Brown, D., Ceranna, L., Prior, M., Mialle, P., Le Bras, R.J., 2014. The IDC Seismic, Hydroacoustic and Infrasound Global Low and High Noise Models. Pure and Applied Geophysics 171, 361–375. doi:10.1007/s00024-012-0573-6.

Browne, B., Szramek, L., 2015. Rates of Magma Ascent and Storage, in: The Encyclopedia of Volcanoes. second ed.. Elsevier, pp. 203–214. doi:10.1016/b978-0-12-385938-9.00009-2.

Buckingham, M., Garcés, M.A., 1996. Canonical model of volcano acoustics. Journal of Geophysical Research 101, 8129–8151.

Burgisser, A., Degruyter, W., 2015. Magma Ascent and Degassing at Shallow Levels, in: The Encyclopedia of Volcanoes. second ed.. Elsevier, pp. 225–236. doi:10.1016/b978-0-12-385938-9.00011-0.

Cannata, A., Montalto, P., Patanè, D., 2013. Joint analysis of infrasound and seismic signals by cross wavelet transform: Detection of Mt. Etna explosive activity. Natural Hazards and Earth System Sciences 13, 1669–1677. doi:10.5194/nhess-13-1669-2013.

Cannata, A., Sciotto, M., Spampinato, L., Spina, L., 2011. Insights into explosive activity at closely-spaced eruptive vents using infrasound signals: Example of Mt. Etna 2008 eruption. Journal of Volcanology and Geothermal Research 208, 1–11. doi:10.1016/j.jvolgeores.2011.09.003.

Caplan-Auerbach, J., Bellesiles, A., Fernandes, J.K., 2010. Estimates of eruption velocity and plume height from infrasonic recordings of the 2006 eruption of Augustine Volcano, Alaska. Journal of Volcanology and Geothermal Research 189, 12–18. doi:10.1016/j.jvolgeores.2009.10.002.

Carr, J.L., Horváth, Á., Wu, D.L., Friberg, M.D., 2022. Stereo Plume Height and Motion

Retrievals for the Record-Setting Hunga Tonga-Hunga Ha'apai Eruption of 15 January 2022. Geophysical Research Letters , 1–7doi:10.1029/2022gl098131.

Carroll, M.R., Holloway, J.R., 2015. Volatiles in magmas, in: Encyclopedia of Volcanoes. second ed.. Elsevier Inc., pp. 1–517. doi:10.1016/b978-0-12-385938-9.00007-9.

Cashman, K.V., Scheu, B., 2015. Magmatic Fragmentation, in: The Encyclopedia of Volcanoes. second ed.. Elsevier Inc., pp. 459–471. doi:10.1016/b978-0-12-385938-9.00025-0.

Cassidy, M., Manga, M., Cashman, K., Bachmann, O., 2018. Controls on explosive-effusive volcanic eruption styles. Nature Communications 9. doi:10.1038/s41467-018-05293-3.

Caudron, C., Taisne, B., Garcés, M., Alexis, L.P., Mialle, P., 2015. On the use of remote infrasound and seismic stations to constrain the eruptive sequence and intensity for the 2014 Kelud eruption. Geophysical Research Letters 42, 6614–6621. doi:10.1002/2015GL064885.

Cerminara, M., Esposti Ongaro, T., Neri, A., 2016. Large Eddy Simulation of gas–particle kinematic decoupling and turbulent entrainment in volcanic plumes. Journal of Volcanology and Geothermal Research 326, 143–171. doi:10.1016/j.jvolgeores.2016.06.018.

Chunchuzov, I.P., Kulichkov, S.N., Popov, O.E., Waxler, R., Assink, J., 2011. Infrasound scattering from atmospheric anisotropic inhomogeneities. Izvestiya - Atmospheric and Ocean Physics 47, 540–557. doi:10.1134/S0001433811050045.

Cimarelli, C., Alatorre-Ibargüengoitia, M.A., Aizawa, K., Yokoo, A., Díaz-Marina, A., Iguchi, M., Dingwell, D.B., 2016. Multiparametric observation of volcanic lightning: Sakurajima Volcano, Japan. Geophysical Research Letters 43, 4221–4228. doi:10.1002/2015GL067445.

Clarke, A.B., Esposti Ongaro, T., Belousov, A., 2015. Vulcanian Eruptions. Second ed., Elsevier Inc. doi:10.1016/B978-0-12-385938-9.00028-6.

Dabrowa, A.L., Green, D.N., Rust, A.C., Phillips, J.C., 2011. A global study of volcanic infrasound characteristics and the potential for long-range monitoring. Earth and Planetary Science Letters 310, 369–379. doi:10.1016/j.epsl.2011.08.027.

Dalton, M.P., Waite, G.P., Watson, I.M., Nadeau, P.A., 2010. Multiparameter quantification of gas release during weak Strombolian eruptions at Pacaya Volcano, Guatemala. Geophysical Research Letters 37. doi:10.1029/2010GL042617.

De Angelis, S., Diaz-Moreno, A., Zuccarello, L., 2019. Recent developments and applications of acoustic infrasound to monitor volcanic emissions. Remote Sensing 11, 1–18. doi:10.3390/rs11111302.

Delle Donne, D., Ripepe, M., 2012. High-frame rate thermal imagery of strombolian explosions: Implications for explosive and infrasonic source dynamics. Journal of Geophysical Research: Solid Earth 117, 1–12. doi:10.1029/2011JB008987.

Delle Donne, D., Ripepe, M., Lacanna, G., Tamburello, G., Bitetto, M., Aiuppa, A., 2016. Gas mass derived by infrasound and UV cameras: Implications for mass flow rate. Journal of Volcanology and Geothermal Research 325, 169–178. doi:10.1016/j.jvolgeores.2016.06.015.

Dewey, J.M., 2018. The Rankine–Hugoniot Equations: Their Extensions and Inversions Related to Blast Waves, in: Sochet, I. (Ed.), Blast Effects, Shock Wave and High Pressure Phenomena. Springer International Publishing. chapter 2, pp. 17–35. doi:10.1007/978-3-319-70831-7_2.

Diaz-Moreno, A., Iezzi, A.M., Lamb, O.D., Fee, D., Kim, K., Zuccarello, L., De Angelis, S., 2019. Volume Flow Rate Estimation for Small Explosions at Mt. Etna, Italy, From Acoustic Waveform Inversion. Geophysical Research Letters 46, 11071–11079. doi:10.1029/2019GL084598.

Dragoni, M., Santoro, D., 2020. A model for the atmospheric shock wave produced by a strong volcanic explosion. Geophysical Journal International 222, 735–742. doi:10.1093/gji/ggaa205.

Duarte, M., Watanabe, R.N., 2018. Notes on scientific computing for biomechanics and motor control. URL: https://github.com/BMClab/BMC.

Ducea, M.N., Saleeby, J.B., Bergantz, G., 2015. The architecture, chemistry, and evolution of continental magmatic arcs. Annual Review of Earth and Planetary Sciences 43, 299–331. doi:10.1146/annurev-earth-060614-105049.

Edwards, W.N., 2010. Meteor Generated Infrasound: Theory and Observation, in: Pichon, A.L., Blanc, E., Hauchecorne, A. (Eds.), Infrasound Monitoring for Atmospheric Studies. Springer, Dordrecht, pp. 361–414. doi:10.1007/978-1-4020-9508-5.

Ekici, I., Bougdah, H., 2003. A review of research on environmental noise barriers. Building Acoustics 10, 289–323. doi:10.1260/135101003772776712.

Elgar, S., Guza, R.T., 1988. Statistics of Bicoherence. IEEE Transactions on Acoustics, Speech, and Signal Processing 36, 1667–1668. doi:10.1109/29.7555.

Embleton, T.F.W., 1996. Tutorial on sound propagation outdoors. The Journal of the Acoustical Society of America 100, 31–48. doi:10.1121/1.415879.

Embleton, T.F.W., Piercy, J.E., Olson, N., 1976. Outdoor sound propagation over ground of finite impedance. The Journal of the Acoustical Society of America 59, 267–277. doi:10.1121/1.380882.

Ettouney, S.M., Fricke, F.R., 1973. Courtyard acoustics. Applied Acoustics 6, 119–132. doi:10.1016/0003-682X(73)90021-2.

Falco, L.E., Atchley, A.A., Gee, K.L., Sparrow, V.W., 2006. Investigation of a single-point nonlinearity indicator in one-dimensional propagation. AIP Conference Proceedings 838, 572–575. doi:10.1063/1.2210421.

Fee, D., Bishop, J.W., Waxler, R., Matoza, R.S., 2020. Infrasound Propagation Working Group (IPWG) Report. Technical Report September. US Defense Threat Reduction Agency (DTRA).

Fee, D., Garces, M., 2007. Infrasonic tremor in the diffraction zone. Geophysical Research Letters 34, 1–5. doi:10.1029/2007GL030616.

Fee, D., Haney, M.M., Matoza, R.S., Van Eaton, A.R., Cervelli, P., Schneider, D.J., Iezzi, A.M., 2017a. Volcanic tremor and plume height hysteresis from Pavlof Volcano, Alaska. Science 355, 45–48. doi:10.1126/science.aah6108.

Fee, D., Izbekov, P., Kim, K., Yokoo, A., Lopez, T., Prata, F., Kazahaya, R., Nakamichi, H., Iguchi, M., 2017b. Eruption mass estimation using infrasound waveform inversion and ash and gas measurements : Evaluation at Sakurajima Volcano , Japan. Earth and Planetary Science Letters 480, 42–52. doi:10.1016/j.epsl.2017.09.043.

Fee, D., Matoza, R.S., 2013. An overview of volcano infrasound: From hawaiian to plinian, local to global. Journal of Volcanology and Geothermal Research 249, 123–139. doi:10.1016/j.jvolgeores.2012.09.002.

Fee, D., Matoza, R.S., Gee, K.L., Neilsen, T.B., Ogden, D.E., 2013a. Infrasonic crackle and supersonic jet noise from the eruption of Nabro. Geophysical Research Letters 40, 4199–4203. doi:10.1002/grl.50827.

Fee, D., McNutt, S.R., Lopez, T.M., Arnoult, K.M., Szuberla, C.A., Olson, J.V., 2013b. Combining local and remote infrasound recordings from the 2009 Redoubt Volcano eruption. Journal of Volcanology and Geothermal Research 259, 100–114. doi:10.1016/j.jvolgeores.2011.09.012.

Fee, D., Steffke, A., Garces, M., 2010. Characterization of the 2008 Kasatochi and Okmok eruptions using remote infrasound arrays. Journal of Geophysical Research Atmospheres 115, 1–15. doi:10.1029/2009JD013621.

Fee, D., Toney, L., Kim, K., Sanderson, R.W., Iezzi, A.M., Matoza, R.S., De Angelis, S., Jolly, A.D., Lyons, J.J., Haney, M.M., 2021. Local Explosion Detection and Infrasound Localization

by Reverse Time Migration Using 3-D Finite-Difference Wave Propagation. Frontiers in Earth Science 9, 1–14. doi:10.3389/feart.2021.620813.

Fee, D., Yokoo, A., Johnson, J.B., 2014. Introduction to an Open Community Infrasound Dataset from the Actively Erupting Sakurajima Volcano, Japan. Seismological Research Letters 85, 1151–1162. doi:10.1785/0220140051.

Fehr, R., 1951. The Reduction of Industrial Machine Noise, in: Proceedings of the National Noise Symposium, USA, October, 1951.

Firstov, P.P., Kravchenko, N.M., 1996. Estimation of the Amount of Explosive Gas Released in Volcanic Eruptions Using Air Waves. Volcanology and Seismology 17, 547–560.

Firth, C.W., Handley, H.K., Cronin, S.J., Turner, S.P., 2014. The eruptive history and chemical stratigraphy of a post-caldera, steady-state volcano: Yasur, Vanuatu. Bulletin of Volcanology 76, 1–23. doi:10.1007/s00445-014-0837-3.

Fitzgerald, R.H., 2019. Yasur Volcano Crater DEM, Republic of Vanuatu. doi:10.5069/G90V89XD.

Fitzgerald, R.H., Kennedy, B.M., Gomez, C., Wilson, T.M., Simons, B., Leonard, G.S., Matoza, R.S., Jolly, A.D., Garaebiti, E., 2020. Volcanic ballistic projectile deposition from a continuously erupting volcano: Yasur Volcano, Vanuatu. Volcanica 3, 183–204. doi:10.30909/vol.03.02.183204.

Freire, S., Florczyk, A.J., Pesaresi, M., Sliuzas, R., 2019. An improved global analysis of population distribution in proximity to active volcanoes, 1975-2015. ISPRS International Journal of Geo-Information 8. doi:10.3390/ijgi8080341.

Friedlander, F.G., 1946. The Diffraction of Sound Pulses. I. Diffraction by a Semi-Infinite Plane. Proceedings of the Royal Society A: Mathematical, Physical and Engineering Sciences 186, 322–344. doi:10.1098/rspa.1946.0046.

Fujiwara, K., Ando, Y., Maekawa, Z., 1977. Noise Control by Barriers - Part 1: Noise Reduction by a Thick Barrier. Applied Acoustics 10.

Gabrielli, S., De Siena, L., Napolitano, F., Del Pezzo, E., 2020. Understanding seismic path biases and magmatic activity at Mount St Helens volcano before its 2004 eruption. Geophysical Journal International 222, 169–188. doi:10.1093/gji/ggaa154.

Gagnon, D.E., 2011. Bispectral Analysis of Nonlinear Acoustic Propagation. Ph.D. thesis. University of Texas at Austin.

Gainville, O., Blanc-Benon, P., Blanc, E., Roche, R., Millet, C., Le Piver, F., Despres, B., Piserchia, P., 2010. Misty Picture: A Unique Experiment for the Interpretation of the Infrasound Propagation from Large Explosive Sources, in: Pichon, A.L., Blanc, E., Hauchecorne, A. (Eds.), Infrasound Monitoring for Atmospheric Studies. Springer Science+Business Media. chapter 18, pp. 575–598. doi:10.1007/978-1-4020-9508-5.

Garces, M., 2013. On Infrasound Standards, Part 1: Time, Frequency, and Energy Scaling. InfraMatics 02, 13–35. doi:10.4236/inframatics.2013.22002.

Garces, M., 2019. Explosion Source Models, in: Le Pichon, A. (Ed.), Infrasound Monitoring for Atmospheric Studies. second ed.. Springer International Publishing, Cham. chapter 8, pp. 273–345. doi:10.1007/978-3-319-75140-5.

Garcés, M., Iguchi, M., Ishihara, K., Morrissey, M., Sudo, Y., Tsutsui, T., 1999. Infrasonic precursors to a Vulcanian eruption at Sakurajima Volcano, Japan. Geophysical Research Letters 26, 2537–2540. doi:10.1029/1998GL005327.

Garces, M.A., 2000. Theory of acoustic propagation in a multi-phase stratified liquid flowing within an elastic-walled conduit of varying cross-sectional area. Journal of Volcanology and Geothermal Research 101, 1–17. doi:10.1016/S0377-0273(00)00155-4.

Garcés, M.A., Fee, D., Matoza, R., 2013. Chapter 16: Volcano Acoustics, in: Fagents, S.,

Gregg, T., Lopes, R. (Eds.), Modeling Volcanic Processes: The Physics and Mathematics of Volcanism. Cambridge University Press, pp. 359–383.

Gee, K., Atchley, A., Falco, L., Shepherd, M., Ukeiley, L., Jansen, B., Seiner, J., 2010. Bicoherence analysis of model-scale jet noise. Journal of the Acoustical Society of America 128, 211–216. doi:10.1121/1.3484492.

Gee, K.L., Gabrielson, T.B., Atchley, A.A., Sparrow, V.W., 2005. Preliminary Analysis of Nonlinearity in Military Jet Aircraft Noise Propagation. AIAA Journal 43. doi:10.2514/1.10155.

Gee, K.L., Miller, K.G., Reichman, B.O., Wall, A.T., 2018. Frequency-domain nonlinearity analysis of noise from a high-performance jet aircraft, in: Proceedings of Meetings on Acoustics, Santa Fe, New Mexico. doi:10.1121/2.0000899.

Gee, K.L., Neilsen, T.B., Atchley, A.A., 2013. Skewness and shock formation in laboratory-scale supersonic jet data. The Journal of the Acoustical Society of America 133, EL491–EL497. doi:10.1121/1.4807307.

Gee, K.L., Shepherd, M.R., Falco, L.E., Atchley, A.A., Ukeiley, L.S., Jansen, B.J., Seiner, J.M., 2007a. Identification of Nonlinear and Near-field Effects in Jet Noise Using Nonlinearity Indicators, in: AIAA/CEAS Aeroacoustics Conference, pp. 1–15. doi:10.2514/6.2007-3653.

Gee, K.L., Sparrow, V.W., Atchley, A., Gabrielson, T.B., 2007b. On the Perception of Crackle in High-Amplitude Jet Noise. AIAA Journal 45, 593–598. doi:10.2514/1.26484.

Gee, K.L., Sparrow, V.W., James, M.M., Downing, J.M., Hobbs, C.M., Gabrielson, T.B., Atchley, A.A., 2008. The role of nonlinear effects in the propagation of noise from high-power jet aircraft. The Journal of the Acoustical Society of America 123, 4082–4093. doi:10.1121/1.2903871.

Genco, R., Ripepe, M., Marchetti, E., Bonadonna, C., Biass, S., 2014. Acoustic wavefield and

Mach wave radiation of flashing arcs in strombolian explosion measured by image luminance. Geophysical Research Letters 41, 7135–7142. doi:10.1002/2014GL061597.

Gestrich, J.E., Fee, D., Matoza, R.S., Lyons, J.J., Ruiz, M.C., 2021. Fitting Jet Noise Similarity Spectra to Volcano Infrasound Data. Earth and Space Science 8, 1–16. doi:10.1029/2021EA001894.

Gol'dberg, Z.A., 1956. Second approximation acoustic equations and the propagation of plane waves of finite amplitude. Soviet Phys. Acoust. 2, 346–350.

Gonnermann, H., Taisne, B., 2015. Magma Transport in Dikes, in: The Encyclopedia of Volcanoes. second ed.. Elsevier Inc., pp. 215–224. doi:10.1016/b978-0-12-385938-9.00010-9.

González, P.J., Samsonov, S.V., Pepe, S., Tiampo, K.F., Tizzani, P., Casu, F., Fernández, J., Camacho, A.G., Sansosti, E., 2013. Magma storage and migration associated with the 2011-2012 El Hierro eruption: Implications for crustal magmatic systems at oceanic island volcanoes. Journal of Geophysical Research: Solid Earth 118, 4361–4377. doi:10.1002/jgrb.50289.

Gossard, E.E., Hooke, W.H., 1975. Waves in the Atmosphere: Atmospheric Infrasound and Gravity Waves — Their Generation and Propagation. Elsevier, New York.

Goto, A., Ripepe, M., Lacanna, G., 2014. Wideband acoustic records of explosive volcanic eruptions at Stromboli: New insights on the explosive process and the acoustic source. Geophysical Research Letters 41, 3851–3857. doi:10.1002/2014GL060143.

Green, D.N., Matoza, R.S., Vergoz, J., Le Pichon, A., 2012. Infrasonic propagation from the 2010 Eyjafjallajkull eruption: Investigating the influence of stratospheric solar tides. Journal of Geophysical Research Atmospheres 117, 1–19. doi:10.1029/2012JD017988.

de Groot-Hedlin, C., 2004. Criteria for discretization of seafloor bathymetry when using a stairstep approximation: Application to computation of T-phase seismograms. The Journal of the Acoustical Society of America 115, 1103–1113. doi:10.1121/1.1643361.

de Groot-Hedlin, C., 2012. Nonlinear synthesis of infrasound propagation through an inhomogeneous, absorbing atmosphere. The Journal of the Acoustical Society of America 132, 646–656. doi:10.1121/1.4731468.

de Groot-Hedlin, C., 2016. Long-range propagation of nonlinear infrasound waves through an absorbing atmosphere. The Journal of the Acoustical Society of America 139, 1565–1577. doi:10.1121/1.4944759.

de Groot-Hedlin, C., 2017. Infrasound propagation in tropospheric ducts and acoustic shadow zones. Journal of the Acoustical Society of America 142, 1816–1827. doi:10.1121/1.5005889.

Grove, T.L., Elkins-Tanton, L.T., Parman, S.W., Chatterjee, N., Müntener, O., Gaetani, G.A., 2003. Fractional crystallization and mantle-melting controls on calc-alkaline differentiation trends. Contributions to Mineralogy and Petrology 145, 515–533. doi:10.1007/s00410-003-0448-z.

Grove, T.L., Till, C.B., Krawczynski, M.J., 2012. The role of H2O in subduction zone magmatism. Annual Review of Earth and Planetary Sciences 40, 413–439. doi:10.1146/annurev-earth-042711-105310.

Hadden, W.J., Pierce, A.D., 1981. Sound diffraction around screens and wedges for arbitrary point source locations. The Journal of the Acoustical Society of America 69, 1266–1276. doi:10.1121/1.385809.

Hall, P.S., Kincaid, C., 2001. Diapiric flow at subduction zones: A recipe for rapid transport. Science 292, 2472–2475. doi:10.1126/science.1060488.

Hamilton, M.F., 2016. Effective Gol'dberg number for diverging waves. Journal of the Acoustical Society of America 140, 4419–4427. doi:10.1121/1.4968787].

Hamilton, M.F., Blackstock, D.T., 2008. Nonlinear Acoustics. Academic Press, Melville, NY. doi:978-0-12-321860-5.

Hamilton, M.F., Morfey, C.L., 2008. Model Equations, in: Hamilton, M.F., Blackstock, D.T. (Eds.), Nonlinear Acoustics. Academic Press, Melville, NY. chapter 3, pp. 41–63.

Harris, A., Ripepe, M., 2007. Synergy of multiple geophysical approaches to unravel explosive eruption conduit and source dynamics - A case study from Stromboli. Chemie der Erde - Geochemistry 67, 1–35. doi:10.1016/j.chemer.2007.01.003.

Haskell, N.A., 1964. Total Energy and Energy Spectral Density of Elastic Wave Radiation from Propagating Faults. Bulletin of the Seismological Society of America 54, 1811–1841. doi:10.1785/BSSA05406A1811.

Hasselmann, K., Munk, W., MacDonald, G., 1963. Bispectra of Ocean Waves, in: Rosenblatt, M. (Ed.), Proceedings of the Symposium on Time Series Analysis. John Wiley & Sons, Inc., New York.

Hildreth, W., 1979. The Bishop Tuff: Evidence for the origin of compositional zonation in silicic magma chambers, in: Geological Society of America Special Papers. Geological Society of America. volume 180, pp. 43–76. doi:10.1130/SPE180-p43.

Hohenwarter, D., 1990. Railway noise propagation models. Journal of Sound and Vibration 141, 17–41. doi:10.1016/0022-460X(90)90510-7.

Hole, M.J., 2015. The generation of continental flood basalts by decompression melting of internally heated mantle. Geology 43, 311–314. doi:10.1130/G36442.1.

Iezzi, A.M., Fee, D., Kim, K., Jolly, A.D., Matoza, R.S., 2019. Three-Dimensional Acoustic Multipole Waveform Inversion at Yasur Volcano, Vanuatu. Journal of Geophysical Research: Solid Earth 124, 8679–8703. doi:10.1029/2018JB017073.

Iezzi, A.M., Matoza, R.S., Fee, D., Kim, K., Jolly, A.D., 2022. Synthetic Evaluation of Infrasonic Multipole Waveform Inversion. Journal of Geophysical Research: Solid Earth 127. doi:10.1029/2021jb023223.

Iezzi, A.M., Schwaiger, H.F., Fee, D., Haney, M.M., 2018. Application of an updated atmospheric model to explore volcano infrasound propagation and detection in Alaska. Journal of Volcanology and Geothermal Research 371, 192–205. doi:10.1016/j.jvolgeores.2018.03.009.

Iguchi, M., 2013. Magma Movement from the Deep to Shallow Sakurajima Volcano as Revealed by Geophysical Observations. Bulletin of the Volcanological Society of Japan 58, 1–18.

Iguchi, M., Tanegyri, T., Ohta, Y., Ueki, S., Nakao, S., 2013. Characteristics of Volcanic Activity at Sakurajima Volcano's Showa Crater During the Period 2006 to 2011. Bulletin of the Volcanological Society of Japan 58, 115–135. doi:10.18940/kazan.58.1_115.

Iguchi, M., Yakiwara, H., Tameguri, T., Hendrasto, M., ichi Hirabayashi, J., 2008. Mechanism of explosive eruption revealed by geophysical observations at the Sakurajima, Suwanosejima and Semeru volcanoes. Journal of Volcanology and Geothermal Research 178, 1–9. doi:10.1016/j.jvolgeores.2007.10.010.

Ishihara, K., 1985. Dynamical analysis of volcanic explosion. Journal of Geodynamics 3, 327–349. doi:10.1016/0264-3707(85)90041-9.

Ishii, K., Yokoo, A., Iguchi, M., Fujita, E., 2020. Utilizing the solution of sound diffraction by a thin screen to evaluate infrasound waves attenuated around volcano topography. Journal of Volcanology and Geothermal Research 402, 106983. URL: 10.1016/j.jvolgeores.2020.106983, doi:10.1016/j.jvolgeores.2020.106983.

Iwamori, H., 1998. Transportation of H2O and melting in subduction zones. Earth and Planetary Science Letters 160, 65–80. doi:10.1016/S0012-821X(98)00080-6.

Jagoutz, O., Müntener, O., Schmidt, M.W., Burg, J.P., 2011. The roles of flux- and decompression melting and their respective fractionation lines for continental crust formation: Evidence from the Kohistan arc. Earth and Planetary Science Letters 303, 25–36. doi:10.1016/j.epsl.2010.12.017.

John, T., Gussone, N., Podladchikov, Y.Y., Bebout, G.E., Dohmen, R., Halama, R., Klemd, R., Magna, T., Seitz, H.M., 2012. Volcanic arcs fed by rapid pulsed fluid flow through subducting slabs. Nature Geoscience 5, 489–492. doi:10.1038/ngeo1482.

Johnson, J., 2019. Local Volcano Infrasound Monitoring, in: Le Pichon, A. (Ed.), Infrasound Monitoring for Atmospheric Studies. second ed.. Springer International Publishing, pp. 989–1022. doi:10.1007/978-3-319-75140-5.

Johnson, J.B., 2003. Generation and propagation of infrasonic airwaves from volcanic explosions. Journal of Volcanology and Geothermal Research 121, 1–14. doi:10.1016/S0377-0273(02)00408-0.

Johnson, J.B., Anderson, J., Marcillo, O., Arrowsmith, S., 2012. Probing local wind and temperature structure using infrasound from Volcan Villarrica (Chile). Journal of Geophysical Research Atmospheres 117, 1–16. doi:10.1029/2012JD017694.

Johnson, J.B., Miller, A.J.C., 2014. Application of the Monopole Source to Quantify Explosive Flux during Vulcanian Explosions at Sakurajima Volcano (Japan). Seismological Research Letters 85, 1163–1176. doi:10.1785/0220140058.

Johnson, J.B., Palma, J.L., 2015. Lahar infrasound associated with Volcán Villarrica's 3 March 2015 eruption. Geophysical Research Letters 42, 6324–6331. doi:10.1002/2015GL065024.

Johnson, J.B., Ripepe, M., 2011. Volcano infrasound: A review. Journal of Volcanology and Geothermal Research 206, 61–69. doi:10.1016/j.jvolgeores.2011.06.006.

Johnson, J.B., Ruiz, M.C., Ortiz, H.D., Watson, L.M., Viracucha, G., Ramon, P., Almeida, M., 2018a. Infrasound Tornillos Produced by Volcán Cotopaxi's Deep Crater. Geophysical Research Letters 45, 5436–5444. doi:10.1029/2018GL077766.

Johnson, J.B., Watson, L.M., Palma, J.L., Dunham, E.M., Anderson, J.F., 2018b. Forecasting the Eruption of an Open-Vent Volcano Using Resonant Infrasound Tones. Geophysical Research Letters 45, 2213–2220. doi:10.1002/2017GL076506.

Jolly, A., Kennedy, B., Edwards, M., Jousset, P., Scheu, B., 2016. Infrasound tremor from bubble burst eruptions in the viscous shallow crater lake of White Island, New Zealand, and its implications for interpreting volcanic source processes. Journal of Volcanology and Geothermal Research 327, 585–603. doi:10.1016/j.jvolgeores.2016.08.010.

Jolly, A.D., Matoza, R.S., Fee, D., Kennedy, B.M., Iezzi, A.M., Fitzgerald, R.H., Austin, A.C., Johnson, R., 2017. Capturing the Acoustic Radiation Pattern of Strombolian Eruptions using Infrasound Sensors Aboard a Tethered Aerostat, Yasur Volcano, Vanuatu. Geophysical Research Letters 44, 9672–9680. doi:10.1002/2017GL074971.

Jonasson, H.G., 1972. Sound reduction by barriers on the ground. Journal of Sound and Vibration 22, 113–126. doi:10.1016/0022-460X(72)90849-8.

Jones, M.R., Riley, J., Georges, T., 1986. HARPA: A Versatile Three-Dimensional Hamiltonian Ray-Tracing Program for Acoustic Waves in the Atmosphere Above Irregular Terrain. U.S. Department of Commerce, National Oceanic and Atmospheric Administration, Boulder.

Kanamori, H., Anderson, D.L., 1975. Theoretical Basis of some Empirical Relations in Seismology. Bulletin of the Seismological Society of America 65, 1073–1095. doi:10.1785/BSSA0650051073.

Kawakatsu, H., Ohminato, T., Ito, H., Kuwahara, Y., 1992. Broadband Seismic Observation at the Sakurajima Volcano, Japan. Geophysical Research Letters 19, 1959–1962. doi:10.1002/ange.201007361.

Kim, K., Fee, D., Yokoo, A., Lees, J.M., 2015. Acoustic source inversion to estimate volume flux from volcanic explosions. Geophysical Research Letters 42, 5243–5249. doi:10.1002/2015GL064466.

Kim, K., Lees, J.M., 2011. Finite-difference time-domain modeling of transient infrasonic wavefields excited by volcanic explosions. Geophysical Research Letters 38, 2–6. doi:10.1029/2010GL046615.

Kim, K., Lees, J.M., 2014. Local Volcano Infrasound and Source Localization Investigated by 3D Simulation. Seismological Research Letters 85, 1177–1186. doi:10.1785/0220140029.

Kim, K., Lees, J.M., Ruiz, M., 2012. Acoustic multipole source model for volcanic explosions and inversion for source parameters. Geophysical Journal International 191, 1192–1204. doi:10.1111/j.1365-246X.2012.05696.x.

Kim, K., Rodgers, A., Seastrand, D., 2018. Local Infrasound Variability Related to In Situ Atmospheric Observation. Geophysical Research Letters 45, 2954–2962. doi:10.1002/2018GL077124.

Kim, Y.C., Powers, E.J., 1979. Digital Bispectral Analysis and Its Applications to Nonlinear Wave Interactions. IEEE Transactions on Plasma Science 7, 120–131. doi:10.1109/TPS.1979.4317207.

Kinney, G.F., Graham, K.J., 1985. Explosive Shock in Air. Springer Science+Business Media, New York.

Kremers, S., Wassermann, J., Meier, K., Pelties, C., van Driel, M., Vasseur, J., Hort, M., 2013. Inverting the source mechanism of Strombolian explosions at Mt. Yasur, Vanuatu, using a multi-parameter dataset. Journal of Volcanology and Geothermal Research 262, 104–122. doi:10.1016/j.jvolgeores.2013.06.007.

Lacanna, G., Ichihara, M., Iwakuni, M., Takeo, M., Iguchi, M., Ripepe, M., 2014. Influence of atmospheric structure and topography on infrasonic wave propagation. Journal of Geophysical Research: Solid Earth 119, 2988–3005. doi:10.1002/2013JB010827.

Lacanna, G., Ripepe, M., 2013. Influence of near-source volcano topography on the acoustic wavefield and implication for source modeling. Journal of Volcanology and Geothermal Research 250, 9–18. doi:10.1016/j.jvolgeores.2012.10.005.

Lacanna, G., Ripepe, M., 2020. Modeling the Acoustic Flux Inside the Magmatic Conduit

by 3D-FDTD Simulation. Journal of Geophysical Research: Solid Earth 125. doi:10.1029/2019JB018849.

Lamb, O.D., De Angelis, S., Lavallée, Y., 2015. Using infrasound to constrain ash plume rise. Journal of Applied Volcanology 4. doi:10.1186/s13617-015-0038-6.

Landès, M., Ceranna, L., Le Pichon, A., Matoza, R.S., 2012. Localization of microbarom sources using the IMS infrasound network. Journal of Geophysical Research: Atmospheres 117, 1–6. doi:10.1029/2011JD016684.

Langmuir, C.H., Klein, E.M., Plank, T., 1992. Petrological Systematics of Mid-Ocean Ridge Basalts: Constraints on Melt Generation Beneath Ocean Ridges, in: Mantle Flow and Melt Generation at Mid-Ocean Ridges, Geophysical Monograph 71. American Geophysical Union,, pp. 183–280. doi:10.1029/gm071p0183.

Lapins, S., Roman, D.C., Rougier, J., De Angelis, S., Cashman, K.V., Kendall, J.M., 2020. An examination of the continuous wavelet transform for volcano-seismic spectral analysis. Journal of Volcanology and Geothermal Research 389, 106728. doi:10.1016/j.jvolgeores.2019.106728.

Lavallée, Y., Dingwell, D.B., Johnson, J.B., Cimarelli, C., Hornby, A.J., Kendrick, J.E., Von Aulock, F.W., Kennedy, B.M., Andrews, B.J., Wadsworth, F.B., Rhodes, E., Chigna, G., 2015. Thermal vesiculation during volcanic eruptions. Nature 528, 544–547. doi:10.1038/nature16153.

Le Pichon, A., Blanc, E., Drob, D., Lambotte, S., Dessa, J.X., Lardy, M., Bani, P., Vergniolle, S., 2005. Infrasound monitoring of volcanoes to probe high-altitude winds. Journal of Geophysical Research Atmospheres 110, 1–12. doi:10.1029/2004JD005587.

Le Pichon, A., Cansi, Y., 2003. PMCC for Infrasound Data Processing. Handbook of Signal Processing in Acoustics , 1–9doi:10.1007/978-0-387-30441-0_77.

Le Pichon, A., Ceranna, L., Vergoz, J., 2012. Incorporating numerical modeling into estimates of the detection capability of the IMS infrasound network. Journal of Geophysical Research Atmospheres 117, 1–12. doi:10.1029/2011JD016670.

Lees, J.M., Ruiz, M., 2008. Non-linear explosion tremor at Sangay, Volcano, Ecuador. Journal of Volcanology and Geothermal Research 176, 170–178. doi:10.1016/j.jvolgeores.2007.08.012.

Li, K.M., Wong, H.Y., 2005. A review of commonly used analytical and empirical formulae for predicting sound diffracted by a thin screen. Applied Acoustics 66, 45–76. doi:10.1016/j.apacoust.2004.06.004.

Lighthill, J., 1978. Waves in Fluids. 2nd ed. ed., Cambridge University Press, Cambridge, U.K.

Lockwood, J.P., Lipman, P.W., 1987. Holocene Eruptive History of Mauna Loa Volcano, in: Decker, R.W., Wright, T.L., Stauffer, P.H. (Eds.), Volcanism in Hawaii, pp. 509–535.

Lonzaga, J.B., Waxler, R.M., Assink, J.D., Talmadge, C.L., 2015. Modelling waveforms of infrasound arrivals from impulsive sources using weakly non-linear ray theory. Geophysical Journal International 200, 1347–1361. doi:10.1093/gji/ggu479.

Loughlin, S., Sparks, S., Brown, S.K., Jenkins, S.F., Vye-Brown, C. (Eds.), 2015. Global Volcanic Hazards and Risk. Cambridge University Press.

Luhr, J.F., Simkin, T., 1993. Paricutin: The Volcano Born in a Mexican Cornfiel. U.S. Geoscience Press, Phoenix.

Macdonald, H.M., 1915. A class of diffraction problems. Proceedings of the London Mathematical Society 2 , 410–427doi:10.1112/plms/s2_14.1.410.

Maekawa, Z., 1968. Noise reduction by screens. Applied Acoustics 1, 157–173. doi:10.1016/0003-682X(68)90020-0, arXiv:1011.1669v3.

Maekawa, Z., Osaki, S., 1985. A simple chart for the estimation of the attenuation by a wedge diffraction. Applied Acoustics 18, 355–368. doi:10.1016/0003-682X(85)90054-4.

Maher, S., Matoza, R.S., de Groot-Hedlin, C., Jolly, A., Gee, K.L., Fee, D., 2019. Investigating the Effect of Nonlinear Acoustic Propagation on Infrasound-Based Volume Flux Estimates at Yasur Volcano, Vanuatu, in: American Geophysical Union, Fall Meeting 2019, abstract #V23F-0277.

Maher, S.P., Matoza, R.S., de Groot-Hedlin, C., Gee, K.L., Fee, D., Yokoo, A., 2020. Investigating Spectral Distortion of Local Volcano Infrasound by Nonlinear Propagation at Sakurajima Volcano, Japan. Journal of Geophysical Research: Solid Earth 125, 1–25. doi:10.1029/2019JB018284.

Maher, S.P., Matoza, R.S., de Groot-Hedlin, C., Kim, K., Gee, K.L., 2021. Evaluating the applicability of a screen diffraction approximation to local volcano infrasound. Volcanica 4, 67–85. doi:10.30909/vol.04.01.6785.

Maher, S.P., Matoza, R.S., Jolly, A.D., de Groot-Hedlin, C., Gee, K.L., Fee, D., Iezzi, A.M., 2022. Evidence for near-source nonlinear propagation of volcano infrasound from strombolian explosions at Yasur volcano, Vanuatu. Bulletin of Volcanology 84. doi:10.1007/s00445-022-01552-w.

Marchetti, E., Ripepe, M., Campus, P., Le Pichon, A., Vergoz, J., Lacanna, G., Mialle, P., Héreil, P., Husson, P., 2019. Long range infrasound monitoring of Etna volcano. Scientific Reports 9, 1–10. doi:10.1038/s41598-019-54468-5.

Marchetti, E., Ripepe, M., Delle Donne, D., Genco, R., Finizola, A., Garaebiti, E., 2013. Blast waves from violent explosive activity at Yasur Volcano, Vanuatu. Geophysical Research Letters 40, 5838–5843. doi:10.1002/2013GL057900.

Marchetti, E., Ripepe, M., Harris, A.J., Delle Donne, D., 2009. Tracing the differences between

Vulcanian and Strombolian explosions using infrasonic and thermal radiation energy. Earth and Planetary Science Letters 279, 273–281. doi:10.1016/j.epsl.2009.01.004.

Marcillo, O., Johnson, J.B., Hart, D., 2012. Implementation, characterization, and evaluation of an inexpensive low-power low-noise infrasound sensor based on a micromachined differential pressure transducer and a mechanical filter. Journal of Atmospheric and Oceanic Technology 29, 1275–1284. doi:10.1175/JTECH-D-11-00101.1.

Maryanto, S., Iguchi, M., Tameguri, T., 2008. Constraints on the source mechanism of harmonic tremors based on seismological, ground deformation, and visual observations at Sakurajima volcano, Japan. Journal of Volcanology and Geothermal Research 170, 198–217. doi:10.1016/j.jvolgeores.2007.10.004.

Matoza, R., Fee, D., Green, D., Mialle, P., 2019a. Volcano Infrasound and the International Monitoring System, in: Le Pichon, A. (Ed.), Infrasound Monitoring for Atmospheric Studies. second ed.. Springer International Publishing, Cham. chapter 33, pp. 1023–1077. doi:10.1007/978-3-319-75140-5_33.

Matoza, R.S., Arciniega-Ceballos, A., Sanderson, R.W., Mendo-Pérez, G., Rosado-Fuentes, A., Chouet, B.A., 2019b. High-Broadband Seismoacoustic Signature of Vulcanian Explosions at Popocatépetl Volcano, Mexico. Geophysical Research Letters 46, 148–157. doi:10.1029/2018GL080802.

Matoza, R.S., Chouet, B.A., Jolly, A.D., Dawson, P.B., Fitzgerald, R.H., Kennedy, B.M., Fee, D., Iezzi, A.M., Kilgour, G.N., Garaebiti, E., Cevuard, S., 2022a. High-rate very-long-period seismicity at Yasur volcano, Vanuatu: Source mechanism and decoupling from surficial explosions and infrasound. Geophysical Journal International doi:10.1093/gji/ggab533.

Matoza, R.S., Fee, D., 2018. The Inaudible Rumble of Volcanic Eruptions. Acoustics Today 14, 17–25.

Matoza, R.S., Fee, D., Garcés, M.A., Seiner, J.M., Ramón, P.A., Hedlin, M.A.H., 2009a. Infrasonic jet noise from volcanic eruptions. Geophysical Research Letters 36, 2–6. doi:10.1029/2008GL036486.

Matoza, R.S., Fee, D., Green, D.N., Le Pichon, A., Vergoz, J., Haney, M.M., Mikesell, T.D., Franco, L., Valderrama, O.A., Kelley, M.R., McKee, K., Ceranna, L., 2018. Local, Regional, and Remote Seismo-acoustic Observations of the April 2015 VEI 4 Eruption of Calbuco Volcano, Chile. Journal of Geophysical Research: Solid Earth 123, 3814–3827. doi:10.1002/2017JB015182.

Matoza, R.S., Fee, D., Lopez, T.M., 2014. Acoustic Characterization of Explosion Complexity at Sakurajima, Karymsky, and Tungurahua Volcanoes. Seismological Research Letters 85, 1187–1199. doi:10.1785/0220140110.

Matoza, R.S., Fee, D., Neilsen, T.B., Gee, K.L., Ogden, D.E., 2013. Aeroacoustics of volcanic jets : Acoustic power estimation and jet velocity dependence. Journal of Geophysical Research: Solid Earth 118, 6269–6284. doi:10.1002/2013JB010303.

Matoza, R.S., Garces, M.A., Chouet, B.A., D'Auria, L., Hedlin, M.A., de Groot-Hedlin, C., Waite, G.P., 2009b. The source of infrasound associated with long-period events at Mount St. Helens. Journal of Geophysical Research: Solid Earth 114, 1–38. doi:10.1029/2008JB006128.

Matoza, R.S., Green, D.N., Le Pichon, A., Shearer, P.M., Fee, D., Mialle, P., Ceranna, L., 2017a. Automated detection and cataloging of global explosive volcanism using the International Monitoring System infrasound network. Journal of Geophysical Research: Solid Earth 122, 2946–2971. doi:10.1002/2016JB013356.

Matoza, R.S., Hedlin, M.A.H., Garcés, M.A., 2007. An infrasound array study of Mount St. Helens. Journal of Volcanology and Geothermal Research 160, 249–262. doi:10.1016/j.jvolgeores.2006.10.006.

Matoza, R.S., Jolly, A., Fee, D., Johnson, R., Chouet, B., Dawson, P., Kilgour, G., Christenson,

B., Garaebiti, E., Iezzi, A., Austin, A., Kennedy, B., Fitzgerald, R., Key, N., 2017b. Seismo-acoustic wavefield of strombolian explosions at Yasur volcano, Vanuatu, using a broadband seismo-acoustic network, infrasound arrays, and infrasonic sensors on tethered balloons, in: J. Acoust. Soc. Am., 141(5), pp. 3566–3566. doi:10.1121/1.4987573.

Matoza, R.S., Le Pichon, A., Vergoz, J., Herry, P., Lalande, J.M., il Lee, H., Che, I.Y., Rybin, A., 2011. Infrasonic observations of the June 2009 Sarychev Peak eruption, Kuril Islands: Implications for infrasonic monitoring of remote explosive volcanism. Journal of Volcanology and Geothermal Research 200, 35–48. doi:10.1016/j.jvolgeores.2010.11.022.

Matoza, R.S., Matoza, R.S., Fee, D., Assink, J.D., Iezzi, A.M., Green, D.N., Kim, K., Lecocq, T., Krishnamoorthy, S., Lalande, J.m., Nishida, K., Gee, K.L., 2022b. Atmospheric waves and global seismoacoustic observations of the January 2022 Hunga eruption , Tonga. Science 7063. doi:10.1126/science.abo7063.

McGary, R.S., Evans, R.L., Wannamaker, P.E., Elsenbeck, J., Rondenay, S., 2014. Pathway from subducting slab to surface for melt and fluids beneath Mount Rainier. Nature 511, 338–340. doi:10.1038/nature13493.

McInerny, S., Downing, M., Hobbs, C., James, M., Hannon, M., 2006. Metrics that characterize nonlinearity in jet noise. AIP Conference Proceedings 838, 560–563. doi:10.1063/1.2210418.

McInerny, S.A., Ölçmen, S.M., 2005. High-intensity rocket noise: Nonlinear propagation, atmospheric absorption, and characterization. The Journal of the Acoustical Society of America 117, 578–591. doi:10.1121/1.1841711.

McKee, K., Fee, D., Rowell, C., Yokoo, A., 2014. Network-Based Evaluation of the Infrasonic Source Location at Sakurajima Volcano, Japan. Seismological Research Letters 85, 1200–1211. doi:10.1785/0220140119.

McKee, K., Fee, D., Yokoo, A., Matoza, R.S., Kim, K., 2017. Analysis of gas jetting and

fumarole acoustics at Aso Volcano, Japan. Journal of Volcanology and Geothermal Research 340, 16–29. doi:10.1016/j.jvolgeores.2017.03.029.

McKee, K., Smith, C.M., Reath, K., Snee, E., Maher, S., Matoza, R.S., Carn, S., Mastin, L., Anderson, K., Damby, D., Roman, D.C., Degterev, A., Rybin, A., Chibisova, M., Assink, J.D., de Negri Leiva, R., Perttu, A., 2021a. Evaluating the state-of-the-art in remote volcanic eruption characterization Part I: Raikoke volcano, Kuril Islands. Journal of Volcanology and Geothermal Research 419, 107354. doi:10.1016/j.jvolgeores.2021.107354.

McKee, K., Smith, C.M., Reath, K., Snee, E., Maher, S., Matoza, R.S., Carn, S., Roman, D.C., Mastin, L., Anderson, K., Damby, D., Itikarai, I., Mulina, K., Saunders, S., Assink, J.D., de Negri Leiva, R., Perttu, A., 2021b. Evaluating the state-of-the-art in remote volcanic eruption characterization Part II: Ulawun volcano, Papua New Guinea. Journal of Volcanology and Geothermal Research 420, 107381. doi:10.1016/j.jvolgeores.2021.107381.

Medici, E.F., Allen, J.S., Waite, G.P., 2014. Modeling shock waves generated by explosive volcanic. Geophysical Research Letters , 414–421doi:10.1002/2013GL058340.Received.

Médici, E.F., Waite, G.P., 2016. Experimental laboratory study on the formation of multiple shock waves observed during volcanic eruptions. Geophysical Research Letters 43, 85–92. doi:10.1002/2015GL066426.Received.

Meier, K., Hort, M., Wassermann, J., Garaebiti, E., 2016. Strombolian surface activity regimes at Yasur volcano, Vanuatu, as observed by Doppler radar, infrared camera and infrasound. Journal of Volcanology and Geothermal Research 322, 184–195. doi:10.1016/j.jvolgeores.2015.07.038.

Métrich, N., Allard, P., Aiuppa, A., Bani, P., Bertagnini, A., Shinohara, H., Parello, F., Di Muro, A., Garaebiti, E., Belhadj, O., Massare, D., 2011. Magma and volatile supply to post-collapse volcanism and block resurgence in Siwi caldera (Tanna Island, Vanuatu arc). Journal of Petrology 52, 1077–1105. doi:10.1093/petrology/egr019.

Miller, K.G., 2016. Theoretical and Experimental Investigation of a quadspectral nonlinearity indicator. Master's Thesis, Brigham Young University .

Miller, K.G., Gee, K.L., 2018. Model-scale jet noise analysis with a single-point, frequency-domain nonlinearity indicator. The Journal of the Acoustical Society of America 143, 3479–3492. doi:10.1121/1.5041741.

Miller, K.G., Gee, K.L., Reichman, B.O., 2016. Asymptotic behavior of a frequency-domain nonlinearity indicator for solutions to the generalized Burgers equation. The Journal of the Acoustical Society of America 140, 522–527. doi:10.1121/1.4971880.

Mills, H.H., 1976. Estimated erosion rates on Mount Rainier, Washington. Geology 4, 401–406. doi:10.1130/0091-7613(1976)4<401:EEROMR>2.0.CO;2.

Miwa, T., Toramaru, A., 2013. Conduit process in vulcanian eruptions at Sakurajima volcano, Japan: Inference from comparison of volcanic ash with pressure wave and seismic data. Bulletin of Volcanology 75, 1–13. doi:10.1007/s00445-012-0685-y.

Moran, S.C., Matoza, R.S., Garcés, M.A., Hedlin, M.A., Bowers, D., Scott, W.E., Sherrod, D.R., Vallance, J.W., 2008. Seismic and acoustic recordings of an unusually large rockfall at Mount St. Helens, Washington. Geophysical Research Letters 35, 2–7. doi:10.1029/2008GL035176.

Morfey, C.L., Howell, G.P., 1981. Nonlinear Propagation of Aircraft Noise in the Atmosphere. AIAA Journal 19, 986–992. doi:10.2514/3.51026.

Morrissey, M., Garces, M., Ishihara, K., Iguchi, M., 2008. Analysis of infrasonic and seismic events related to the 1998 Vulcanian eruption at Sakurajima. Journal of Volcanology and Geothermal Research 175, 315–324. doi:10.1016/j.jvolgeores.2008.03.008.

Morrissey, M.M., Chouet, B.A., 1997. Burst Conditions of Explosive Volcanic Eruptions Recorded on Microbarographs. Science 275, 1290–1293. doi:10.1126/science.275.5304.1290.

Morse, P., Ingard, K., 1986. Theoretical acoustics. Princeton University Press, Princeton, N.J.

Muhlestein, M., Gee, K., 2011. Experimental investigation of a characteristic shock formation distance in finite-amplitude noise propagation. Proceedings of Meetings on Acoustics 12. doi:10.1121/1.3609881.

Muhlestein, M.B., Gee, K.L., Thomas, D.C., Neilsen, T.B., 2012. Prediction of nonlinear propagation of noise from a solid rocket motor. Proceedings of Meetings on Acoustics 18, 040006. doi:10.1121/1.4755357.

Muramatsu, D., Aizawa, K., Yokoo, A., Iguchi, M., Tameguri, T., 2018. Estimation of Vent Radii From Video Recordings and Infrasound Data Analysis: Implications for Vulcanian Eruptions From Sakurajima Volcano, Japan. Geophysical Research Letters 45, 12,829–12,836. doi:10.1029/2018GL079898.

Nairn, I.A., 1976. Atmospheric shock waves and condensation clouds from Ngauruhoe explosive eruptions. Nature 259, 190–192. doi:10.1038/259190a0.

Nappo, C.J., 2013. An Introduction to Atmospheric Gravity Waves. Second ed., Elsevier, Oxford.

Needham, C.E., 2010. Blast Waves. Springer, Heidelberg. doi:10.1007/978-3-642-05288-0.

Nief, G., Talmadge, C., Rothman, J., Gabrielson, T., 2019. New Generations of Infrasound Sensors: Technological Developments and Calibration, in: Infrasound Monitoring for Atmospheric Studies. second ed.. Springer International Publishing, Cham, pp. 63–89. doi:10.1007/978-3-319-75140-5.

Normark, W.R., Moore, J.G., Torresan, M.E., 1993. Giant volcano-related landslides and the development of the Hawaiian Islands. U.S. Geological Survey Bulletin 2002 , p. 184–196.

Oguchi, T., Oguchi, C.T., 2009. Mt. Fuji: The Beauty of a Symmetric Stratovolcano, in: Migon, P. (Ed.), Geomorphological Landscapes of the World. Springer, New York, pp. 303–209. doi:10.1007/978-90-481-3055-9.

Olson, J.V., Szuberla, C.A., 2008. Processing Infrasonic Array Data. Handbook of Signal Processing in Acoustics , 1487–1496doi:10.1007/978-0-387-30441-0_81.

Oppenheim, A.V., Schafer, R.W., Buck, J., 1999. Discrete-time signal processing. Second ed., Prentice Hall, Upper Saddle River.

Oppenheimer, C., Bani, P., Calkins, J.A., Burton, M.R., Sawyer, G.M., 2006. Rapid FTIR sensing of volcanic gases released by Strombolian explosions at Yasur volcano, Vanuatu. Applied Physics B: Lasers and Optics 85, 453–460. doi:10.1007/s00340-006-2353-4.

Ortiz, H.D., Johnson, J.B., Ramón, P.G., Ruiz, M.C., 2018. Using infrasound waves to monitor tropospheric weather and crater morphology changes at Volcán Tungurahua, Ecuador. Journal of Volcanology and Geothermal Research 349, 205–216. doi:10.1016/j.jvolgeores.2017.11.001.

Ortiz, H.D., Matoza, R.S., Johnson, J.B., Hernandez, S., Anzieta, J.C., Ruiz, M.C., 2021. Autocorrelation Infrasound Interferometry. Journal of Geophysical Research: Solid Earth 126, 1–14. doi:10.1029/2020jb020513.

Ostashev, V.E., Wilson, D.K., Liu, L., Aldridge, D.F., Symons, N.P., Marlin, D., 2005. Equations for finite-difference, time-domain simulation of sound propagation in moving inhomogeneous media and numerical implementation. The Journal of the Acoustical Society of America 117, 503–517. doi:10.1121/1.1841531.

Peacock, S.M., 1990. Fluid processes in subduction zones. Science 248, 329–337. doi:10.1126/science.248.4953.329.

Perron, J.T., Kirchner, J.W., Dietrich, W.E., 2008. Spectral signatures of characteristic spatial scales and nonfractal structure in landscapes. Journal of Geophysical Research: Earth Surface 113, 1–14. doi:10.1029/2007JF000866.

Perttu, A., Taisne, B., De Angelis, S., Assink, J.D., Tailpied, D., Williams, R.A., 2020. Esti-

mates of plume height from infrasound for regional volcano monitoring. Journal of Volcanology and Geothermal Research 402, 106997. doi:10.1016/j.jvolgeores.2020.106997.

Pestorius, F.M., Williams, S.B., 1974. Upper limit on the use of weak-shock theory. Journal of the Acoustical Society of America 55, 1334–1335. doi:10.1121/1.1914705.

Petersen, T., De Angelis, S., Tytgat, G., McNutt, S.R., 2006. Local infrasound observations of large ash explosions at Augustine Volcano, Alaska, during January 11-28, 2006. Geophysical Research Letters 33, 1–5. doi:10.1029/2006GL026491.

Petitjean, B.P., Viswanathan, K., McLaughlin, D.K., 2006. Acoustic Pressure Waveforms Measured in High Speed Jet Noise Experiencing Nonlinear Propagation. International Journal of Aeroacoustics 5, 193–215. doi:10.1260/147547206777629835.

Pierce, A.D., 1974. Diffraction of sound around corners and over wide barriers. The Journal of the Acoustical Society of America 55, 941. doi:10.1121/1.1914668.

Pierce, A.D., 1981. Acoustics: An Introduction to Its Physical Principles and Applications. McGraw-Hill, New York, New York.

Piercy, J.E., Embleton, T.F.W., Sutherland, L.C., 1977. Review of noise propagation in the atmosphere. The Journal of the Acoustical Society of America 61, 1403–1418. doi:10.1121/1.381455.

Pineau, P., Bogey, C., 2021. Numerical investigation of wave steepening and shock coalescence near a cold Mach 3 jet. The Journal of the Acoustical Society of America 149, 357–370. doi:10.1121/10.0003343.

Plotkin, K.J., Sutherland, L.C., Vu, B.T., 2009. Lift-off acoustics predictions for the Ares I launch pad. 15th AIAA/CEAS Aeroacoustics Conference (30th AIAA Aeroacoustics Conference) , 11–13doi:10.2514/6.2009-3163.

Portnyagin, M., Hoernle, K., Plechov, P., Mironov, N., Khubunaya, S., 2007. Constraints on mantle melting and composition and nature of slab components in volcanic arcs from volatiles (H2O, S, Cl, F) and trace elements in melt inclusions from the Kamchatka Arc. Earth and Planetary Science Letters 255, 53–69. doi:10.1016/j.epsl.2006.12.005.

Prata, A.J., 2009. Satellite detection of hazardous volcanic clouds and the risk to global air traffic. Natural Hazards 51, 303–324. doi:10.1007/s11069-008-9273-z.

Prata, F., Rose, B., 2015. Volcanic Ash Hazards to Aviation. Second edi ed., Elsevier Inc. doi:10.1016/b978-0-12-385938-9.00052-3.

Press, W.H., Teukolsky, S.A., Vetterling, W., Flannery, B.P., 1996. Numerical Recipes in Fortran77. 2nd ed., Cambridge University Press, New York.

Prunty, S., 2019. Waves of Finite Amplitude, in: Graham, R.A., Davidson, L., Horie, Y. (Eds.), Introduction to Simple Shock Waves in Air. Springer Nature, Cham, pp. 35–79. doi:10.1007/978-3-030-02565-6_2.

Purcell, J.B.C., 1957. Control of Airborne Sound by Barriers. Noise Control 3, 20–58. doi:10.1121/1.2369268.

Raspet, R., 1998. Shock Waves, Blast Waves, and Sonic Booms, in: Crocker, M.J. (Ed.), Handbook of Acoustics. John Wiley & Sons, Inc., Hoboken. 5. chapter 27, pp. 329–339. doi:10.1002/9780470172513.ch31.

Reed, J., 1987. Air Pressure Waves From Mount St. Helens Eruptions. Journal of Geophysical Research 92, 11979–11992. doi:10.1029/JD092iD10p11979.

Reed, J.W., 1977. Atmospheric attenuation of explosion waves. The Journal of the Acoustical Society of America 61, 39. doi:10.1121/1.381266.

Reichman, B.O., Gee, K.L., Neilsen, T.B., Miller, K.G., 2016a. Quantitative analysis of a frequency-domain nonlinearity indicator. The Journal of the Acoustical Society of America 139, 2505–2513. doi:10.1121/1.4945787.

Reichman, B.O., Muhlestein, M.B., Gee, K.L., Neilsen, T.B., Thomas, D.C., 2016b. Evolution of the derivative skewness for nonlinearly propagating waves. The Journal of the Acoustical Society of America 139, 1390–1403. doi:10.1121/1.4944036.

Richardson, P., Karlstrom, L., 2019. The multi-scale influence of topography on lava flow morphology. Bulletin of Volcanology 81. doi:10.1007/s00445-019-1278-9.

Riedel, K., Sidorenko, A., 1995. Minimum Bias Multiple Taper Spectral Estimation. IEEE Transactions on Signal Processing 43, 188–195. doi:10.1109/78.365298.

Ripepe, M., Bonadonna, C., Folch, A., Delle Donne, D., Lacanna, G., Marchetti, E., Höskuldsson, A., 2013. Ash-plume dynamics and eruption source parameters by infrasound and thermal imagery: The 2010 Eyjafjallajökull eruption. Earth and Planetary Science Letters 366, 112–121. doi:10.1016/j.epsl.2013.02.005.

Ripepe, M., De Angelis, S., Lacanna, G., Poggi, P., Williams, C., Marchetti, E., Donne, D.D., Ulivieri, G., 2009. Tracking pyroclastic flows at soufrière hills volcano. Eos 90, 229–230. doi:10.1029/2009EO270001.

Ripepe, M., Lacanna, G., Pistolesi, M., Silengo, M.C., Aiuppa, A., Laiolo, M., Massimetti, F., Innocenti, L., Della Schiava, M., Bitetto, M., La Monica, F.P., Nishimura, T., Rosi, M., Mangione, D., Ricciardi, A., Genco, R., Coppola, D., Marchetti, E., Delle Donne, D., 2021. Ground deformation reveals the scale-invariant conduit dynamics driving explosive basaltic eruptions. Nature Communications 12. doi:10.1038/s41467-021-21722-2.

Ripepe, M., Marchetti, E., 2002. Array tracking of infrasonic sources at Stromboli volcano. Geophysical Research Letters 29, 33–1–33–4. doi:10.1029/2002GL015452.

Ripepe, M., Poggi, P., Braun, T., Gordeev, E., 1996. Infrasonic waves and volcanic tremor at Stromboli. Geophysical Research Letters 23, 181–184.

Rogers, N., 2015. The Composition and Origin of Magmas, in: The Encyclopedia of Volcanoes. second ed.. Elsevier Inc., pp. 93–112. doi:10.1016/b978-0-12-385938-9.00004-3.

Rogers, P.H., 1977. Weak-shock solution for underwater explosive shock waves. Journal of the Acoustical Society of America 62, 1412–1419. doi:10.1121/1.381674.

Rogers, P.H., Gardner, J.H., 1980. Propagation of sonic booms in the thermosphere. J. Acoust. Soc. Am 67, 78–91. doi:10.1121/1.383793.

Rowell, C.R., Fee, D., Szuberla, C.A., Arnoult, K., Matoza, R.S., Firstov, P.P., Kim, K., Makhmudov, E., 2014. Three-dimensional volcano-acoustic source localization at Karymsky Volcano, Kamchatka, Russia. Journal of Volcanology and Geothermal Research 283, 101–115. doi:10.1016/j.jvolgeores.2014.06.015.

Rudenko, O.V., Hedberg, C.M., 2013. Strong and weak nonlinear dynamics: Models, classification, examples. Acoustical Physics 59, 644–650. doi:10.1134/S1063771013060171.

Ruprecht, P., Bachmann, O., 2010. Pre-eruptive reheating during magma mixing at Quizapu volcano and the implications for the explosiveness of silicic arc volcanoes. Geology 38, 919–922. doi:10.1130/G31110.1.

Sabatini, R., Bailly, C., Marsden, O., Gainville, O., 2016a. Characterization of absorption and non-linear effects in infrasound propagation using an augmented Burgers' equation. Geophysical Journal International 207, 1432–1445. doi:10.1093/gji/ggw350.

Sabatini, R., Marsden, O., Bailly, C., Bogey, C., 2016b. A numerical study of nonlinear infrasound propagation in a windy atmosphere. Journal of the Acoustical Society of America 140. doi:10.1121/1.4958998.

Sakai, T., Yamasoto, H., Uhira, K., 1996. Infrasound accompanying C-type tremor at Sakurajima volcano. Bulletin of the Volcanological Society of Japan 41, 181–185.

Sanderson, R.W., Matoza, R.S., Fee, D., Haney, M.M., Lyons, J.J., 2020. Remote detection and location of explosive volcanism in Alaska with the EarthScope Transportable Array. Journal of Geophysical Research 125. doi:10.1029/2019JB018347.

Sawada, Y., 1996. Detection of Explosive Eruptions and Regional Tracking of Volcanic Ash Clouds with Geostationary Meteorological Satellite (GMS), in: Scarpa, R., Tilling, R.I. (Eds.), Monitoring and Mitigation of Volcano Hazards. Springer-Verlag, Berlin Heidelberg, pp. 299–314. doi:10.1007/978-3-642-80087-0_9.

Scarpa, R., Tilling, R.I., 1996. Monitoring and Mitigation of Volcano Hazards. Springer, Berlin.

Schminke, H.U., 2004. Volcanism. Second ed., Springer-Verlag, Berlin Heidelberg. doi:10.1007/978-3-642-18952-4.

Scholes, W.E., Salvidge, A.C., Sargent, J.W., 1971. Field performance of a noise barrier. Journal of Sound and Vibration 16, 627–642. doi:10.1016/0022-460X(71)90668-7.

Shapiro, A.H., 1954. The Dynamics and Thermodynamics of Compressible Fluid Flow. Ronald Press, New York.

Shepherd, M.R., Gee, K.L., Hanford, A.D., 2011. Evolution of statistical properties for a nonlinearly propagating sinusoid. The Journal of the Acoustical Society of America 130, EL8–EL13. doi:10.1121/1.3595743.

Sides, I.R., Edmonds, M., Maclennan, J., Swanson, D.A., Houghton, B.F., 2014. Eruption style at Kilauea Volcano in Hawai'i linked to primary melt composition. Nature Geoscience 7, 464–469. doi:10.1038/ngeo2140.

de Silva, S., Lindsay, J.M., 2015. Primary Volcanic Landforms, in: The Encyclopedia of Volcanoes. second ed.. Elsevier Inc., pp. 273–297. doi:10.1016/b978-0-12-385938-9.00015-8.

Simons, B.C., Jolly, A.D., Eccles, J.D., Cronin, S.J., 2020. Spatiotemporal Relationships between Two Closely-spaced Strombolian-style Vents, Yasur, Vanuatu. Geophysical Research Letters 47. doi:10.1029/2019GL085687.

Smith, C.M., Van Eaton, A.R., Charbonnier, S., McNutt, S.R., Behnke, S.A., Thomas, R.J., Edens, H.E., Thompson, G., 2018. Correlating the electrification of volcanic plumes with

ashfall textures at Sakurajima Volcano, Japan. Earth and Planetary Science Letters 492, 47–58. doi:10.1016/j.epsl.2018.03.052.

Sparks, R.S., 1978. The dynamics of bubble formation and growth in magmas: A review and analysis. Journal of Volcanology and Geothermal Research 3, 1–37. doi:10.1016/0377-0273(78)90002-1.

Spera, F.J., Schmidt, J.S., Bohrson, W.A., Brown, G.A., 2016. Dynamics and thermodynamics of magma mixing: Insights from a simple exploratory model. American Mineralogist 101, 627–643. doi:10.2138/am-2016-5305.

Spina, L., Taddeucci, J., Cannata, A., Gresta, S., Lodato, L., Privitera, E., Scarlato, P., Gaeta, M., Gaudin, D., Palladino, D.M., 2016. "Explosive volcanic activity at Mt. Yasur: A characterization of the acoustic events (9–12th July 2011). Journal of Volcanology and Geothermal Research 322, 175–183. doi:10.1016/j.jvolgeores.2015.07.027.

Spina, L., Taddeucci, J., Cannata, A., Sciotto, M., Del Bello, E., Scarlato, P., Kueppers, U., Andronico, D., Privitera, E., Ricci, T., Pena-Fernandez, J., Sesterhenn, J., Dingwell, D.B., 2017. Time-series analysis of fissure-fed multi-vent activity: a snapshot from the July 2014 eruption of Etna volcano (Italy). Bulletin of Volcanology 79. doi:10.1007/s00445-017-1132-x.

Stambaugh, M.C., Guyette, R.P., 2008. Predicting spatio-temporal variability in fire return intervals using a topographic roughness index. Forest Ecology and Management 254, 463–473. doi:10.1016/j.foreco.2007.08.029.

Stern, R.J., 2002. Subduction zones. Reviews of Geophysics 40, 3–1–3–38. doi:10.1029/2001RG000108.

Sutherland, L.C., Bass, H.E., 2004. Atmospheric absorption in the atmosphere up to 160 km. The Journal of the Acoustical Society of America 115, 1012–1032. doi:10.1121/1.1631937.

Taddeucci, J., Edmonds, M., Houghton, B., James, M.R., Vergniolle, S., 2015. Hawaiian and

Strombolian Eruptions. Second edi ed., Elsevier Inc. doi:10.1016/b978-0-12-385938-9.00027-4.

Taddeucci, J., Peña Fernández, J.J., Cigala, V., Kueppers, U., Scarlato, P., Del Bello, E., Ricci, T., Sesterhenn, J., Panunzi, S., 2021. Volcanic Vortex Rings: Axial Dynamics, Acoustic Features, and Their Link to Vent Diameter and Supersonic Jet Flow. Geophysical Research Letters 48. doi:10.1029/2021gl092899.

Taddeucci, J., Sesterhenn, J., Scarlato, P., Stampka, K., Del Bello, E., Pena Fernandez, J., Gaudin, J., 2014. High-speed imaging, acoustic features, and aeroacoustic computations of jet noise from Strombolian (and Vulcanian) explosions. Geophysical Research Letters 41, 3096–3102. doi:10.1002/2014GL059393.

Taflove, A., Hagness, S.C., 2005. Computational Electrodynamics: The Finite-Difference Time-Domain Method.

Taisne, B., Jaupart, C., 2011. Magma expansion and fragmentation in a propagating dyke. Earth and Planetary Science Letters 301, 146–152. doi:10.1016/j.epsl.2010.10.038.

Tameguri, T., Iguchi, M., Ishihara, K., 2002. Mechanism of Explosive Eruptions from Moment Tensor Analyses of Explosion Earthquakes at Sakurajima Volcano, Japan. Bulletin of the Volcanological Society of Japan 47, 197–215. doi:10.18940/kazan.47.4_197.

Tatge, R.B., 1973. Barrier-wall attenuation with a finite-sized source. The Journal of the Acoustical Society of America 53, 1317–1319. doi:10.1121/1.1913472.

Thompson, G., 2015. Seismic Monitoring of Volcanoes, in: Encyclopedia of Earthquake Engineering. Springer-Verlag, Berlin Heidelberg. doi:10.1007/978-3-642-36197-5_41-1.

Uhira, K., Takeo, M., 1994. The source of explosive eruptions of Sakurajima volcano, Japan. Journal of Geophysical Research 99, 17775–17789. doi:10.1029/94JB00990.

Vaughn, A.B., Leete, K.M., Gee, K.L., Adams, B.R., Downing, J.M., 2021. Evidence for nonlinear reflections in shock-containing noise near high-performance military aircraft. The Journal of the Acoustical Society of America 149, 2403–2414. doi:10.1121/10.0003932.

Vergniolle, S., Boichu, M., Caplan-Auerbach, J., 2004. Acoustic measurements of the 1999 basaltic eruption of Shishaldin volcano, Alaska 1. Origin of Strombolian activity. Journal of Volcanology and Geothermal Research 137, 109–134. doi:10.1016/j.jvolgeores.2004.05.003.

Vergniolle, S., Caplan-Auerbach, J., 2006. Basaltic thermals and Subplinian plumes: Constraints from acoustic measurements at Shishaldin volcano, Alaska. Bulletin of Volcanology 68, 611–630. doi:10.1007/s00445-005-0035-4.

Vergniolle, S., Métrich, N., 2016. A bird's eye view of "Understanding volcanoes in the Vanuatu arc". Journal of Volcanology and Geothermal Research 322, 1–5. doi:10.1016/j.jvolgeores.2016.08.012.

Vu, B., 2007. Predicting the Acoustic Environment Induced by the Launch of the Ares I Vehicle. Technical Report. National Aeronautics and Space Administration. KSC Technology Development and Application 2006-2007.

Walowski, K.J., Wallace, P.J., Clynne, M.A., Rasmussen, D.J., Weis, D., 2016. Slab melting and magma formation beneath the southern Cascade arc. Earth and Planetary Science Letters 446, 100–112. doi:10.1016/j.epsl.2016.03.044.

Watson, L.M., Dunham, E.M., Johnson, J.B., 2019. Simulation and inversion of harmonic infrasound from open-vent volcanoes using an efficient quasi-1D crater model. Journal of Volcanology and Geothermal Research 380, 64–79. doi:10.1016/j.jvolgeores.2019.05.007.

Watson, L.M., Dunham, E.M., Mohaddes, D., Labahn, J., Jaravel, T., Ihme, M., 2021. Infra-

sound Radiation From Impulsive Volcanic Eruptions: Nonlinear Aeroacoustic 2D Simulations. Journal of Geophysical Research: Solid Earth 126, 1–28. doi:10.1029/2021jb021940.

Watson, L.M., Iezzi, A.M., Toney, L., Maher, S.P., Fee, D., Mckee, K., Ortiz, H.D., Matoza, R.S., Gestrich, J.E., Bishop, J.W., Witsil, A.J.C., Anderson, J.F., Johnson, J.B., 2022. Volcano infrasound : progress and future directions. Bulletin of Volcanology , 1–13doi:10.1007/s00445-022-01544-w.

Waxler, R., Assink, J., 2019. Propagation Modeling Through Realistic Atmosphere and Benchmarking, in: Pichon, A.L., Blanc, E., Hauchecorne, A. (Eds.), Infrasound Monitoring for Atmospheric Studies. Springer, Cham. chapter 15, pp. 509–549. doi:10.1007/978-1-4020-9508-5.

Whitaker, R.W., Norris, D.E., 2008. Infrasound Propagation, in: Havelock, D., Kuwano, S., Vorlander, M. (Eds.), Handbook of Signal Processing in Acoustics. Springer, New York, New York, pp. 1497–1519. doi:10.1007/978-0-387-30441-0_82.

Witsil, A.J., Johnson, J.B., 2018. Infrasound explosion and coda signal investigated with joint analysis of video at Mount Erebus, Antarctica. Journal of Volcanology and Geothermal Research 357, 306–320. doi:10.1016/j.jvolgeores.2018.05.002.

Wohletz, K.H., McGetchin, T.R., Sandford, M.T., Jones, E.M., 1984. Hydrodynamic aspects of caldera-forming eruptions: numerical models. Journal of Geophysical Research 89, 8269–8285. doi:10.1029/JB089iB10p08269.

Woods, A.W., 1995. A model of vulcanian explosions. Nuclear Engineering and Design 155, 345–357. doi:10.1016/0029-5493(94)00881-X.

Woulff, G., McGetchin, T.R., 1976. Acoustic noise from volcanos - theory and experiment. Geophysical Journal of the Royal Astronomical Society 45, 601–616. doi:10.1111/j.1365-246X.1976.tb06913.

Wright, W.M., 1983. Propagation in air of N waves produced by sparks. Journal of the Acoustical Society of America 73, 1948–1955. doi:10.1121/1.389585.

Yamada, T., Aoyama, H., Nishimura, T., Iguchi, M., Hendrasto, M., 2017. Volcanic eruption volume flux estimations from very long period infraound signals. Geophysical Research Letters 44, 143–151. doi:10.1007/s00445-018-1244-y.

Yamamoto, K., Takagi, K., 1992. Expressions of Maekawa's chart for computation. Applied Acoustics 37, 75–82. doi:10.1016/0003-682X(92)90012-H.

Yokoo, A., Iguchi, M., Tameguri, T., Yamamoto, K., 2013. Processes Prior to Outbursts of Vulcanian Eruption at Showa Crater of Sakurajima Volcano. Bull. Volcanol. Soc. Japan 58, 163–181. doi:10.18940/kazan.58.1_163.

Yokoo, A., Ishihara, K., 2007. Analysis of pressure waves observed in Sakurajima eruption movies. Earth, Planets and Space 59, 177–181. doi:10.1186/BF03352691.

Yokoo, A., Suzuki, Y.J., Iguchi, M., 2014. Dual Infrasound Sources from a Vulcanian Eruption of Sakurajima Volcano Inferred from Cross-Array Observation. Seismological Research Letters 85, 1212–1222. doi:10.1785/0220140047.

Yokoo, A., Tameguri, T., Iguchi, M., 2009. Swelling of a lava plug associated with a Vulcanian eruption at Sakurajima Volcano, Japan, as revealed by infrasound record: Case study of the eruption on January 2, 2007. Bulletin of Volcanology 71, 619–630. doi:10.1007/s00445-008-0247-5.

Young, S.M., Gee, K.L., Neilsen, T.B., Leete, K.M., 2015. Outdoor measurements of spherical acoustic shock decay. The Journal of the Acoustical Society of America 138, EL305. doi:10.1121/1.4929928.